Vacuum decay, gravitational waves and magnetic fields in the early universe

Wickens, Alastair

Awarding institution:
King's College London

Vacuum Decay, Gravitational Waves and Magnetic Fields in the Early Universe

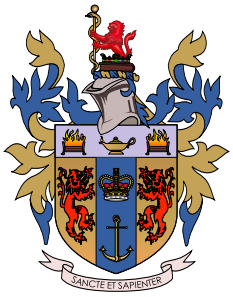

Alastair Wickens

Department of Physics
King's College London

This dissertation is submitted for the degree of
Doctor of Philosophy

August 2021

To Mum and Dad

Acknowledgements

I am extremely grateful to my supervisor Professor Malcolm Fairbarn for his guidance, support and patience during the course of my PhD.

Abstract

If a quantum field gets stuck in a meta-stable false vacua it can decay via a first order phase transition to a lower energy vacuum, either by thermally jumping over the potential barrier or tunnelling through it. Bubbles of true vacuum nucleate and if the nucleation rate is large enough expand to engulf the universe. In this thesis we study the underlying tunnelling process by which this can happen as well as the observational consequences of first order transitions in the early universe.

With regard to the tunnelling process we numerically investigate false vacuum decay to a non-adjacent minima of a potential with numerous meta-stable vacua, as motivated by modern conceptions of the string theory landscape. Our code finds stable tunnelling solutions to non-adjacent minima for certain single and two field toy-model landscapes.

With regard to observational consequences we study the characteristic frequency spectrum of gravitational waves produced by a first order phase transition in a very cold $\mathrm{SU}(2)$ hidden sector, polarisation of the stochastic gravitational wave background generated by a period of helical MHD plasma turbulence that can follow a generic transition and finally, primordial magnetic fields generated from a first order transition in two Standard Model extensions (SM+H^6 and SM_{B-L}) which can evolve to intergalactic scales if helicity is initially seeded in the gauge field or kinetically in the plasma.

Table of contents

Chapter 1

Introduction

Phase changes are ubiquitous in nature. We observe them when boiling water in a kettle, when spins align in a ferromagnet and also expect them to have taken place moments after the Big Bang when fundamental quantum fields of the universe took on new values. It is with the impact of the last of these scenarios that this thesis will be concerned.

Examples of phase changes in the early universe include the electroweak phase transition which endowed particles with mass via the Higgs mechanism and the QCD phase transition which bound quarks into hadrons forming most of the matter we see today. Under our current understanding of the universe, based on the Standard Model of particle physics, it is thought both these phase change examples would have taken place via a cross-over transition where the field rolled down its potential and the universe smoothly transitioned from the high energy to low energy phase. However we know that our understanding of the universe is not complete and so, whilst the Standard Model is one of the crowning achievements of physics in the 20th century, we know it needs modifications. Many such modifications (Chapter 5) induce potential barriers between the high energy and low energy phases of the fields that permeate the universe, such that the universe gets trapped in the meta-stable 'false vacuum' phase. Similar to the analogous process in 1D quantum mechanics (Chapter 2) these fields can then decay to a lower energy 'true vacuum' by tunnelling through the barrier whilst in thermal settings fluctuations can alternatively jump over it.

A novel interpretation of false vacuum decay via tunnelling (Chapter 3) in terms of a bubble nucleation process, similar to that seen in a super-heated fluid, was suggested in 1977 by Sydney Coleman [1] and later adapted to thermal scenarios in [2]. Coleman's insight predicted that scalar field bubbles of the true vacuum would nucleate at a significant rate in scenarios where tunnelling to the true vacuum was energetically favourable and that these bubbles would subsequently expand and engulf the universe. It is generally expected that a significant amount of energy was instantaneously released during such cosmological phase transitions, creating violent events in the history of the early universe that could

leave observational traces we can search for today such as a background of primordial gravitational waves (GW).

Primordial gravitational waves propagate unimpeded until today, only being stretched by the expansion of the universe and as such provide us with a natural means of observing the universe mere moments after it was created. With the first detection of gravitational waves from the collision of two binary black holes in 2015 [3] and the ambitious new generation of detectors that are expected to soon come online, it is widely expected gravitational waves will become the de-facto diagnostic tool with which we can further our understanding of the universe. Indeed, in perhaps a teaser of the potential discoveries of new physics to come, in [4] the NanoGrav collaboration made a detection of a gravitational wave signal that could have cosmological origin, such as from a first order phase transition in a hidden sector [5–7] as we consider in Chapter 7 or some other early universe source [8–12].

In this thesis we investigate the production and detection of gravitational waves from cold hidden sectors [13] (Chapters 6 & 7), polarisation of the stochastic gravitational wave background [14] (Chapter 8) and primordial magnetic fields [15] (Chapter 9), all following a cosmological phase transition. In addition we consider the possibility for tunnelling events to occur in some single and multi-field potentials which contain numerous false vacua (Chapter 4) as motivated by modern considerations of the 'string theory landscape'.

1.1 Thesis Structure

The outline of this thesis is as follows.

In Chapter 2 we will both motivate and develop the mathematical formalism of Euclidean tunnelling solutions in 1D quantum mechanics, culminating in the non-perturbative solutions that describe decaying metastable states. We finish the chapter by discussing characteristic properties of these solutions and their associated Euclidean action which will prove crucial when we generalise them to quantum field theory (QFT).

In Chapter 3 we generalise the formalism of our 1D Euclidean tunnelling solutions to bounce solutions in QFT, which will be the fundamental mathematical objects underpinning the remainder of the thesis. We describe in detail the conceptual interpretation of false vacuum decay via a bubble nucleation process, as pioneered by Coleman in the late 1970's [1]. We will then outline the 'overshoot/undershoot' algorithm which is the most commonly used method of calculating bounce solutions and vacuum bubble nucleation rates, before finally finishing the chapter by exploring the qualitatively different solutions one can obtain by varying the shape of the potential.

In Chapter 4 we explore the possibility of tunnelling to non-adjacent minima in a potential with many fields, as motivated by modern notions of a 'landscape' of metastable

vacua in string theory. The extreme numerical sensitivities expected using traditional shooting based methods lead us to search for a new numerical approach using 'tunnelling potentials' [16, 17] to calculate false vacuum decay solutions. We provide a detailed description of our numerical algorithm before applying it to some example potential landscapes in both the single field and two field case. Rather than exclusively focusing on potentials with a concrete physical interpretation, we will rather attempt to identify the qualitative features of those potentials which succeed in finding a solution and those that fail. This can form the basis of any further investigation into the characteristic features of multi-minima potential landscapes which concretely don't permit false vacuum decay solutions and those that do.

In Chapter 5 we discuss how false vacuum decay can take place in the early universe in the form of cosmological first order phase transitions. We outline the two main mechanisms by which bubbles can nucleate and engulf the universe: quantum tunnelling through the potential barrier or thermal fluctuations that jump over it. We go on to detail the dynamics of bubble walls expanding in the early universe thermal plasma, a crucial area of current research due to the role it has in dictating where most of the energy is stored after the transition which directly affects the shape of any gravitational wave signal. Finally we conclude the chapter by detailing three possible extensions to the Standard Model that admit first order phase transitions, each of which we will use in our study of gravitational wave emission and primordial magnetic field generation in later chapters.

In Chapter 6 we study phase transitions in cold hidden sectors and the qualitatively different behavior they exhibit as compared to hidden sectors that are at the same temperature as the visible sector. Adopting an SU(2) hidden sector as our generic toy model we discuss mechanisms by which a temperature hierarchy could be generated between the hidden and visible sectors and summarise the cosmological bounds on hidden sectors when they are colder than the visible sector. We discuss a possible phase transition evolution unique to this situation whereby a sufficiently cold hidden sector could fail to undergo a thermal transition and subsequently transition through the nucleation of bubbles by quantum tunnelling. Finally we analyse the dynamics of the hidden scalar field bubble walls expansion in the hidden plasma, which governs the form of the gravitational wave signal, and see that in the case of the tunnelling transition the bubble walls might accelerate with completely negligible friction. This chapter is based on the work done in [13] and my personal contributions include: the cosmological constraints in Sec. 6.1 and parts of Appendix B, my own independent numerical implementation to verify the results of Fig. 6.1, and the design of the plot in Fig. 6.3.

In Chapter 7 we study the spectrum of gravitational waves produced by a first order phase transition in a hidden sector that is colder than the visible sector. We show the impact a cold hidden sector undergoing a thermally induced transition can have on the gravitational wave signal compared to if the hidden sector was at the same temperature

as the visible sector and use our results to show this could lead to signals in a frequency range that would otherwise be ruled out by constraints from Big Bang nucleosynthesis. Alternatively, we show that if the hidden sector is sufficiently cold so that it goes through a tunnelling transition then the resulting gravitational wave spectrum has a characteristic frequency dependence, which may allow such cold hidden sectors to be distinguished from models in which the hidden and visible sector temperatures are similar. We compare our results to the sensitivity of the future gravitational wave experimental programme. This chapter is again based on the work done in [13] and my personal contributions include: the review material in the early parts of the chapter, the design and creation of Figs. 7.1-7.3, and parts of the analysis in the text.

In Chapter 8 we study how helical magnetohydrodynamic turbulence in the primordial plasma after a phase transition may source polarisation in the stochastic gravitational wave background (SGWB). We first consider how the presence of helical turbulence in the primordial plasma can trigger an inverse cascade process that boosts the gravitational wave signal. We then go on to explore whether any sign of this epoch could be found imprinted on the SGWB via its intrinsic circular polarisation, presenting our results in terms of their sensitivity to the LISA experiment. This chapter is based on the work done in [14] and my personal contributions include the vast majority of the plots and text, apart from: Fig. 8.3, the first part of Sec. 8.6.1, and Appendix D.

Finally, in Chapter 9 we study the possibility of generating a primordial magnetic field from a first order phase transition which could seed the unexplained large scale magnetic fields we currently observe in cosmic voids. We first discuss the generation and subsequent evolution of the primordial field in a plasma background of helical turbulence and review current experimental constraints on any intergalactic magnetic field (IGMF). Finally, we present illustrative results in the two scenarios we study, SM+H^6 and SM$_{BL}$, correlating the calculated IGMF in these models with their possible GW and collider signals. This chapter is based on the work done in [15] and my personal contributions include everything from Sec. 9.1-9.5.

Chapter 2

Tunnelling in Quantum Mechanics

The traditional approach to solving tunnelling problems in 1D quantum mechanics involves using a method called the WKB approximation [18]. The WKB method provides us with a systematic way of estimating the probability that an incident quantum particle penetrates a potential barrier, $V(x)$, by approximating the potential $V(x)$ in the classically disallowed region $E \leq V$ as a series of rectangular barriers of width ε as seen in Fig. 2.1. Using well known results for rectangular barrier penetration and enforcing continuity boundary conditions on the solution at the classical turning points one can integrate over x to find this barrier penetration probability.

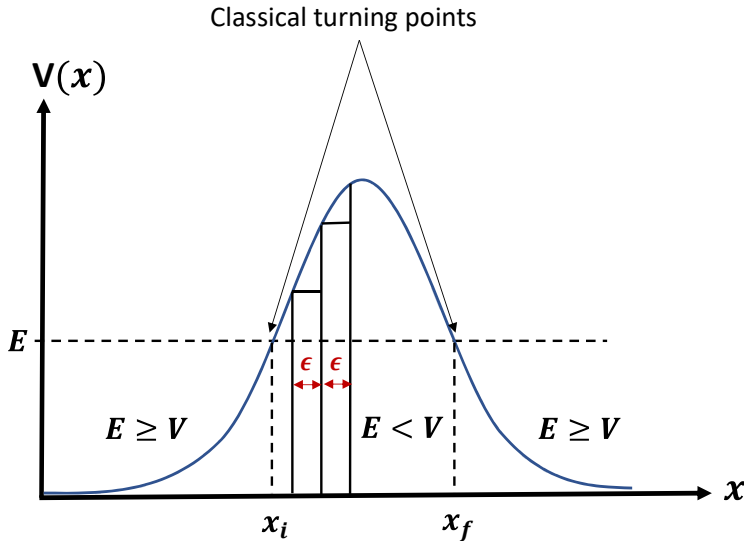

Fig. 2.1 *The WKB Approach.*

Although this approach is succesful in 1D quantum mechanics and can even be generalised to a case with many degrees of freedom [19], when we attempt to generalise this method one step further to that of a quantum field with infinite degrees of freedom

things become significantly more difficult [20]. In this Chapter we aim to develop an alternative prescription of tunnelling in 1D quantum mechanics that can be more readily applied to the false vacuum decay scenarios in QFT which we know could be so crucial to our understanding of the universe. This new prescription will be based upon one of the fundamental constructs of modern quantum field theory: the path integral.

2.1 Euclidean Tunnelling

In this section we will seek to develop a general description of tunnelling in quantum mechanics in terms of path integrals. This will naturally lead us to consider tunnelling as a process that takes place not in the usual Minkwoski space of Special Relativity but in Euclidean space via a class of non-perturbative objects called instantons [21]. In precise terms, these are solutions to the classical equations of motion that emerge when approaching tunnelling problems in Euclidean space. The specific case that will ultimately be of interest to us is their use when considering scenarios in 1D quantum mechanics with a metastable state decaying via tunnelling through the potential barrier as discussed in Sec 2.2. This will provide us with a means of tackling false vacuum decay in a QFT setting in Chapter 3.

2.1.1 The sum over histories approach

A single quantum particle of unit mass moving in one spatial dimension in a potential $V(x)$, from time $-T/2$ to time $+T/2$, has action

$$S = \int_{-T/2}^{T/2} dt L(x,\dot{x}) = \int_{-T/2}^{T/2} dt \left[\frac{1}{2}\left(\frac{dx}{dt}\right)^2 - V(x)\right], \tag{2.1}$$

where L is the Lagrangian and $\dot{x} = \frac{dx}{dt}$. We can then express the probability amplitude for such a particle to begin at $(x_i, -T/2)$ and evolve to $(x_f, T/2)$ using Feymann's sum over histories approach [22] with the path integral

$$\langle x_f | e^{-iHT/\hbar} | x_i \rangle = N \int D[x(t)] e^{iS/\hbar}, \tag{2.2}$$

where H is the Hamiltonian and N is a normalisation constant. For clarity we review the significance of each side of this equation. First examining the LHS of Eq. (2.2), $|x_i\rangle$ and $|x_f\rangle$ are the particle's initial and final position eigenstates with $e^{-iHT/\hbar}$ the time evolution operator. On the RHS we have a functional integral that serves to integrate over all possible trajectories $x(t)$ between $(x_i, -T/2)$ and $(x_f, T/2)$. Each trajectory is weighted by a phase factor, $e^{iS/\hbar}$, which upon extremising the action gives us the dominating in-phase

contribution to the quantum probability amplitude we seek. Solutions to Eq. (2.2) will be a sum of oscillating exponentials [21].

2.1.2 Wick rotation and Euclidean space

A simple observation regarding the 1D tunnelling scenario in Fig. 2.1 will turn out to have a profound influence on our treatment of tunnelling throughout the rest of this thesis. If we were to interpret a particle with constant energy E tunnelling in the classically disallowed region $E < V$ as having a negative kinetic energy $K = -k_1$ then we can write

$$\begin{aligned} \frac{1}{2}\left(\frac{dx}{dt}\right)^2 &= -k_1 \\ \implies \frac{dx}{dt} &= i\sqrt{2k_1}, \end{aligned} \tag{2.3}$$

where the particle has an imaginary velocity. Alternatively, making the co-ordinate transformation (termed Wick rotation) $t = -i\tau$ so that $\frac{d\tau}{dt} = i$ then we can write

$$\begin{aligned} \frac{1}{2}\left(\frac{d\tau}{dt}\frac{dx}{d\tau}\right)^2 &= -k_1 \\ \implies \frac{dx}{d\tau} &= \sqrt{2k_1}, \end{aligned} \tag{2.4}$$

where $\frac{dx}{d\tau}$ is real and is in some sense a particle 'velocity' within the barrier. This approach allows us to parametrise the configuration space within the barrier and is crucial to our later study of QFT tunnelling in Chapter 3. This imaginary time space is also termed Euclidean space for reasons that will become clear as we proceed through this chapter.

We now employ this Euclidean approach to uncover the wealth of new and insightful physics that instanton methods give us. Wick rotating Eq. (2.1) to Euclidean space by making the transformation $t = -i\tau$ so that $\frac{d\tau}{dt} = i$ gives us that

$$\begin{aligned} S &= \int_{-T/2}^{T/2} dt \left[\frac{1}{2}\left(\frac{d\tau}{dt}\frac{dx}{d\tau}\right)^2 - V(x)\right] \\ &= i\int_{-\tau_0/2}^{\tau_0/2} d\tau \left[\frac{1}{2}\left(\frac{dx}{d\tau}\right)^2 + V(x)\right]. \end{aligned} \tag{2.5}$$

So therefore we can write

$$iS \to -S_E = -\int_{-\tau_0/2}^{\tau_0/2} d\tau \left[\frac{1}{2}\left(\frac{dx}{d\tau}\right)^2 + V(x)\right], \tag{2.6}$$

where $S_E = S_E(x,\dot{x})$ is the Euclidean action

$$S_E(x,\dot{x}) = \int_{-\tau_0/2}^{\tau_0/2} d\tau \left[\frac{1}{2}\left(\frac{dx}{d\tau}\right)^2 + V(x)\right]. \tag{2.7}$$

Therefore Wick rotating the LHS of Eq. (2.2) and making the replacement in Eq. (2.6) to its RHS, we obtain the Euclidean (or imaginary time) version of Feynman's sum over histories

$$\langle x_f|e^{-H\tau_0/\hbar}|x_i\rangle = N\int D[x(\tau)]e^{-S_E/\hbar}. \tag{2.8}$$

Expanding the LHS of Eq. (2.8) in terms of the complete set of energy Eigenstates of the Hamiltonian (H is not a function of time and therefore is unchanged by a Wick rotation)

$$H|n\rangle = E_n|n\rangle \tag{2.9}$$

and by inserting a resolution of the identity, we then obtain

$$\langle x_f|e^{-H\tau_0/\hbar}|x_i\rangle = \sum_n e^{-E_n\tau_0/\hbar}\langle x_f|n\rangle\langle n|x_i\rangle. \tag{2.10}$$

Solutions to Eq. (2.10) are clearly no longer oscillatory as in Eq. (2.2) but are exponentially decaying.

Now, looking at the form of Eq. (2.10) we see that, when τ_0 is large, the leading order term of the sum, where $n = 0$, dominates all other terms with $n > 0$ due to the exponential decay factor [21]. Therefore in the limit $\tau_0 \to \infty$ we can write

$$\begin{aligned}\langle x_f|e^{-H\tau_0/\hbar}|x_i\rangle &\approx e^{-E_0\tau_0/\hbar}\langle x_f|0\rangle\langle 0|x_i\rangle \\ &= e^{-E_0\tau_0/\hbar}\psi_0(x_f)\psi_0^*(x_i),\end{aligned} \tag{2.11}$$

where E_0 is the energy of the ground energy eigenstate and $\psi_0(x)$ is the wave function of the ground energy eigenstate. Thus in the limit $\tau_0 \to \infty$ equation Eq. (2.11) gives us both the ground state energy E_0 and the ground state wave function $\psi_0(x)$.

2.1.3 The classical Euclidean action

Having analysed the LHS of Eq. (2.8) we now turn to the task of evaluating the RHS. Each of the paths this Euclidean functional integral describes are weighted by a factor $e^{-S_E/\hbar}$. Now if S_E is taken to be large then the quasi-classical approximation assumes the path integral is dominated by those trajectories that are in the immediate vicinity of the classical stationary path [21]. This can be seen by the fact that trajectories close to the classical trajectory have comparable actions and thus similar weight factors whereas the contribution from paths further away are exponentially suppressed the further you get

from the minimum. This results in a strong contribution to the probability amplitude in the region of the classical path. Those paths close to the classical path are known as 'quantum corrections'.

With this knowledge we can see that we can re-express Eq. (2.8) in the rather more heuristic form

$$\langle x_f|e^{-H\tau_0/\hbar}|x_i\rangle = e^{-S_{cl}/\hbar} \times (\text{quantum corrections}), \tag{2.12}$$

where $S_{cl} = S_{cl}(x,\dot{x})$ is the classical Euclidean action (i.e. the stationary action) and is assumed to be large. For simplicity, we also assume $S_{cl}(x,\dot{x})$ is the single stationary point of the action. If there were more than one, we would have to sum over them [21].

2.1.4 The Euclidean equations of motion

We now look to explore the behaviour of our theory along its stationary path [21], which we do by finding the extremal of the action. First we assume a small perturbation, $\delta x(\tau)$, from the single stationary path, $x_{cl}(\tau)$, that minimises the Euclidean action in Eq. (2.7). Thus we can write

$$\begin{aligned} 0 = \delta S_E &= S_E[x_{cl}(\tau)+\delta x(\tau)] - S_E[x_{cl}(\tau)] \\ &= \delta x \frac{\partial S_E}{\partial x}\bigg|_{x=x_{cl}} + \delta\dot{x}\frac{\partial S_E}{\partial \dot{x}}\bigg|_{x=x_{cl}} + \ldots \\ &= \delta x \frac{\partial S_E}{\partial x}\bigg|_{x=x_{cl}} + \left[\frac{d}{d\tau}\delta x\right]\frac{\partial S_E}{\partial \dot{x}}\bigg|_{x=x_{cl}} + \ldots \\ &= \delta x \frac{\partial S_E}{\partial x}\bigg|_{x=x_{cl}} + \frac{d}{d\tau}\left[\delta x \frac{\partial S_E}{\partial \dot{x}}\bigg|_{x=x_{cl}}\right] - \delta x \frac{d}{d\tau}\left[\frac{\partial S_E}{\partial \dot{x}}\bigg|_{x=x_{cl}}\right] + \ldots \end{aligned} \tag{2.13}$$

Using Eq. (2.7) we can evaluate $\frac{\partial S_E}{\partial x}|_{x=x_{cl}}$ and $\frac{\partial S_E}{\partial \dot{x}}|_{x=x_{cl}}$ in the last line of Eq. (2.13) to obtain

$$0 = \delta S_E = \int_{-\tau_0/2}^{\tau_0/2} d\tau \left[V'(x_{cl}) - \frac{d^2x_{cl}}{d\tau^2}\right]\delta x(\tau), \tag{2.14}$$

where $V'(x)$ is a spatial derivative and we have used integration by parts and have also applied the boundary conditions

$$\delta[x(\pm\tau_0/2)] = 0. \tag{2.15}$$

Since the perturbation, $\delta x(\tau)$, in Eq. (2.14) is arbitrary, the Euclidean equations of motion are

$$\frac{d^2x_{cl}}{d\tau^2} = \frac{dV(x_{cl})}{dx}. \tag{2.16}$$

Inspecting Eq. (2.16), we see it has the same form as as the usual classical equations of motion apart from an additional minus sign and therefore we interpret it as describing

motion of a particle moving in a negative potential $-V(x_{cl})$ [1]. This particle-like solution is often referred to as a 'pseudoparticle' in the literature [23]. This is a key analogy that we will repeatedly make use of throughout the rest of this thesis. Under this analogy, the energy, E, is therefore a constant of the motion that can be written

$$E = \frac{1}{2}\left(\frac{dx_{cl}}{d\tau}\right)^2 - V(x_{cl}) = \text{Constant}. \tag{2.17}$$

The key take away from this section is that the classical Euclidean action describes the motion of a particle that is moving in a negative potential $-V(x)$ (see Eq. (2.16)), which we can solve to find a set of solutions that can then be analytically continued back to Minkowski space. In other words if we have a scenario in Minkowski space involving particle motion in some potential $V(x)$, then, by simply switching the sign of $V(x)$ and solving the resulting equations of motion in the 'upside down' potential, we can unearth a wealth of new solutions to the motion of the particle that were previously hidden to us. Such solutions go by the name of instantons and as we will see are extremely useful for describing tunnelling effects.

2.1.5 The instanton solution to a double well potential

It it is possible to verify the validity of our Euclidean path integral method by deriving known results for the quantum harmonic oscillator as done in [21], but we move directly onto a scenario that is more relevant for our purposes.

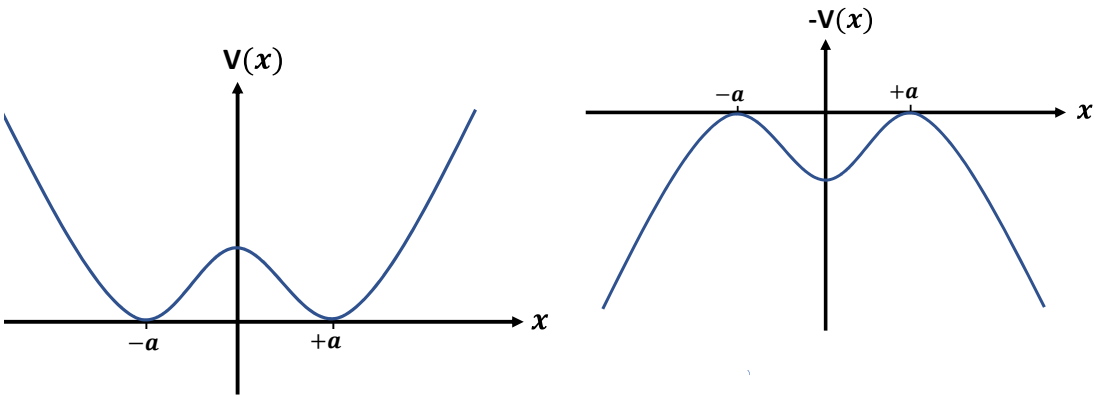

(a) *A double well potential* ***(b)*** *A double well potential after Wick rotation*

Fig. 2.2 *A symmetric double well potential with two degenerate minima.*

In Fig. 2.2a we consider an example with a particle in a 1D symmetric double well potential, $V(x)$, with 2 degenerate minima at $x = \pm a$. We assume the potential is symmetric (i.e. $V(-x) = V(x)$) and put $V''(\pm a) = \omega^2$, as is defined in the single well case [21]. After Wick rotating to imaginary time, we consider mechanical motion of our pseudoparticle in the upside down potential $-V(x)$ as seen in Fig. 2.2b. From Eq. (2.17) we require constant 'energy' solutions satisfying the Euclidean equations of motion in Eq. (2.16) and boundary conditions $x(-\tau_0/2) = x_i$ and $x(\tau_0/2) = x_f$. We also enforce the additional condition that the particle is stationary at the boundaries i.e. $\frac{dx(\pm\tau_0/2)}{d\tau} = 0$. This additional constraint means that we can take $\tau_0 \to \infty$, as is required by Eq. (2.11), to generate solutions of finite energy defined by the ground energy eigenstate with energy E_0.

Appart from the trivial solutions describing a quantum harmonic oscillator [21] where the particle begins and ends $x = a$ and the other where it begins and ends at $x = -a$, there is one additional class of constant energy solutions where the particle begins atop the hill at $x = -a$, falls into the well, and comes to rest on the peak of the right-hand hill at $x = a$.

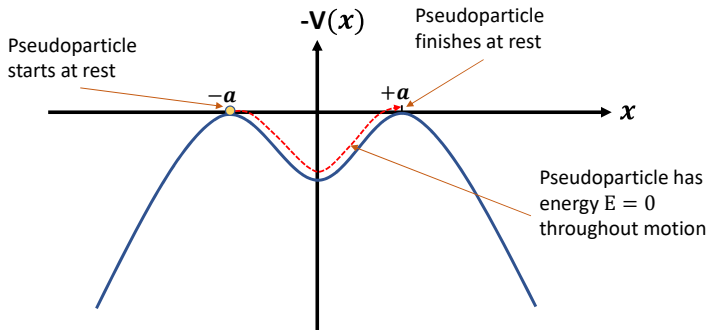

Fig. 2.3 *Instanton mechanical motion analogy.*

This trajectory is shown in Fig. 2.3 and solutions of this type are called instantons. If we were to Wick rotate back to real time and view solutions of this type in the right-way up potential $V(x)$ then we would see that they describes motion in the classically forbidden region $E < V$. In other words, the solution describes the barrier penetration path of a particle that begins at rest from the minimum at $x = -a$, tunnels through the barrier in $V(\phi)$, and emerges at the other minimum at $x = a$ where it comes to rest. By a symmetry argument we could also solve this problem for the particle beginning at $x = a$ and ending at $x = -a$ and we call this object an anti-instanton.

Again returning to our mechanical motion analogy, with the knowledge that our instanton solutions will be of constant energy we can see from Fig. 2.3 that we are free to choose energy $E = 0$. Then from Eq. (2.17) we have

$$\frac{dx_I}{d\tau} = (2V)^{\frac{1}{2}}, \tag{2.18}$$

where $x_I(\tau)$ is the path of the instanton.

Now for $\tau_0 \to \infty$ we require that $\frac{dx_I}{d\tau} \to 0$ as $x_I \to a$ and so we can series expand V around $x = a$ in Eq. (2.18) so that to second order

$$\begin{aligned} \frac{dx_I}{d\tau} &= \left[2V(a) + 2V'(a)(x-a) + V''(a)(x-a)^2\right]^{\frac{1}{2}} \\ &= \omega(a-x), \end{aligned} \tag{2.19}$$

where we have used that $V(a) = 0$, $V'(a) = 0$ and $V''(a) = \omega^2$. Therefore for $\tau_0 \to +\infty$ we have from the result in Eq. (2.19)

$$(a-x) \propto e^{-\omega\tau} \tag{2.20}$$

and can conclude from this that the instanton has a well defined size in imaginary time $\tau \sim \frac{1}{\omega}$ [24].

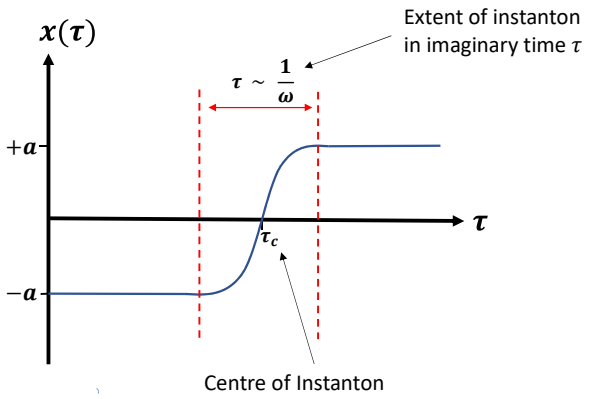

Fig. 2.4 *A 1D instanton solution.*

This can be seen in Fig. 2.4 where we note that the centre of the instanton τ_c specifies its temporal size. Their finite extent in τ is a key property of instantons that gives rise to many of their unique characteristics, as we will soon see.

Substituting Eq. (2.18) into Eq. (2.7) we can express the Euclidean action S_I for the instanton solution $x_I(\tau)$, starting from stationary at $x_I(-\tau_0/2) = -a$ and coming to rest at $x_I(\tau_0/2) = a$ as

$$\begin{aligned} S_I &= \int_{-\tau_0/2}^{\tau_0/2} d\tau (2V) \\ &= \int_{-a}^{a} dx (2V)^{\frac{1}{2}}. \end{aligned} \tag{2.21}$$

Making a transformation $\tau_0 \to \tau + \delta\tau$ to the result of Eq. (2.21) and we see that the action S_I remains unchanged.

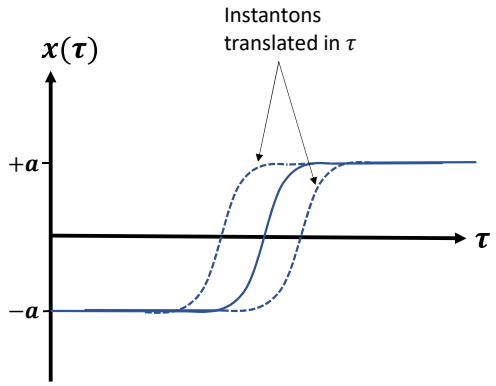

Fig. 2.5 *A 1D instanton solution translated in imaginary time τ.*

Intuitively, we can also see this from Fig. 2.5 where the instanton solution can be translated in τ and will have exactly the same profile. As we are integrating over the whole range of τ and the instanton is localised in extent, we can see that the action of the instanton will be the same regardless of where its centre τ_c lies. Thus we can conclude the instanton solution exhibits translational invariance in the imaginary time co-ordinate τ. Indeed, in solving the Euclidean equations of motion, a family of instanton solutions are mapped out that are well separated in τ. Such a set of solutions can be interpreted as multiple tunnelling events as discussed in [25].

From Eq. (2.12), the probability amplitude for one such instanton tunnelling event is expressed

$$\begin{aligned} \langle x = a | e^{-H\tau_0/\hbar} | x = -a \rangle &= e^{-E_0\tau_0/\hbar} \psi_0(a) \psi_0^*(-a) \\ &= N e^{-S_I/\hbar} \times (\text{quantum corrections}), \end{aligned} \tag{2.22}$$

where the instanton $x_I(\tau)$ is a stationary path of the action and we have taken $\tau_0 \to \infty$ so that the position eigenstates $|x = \pm a\rangle$ refer to particles in the ground state. The quantum correction factor in Eq. (2.22) arises from isolating and integrating over [26] the zero eigenmode that arises from the τ translational invariance of the the instanton as discussed above.

2.2 The Bounce Solution in 1D Quantum Mechanics

When we consider a scenario with a metastable state decaying due to barrier penetration then we stumble upon perhaps the most useful instanton type solution that can be readily generalised to QFT: the bounce solution.

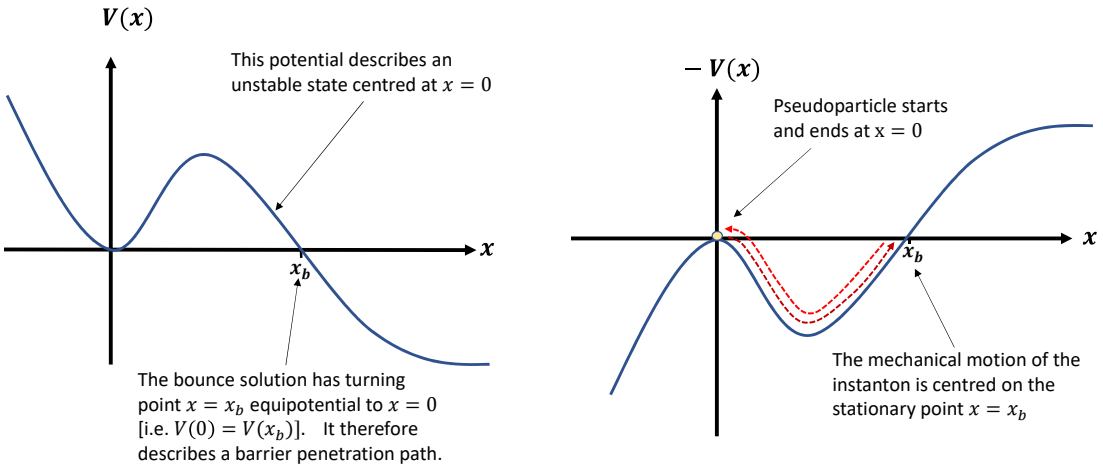

(a) *Before Wick rotation*

(b) *After Wick rotation, showing the stationary bounce path*

Fig. 2.6 *The potential for an unstable state before and after Wick rotation.*

Let us consider the potential of Fig. 2.6a which we can invert by means of a Wick rotation to obtain the potential in Fig. 2.6b. Considering mechanical motion of our pseudoparticle in Fig. 2.6b we can see a non-trivial solution exists where the particle begins and ends at rest at $x = 0$. Such motion involves the pseudoparticle dropping into the well and travelling to the classical turning point at $x = x_b$ at which point it changes direction and returns to $x = 0$. We call this motion the bounce [1] and enforce the following boundary conditions on the motion

$$\begin{aligned} \lim_{\tau \to \pm\infty} x(\tau) &= 0 \\ \frac{dx(0)}{d\tau} &= 0. \end{aligned} \tag{2.23}$$

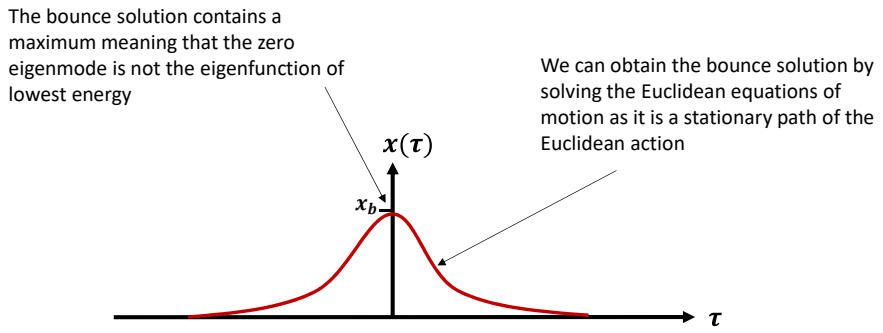

Fig. 2.7 *The profile of the bounce solution.*

In Fig. 2.7 we sketch out the profile of a typical bounce solution. In a similar manner to the 1D instanton, we can heuristically write down the probability amplitude for such a bounce solution as

$$\langle 0|e^{-H\tau_0/\hbar}|0\rangle = \int [dx(\tau)]e^{-S[x(\tau)]} = \exp[e^{-S(x_b)}] \times (\text{quantum corrections}), \qquad (2.24)$$

Upon closer inspection of Fig. 2.7 we notice a peculiarity that points to a subtle but critical general property of the bounce solution which will motivate us seeking an alternative approach to calculating multi-minima tunnelling solutions in Chapter 4. In particular we can clearly see from Fig. 2.7 that the bounce trajectory has a maximum, telling us that the particle's wavefunction has a node. However, we know that the wavefunction of lowest energy strictly must be nodeless and so there must exist a wavefunction of lower energy [27]. From Eq. (2.21) we know a zero eigenvalue mode exists due to translational invariance of the bounce in τ and thus the lower energy wave function must have negative energy eigenvalue.

It is instructive to explore the underlying source of this negative mode by qualitatively comparing our double well instanton scenario (Sec. 2.1.5) to our bounce scenario. When considering the double well instanton solutions we recall that the path was constrained to tunnelling from an initial at rest starting position x_i to an equipotential final rest position x_f (the instanton) and at some later τ back again (the anti-instanton). Therefore this scenario, by definition, is restricted to only look at those paths that precisely describe barrier penetration. The instanton path between these two position eigenstates dominates the contribution to the barrier penetration integral over these boundary conditions as it has minimum Euclidean action out of all the possible barrier penetration paths.

In contrast, when we are dealing with a bounce solution we calculate the Euclidean action over all paths that begin and end at x_i and have some turning point p upon which each solution is centred. Therefore the Euclidean action is not restricted to only include

those barrier penetration paths which tunnel to the bounce value $p = x_b$, 'bounce' off it and return to x_i.

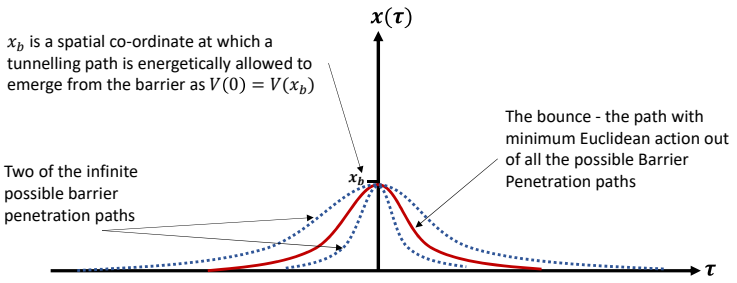

Fig. 2.8 *The bounce: the optimal barrier penetration path (solid line) through Euclidean space.*

As shown in Fig. 2.8, the bounce solution has minimal Euclidean action out of all the paths that describe barrier penetration. However, the Euclidean action for this scenario will also permit those paths where the trajectory both overshoots and undershoots $p = x_b$ before returning back to x_i. Paths that are centred at $p > x_b$ tunnel beyond the potential barrier and into the classically allowed region, whereas paths centred at $p < x_b$ fall short of the barrier boundary and remain inside the barrier for the entirety of the motion.

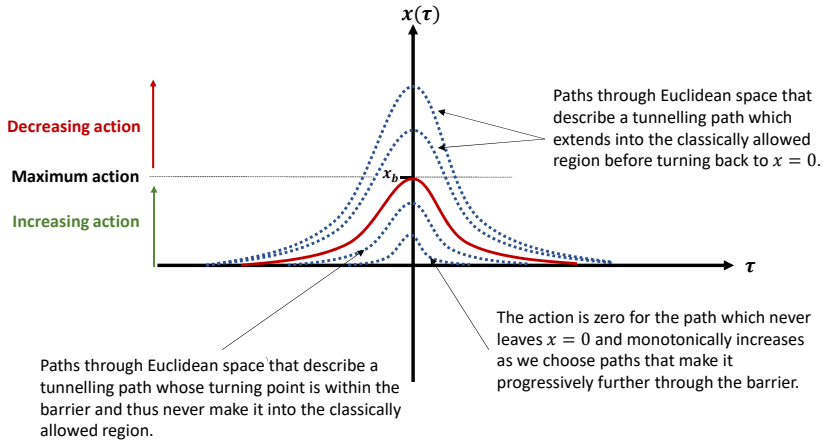

Fig. 2.9 *The bounce has maximal Euclidean action out of all paths that undershoot and overshoot $x = x_b$ and has minimal Euclidean action out of all barrier penetration paths. The bounce is therefore a saddle point of the Euclidean action.*

As shown in Fig. 2.9 the action is zero for the trivial $x = 0$ path and monotonically increases as we choose paths that make it progressively further through the barrier. On the other hand, the action monotonically decreases when we choose paths $p > x_b$ that make it progressively further into the classically allowed region before reaching their

turning point at p. This is because after the path emerges from the barrier with potential energy $V(x_b) = 0$ and zero kinetic energy, its potential becomes increasingly negative as it propagates classically and rolls down the hill before reaching p and turning round for its return leg. Therefore the bounce solution which is centred on $x = x_b$ has maximal Euclidean action out of all those paths that undershoot and overshoot x_b.

This local maximum is precisely where the negative eigenmode originates from as perturbations to the classical path in the direction of this functional mode cause the action to decrease. It then becomes clear that the bounce solution is in fact a saddle point of the Euclidean action [26].

We can deal with this negative eigenmode via a process of analytic continuation [27] which introduces an imaginary term into the expression for the ground state energy. We can interpret this imaginary part of the energy as a decay rate Γ [28] of the false vacuum

$$\Gamma = Ke^{-S_b}, \tag{2.25}$$

where S_b is the action for the bounce solution and K is a factor containing a ratio of functional determinants that accounts for the quantum corrections to the classical path with both the zero and negative mode accounted for.

The fact that the bounce solution lies at a saddle point in the Euclidean action is one of the primary reasons why finding bounce solutions for exotic potentials can be extremely challenging. Numerical approaches like the usual 'overshoot/undershoot' method inspired by Coleman and described in Sec. 3.1.2 can be too sensitive to the negative mode to find a reliable solution. As such, in Chapter 4 we study an alternative approach to finding tunnelling solutions that reformulates the Euclidean action in terms of a new action surface which has the crucial property that the bounce solution lies at the minimum of this surface. We go on to apply this approach to the numerically challenging scenario of tunnelling in single and multi-field potentials with multiple minima.

2.3 Zero-modes, Negative-modes and QFT

Before we move from the 1D analysis of this chapter to a system with infinitely many degrees of freedom that a quantum field theory describes, a few brief comments are worth making regarding the existence of negative-modes and zero-modes in QFT. It is clear that in moving to an infinite number of degrees of freedom many further zero-modes may arise from extra symmetries in the theory. These zero-modes can be isolated and integrated over in a similar manner to how the zero-mode from translational invariance of the bounce is dealt with [26].

However, extra negative modes may also appear in addition to the single negative one already outlined. This is where we must enforce a hard constraint on the class of permitted Euclidean tunnelling solutions. Euclidean solutions of field theories with more than one negative eigenvalue do not describe tunnelling and thus for our purposes should be discarded [29].

Chapter 3

False Vacuum Decay in Quantum Field Theory

3.1 The Bounce Solution in QFT

We are now in a position to generalise the formalism we have developed in the previous chapter from the single degree of freedom seen in one dimension to the infinite number of degrees of freedom that a quantum field theory describes[1]. As we will see this takes place in a very natural fashion and immediately has direct applications to the phenomena of quantum tunnelling in a field theory.

3.1.1 Wick rotation

We will begin by considering the theory of a single scalar field, ϕ, in four dimensional Minkowski spacetime and thus make the following field theory replacements to the 1D scenario of Eq. (2.1)

$$\begin{aligned} x(t) &\to \phi(\mathbf{x},t) \\ V(x) &\to V(\phi(\mathbf{x},t)) = V(\phi), \end{aligned} \tag{3.1}$$

where the potential $V(x)$ becomes a potential energy density $V(\phi)$. We then have the following action

$$S(\phi) = \int d^4x \left[\frac{1}{2}(\partial_\mu \phi)(\partial^\mu \phi) - V(\phi) \right]. \tag{3.2}$$

[1]To avoid repetition, we chose not to take the additional intermediate step of first generalising to a system with many degrees of freedom but see [19] for a detailed derivation of this

We can express the probability amplitude for a field to start in initial field configuration ϕ_i and after time t_0 end up in final configuration ϕ_f as a path integral

$$\langle \phi_f | e^{-iHt_0/\hbar} | \phi_i \rangle = N \int D[\phi(t,\mathbf{x})] e^{iS/\hbar}, \tag{3.3}$$

where $e^{-iHt_0\hbar}$ is the time evolution operator, H is the Hamiltonian and N is a normalisation constant. Then following the general prescription from Sec. 2.1.2 and Wick rotating Eq. (3.3) we obtain the Euclidean path integral

$$\langle \phi_f | e^{-H\tau_0/\hbar} | \phi_i \rangle = N \int D[\phi(\tau,\mathbf{x})] e^{-S_E/\hbar}, \tag{3.4}$$

where S_E is the Euclidean action obtained by Wick rotating Eq. (3.2) to give

$$\begin{aligned} S_E &= \int d^4x \left[\frac{1}{2} (\partial_\mu \phi)(\partial^\mu \phi) + V(\phi) \right] \\ &= \int d\tau d^3x \left[\frac{1}{2} (\frac{\partial \phi}{\partial \tau})^2 + (\nabla \phi)^2 + V(\phi) \right]. \end{aligned} \tag{3.5}$$

The potential energy of the Euclidean system is obtained by integration over all space. [2]

$$U[\phi(\tau)] = \int d^3x \left[\frac{1}{2} (\nabla \phi)^2 + V(\phi) \right]. \tag{3.6}$$

Note that henceforth, for simplicity, we often refer to the potential energy density, $V(\phi)$, as simply the potential. Its usage should be clear from the context. Furthermore, we assume that $\tau_0 \to \infty$ in Eq. (3.4) so that we only need to consider the lowest lying energy eigenstates that will provide dominating contributions to our result (section 2.1.2). We can then calculate the Euclidean equations of motion for this field theory by extremising Eq. (3.5) to give

$$\frac{\partial^2 \phi}{\partial \tau^2} + \nabla^2 \phi = \frac{dV}{d\phi}. \tag{3.7}$$

3.1.2 Bounces in scalar QFT

The primary goal of this section is to find a meaningful description of tunnelling phenomena in quantum field theory. In Chapter 2 we considered a problem in 1D quantum mechanics with an unstable minima (Sec. 2.2). We saw that by solving the equations of motion that arose from the stationary Euclidean action with appropriate boundary conditions, we could find the barrier penetration amplitude. This solution, known as the bounce, provided us with a working description of barrier penetration effects in 1D quantum mechanics. With

[2] It is worth noting that the potential energy has picked up an additional gradient term arising from the spatial part of the derivative term in the first line of Eq. (3.4).

this in mind, our plan is to take this bounce formalism and directly generalise it to quantum field theory.

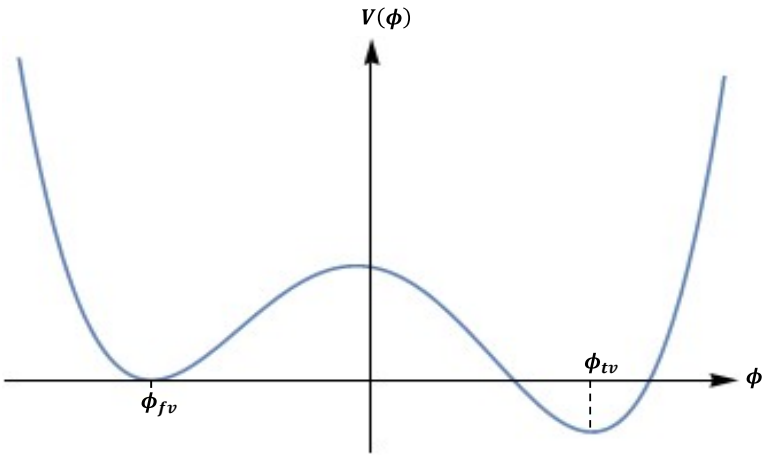

Fig. 3.1 *An offset double well potential.*

We consider a theory with an offset double well potential $V(\phi)$ of the form seen in Fig. 3.1. In an analogous manner to the 1D quantum mechanical case, this describes a situation where the minimum of the potential at $\phi = \phi_{fv}$ is deemed unstable due to barrier penetration effects. The minimum at ϕ_{fv} is thus known as the false vacuum, whilst the minimum at $\phi = \phi_{tv}$ we call the true vacuum of the theory.

Wick rotating our theory we obtain the Euclidean action in Eq. (3.5) from which we can compute the Euclidean equations of motion in Eq. (3.7). To have any hope of finding a bounce solution, $\bar{\phi}$, to Eq. (3.7) we also need to generalise the 1D boundary conditions in Eq. (2.23) and in doing so obtain

$$\begin{aligned} \lim_{\tau\to\pm\infty} x(\tau) &= x_0 \\ \left.\frac{dx}{d\tau}\right|_{\tau=0} &= 0. \end{aligned} \tag{3.8}$$

We achieve this by making the replacements for QFT

$$\begin{aligned} x(\tau) &\to \phi(\tau, \mathbf{x}) \\ x_0 &\to \phi_{fv}, \end{aligned} \tag{3.9}$$

to obtain

$$\lim_{\tau\to\pm\infty} \bar{\phi}(\tau, \mathbf{x}) = \phi_{fv} \tag{3.10}$$

and

$$\left.\frac{\partial\bar{\phi}(\tau,\mathbf{x})}{\partial\tau}\right|_{\tau=0}=0, \tag{3.11}$$

where $\bar{\phi}(\tau,\mathbf{x})$ is the required bounce solution. To ensure the action remains finite we also enforce the condition

$$\lim_{|\mathbf{x}|\to\infty}\bar{\phi}(\tau,\mathbf{x})=\phi_{fv}. \tag{3.12}$$

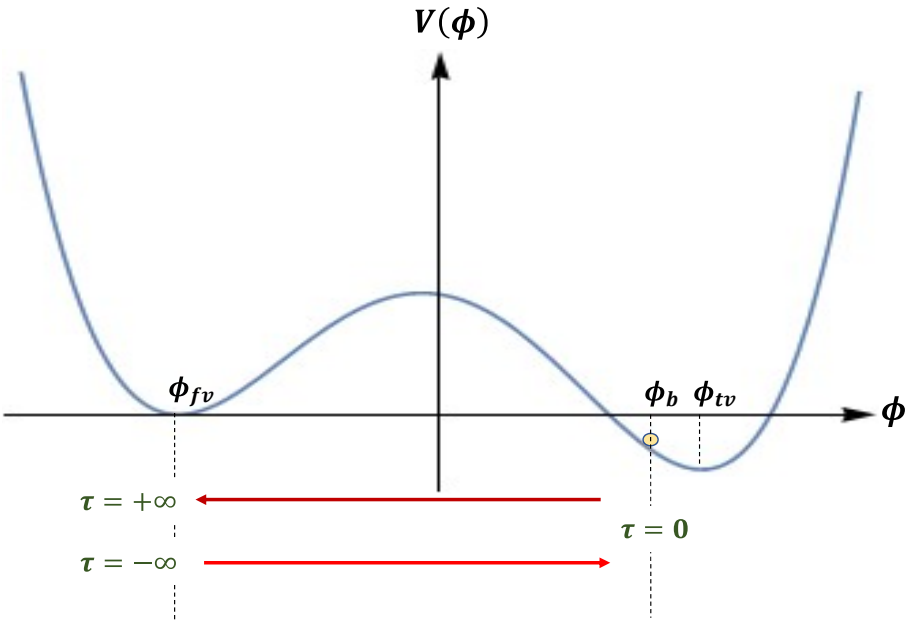

Fig. 3.2 *The bounce solution paramterised by imaginary time τ.*

Fig. 3.2 shows the potential barrier and the τ parameter that, for the bounce solution, is a parametrisation along the optimal barrier penetration path through configuration space. The diagram thus illustrates the requirement Eq. (3.10) that our solution, $\bar{\phi}(\tau,\mathbf{x})$, begins from the false vacuum, $\phi=\phi_{fv}$, at $\tau\to-\infty$ and must return to ϕ_{fv} as $\tau\to+\infty$. Therefore, from Eq. (3.11), there exists an intermediate stationary point that can be chosen with field value $\phi(\tau=0,\mathbf{x}=\mathbf{0})=\phi_b$. Fig. 3.2 also shows that the potential energy density $V(\phi_b)\neq V(\phi_{fv})$. However we still require that the solution conserves potential energy, $U(\phi)$, and so must have that $U(\phi_b)=U(\phi_{fv})$.

The false vacuum decay rate for quantum field theory can be directly generalised from the decay rate in Eq. (2.25) for a unstable state in 1D quantum mechanics. For QFT we pick up an extra spacetime volume factor V when we integrate over the whole of spacetime. The decay rate is then expressed as a false vacuum decay rate per unit volume as

$$\Gamma/V=|K|e^{-S_b}, \tag{3.13}$$

where $\hbar$ is set to unity and S_b is the Euclidean action of the bounce solution. The pre-factor K physically represents quantum corrections to the bounce solution and is expressed using a ratio of functional determinants, similar to in the 1D QM case, which contain the single negative eigenmode and the numerous zero eigenmodes as mentioned in Sec. 2.3.

It is generally a difficult task to exactly calculate such prefactors but fortunately we can often suppress these factors on dimensional grounds when calculating false vacuum decay rates [26]. Therefore in this thesis we shall not consider this prefactor term and unless otherwise stated assume it is $\sim \mathcal{O}(1)$. Having said this, the accurate computation of this factor is crucial when one wants to to assess the effect of quantum corrections to the decay rate and a strategy for calculating the functional determinant pre-factor is outlined in [30].

The homogeneity conditions Eq. (3.10) and Eq. (3.12) lead to a particularly enlightening interpretation of tunnelling in quantum field theories in terms of vacuum bubbles. We expand on this in detail in Sec. 3.1.3 but for now I will simply describe the essence of this interpretation.

We begin in a homogeneous false vacuum field configuration ϕ_{fv} that extends over all of spacetime. Now consider that a vanishingly small region of spacetime finds the true vacuum due to quantum fluctuations. The required bounce solution, $\bar{\phi}$, provides a means of transitioning the false vacuum field configuration at the exterior of this region to the true vacuum field configuration ϕ_{tv}. Heuristically, we can see that such a process will have the shape of a bubble in Minkowksi space where the bubble wall drives the transition of the scalar field value.

In an analogous manner to superheated fluids [1], in most cases the bubble will immediately shrink to nothing instead of nucleating in Minkwoski space due to the energy cost of the bubble wall being greater than the energy gain from the bubble volume. However, there will be a critical bubble volume for which it is energetically favourable for the bubble to physically nucleate in Minkowski space, after which point it will expand over the whole of spacetime and convert the universe to the true vacuum phase.

Such an interpretation is attractive as it avoids any inconsistencies with energy conservation where one needs to simultaneously convert the whole universe from false vacuum configuration to true. This of course would require overcoming an infinite potential well.

Equipped with this intuitive picture in our head, along with the fact that Eqs. (3.7), (3.10) and (3.12) are $\mathrm{O}(4)$ invariant, it seems a natural step to make the conjecture that the bounce solution itself is also invariant under 4D Euclidean rotations. Indeed the conjecture that there always exists an $\mathrm{O}(4)$ invariant bounce solution is proved in [31]. With this knowledge we define χ to be a radial co-ordinate in four-dimensional Euclidean space, with center of symmetry at the origin, where

$$\chi = \sqrt{\tau^2 + \mathbf{x}^2}, \tag{3.14}$$

so that the bounce $\bar{\phi}$ is a function of χ. Making this substitution into Eq. (3.7) the Euclidean equation of motion for the bounce become

$$\frac{d^2\bar{\phi}}{d\chi^2} + \frac{3}{\chi}\frac{d\bar{\phi}}{d\chi} = \frac{dV}{d\phi}, \tag{3.15}$$

where the boundary conditions in Eq. (3.10) and Eq. (3.12) become

$$\lim_{\chi\to\infty} \bar{\phi}(\chi) = \phi_{fv} \tag{3.16}$$

and we require

$$\left.\frac{d\bar{\phi}}{d\chi}\right|_{\chi=0} = 0, \tag{3.17}$$

so that $\bar{\phi}$ is non-singular at the origin. We can also rewrite the Euclidean action from Eq. (3.5) in terms of χ by noting that the surface area of a 4D hyper-surface of radius χ is $2\pi^2\chi^3$ to give

$$S_E = 2\pi^2 \int_0^\infty \chi^3 d\chi \left[\frac{1}{2}\left(\frac{d\bar{\phi}}{d\chi}\right)^2 + V(\bar{\phi})\right]. \tag{3.18}$$

At this point, following [1], we gain some insight with far-reaching consequences if we now interpret ϕ as a position and χ as a time in solving Eq. (3.15). Under this analogy the Euclidean equations of motion in Eq. (3.15) then describe particle motion in a negative potential, $-V(\phi)$, where the particle is being exposed to an additional viscous drag force, $-\frac{3}{\chi}\frac{d\bar{\phi}}{d\chi}$, that decreases in magnitude with increasing 'time' χ.

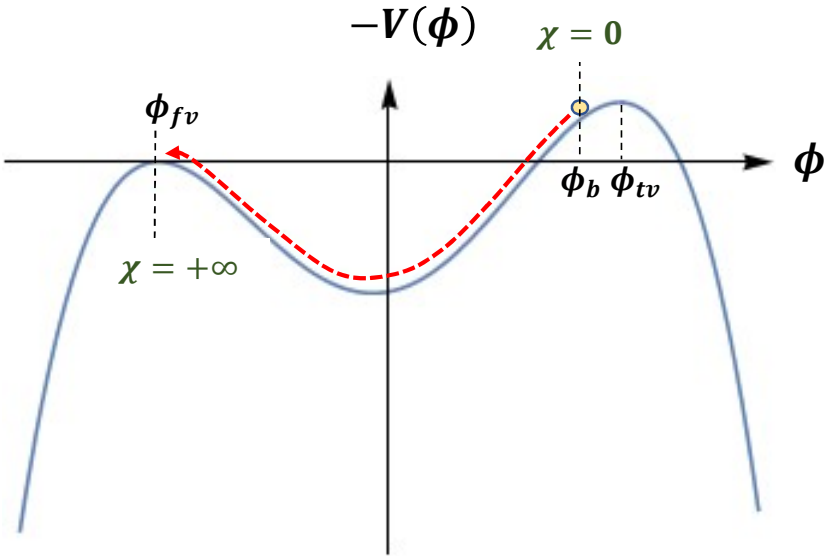

Fig. 3.3 *A mechanical analogy of the bounce solution.*

As shown in Fig. 3.3 the bounce solution to Eq. (3.15) then describes mechanical motion of a particle beginning at rest at some initial position ϕ_b at $\chi = 0$ and subject to this time dependent drag force while moving in the potential $-V(\phi)$. The starting position ϕ_b has to be carefully chosen such that the particle can overcome the drag force and successfully traverse the potential valley, $-V(\phi)$, before coming to rest at $\phi = \phi_{fv}$ in the limit $\chi \to \infty$. This mechanical analogy will prove to be an extremely useful interpretation when we look to solve the Euclidean equations of motion for the bounce solution throughout the rest of this thesis.

Remaining with our mechanical analogy we aim to show that there always exists an initial field value ϕ_b that can be chosen such that the particle will come to rest at ϕ_{fv} in the limit $\chi \to \infty$. We will show this via an 'overshoot/undershoot' argument following [1].

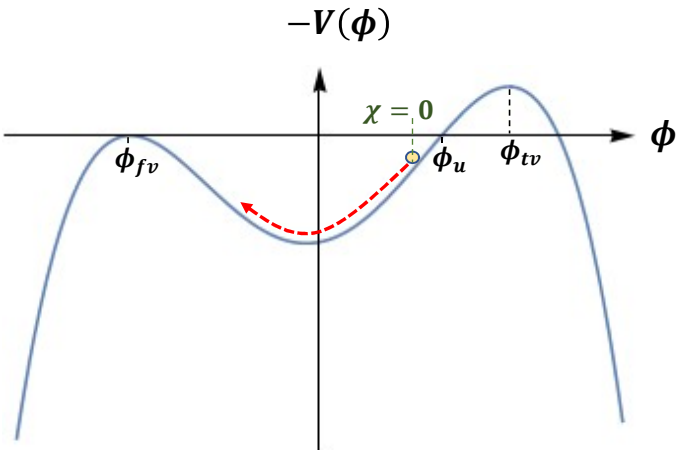

***(a)** Under Shoot*

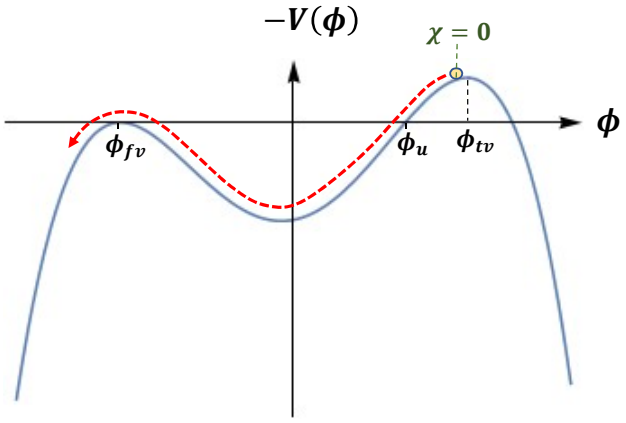

***(b)** Over Shoot*

***Fig. 3.4** Showing a bounce solution exists by mechanical analogy.*

First, in Fig. 3.4a we consider releasing the particle from rest on the right hand hill at some field value $\phi < \phi_u$ where $V(\phi_{fv}) = V(\phi_u)$. In this case the particle will clearly not

have enough kinetic energy to climb the left-hand hill to finish at $\phi = \phi_{fv}$ and so we have demonstrated the existence of paths that undershoot $\phi = \phi_{fv}$.

On the other hand if we release the particle arbitrarily close to the maximum at $\phi = \phi_{tv}$ as shown in Fig. 3.4b then it can be shown [1] that the particle can stay there for arbitrarily large 'time' χ. However, once enough time has passed and χ is large enough, the drag term will become negligible as it is inversely proportional to χ. Thus at late times, the particle is located at $\phi > \phi_u$ and has no drag term acting which means that it drops into the valley and has sufficient energy that it overshoots the peak at ϕ_{fv}. Therefore if the particle has a starting position for which it overshoots and a starting position for which it undershoots, by continuity it must have an intermediate starting point in which it comes to rest at $\phi = \phi_{fv}$ in the limit $\chi \to \infty$.

3.1.3 Constructing a bubble model

At this point we are in a good position to build a detailed conceptual model for the phenomena of vacuum decay in a quantum field theory. This will provide us with a strong foundation to build our theory around and maintain an intuitive picture of what is taking place when we look to develop the theory further.

In his seminal paper on the subject in [1], Sidney Coleman offered a compelling interpretation of vacuum decay in a quantum field theory in terms of vacuum bubbles, drawing an analogy to the boiling of a superheated fluid.

Briefly recapping this well known theory, bubbles of vapour can nucleate in a homogeneous superheated liquid due to thermodynamical fluctuations. If the energy given off in creating the vacuum bubble is outweighed by the energy required to counteract the surface tension at the wall then the bubble will immediately shrink to nothing. If however the energy given off by the bubble's volume outweighs the surface tension, then it is energetically favourable for the bubble to grow, rapidly converting all the liquid to the vapour phase.

Coleman's insight was borne out of identifying a superheated liquid's fluid phase with the homogeneous false vacuum field configuration and its vapour phase with the true vacuum. He additionally identified the thermodynamic fluctuations causing the bubbles to nucleate with quantum mechanical fluctuations. Thus he suggested that if a bubble of true vacuum of a certain radius were to nucleate in Minkowski space such that it is energetically favourable for it to expand then, by energy arguments, it would do so over all of spacetime. Thus the expanding bubble would cause the decay of the false vacuum and convert the homogeneous false vacuum to true vacuum phase.

To see how this true vacuum bubble analogy arises we must return to the concept of imaginary time that engendered the rise of the bounce solutions that make up the core theme of this thesis. As we will see, the introduction of an imaginary component to the real

time axis has exceptionally rich implications to our conceptual interpretation of tunnelling in a quantum field theory.

It is important to underline at the outset, that imaginary time, τ, is not a time at all in the conventional sense, but rather a parameter along a given path in the configuration space of the field. In the special case of the bounce solution of Sec. 3.1.2, τ then parameterises the optimal barrier penetration path through configuration space.

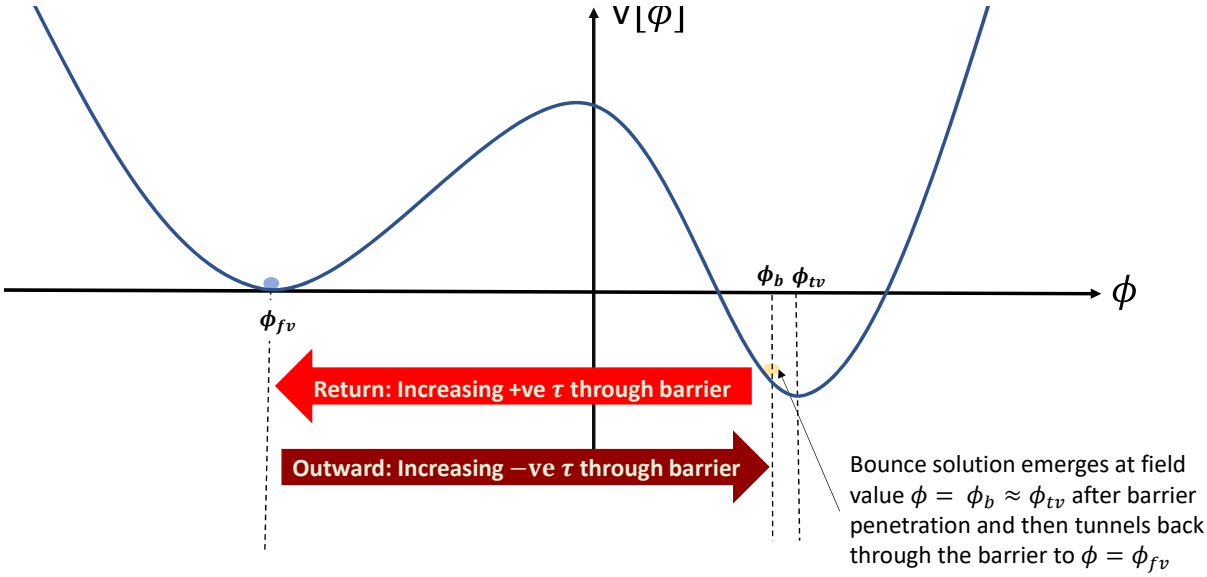

Fig. 3.5 *The bounce solution parameterised by imaginary time τ through the barrier.*

As shown pictorially in Fig. 3.5, the bounce enforces a solution that begins in a homogeneous false vacuum field configuration $\phi = \phi_{fv}$ at $\tau \to -\infty$. It then tunnels to a field value $\phi = \phi_b$, close to the true vacuum $\phi = \phi_{tv}$, which it arrives at $\tau = 0$. The solution then 'bounces' off ϕ_b and returns again to ϕ_{fv} at $\tau \to +\infty$.

Before proceeding, it is critical that we clearly distinguish between a Euclidean space bubble that exists in the $(\textit{imaginary time}, \textit{real space})$ plane and a Minkowski bubble that exists in the $(\textit{real time}, \textit{real space})$ plane of Minkowski space. The nucleation of the physical bubble that we actually see therefore takes place in Minkowski space and evolves in real time which we look at in more detail in Sec. 3.1.4.

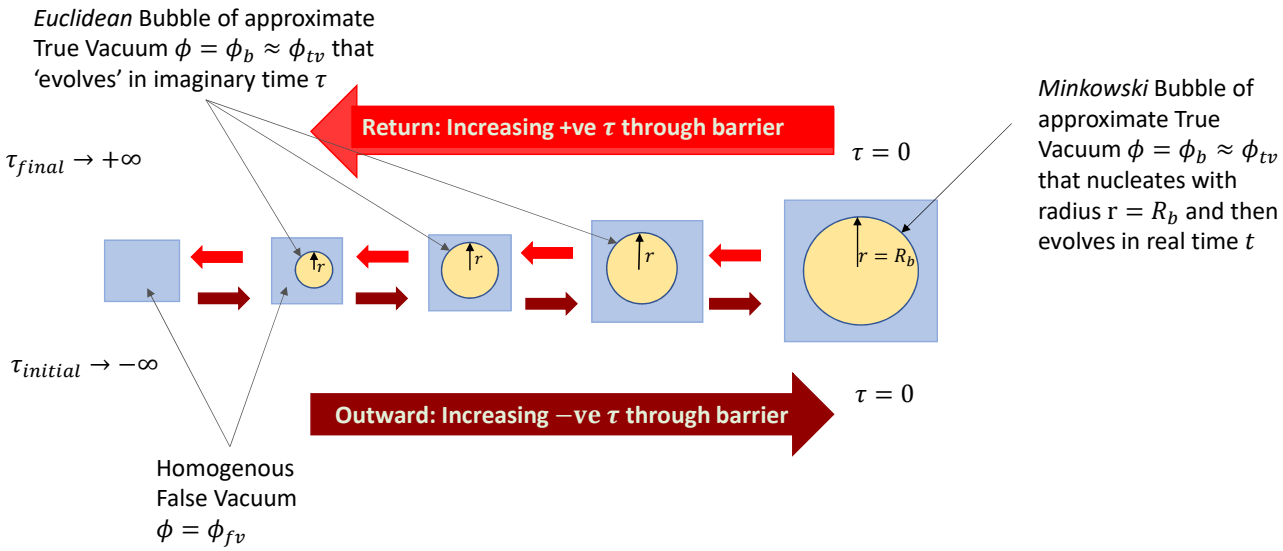

Fig. 3.6 *A view of the bounce path through configuration space in terms of vacuum bubbles inspired by Fig. 12.2 of [26].*

In Fig. 3.6 we show a schematic diagram of the process that envisages a Euclidean bubble of true vacuum with radius defined by the spatial value $r = |\mathbf{x}|$, at each subsequent snapshot of imaginary time $-\infty < \tau < 0$ that parameterises the outward tunnelling path through the barrier from ϕ_{fv}. At imaginary time $\tau = 0$ the bubble has its maximum spatial radius of R_b that it obtains upon the bounce solution reaching the field value $\phi_b \approx \phi_{tv}$. At this point the bubble physically nucleates in Minkowksi space and then evolves in real time t.

The bounce solution itself then bounces off ϕ_b at zero imaginary time (see Fig. 3.3) and comes back through the barrier (see Fig. 3.2) to return to the false vacuum configuration ϕ_{fv}. This second half of the solution mirrors the first half except we are now moving through positive imaginary time. Thus at each snapshot of positive imaginary time τ that parametrises our return journey through the barrier, we have a Euclidean space bubble of decreasing radius. The vacuum bubble radius, $r = |\mathbf{x}|$, continues to decrease until we finally return to ϕ_{fv} and the Euclidean bubble vanishes completely.

A particularly interesting representation of this bounce solution arises when we plot it in 4D spherical polar co-ordinates with $\chi = \sqrt{\tau^2 + r^2}$. The bounce solution then maps out a static 4-sphere of approximate true vacuum in Euclidean space, centred at radial co-ordinate $\chi = 0$. This true vacuum 4-sphere has radius $\chi = R_b$ and resides in the $t = 0$ (i.e. vanishing real time) plane.

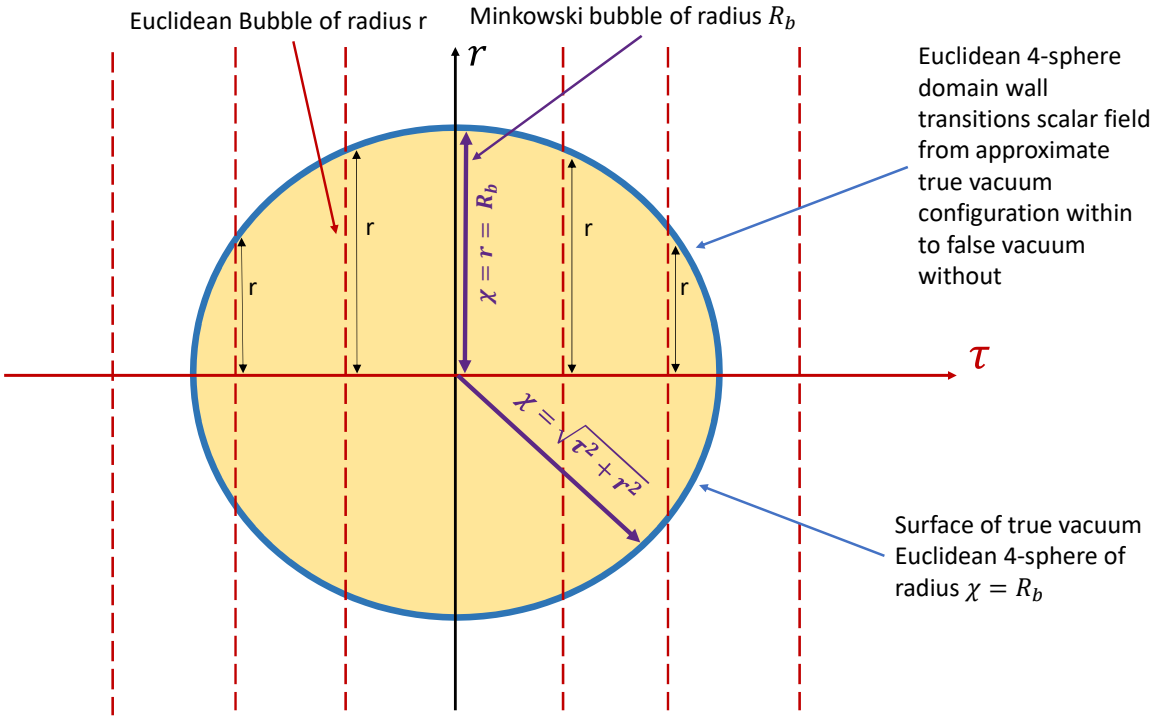

Fig. 3.7 *A thin walled bounce solution in Euclidean space inspired by Fig. 12.3 of [26].*

In Fig. 3.7 we represent this as a circle of radius $\chi = R_b$ in the $t = 0$ plane. This circle is simply a projection of the static Euclidean 4-sphere onto our co-ordinates. At each snapshot of imaginary time τ we have a 1D line of length $2r$ on our diagram. Each of these 1D lines in fact represent a Euclidean bubble of spatial radius r. The Minkowski bubble of radius R_b that physically nucleates in Minkowski space, ready to evolve in real time, is also represented on the diagram by a 1D line of length $\chi = r = R_b$ at $\tau = 0$.

With this picture it becomes clear how we can interpret bounce profiles such as those seen in Sec. 3.1.2 in terms of our bubble model. As we move out radially from the centre of co-ordinates of our Euclidean 4-sphere we remain in the approximate true vacuum $\phi_b \approx \phi_{tv}$. At some radius $\chi = R_b$ we reach the domain wall of the 4-sphere and the solution smoothly transitions us from true vacuum value to false vacuum value. Thus we can interpret the part of the bounce solution that transitions our scalar field value as forming the wall of our Euclidean 4-sphere of approximate true vacuum.

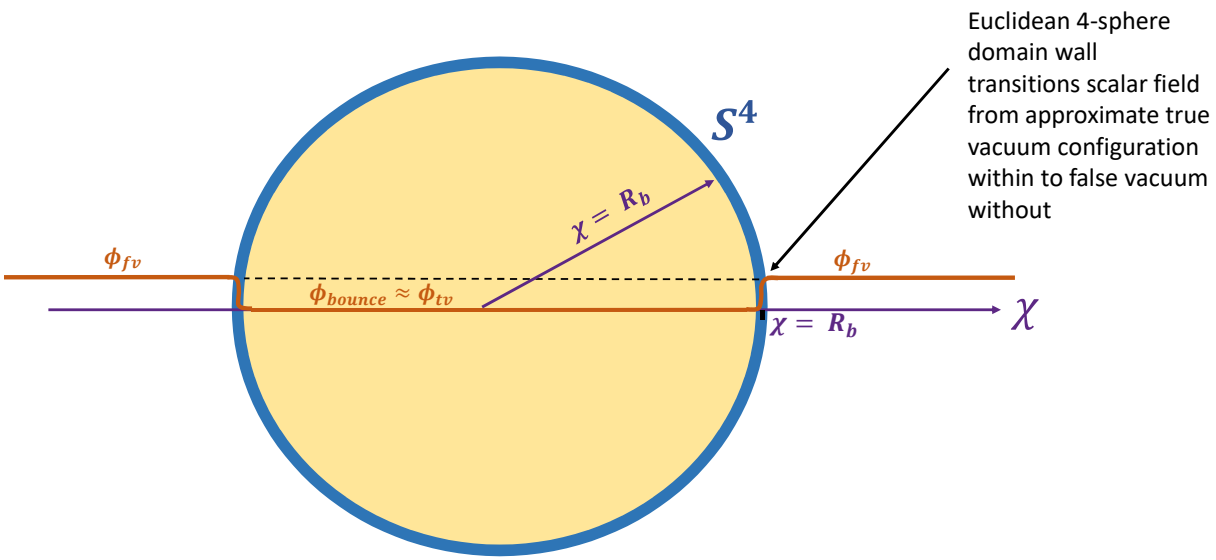

Fig. 3.8 *The Euclidean 4-sphere bounce solution.*

In Fig. 3.8 we show a schematic diagram of this interpretation. In this case we have modelled the domain wall as thin, reflecting a transition of the scalar field value that takes place over a negligible distance compared to the radius of the 4-sphere. As we will see in Sec. 3.1.6, if such an approximation is valid then we can clearly identify the wall region with a 1D instanton (Sec. 2.1.5) transitioning the scalar field value from true to homogeneous false vacuum.

As previously touched upon, our bubble in fact does not physically nucleate in Minkowski space until it has zero imaginary time component. This makes sense from an intuitive perspective as real world objects only propagate in time that is purely real and has no imaginary component.

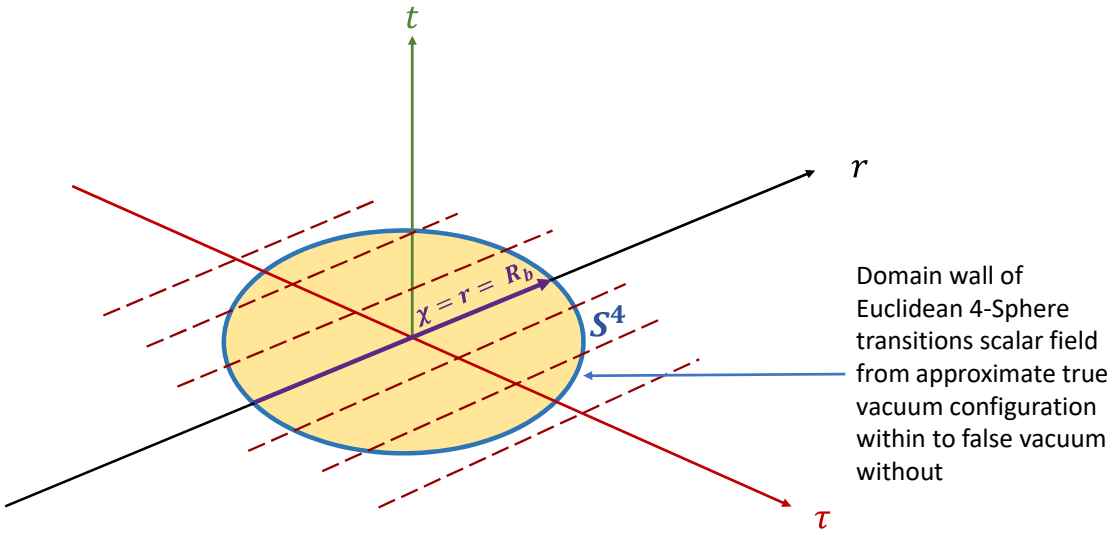

Fig. 3.9 *The bounce solution projected into real time at* $t = 0$.

In Fig. 3.9 we graphically demonstrate a key result that the spacetime radius of the bubble when it nucleates at real time $t = 0$ is precisely dictated by the radius of the Euclidean 4-sphere, $\chi = R_b$. From this perspective, the Euclidean bounce 4-sphere sets the initial conditions of the Minkwoski bubble at its point of nucleation, namely, its spacetime radius R_b and also its shape as we will see in a moment. After nucleation, the Minkowski bubble's future evolution is then governed by its propagation through real time with spacetime radius R_b as one might expect.

3.1.4 Bubble evolution in spacetime

This brings us back to something we touched upon previously: the evolution of the bubble in Minkowski space. Based on pictorial arguments that we have discussed thus far, it is easy to see that it should be possible to analytically continue our bounce solution to Minkowski space by taking the intersection of Euclidean space with Minkowski space, $t = i\tau = 0$.

The $O(4)$ invariance of the bounce solution in Euclidean space

$$\phi_E = \bar{\phi}(\sqrt{\mathbf{x}^2 + \tau^2}), \tag{3.19}$$

then becomes $O(3,1)$ invariance in Minkowski space [1]

$$\phi_M = \bar{\phi}(\sqrt{\mathbf{x}^2 - t^2}), \tag{3.20}$$

meaning the bubble maintains its spherical shape to all Lorentz observers.

The wall of the bubble expands according to

$$|\mathbf{x}|^2 - (t^2) = R_b^2, \tag{3.21}$$

which maps out hyperbolas in spacetime that reflect the expansion of the bubble over the whole universe, converting the homogeneous false vacuum to the true vacuum configuration. This can be seen in Fig. 3.10, where we show the bubble's 'evolution' from early imaginary 'time' $\tau \to -\infty$ to $\tau = 0$ through to its evolution in real time $t > 0$.

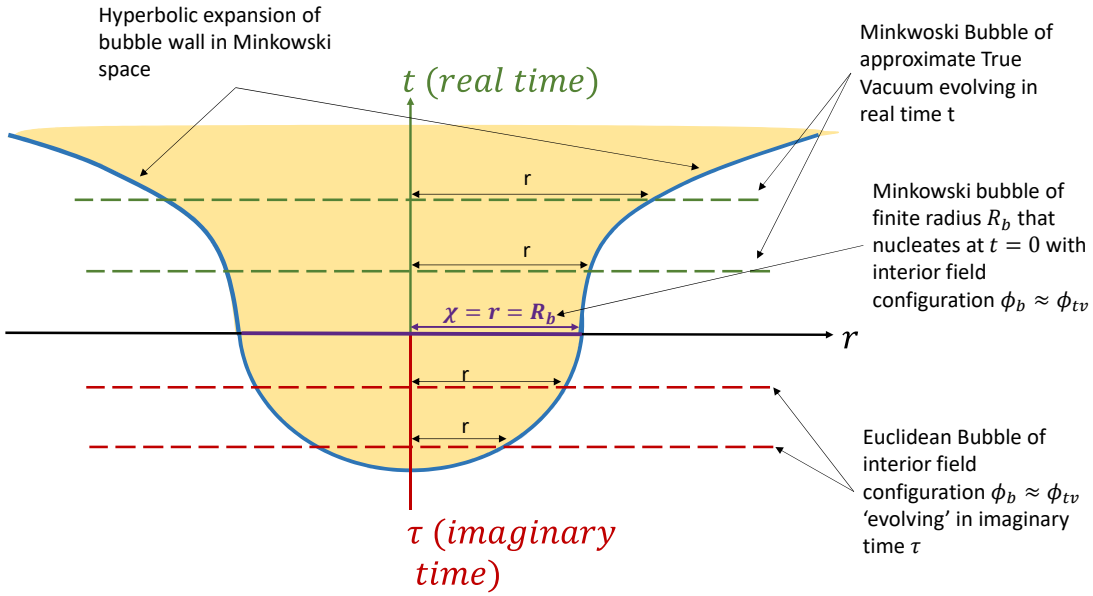

Fig. 3.10 *The bounce solution matched to the Minkowski bubble's real time evolution.*

In Fig. 3.10 we put together our previous analysis, showing the $-\infty < \tau < 0$ region of the bounce representing a half-sphere projection of the true vacuum Euclidean 4-sphere and join to this the $t > 0$ real time evolution of the bubble as it expands in Minkowski space.

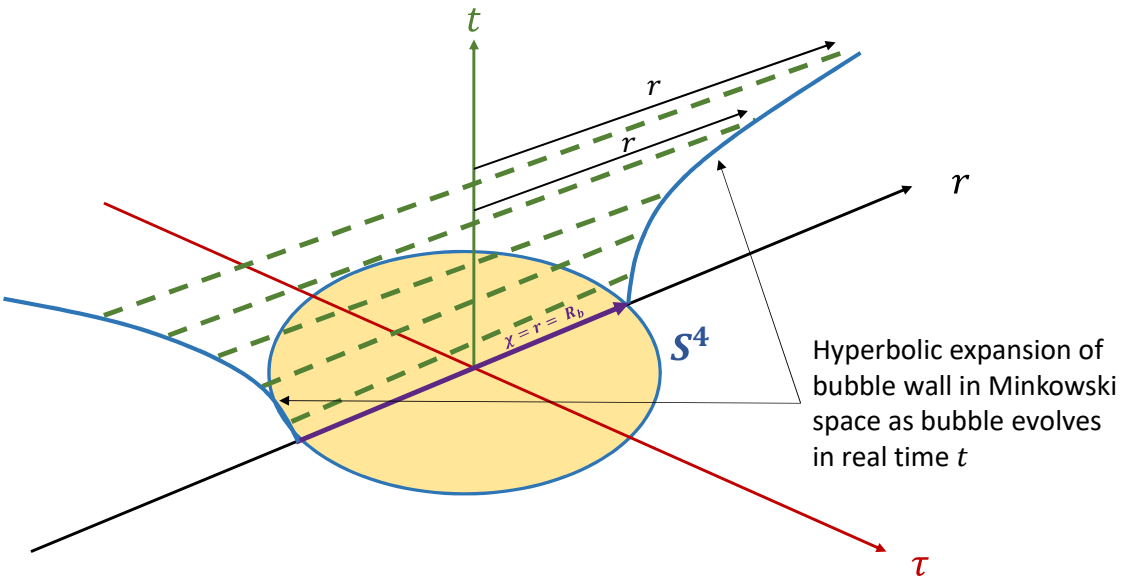

Fig. 3.11 *The bounce solution anlaytically continued into real time.*

In 3.11 we weave the different threads of the above model into one consistent diagram. The circle in the $(imaginary\ time, real\ space)$ plane centred at $\chi = 0$ is a projection of the static Euclidean 4-sphere of approximate true vacuum. The radius of the 4-sphere, $\chi = R_b$, sets the spacetime radius of the nucleated Minkowski bubble. This is exactly the same as in Fig. 3.9 and by similar arguments the bubble only nucleates in the $(real\ time, real\ space)$ plane we know as Minkowski space. In Fig. 3.11 the initially nucleated bubble of radius R_b is again represented as a 1D projection of length $2R_b$ at $t = i\tau = 0$. The evolution of this $(3+1)$ dimensional bubble of radius r in real time is then represented on our digram by subsequent 1D dashed line projections of increasing length $2r$ as t increases. This sequence of projections in the $(real\ time, real\ space)$ plane reflect the hyperbolic expansion of the $(3+1)$ dimensional Minkowski bubble over all of spacetime, converting the homogeneous false vacuum configuration to true vacuum.

3.1.5 An energy argument for bubble nucleation in Minkowski space

To conclude this section and complete our model of false vacuum decay via bubble nucleation, we consider the process in terms of energy arguments. We again assume the transition of the scalar field value happens over a negligible distance compared to the radius of the bubble so that the bubble wall is thin. The surface tension in the Euclidean bubble has an energy cost per unit volume arising from the transition of the scalar field value at its wall. The interior of the bubble, on the other hand, supplies energy per unit volume from its scalar field value being at a lower potential value $V(\phi_b) < V(\phi_{fv})$.

As $\tau < 0$ increases through the first part of the bounce solution, the surface tension cost at the wall of each successive Euclidean bubble outweighs the energy released from its interior volume; such a bubble cannot physically nucleate by energy arguments. As τ further increases, each subsequent Euclidean bubble has a larger radius and thus larger energy available to counteract the surface tension cost of the wall. Finally when the solution reaches $\tau = 0$ the energy acquired from the bubble interior precisely counteracts the surface tension cost at the bubble wall, and as a result the bubble nucleates in Minkowski space.

3.1.6 The thin wall approximation

Looking at the form of the bounce equations of motion in Eq. (3.15), we can see that the primary object that is going to affect the bounce solution profile obtained is going to be the form of the potential $V(\phi)$.

In the following sections we will thus begin exploring the different types of bounce solutions that can be obtained through varying the form of the potential $V(\phi)$. From this we can calculate the critical radius for the bubble to nucleate in Minkowski space, R_b, as well as the decay rate of the false vacuum. These are physical results that one can in principle use to compare the vacuum decay properties of different quantum field theories. The first shape of potential we will explore is that for which the bubble wall is vanishingly thin and as such this is called the thin wall approximation.

Lets assume we have a symmetric double well function $V(\phi)$ where one of the degenerate minima has been been offset a small distance ε in the $V(\phi)$ axis. We have now generated a theory with a false vacuum potential.

Following Coleman [1], we describe this scenario with the toy model potential

$$V(\phi) = V_0 + \frac{\varepsilon}{2a}(\phi - a), \tag{3.22}$$

where V_0 is a symmetric double well potential with two degenerate minima at $\phi = \pm a$ and the second term is an epsilon offset in the potential of the left-hand minima $\phi = -a$.

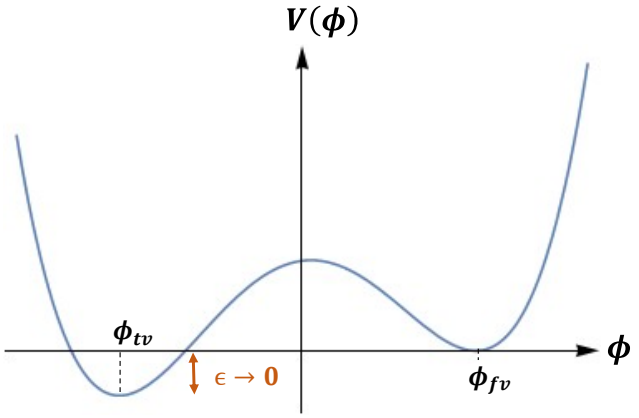

(a) Offset double well

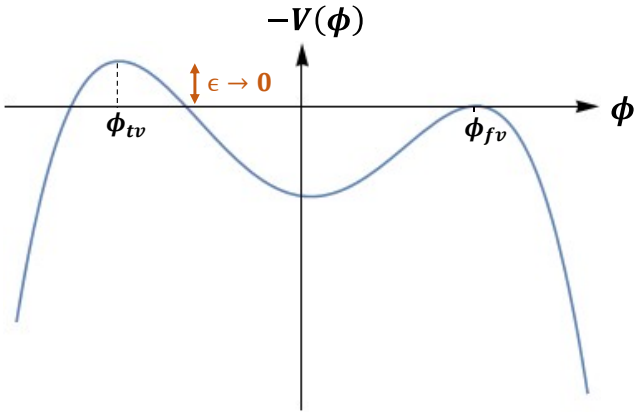

(b) Inverted offset double well

Fig. 3.12 *A thin wall potential.*

We then obtain a potential of the form shown in Fig. 3.12a where the minimum at ϕ_{fv} describes a false vacuum mode unstable due to barrier penetration, with ϕ_{tv} the true vacuum. To find the form of the bounce solution for this theory we need to solve the Euclidean ODE in Eq. (3.15) which corresponds to particle motion in an upside down potential $-V(\phi)$ as shown in Fig. 3.12b. We would do well to keep in mind that even though it is helpful to interpret χ as a time co-ordinate due to the strong resemblance Eq. (3.15) has with standard mechanical equations of motion, in reality it is simply a 4D radial co-ordinate.

Given our set up, there are two main simplifications we can make to the problem. Firstly, we approximate ε to be vanishingly small. Secondly, for $\chi \approx R_b$ and $\chi > R_b$ we approximate the drag term in Eq. (3.15) to be negligible by making R_b large (see Sec. 3.2.3 for scenarios where this approximation is not valid).

These two approximations have the following effect on the bounce solution. For very small ε we must have a starting point of the bounce, $\bar{\phi}(0) = \phi_b$, that is arbitrarily close to

the true vacuum peak $\phi = \phi_{tv}$. In regions very close to the maximum value the gradient is very small, meaning the particle will not move far from its starting value for early times χ. This effect is amplified further by the fact that at early times the drag term is large.

Once we reach some late time $\chi \approx R_b$ where R_b is large, then the drag term will have become negligible at which point the particle quickly drops into the valley and and comes to rest at $\phi = \phi_{fv}$ at time $\chi \to \infty$.

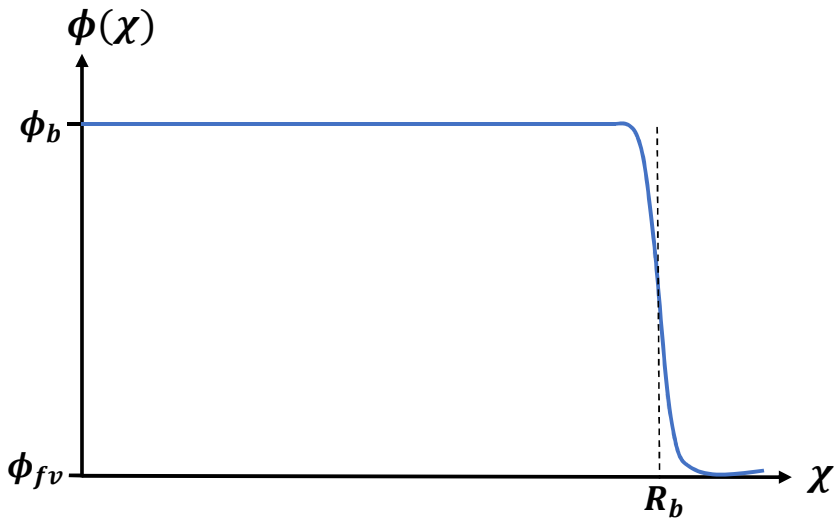

Fig. 3.13 *A thin wall bounce profile.*

In Fig. 3.13 we show the form of the bounce profile describing this scenario.

Now if we translate this mechanical interpretation of the bounce motion back into our vacuum bubble description (Sec. 3.1.3), our bounce solution describes a 4-sphere of approximate true vacuum embedded in a Euclidean space with a homogeneous false vacuum background. This 4-sphere has a vanishingly thin wall at radius $r \approx R_b$. We can think of the 4-sphere domain wall itself as being made up of the instanton part of our bounce solution, with the job of transitioning the field value from true vacuum within to false vacuum outside (Fig. 3.8).

Next we want to actually calculate the radius, R_b, of the thin walled bubble that nucleates in Minkowski space and the decay rate of the false vacuum for our potential, under this approximation. To do this we will need to solve the Euclidean equations of motion in Eq. (3.15) under the bounce boundary conditions in Eqs. (3.16) & (3.17). We can then compute the bounce action S_B which is specified in the exponent of the false vacuum decay rate Γ/V as seen in Eq. (3.13).

In the thin wall approximation we make ε so small that the ε term in $V(\phi)$ can be neglected due to its relative size compared to the other terms. On grounds discussed previously, we also can neglect the viscous drag term in the Euclidean equations of motion (Eq. (3.15)) as in the thin wall approximation R_b is large and so for $\chi \approx R_b$ the damping

term is negligible. We therefore have the bounce ODE

$$\frac{d^2\bar{\phi}}{d\chi^2} = V_0'(\phi), \tag{3.23}$$

where $V_0'(\phi)$ is a derivative with respect to ϕ. This is analogous to our equations of motion for a 1D instanton in Eq. (2.16). Thus the solution has the profile seen in Fig. 3.13 of a localised 1D insanton (Sec. 2.1.5), centred at $\chi = R_b$, transitioning from true vacuum value ϕ_{tv} to false vacuum value ϕ_{fv}

To calculate the Euclidean bounce action using Eq. (3.18), we split the problem into three regions in Euclidean space and compute the contribution of each to the action. First let us consider the region outside the domain wall of the bounce solution where $\chi > R_b$ and the field value is $\phi = \phi_{fv}$. The solution has $\frac{d\bar{\phi}(\chi)}{d\chi} = 0$ in this region and so, in our mechanical analogy, has zero kinetic energy here (Sec. 3.1.2). We also have that $V(\phi_{fv}) = 0$ so that the value of the Euclidean action (Eq. (3.18)) in this region is then

$$S_{exterior} = 0. \tag{3.24}$$

Next we look to compute the value of the Euclidean action in the interior region of the bounce 4-sphere, $\chi \approx R_b$. Taking the difference in energy density ε between true and false vacua as negligible, we only consider the symmetric part of the potential V_0. We thus see that in this approximation the thin wall region will describe a 1D instanton solution to a symmetric double well potential (Sec. 2.1.5). The Euclidean action for the thin wall region is then

$$\begin{aligned} S_{wall} &= 2\pi^2 R_b^3 \int d\chi \left[\frac{1}{2}\left(\frac{d\bar{\phi}}{d\chi}\right)^2 + V(\bar{\phi}) \right] \\ &= 2\pi^2 R_b^3 \int d\chi \Big[2V(\bar{\phi}) \Big], \end{aligned} \tag{3.25}$$

where we have used energy conservation and that $E = 0$ for our 1D instanton solution. Thus, we can also write

$$\begin{aligned} \frac{1}{2}\left(\frac{d\bar{\phi}(\chi)}{d\chi}\right)^2 &= V_0 \\ \implies d\chi &= \frac{1}{\sqrt{2V_0}} d\bar{\phi}. \end{aligned} \tag{3.26}$$

Substituting this change of variables into the result from Eq. (3.25) and changing the limits of integration accordingly, we can compute the Euclidean action for the bounce wall region

as

$$\begin{aligned} S_{wall} &= 2\pi^2 R_b^3 \int_{-a}^{a} d\bar{\phi}\sqrt{2V_0} \\ &= 2\pi^2 R_b^3 S_I, \end{aligned} \tag{3.27}$$

where S_I is the action for a 1D instanton that we calculated in Eq. (2.21). This result is dimensionally consistent with what we would expect for an action evaluated across the 3D surface of our 4-sphere.

Finally we calculate the action of the bounce solution in the region $\chi < R_b$ which is on the interior of the Euclidean 4-sphere. In this region $\phi = \phi_{tv} = -a$, $V(-a) = -\varepsilon$ and $\frac{d\bar{\phi}(\chi)}{d\chi} = 0$ so that, again using Eq. (3.18), the Euclidean action reads

$$\begin{aligned} S_{interior} &= -2\pi^2\varepsilon \int_0^{R_b} \chi^3 d\chi \\ &= -\frac{1}{2}\pi^2 R_b^4 \varepsilon. \end{aligned} \tag{3.28}$$

This result is dimensionally consistent with what we would expect for an expression evaluating the action for converting a 4D volume of false vacuum to true vacuum.

Now adding our contributions from each of the three regions together we get the total action for our thin wall bounce solution

$$S_b = -\frac{1}{2}\pi^2 R_b^4 \varepsilon + 2\pi^2 R_b^3 S_I. \tag{3.29}$$

We can then find the radius of our Euclidean 4-sphere bounce solution and thus the critical radius at which our bubble nucleates in Minkowski space by extremising the action (Eq. (3.29))

$$\begin{aligned} \frac{dS_b}{dR_b} &= -2\pi^2 R^3 \varepsilon + 6\pi^2 R^2 S_I = 0 \\ \implies R_b &= \frac{3S_I}{\varepsilon}, \end{aligned} \tag{3.30}$$

where we have used that the bounce solution is a stationary point of the Euclidean action. This result is consistent with our intuitive picture where the bounce radius approaches infinity in the limit where the energy density difference between true and false vacua tends to zero.

The meaning of this critical bubble radius for the thin wall approximation can be understood from a few different perspectives when put in the context of our conceptual model set out in Sec. 3.1.3. Fundamentally it is the radius at which the Euclidean action is stationary. Therefore it directly describes the radius of the Euclidean bounce 4-sphere and thus the optimal tunnelling path through configuration space that penetrates the potential

barrier $V(\phi)$. Assuming the thin wall approximation, if a false vacuum decay event were to occur in this theory then Eq. (3.30) specifies the radius in Minkowski space that the nucleated thin wall bubble of true vacuum would have.

Furthermore, Eq. (3.30) specifies the spacelike spacetime separation, $2R_b$, of antipodal points on the nucleated bubble and thus provides us with a complete description of its evolution in Minkwoski space as outlined in Sec. 3.1.4. Aligning these two perspectives with each other, for the thin wall approximation, we can think of Eq. (3.30) as both setting the initial conditions for the bubble at its point of nucleation as well as describing its future expansion in vacuum[3] over all spacetime, as it converts false vacuum to true.

Substituting the critical bubble radius (Eq. (3.30)) back into the thin wall bounce action (Eq. (3.29)) we obtain

$$\begin{aligned} S_b &= -\frac{1}{2}\pi^2\left(\frac{3S_I}{\varepsilon}\right)^4\varepsilon + 2\pi^2\left(\frac{3S_I}{\varepsilon}\right)^3 S_I \\ &= \frac{27\pi^2 S_I^4}{2\varepsilon^3}. \end{aligned} \tag{3.31}$$

Of course this approximation to the Euclidean action is only valid when the radius of the bubble is much larger than the bubble wall. Now we can substitute Eq. (3.31) into Eq. (3.13) to obtain an expression for the decay rate per unit volume of the false vacuum

$$\Gamma/V = Ae^{-\frac{27\pi^2 S_1^4}{2\varepsilon^3}}. \tag{3.32}$$

3.2 Examples of Bounce Solutions

At this point it is instructive to look at a concrete example that we can then use to compute some exact bounce solutions and put our intuitive understanding to the test. With this grounding it will then be easier to bring together the different threads of the conceptual understanding we have developed thus far into a fully functional model of what is taking place when the false vacuum decays.

In previous sections we have taken care to make the distinction between the initially nucleated bubble in Minkowski space and the bounce solution that is a 4-sphere in Euclidean space. For the remainder of this thesis, for convenience, we use the blanket term 'bubble' to cover both the 4-sphere Euclidean bounce solution and the nucleated Minkowski bubble. This works because the bounce solution $\bar{\phi}(\chi)$ is also the Minkowski bubble solution, $\bar{\phi}(r)$, where r is the spacetime separation (Sec. 3.1.4).

[3] In Sec. 5.3 we discuss the dynamics of the bubble wall's expansion in non vacuum scenarios, such as in the presence of a plasma.

3.2.1 A numerical approach: shooting

First we will detail the most common numerical approach typically used to find a bounce solution from any given potential, which can subsequently be used to compute the nucleation rate of bubbles of true vacuum via quantum tunnelling using Eq. (3.13). Indeed, this approach is directly used to obtain our results in Chapters 6 and 9. The numerical scheme is based on Coleman's 'overshoot/undershoot' argument outlined in Sec. 3.1.2 and is best demonstrated by example.

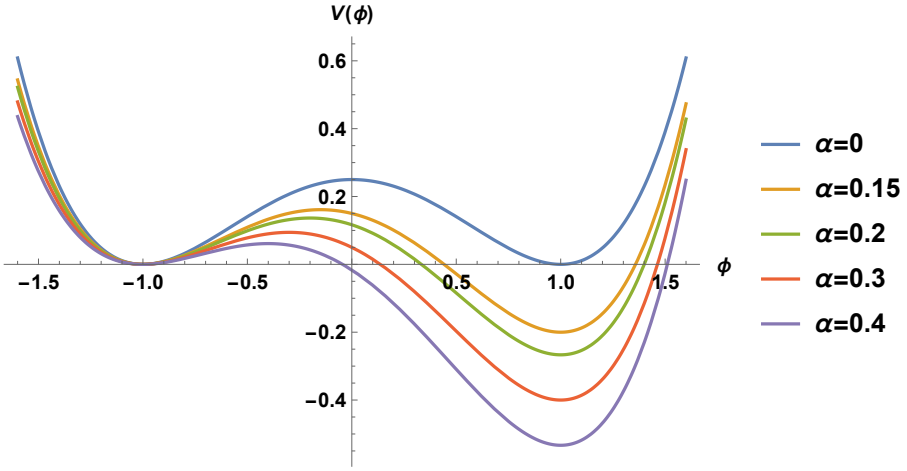

Fig. 3.14 *A range of false vacuum potentials in the thin wall regime.*

In Fig. 3.14 we plot an offset double well potential of the form [26]

$$V(\phi) = \frac{1}{4}(\phi^2 - 1)^2 + \frac{4\alpha}{3}(\phi^3 - 3\phi - 2), \tag{3.33}$$

with false vacuum at $\phi_{fv} = -1$ and true vacuum at $\phi_{tv} = 1$. We can clearly see that the difference in energy density $V(\phi)$ between true and false vacua increases with increasing α. When $\alpha = 0$, we have a symmetric double well potential with 2 degenerate minima.

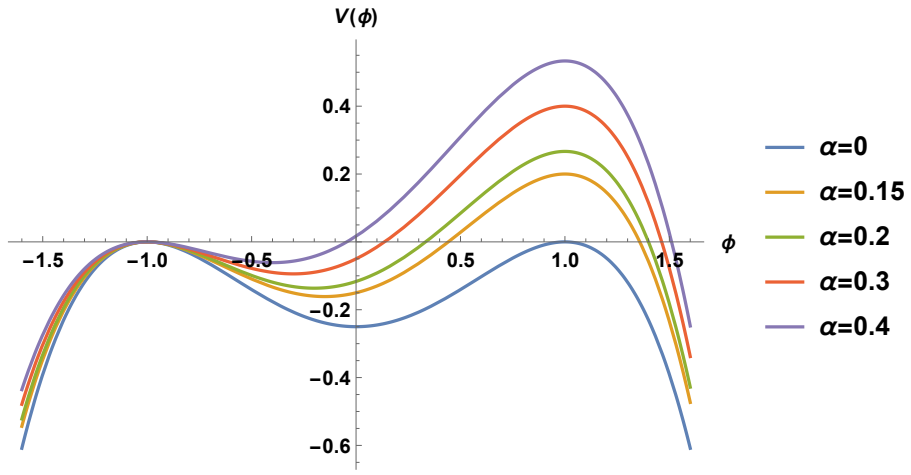

Fig. 3.15 *A range of inverted false vacuum potentials in the thin wall regime.*

We obtain Fig. 3.15 after rotating to Euclidean space and thus flipping the sign of the potential in Eq. (3.33). We then need to solve the Euclidean equation of motion (Eq. (3.15)) with the boundary conditions (Eqs. (3.16) & (3.17)) for our potential to find the bounce solution. To do this we use the overshoot/undershoot method (Sec. 3.1.2) to vary the initial position of ϕ_b to numerically solve the ODE for different values of α.

We will quickly recap this method employing our mechanical particle analogy to help us. Our aim is to find the stationary field value ϕ_b, close to $\phi = \phi_{tv} = 1$, that will map out a solution for which the particle begins at $\phi(\chi = 0) = \phi_b$ and comes to rest at $\phi = \phi_{fv} = -1$ in the limit $\chi \to \infty$.

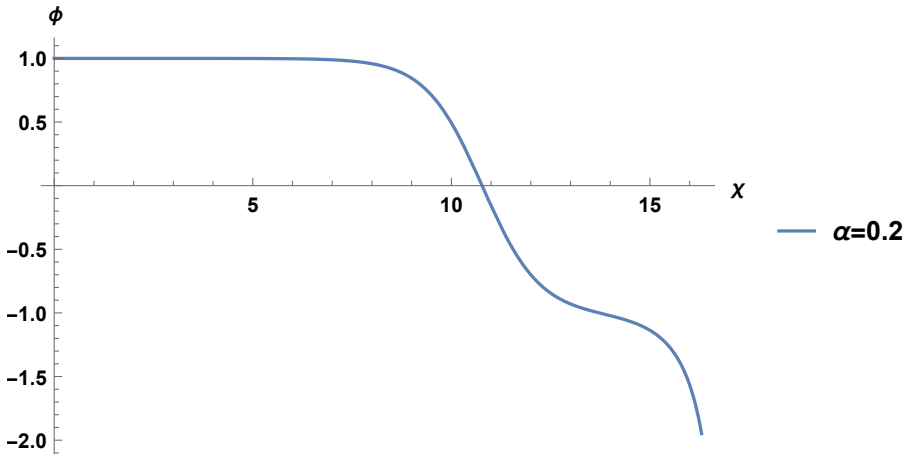

Fig. 3.16 *ϕ_b chosen such that solution overshoots.*

As seen in Fig. 3.16 for $\alpha = 0.2$, if we choose values of ϕ_b too close to $\phi = 1$ then the particle will have too much kinetic energy upon reaching $\phi = -1$ so that it will overshoot this value and the solution will be divergent.

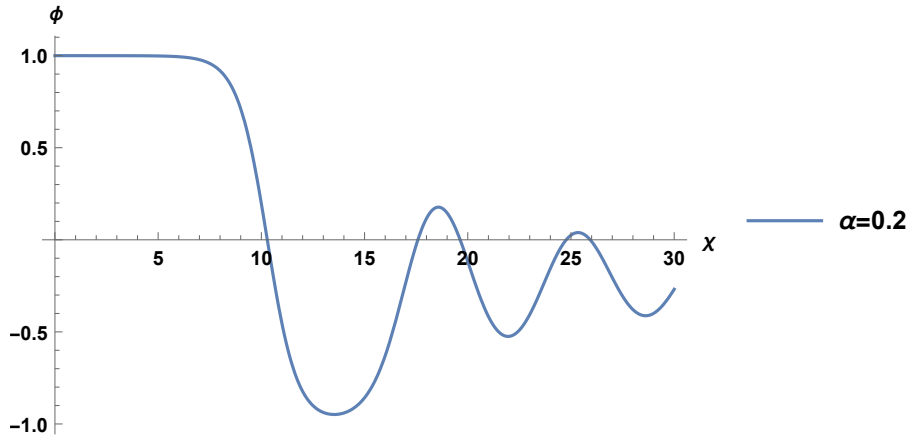

Fig. 3.17 *ϕ_b chosen such that solution undershoots.*

Conversely, as seen for $\alpha = 0.2$ in Fig. 3.17, if we choose values for ϕ_b too far down the hill from $\phi = 1$ the particle will be heavily influenced by the drag term and will not have enough kinetic energy to make it up the right hand hill. Thus the solution will be oscillatory.

By continuity there will always be a solution (Sec. 3.1.2) that stops at $\phi = -1$ in the limit $\tau \to \infty$ and this is the solution we wish to determine numerically by iterating the ϕ_b initial condition to the desired degree of accuracy, $\phi(\chi = 0) \approx \phi_b$.

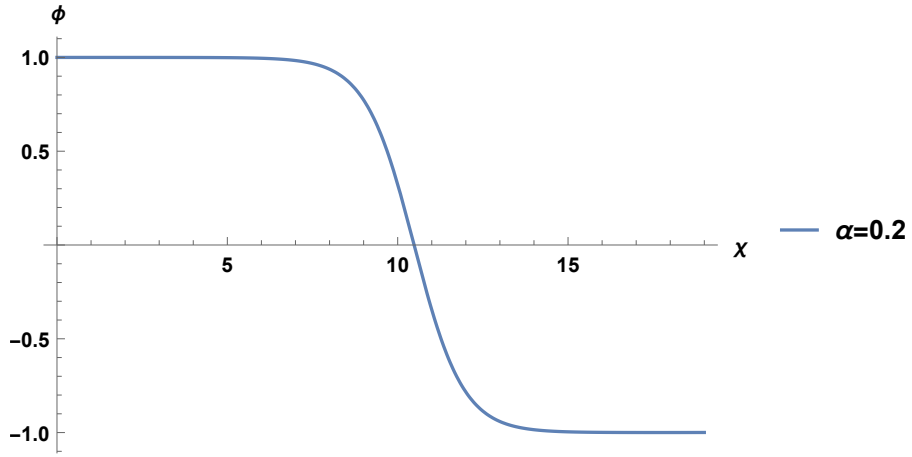

Fig. 3.18 *ϕ_b chosen to give correct solution (the bounce).*

An example of the instanton profile for $\alpha = 0.2$ obtained by this numerical method is shown in Fig. 3.18. Interpreting the solution in Fig. 3.18 in terms of a vacuum bubble, we start in the centre of our bubble of approximate true vacuum $\phi = 1$ and move out radially. At radius $\chi \approx 9$ we reach the thin wall of the bubble and as we move through it with increasing χ the field is smoothly transitioned from true vacuum value within to false vacuum value without. Thus, we exit the bubble wall into a homogeneous false vacuum field configuration that extends over the whole of Euclidean space. In this case

the transition from true to false vacuum takes place at a radius large compared to the wall width. Therefore the vacuum bubble is said to have a thin wall.

3.2.2 Thin walls

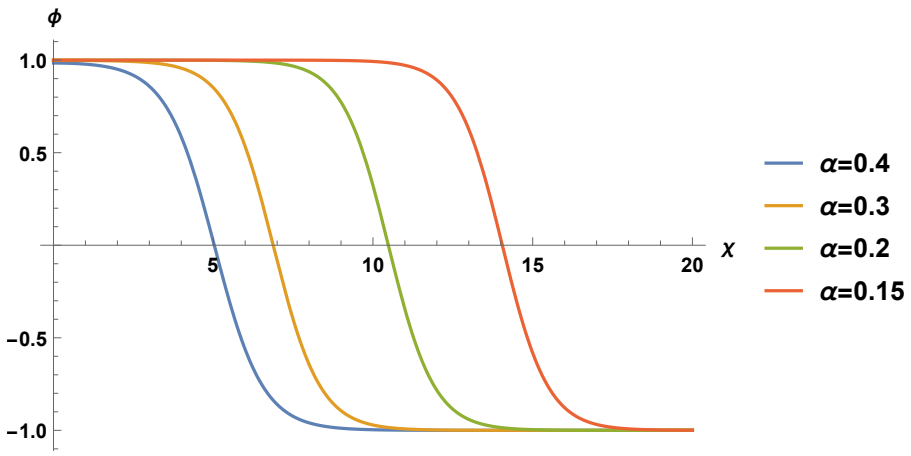

Fig. 3.19 *A range of approximate true vacuum bounce solutions in the thin wall regime.*

In Fig. 3.19 we show our results after repeating the above numerical method for each value of α in Fig. 3.14. As the difference in energy density between true and false vacuum ε increases (i.e. with increasing α), the spacetime radius $r = R_b$ of the nucleated Minkowksi bubble decreases. Furthermore, the field value of the interior region of the bubble, ϕ_b, remains approximately at the true vacuum $\phi = 1$. This can be explained by the fact that as the difference in energy density $\varepsilon = |V(\phi_{fv}) - V(\phi_{tv})|$ increases, more energy per unit volume is available to the bubble in transitioning from $\phi_b \approx 1$ to the false vacuum $\phi_{fv} = -1$. Thus less volume of bubble is required to counteract the surface tension cost at the bubble wall and so the radius of the Minkowski bubble decreases.

We can also see from Fig. 3.19 that as the bubble radius decreases, the profile of the wall region remains similar. Therefore the bubble wall has an increasingly significant contribution to the total bubble volume. It is clear that we have then moved out of the realms of the thin wall approximation into false vacuum decay scenarios with an increasingly thick wall profile.

To calculate the decay rate for this theory we need to evaluate the Euclidean action for each of our given bounce solutions using Eq. (3.18) which we can then substitute into Eq. (3.13) to obtain the false vacuum decay rates per unit volume for each value α. When we do this we find that as expected, the closer to the thin wall limit our theory is (i.e. the smaller the α value) the smaller the false vacuum decay rate per unit volume is. Or perhaps more succinctly, taller and wider barriers make tunnelling more difficult which results in less bubbles nucleated per unit volume.

3.2.3 Thick walls

Thus far, we have only assumed the difference in energy density between the false vacuum, ϕ_{fv}, and true vacuum, ϕ_{tv}, to be negligible compared to the height of the barrier in $V(\phi)$. The resulting bounce solution specified that the initially nucleated bubble in Minkowski space would have a thin wall. We argued this by interpreting the bubble wall as a 1D instanton and noted that, under our approximation, this was negligible in extent compared to the radius of the bubble.

A natural development to this model arises when we consider vacuum decay for potentials where the difference in energy density between ϕ_{fv} and ϕ_{tv} is much larger than the height of the barrier in $V(\phi)$ as is the case when we consider the potential in Eq. (3.33) for $0.6 \leq \alpha \leq 1.0$. For $|\alpha| \leq -1$ the barrier disappears completely and we move into a qualitatively different scenario.

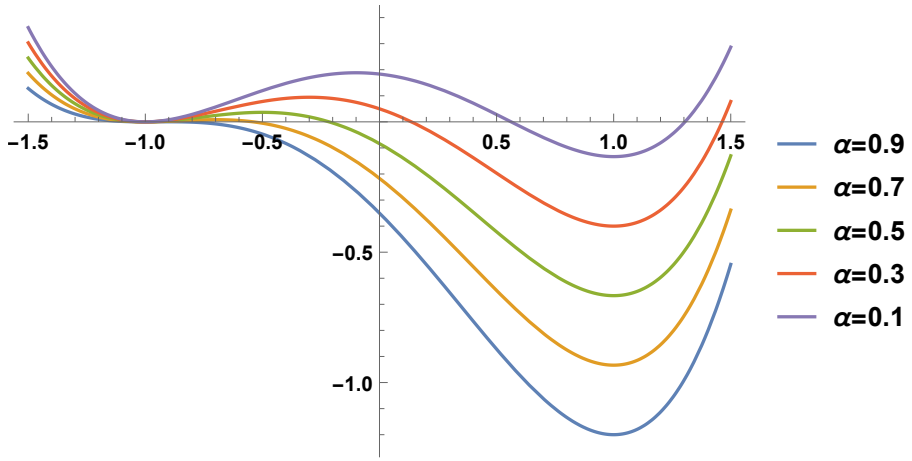

Fig. 3.20 *A full range of false vacuum potentials in the thick and thin wall regime.*

In our analysis in the previous section we saw that bounce solutions for potentials having $\alpha \approx 0$ described thin walled bubbles with interior field value ϕ_b. As we moved away from the thin wall approximation we saw that the radius of the bounce and thus also the radius of the nucleated Minkwoski bubble decreased. This reflected the fact that a smaller volume of ϕ_b was required for the bubble to nucleate in Minkowski space due to the increase in energy density between true and false vacuum $|V(\phi_{tv}) - V(\phi_{fv})|$. As the bubble decreased in radius the volume contribution from its wall region became increasingly significant and it moved out of the thin wall realm into a class of false vacuum decay bubbles with increasingly thick walls.

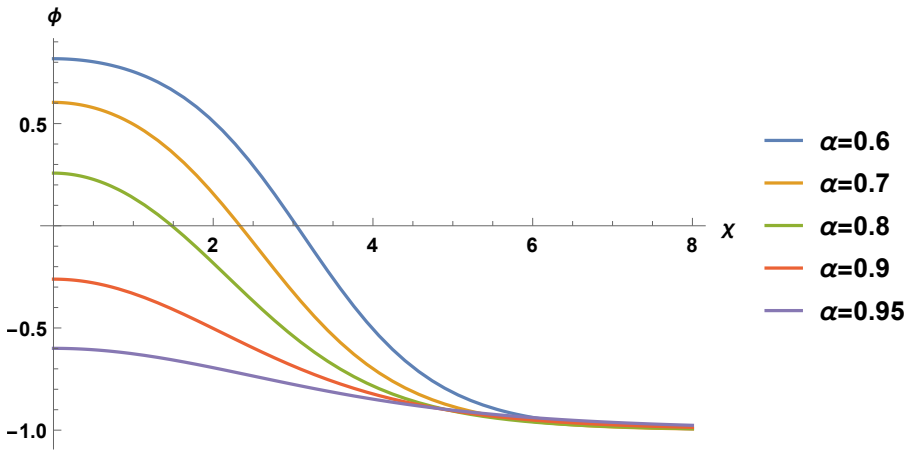

Fig. 3.21 *A range of thick wall bounce solutions.*

Inspecting Fig. 3.21 we see how the profile of the bounce solution varies with increasing α in the region $0.6 \leq \alpha < 1$ and get a flavour of its behaviour in the limit $\alpha \to 1$ where the barrier disappears entirely. Fig. 3.21 shows that with increasing α the field gradient in the thick walled bubble decreases. This is to be expected as the field value at the center of the bubble is becoming closer to the false vacuum. Indeed in the limit $\alpha \to 1$, the difference in energy density, $|V(\phi_b) - V(\phi_{fv})|$, becomes vanishingly small and the 'bubble' approaches homogeneity.

From a conceptual standpoint we can see that the notion of a bubble wall becomes increasingly diffuse compared to its well localised thin walled counterpart. Indeed in the thick wall limit $\alpha \to 1$ where the barrier in $V(\phi)$ disappears, 'bubbles' can form of radius $r \to \infty$ with interior field value $\phi_b \to \phi_{fv}$ [32].

In this thick wall limit, vacuum decay may well be inclined to take place via a homogeneous rolling process rather than a process of bubble nucleation. This makes sense from an intuitive perspective as if no barrier in $V(\phi)$ is present then rolling solutions will exist where the field homogeneously transitions from false vacuum configuration to true vacuum

at the minimum of $V(\phi)$. Thus, in this case, the solution has evolved classically and no tunnelling event has taken place.[4]

To find the decay rate of the false vacuum per unit volume in each of these thick wall scenarios we need to calculate the Euclidean action for each using Eq. (3.18) and substitute the result into Eq. (3.13). After doing this we find that the decay rate increases with decreasing barrier height and width and so more bubbles are nucleated per unit volume for barriers that are smaller in size.

[4]In the case where no barrier exists in $V(\phi)$, there still may exist tunnelling solutions that directly compete against these rolling solutions if there still exists a barrier in the full potential function $U(\phi)$ in Eq. (3.6) which includes both $V(\phi)$ and the spatial gradient term $(\nabla\phi)^2$ [33].

Chapter 4

False Vacuum Decay with Multiple Minima

Having developed the formalism for calculating false vacuum decay rates in theories with a single scalar field which decays to an adjacent lower energy 'true' vacuum, a natural further avenue to consider is the possibility of tunnelling to a far away minimum in a potential landscape with multiple vacua. Such a problem would require a tunnelling path that traverses the numerous intermediate minima in the landscape before it reaches its destination. This can make finding a solution extremely challenging [34] and in some cases can even result in no solution existing at all [35].

Whilst studies have been performed to explore how the tunnelling probability scales with the number of fields in a potential landscape [34, 36], to our knowledge little progress has been made towards solving problems that involve tunnelling to far away vacua. This can perhaps be attributed to the extreme numerical sensitivities of the solution space often seen when adopting traditional 'overshoot/undershoot' approaches [34], as we discuss further in Sec. 4.2. In light of this, in this Chapter we seek to perform a preliminary investigation into this problem. We we will attempt to identify and, where possible, categorise potentials for which we are able to find a tunnelling solution to a non-adjacent true minimum.

To do this we employ a novel approach first outlined in [16] and later generalised to multi-field scenarios in [17] which sought to reformulate the problem in terms of a new action, S_t, defined using objects called 'tunnelling potentials'. This new action quantity has the crucial property that it can be minimised to find the bounce solution, which puts it in stark contrast to the Euclidean action for which the bounce lies at a saddle point. This means that in more complex false vacuum configurations, the S_t action can be less sensitive to numerical instabilities when employing it to compute false vacuum decay rates compared to its Euclidean counterpart. We use a numerical algorithm to calculate the minimum of S_t that is inspired by the work in [17], as it allows us to tackle this problem in

both single-field (see Sec. 4.5) and multi-field (see Sec. 4.6) scenarios. We describe our numerical algorithm in detail in Sec. 4.4.

In Sec. 4.5 we show that it is possible for a single field trapped in a meta-stable vacuum to tunnel to non-adjacent minima in its potential. However, we find that the detailed shape of the potential and the relationship between the energy density of successive minima can determine whether a solution can be found with our approach. This could be due to either numerical issues or the possibility that tunnelling directly to non-adjacent minima is not possible for these potentials and so would have to take place via successive tunnelling events between neighbouring minima.

In Sec. 4.6 we show that tunnelling from a metastable vacuum to a non-adjacent minima is also possible in scenarios with two coupled fields. However, constructing a potential for which our code finds a solution is far more challenging than the single field case, primarily attributed to the extra degrees of freedom available to the solution space. Improvements to our numerical algorithm, such as adopting regularisation schemes similar to that used in [37], would make it possible to conduct a more systematic investigation into the qualitative properties of coupled multi-field potential landscapes that admit tunnelling solutions to non-adjacent minima.

4.1 Motivation: the String Theory Landscape

String theory generically admits a myraid number of different vacuum solutions arising from flux compactifications, [38] estimates as high as 2^{500}. Taken together, these vacuum states can collectively be interpreted as forming a wider construction known as 'the string theory landscape' [39] where each of the vacua are meta-stable [40] and thus permit barrier penetration via quantum tunnelling with some finite probability.

In this landscape the vacuum energy of each of the different minima can typically take on a range of different values [41] which has motivated many anthropic arguments to solve the cosmological constant problem.[1] Such arguments are broadly based on the assumption that our universe resides in a vacuum of the landscape where the cosmological constant takes on the tiny value we measure and that tunnelling from this minimum is exponentially suppressed. However, attempts to provide a more satisfying solution to the puzzle have motivated some to consider mechanisms by which the universe came to reside in such a minimum.

One idea envisages a dynamical mechanism [43] where the universe starts out in a minimum of the potential landscape where the vaccum energy is comparatively large. The universe then subsequently undergoes a series of rapid tunnelling events, traversing the landscape until it reaches a vacuum where the cosmological constant takes on the

[1] See [42] for a discussion of these approaches and a broader historical summary of the subject in general.

vanishingly small value seen today. Similar mechanisms are discussed in the context of chain inflation scenarios in [44–46].

For a dynamical mechanism taking place in such a vast potential landscape, it is not difficult to imagine scenarios where the universe decays directly to far away minima during its early evolution and, in doing so, skips out the neighbouring minima where the tunnelling rate may be exponentially suppressed in comparison [43]. Unfortunately, little is known about the shape of the string landscape's potential between well separated minima and this makes a concrete phenomenological study into this mechanism challenging.

Given the many unknowns related to the form of the potential, as well as the numerical challenges faced with tunnelling to far away minima, our study simply focuses on a preliminary analysis into classifying the types of potential landscapes that admit tunnelling solutions directly to non-adjacent minima. As further discoveries related to the shape of the potential are made, along with certain improvements to our numerical algorithm (see Sec. 4.7), we expect our results can be refined and the scope of our investigation more focused.

4.2 Difficulties with Shooting in Multi-minima Potentials

Before going any further we should asses the suitability of using a standard numerical approach based on the 'undershoot/overshoot' method (see Sec. 3.2.1) to solve our problem of calculating tunnelling paths in scenarios with a potential landscape that has many minima. Several efficient public numerical packages exist that employ approaches broadly based on shooting or some hybrid of it [34, 35, 47] and thus understanding some of the core issues with vanilla shooting methods will help us asses to what degree they might be of use for our purposes.

Whilst shooting methods are largely accurate when tunnelling to neighbouring minima, the situation becomes much more complicated when tunnelling to non-adjacent vacua as the bounce solution we are trying to calculate can be extremely sensitive to other unwanted growing bounce modes. In some cases this can make it very difficult or impossible to isolate and accurately find the solution of interest, whilst in other cases a solution may not even exist at all [35].

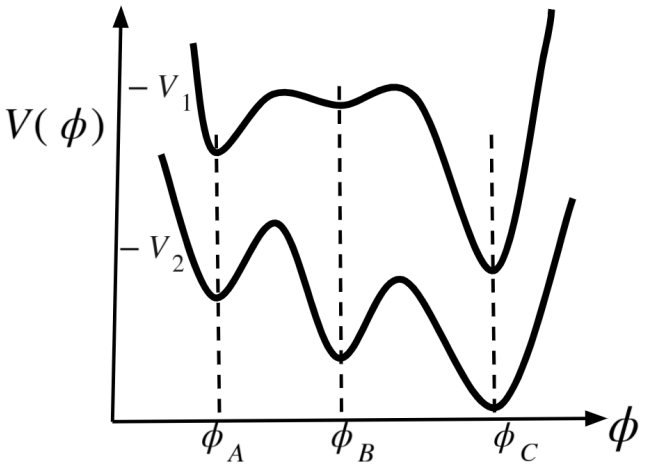

(a) *Example potentials.*

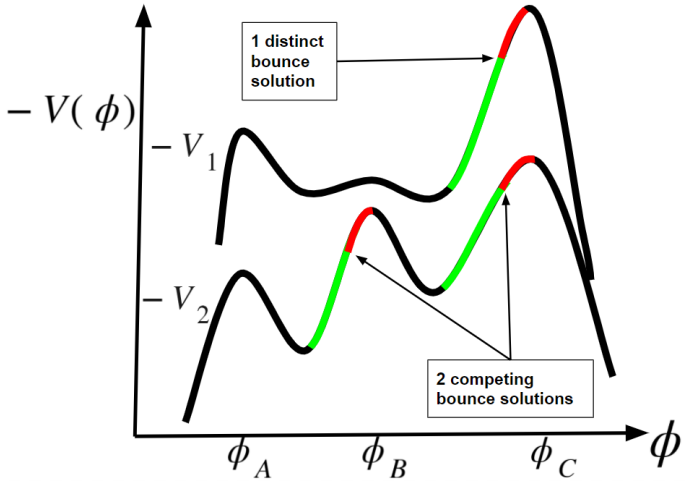

(b) *Wick rotated example potentials for visualising rolling analogy of solution spaces.*

Fig. 4.1 *Two example potentials with qualitatively different tunnelling solution spaces as inspired by Fig. 3 of [35] and Fig. 3 of [34].*

In Fig. 4.1 we identify two heuristic examples of multi-minima potentials that exhibit different qualitative behaviour in relation to the existence of tunnelling solutions between the false vacuum at ϕ_A and the minimum at ϕ_C. Using Fig. 4.1b, we will now discuss both of these cases under the usual analogy of a pseudo-particle rolling in the upside down potential, $-V$, as described in Sec. 3.1.2.

Finding a bounce solution between ϕ_A and ϕ_C for the top potential in Fig. 4.1 should be relatively straight forward using a shooting method. This is clear after inspecting its Wick rotated form in the top curve of Fig. 4.1b, where if we release the pseudo-particle from near the bottom of the hill whose summit is ϕ_C it will clearly undershoot the false vacuum at ϕ_A. As we increase the release point, ϕ_0, up the hill it will continue to undershoot but will get increasingly closer to ϕ_A before dropping back into the valley. This will continue to be the case until we reach a critical ϕ_0 release value after which the particle has too

much energy and will always overshoot ϕ_A. Thus, as is the case for the usual false vacuum decay scenarios discussed in Sec. 3.2, there exists a single bounce solution for this problem and it lies at the single critical ϕ_0 value at which the particle goes from undershooting the true vacuum (green region) to overshooting it (red region), which means finding the solution using a shooting method should not prove too difficult.

Finding a tunnelling solution between ϕ_A and ϕ_C for the bottom potential of Fig. 4.1 can prove to be significantly more challenging or impossible using a shooting method [34, 35]. This is due to the fact that in this scenario we either expect more than one bounce solution to exist in the vicinity of ϕ_A and ϕ_C, or no bounce solution to exist at all.

We demonstrate the case of more than once bounce solution existing in the bottom curve of Fig. 4.1b, where a bounce solution is premised to exist between ϕ_A and ϕ_C shown by the point at which the undershoot region (green) transitions to the overshoot region (red) on the right most ϕ_C hill. However, from Coleman's 'overshoot/undershoot' argument detailed at the end of Sec. 3.1.2 we know a second bounce solution must also exist that asymptotically approaches ϕ_A but starts close to the intermediate minima at ϕ_B. We have no interest in this second bounce solution and it only serves to cause significant numerical instability when using a numerical shooting method. The instability arises because the solution we are interested in must compete against the growing mode from the unwanted solution in this region. This can make finding the bounce solution between ϕ_A and ϕ_C an extremely difficult or impossible task [34].

Adding to the complexity of this scenario, it is also possible that the bottom curve of Fig. 4.1b could exhibit no bounce solutions at all. In this case it could be that if the pseudo-particle starting near ϕ_C has enough energy to pass ϕ_B, then it always overshoots the false vacuum at ϕ_A [35]. As no direct tunnelling solution exists from ϕ_A to ϕ_C the field would first have to tunnel to ϕ_B and then to ϕ_C in independent tunnelling events.

This problem of multiple bounce solutions causing instability in our numerical scheme can in some cases be avoided by employing more sophisticated shooting techniques such as multiple shooting schemes [48] that seek to iteratively partition the solution into a fixed number of regions that provide a means to isolate the bounce solution of interest. One can then demand that each region of the solution must match at its boundaries before going on to iterate the entire solution numerically. Whilst such numerical schemes can in some cases work reasonably well, one would expect them to be cumbersome when there are numerous intermediate minima as the number of intermediate solution regions must also increase. One would expect the efficiency of the numerical scheme to be impacted even further when many fields are present.

An intimately related issue with traditional shooting schemes that are trying to estimate false vacuum decay rates in exotic potential landscapes is that the bounce lies at a saddle point of the Euclidean action, as discussed in Sec. 2.2. This means that any numerical approaches, like shooting to stationary points, can be highly susceptible to suffering from

stability issues as small pertubations of the bounce in the direction of the negative mode can cause the action to diverge. These sensitivity issues that are so ingrained in approaches that involve using the Euclidean action to calculate false vacuum decay rates can only be compounded when they are applied to scenarios with multiple minima and multiple fields. This motivates us to search for a new more robust approach that we can employ to solve such a problem.

4.3 A Multi-field Shooting Alternative: Tunnelling Potentials

One promising alternative approach, recently suggested in [16] and generalised to situations with many fields in [17], involves re-formulating the problem in terms of a 'tunnelling potential'. This quantity is defined as

$$V_t(\varphi) \equiv V(\underset{\sim}{\phi}) - \frac{\dot{\underset{\sim}{\phi}}^2}{2}, \tag{4.1}$$

where $\underset{\sim}{\phi}$ is the solution to the Euclidean multi-field equations of motion (EoM) and is itself a function of the canonical scalar field, φ, that parameterises the field space distance travelled along the generally curved solution path. Note that along the path φ, $V_t(\varphi) \leq V(\underset{\sim}{\phi})$ as $\dot{\underset{\sim}{\phi}}^2 \geq 0$.

Although at first sight the benefit of defining such a quantity is not immediately clear, we will later see that it allows us to eliminate all references to $\underset{\sim}{\phi}$ in our equations and proceed with this tunnelling potential object as our fundamental quantity. We will see later that these objects possess some useful properties as we discuss in Sec. 4.3.3. After making this switch it will then allow us to define a new action quantity which we call the tunnelling potential action, S_t, which enjoys some significant advantages over the usual Euclidean action used to find false vacuum decay rates. Chief of these is the property that the bounce solution describing false vacuum decay lies at the minimum of this S_t action and not at a saddle point as is the case for the Euclidean action. As we will see, this crucial property of the S_t action applies in both the single field [16] and multi-field [17] applications of this approach and is attractive as it allows us to build a numerical algorithm purely geared around finding the minimum of a function, which is a very well studied problem. In Sections 4.5 and 4.6 we will show that this approach enables solutions to be found for tunnelling between non-adjacent minima in both single and multi-field scenarios.

4.3.1 Tunnelling potentials from first principles

In Sec. 4.2 we outlined the numerical shortcomings of accurately solving the multi-field Euclidean EoM [2],

$$\ddot{\underset{\sim}{\phi}} + \frac{3}{r}\dot{\underset{\sim}{\phi}} = \underset{\sim}{\nabla} V, \tag{4.2}$$

with boundary conditions

$$\dot{\underset{\sim}{\phi}}_b(r=0) = \underset{\sim}{0}, \quad \underset{\sim}{\phi}_b(r\to\infty) = \underset{\sim}{\phi}_{fv} \tag{4.3}$$

for the bounce solution, $\underset{\sim}{\phi}_b(r)$, in scenarios with multiple minima and multiple fields. Here $\dot{\underset{\sim}{\phi}}$ and $\ddot{\underset{\sim}{\phi}}$ denote first and second derivatives with respect to the Euclidean radial co-ordinate r and $\underset{\sim}{\phi}_{\rm fv}$ is the false vacuum. In this section we will seek to eliminate any reference to the Euclidean solution, $\underset{\sim}{\phi}$, in Eq. (4.2) and in doing so will derive the tunnelling potential quantity in Eq. (4.1) from first principles.

First we note that if we take the dot product of Eq. (4.2) with $\dot{\underset{\sim}{\phi}}$ and rearrange we can express the Euclidean radial co-ordinate r as,

$$r = \frac{3(\dot{\underset{\sim}{\phi}}\cdot\dot{\underset{\sim}{\phi}})}{(\underset{\sim}{\nabla} V - \ddot{\underset{\sim}{\phi}})\cdot\dot{\underset{\sim}{\phi}}} = \frac{3(\dot{\underset{\sim}{\phi}}\cdot\dot{\underset{\sim}{\phi}})}{\underset{\sim}{\nabla} V\cdot\dot{\underset{\sim}{\phi}} - \ddot{\underset{\sim}{\phi}}\cdot\dot{\underset{\sim}{\phi}}}. \tag{4.4}$$

A natural way to paramterise the path $\underset{\sim}{\phi}$ is in terms of its path length in field space φ, $\underset{\sim}{\phi}(\varphi)$. So expressing the denominator of Eq. (4.4) in terms of φ we obtain

$$\underset{\sim}{\nabla} V\cdot\dot{\underset{\sim}{\phi}} = \frac{dV}{d\varphi}\cdot\frac{d\varphi}{dr} = \frac{dV}{dr} \tag{4.5}$$

where we have used that the gradient of the potential along the tangent to the path is

$$\underset{\sim}{\nabla} V\cdot d(\dot{\underset{\sim}{\phi}}(\varphi)) = \frac{dV}{d\varphi}d\varphi. \tag{4.6}$$

Then, given that we can write

$$\begin{aligned}\frac{d}{dr}(\frac{1}{2}\dot{\underset{\sim}{\phi}}\cdot\dot{\underset{\sim}{\phi}}) &= \frac{d}{dr}(\frac{1}{2}|\dot{\underset{\sim}{\phi}}|^2)\\ &= \ddot{\underset{\sim}{\phi}}\cdot\dot{\underset{\sim}{\phi}}\end{aligned} \tag{4.7}$$

we can express the denominator of Eq. (4.4) as

$$\underset{\sim}{\nabla} V\cdot\dot{\underset{\sim}{\phi}} - \ddot{\underset{\sim}{\phi}}\cdot\dot{\underset{\sim}{\phi}} = \frac{d}{dr}\left(V - \frac{1}{2}\dot{\underset{\sim}{\phi}}\cdot\dot{\underset{\sim}{\phi}}\right). \tag{4.8}$$

[2]For the remainder of the thesis we take r to be the Euclidean radial co-ordinate appearing in the Euclidean EoM instead of χ, used in Chapter 3. This is to make clear the direct interpretation this co-ordinate has for the bounce solution, in terms of bubble radius in Minkowski space

We can see that the 'tunnelling potential' quantity defined in Eq. 4.1 appears in Eq. 4.8,

$$\begin{aligned} V_t(\varphi) &= V(\varphi) - \frac{1}{2}\dot{\underset{\sim}{\phi}}(\varphi)\cdot\dot{\underset{\sim}{\phi}}(\varphi) \\ &= V(\varphi) - \frac{1}{2}\dot{\varphi}^2, \end{aligned} \tag{4.9}$$

where we have used that $|\dot{\underset{\sim}{\phi}}| = \dot{\varphi}$ because $d\varphi^2 = d\underset{\sim}{\phi}(\varphi)\cdot d\underset{\sim}{\phi}(\varphi)$. Then we can write

$$\dot{\varphi}^2 = 2[V(\varphi) - V_t(\varphi)], \tag{4.10}$$

Finally, using Eq. (4.10) we can eliminate any reference to the bounce in Eq. (4.4) to obtain

$$\begin{aligned} r = \frac{3(\dot{\underset{\sim}{\phi}}\cdot\dot{\underset{\sim}{\phi}})}{\frac{dV_t(\varphi)}{dr}} = \frac{3\dot{\varphi}^2}{\frac{dV_t(\varphi)}{d\varphi}\frac{d\varphi}{dr}} &= \frac{3\dot{\varphi}}{V_t'} \\ &= 3\sqrt{\frac{2(V-V_t)}{(V_t')^2}} \end{aligned} \tag{4.11}$$

where $V_t' \equiv \frac{dV_t}{d\varphi}$ and we have used Eq. (4.10) in the last line.

Taking the derivative of Eq. (4.11) with respect to r we then obtain a differential equation that replaces the Euclidean EoM in Eq. (4.2),

$$(4V_t' - 3V')V_t' = 6(V_t - V)V_t'' \tag{4.12}$$

with boundary conditions,

$$V_t(\underset{\sim}{\phi}_{fv}) = V(\underset{\sim}{\phi}_{fv}), \quad V_t(\underset{\sim}{\phi}_0) = V(\underset{\sim}{\phi}_0) \tag{4.13}$$

which replace the usual boundary conditions for the bounce shown in Eq. (4.3). We call $\underset{\sim}{\phi}_0$ the release point of the field in reference to the pseudo-particle rolling analogy, under the understanding that in Eq. (4.13) this release point coincides with the release point of the bounce solution i.e. $\underset{\sim}{\phi}_0 = \underset{\sim}{\phi}_b(r=0)$.

The only thing that remains for us to do is to is to eliminate any reference of the Euclidean solution $\underset{\sim}{\phi}$ from the Euclidean action. To do this we first write the Euclidean action in terms of the path length parameter φ,

$$S_E = 2\pi^2 \int_{\varphi_{fv}}^{\varphi_0} dr r^3 \left[\frac{1}{2}\left(\left|\frac{d\underset{\sim}{\phi}(\varphi)}{dr}\right|\right)^2 + V(\underset{\sim}{\phi}(\varphi))\right] \tag{4.14}$$

Using Derrick's theorem [49], which allows us to equate the potential energy contribution to the action with the kinetic energy contribution, we then have

$$\begin{aligned} S_E &= \frac{\pi^2}{2}\int_{\varphi_{fv}}^{\varphi_0} dr r^3 \left(\left|\frac{d\underset{\sim}{\phi}(\varphi)}{dr}\right|\right)^2 \\ &= \frac{\pi^2}{2}\int_{\varphi_{fv}}^{\varphi_0} r^3 \frac{dr}{d\varphi} d\varphi \left(\frac{d\varphi}{dr}\right)^2. \end{aligned} \tag{4.15}$$

Substituting Eq. (4.10) and Eq. (4.11) into Eq. (4.15) we obtain a new action in terms of tunnelling potentials

$$S_t[V_t] = 54\pi^2 \int_{\varphi_{fv}}^{\varphi_0} \frac{(V-V_t)^2}{(-V_t')^3} d\varphi \tag{4.16}$$

where we have used that

$$r^3 \frac{dr}{d\varphi} d\varphi = 54 \frac{(V-V_t)}{(-V_t')^3} d\varphi \tag{4.17}$$

Note that the 'release point' $\varphi_0 \equiv \underset{\sim}{\phi}_0$ in Eq. (4.16) can, in general, describe any chosen release point of the field between the true vacuum, $\underset{\sim}{\phi}_{tv}$, and the false vacuum $\underset{\sim}{\phi}_{fv}$. However, at the global minimum of S_t, this $\underset{\sim}{\phi}_0$ release value exactly coincides with the release value of the bounce solution as we discuss next.

4.3.2 Finding tunnelling solutions with the S_t action

In [17] they prove that requiring the S_t action in Eq. (4.16) to be stationary, $\delta S_t = 0$, under variations of the path $\underset{\sim}{\phi}$ or tunnelling potential V_t returns the EoM in Eq. (4.12). This amounts to one crucial benefit of this new 'Tunnelling Potential action', in that the bounce solution describing tunnelling lies at its *minimum* [17].

This key result means that when we look to cook up a numerical algorithm to find false vacuum decay solutions using a tunnelling potentials based approach in Sec. 4.4, we will be less interested in the differential formulation of the problem from Eq. (4.12). Instead, we will base our numerical approach around finding the minimum value of the integral description in Eq. (4.16) as finding the minimum of a function is a very well understood numerical problem.

This is, of course, in contrast to using a shooting method where one must employ the Euclidean action in Eq. (3.18) for which the bounce solution only resides at a saddle point of this quantity as discussed in Sec. 2.2. Whilst the presence of a saddle point in the Euclidean action at the bounce is not such a problem when using a shooting method in single field scenarios and can even be dealt with in certain two field scenarios via methods like multi-shooting, when more scalar fields or more intermediate minima are introduced then finding the bounce via shooting becomes no longer a feasible strategy as discussed in Sec. 4.2.

4.3.3 Properties of V_t

Tunnelling potentials possess some particularly useful attributes, which will be important later when building our numerical algorithm to efficiently compute false vacuum decay solutions.

One of the most important properties of $V_t(\varphi)$ that we will use later is that it is a monotonic function with $V_t(\varphi) \leq V(\underset{\sim}{\phi}(\varphi))$. This becomes clear when we think about the problem in terms of a particle moving in an inverted potential analogy from Sec. 3.1.2, where we can add kinetic and potential energy contributions to obtain the total 'Euclidean' energy of the system $E = \frac{\dot{\phi}^2}{2} - V(\underset{\sim}{\phi})$. This Euclidean energy is monotonically dissipated by the effective friction term in Eq. (4.2) as the pseudo-particle travels, with increasing r, from $\underset{\sim}{\phi}_0$ and through the inverted potential to $\underset{\sim}{\phi}_{fv}$. This can be seen by using Eq. (4.8) to integrate the ODE in Eq. (4.2) for the bounce, $\underset{\sim}{\phi}_b$, to obtain

$$\frac{d}{dr}\left(\frac{1}{2}|\dot{\underset{\sim}{\phi}}_b|^2 - V(\underset{\sim}{\phi}_b)\right) = -\frac{3}{r}|\dot{\underset{\sim}{\phi}}_b|^2 \leq 0. \tag{4.18}$$

In terms of the tunnelling potential defined in Eq. (4.1) we then have

$$\frac{d}{dr}(V_t(\underset{\sim}{\phi}_b)) = \frac{3}{r}|\dot{\underset{\sim}{\phi}}_b|^2 \geq 0 \tag{4.19}$$

which demonstrates that V_t increases monotonically with r as we move from $\underset{\sim}{\phi}_0$ to $\underset{\sim}{\phi}_{fv}$. As $\underset{\sim}{\phi}_b$ is monotonically decreasing between $\underset{\sim}{\phi}_0$ and $\underset{\sim}{\phi}_{fv}$ it means r must be monotonically increasing. But as we have just shown, r also increases monotonically with V_t between $\underset{\sim}{\phi}_0$ and $\underset{\sim}{\phi}_{fv}$ and therefore the function $V_t(\underset{\sim}{\phi})$ is monotonically increasing between $\underset{\sim}{\phi}_0$ and $\underset{\sim}{\phi}_{fv}$.

The second property of $V_t(\underset{\sim}{\phi})$ is that it is a function that is only defined between $\underset{\sim}{\phi}_0$ and $\underset{\sim}{\phi}_{fv}$. This is clear when we consider that the bounce solution, $\underset{\sim}{\phi}_b$, is defined in the domain $r \in (0,\infty)$ whose end points take the values $\underset{\sim}{\phi}_b(r=0) = \underset{\sim}{\phi}_0$ and $\underset{\sim}{\phi}_b(r\to\infty) = \underset{\sim}{\phi}_{fv}$.

A further property of $V_t(\underset{\sim}{\phi})$ is that $V_t = V$ at the $\underset{\sim}{\phi}_0$ and $\underset{\sim}{\phi}_{fv}$ boundaries. This follows directly from the definition of the tunnelling potential in Eq. (4.1) when we note that the bounce solution at the domain boundaries must also satisfy $\dot{\underset{\sim}{\phi}}_b(r=0) = \dot{\underset{\sim}{\phi}}_b(r\to\infty) = 0$. Furthermore, using that the gradient of the potential vanishes at the false vacuum, $V'(\underset{\sim}{\phi}_{fv}) = 0$, one can show that $V_t'(\underset{\sim}{\phi}_{fv}) = 0$ and $V_t'(\underset{\sim}{\phi}_0) = 3V'(\underset{\sim}{\phi}_0)/4$.

In the remainder of this chapter we seek to utilise the attractive properties of the tunnelling potential listed above to construct an algorithm that minimises the tunnelling potential action, S_t. We will then use this algorithm to solve the otherwise challenging task of finding tunnelling solutions in a potential landscape with both many vacua and many fields.

4.4 A Numerical Approach using Tunnelling Potentials

In this section we describe in detail our numerical algorithm to locate the minimum value of our tunnelling potential action, S_t, for the destination true vacuum, $\underset{\sim}{\phi}_{tv}$, we choose to tunnel to. Given that the action value at this minimum coincides with the Euclidean action value of the bounce we can conclude that finding this minimum will amount to finding a solution that describes tunnelling. Broadly speaking, we tackle this minimisation problem by splitting up the procedure into two independent steps: a Newton step to find the path that optimises $V_t(\underset{\sim}{\phi})$ between $\underset{\sim}{\phi}_{fv}$ and the chosen $\underset{\sim}{\phi}_0$ release point [17]; and a gradient descent step to iterate $\underset{\sim}{\phi}_0$ in a direction where the Newton optimised $V_t(\underset{\sim}{\phi})$ has a smaller action.

In the first step we find the tunnelling potential function, $V_t(\underset{\sim}{\phi})$, that has minimum S_t action for a fixed $\underset{\sim}{\phi}_0$ release point. We tackle this problem by using an approach broadly based on Newton's method where we use information about the first and second derivative of the $S_t[V_t]$ action surface to inform us how to arrange our $\underset{\sim}{\phi}$ points to best approximate the $V_t(\underset{\sim}{\phi})$ curve with minimum action for the $\underset{\sim}{\phi}_0$ release point considered. If we were to repeat this Newton's method step for a range of different $\underset{\sim}{\phi}_0$ release input values it would map out a $S_t[\underset{\sim}{\phi}_0]$ function that defines the minimum S_t action values as a function of the $\underset{\sim}{\phi}_0$ release value of the path.

The second step of our numerical scheme involves implementing a gradient descent algorithm that uses information regarding the first derivative of $S_t[\underset{\sim}{\phi}_0]$ to find the $\underset{\sim}{\phi}_0$ release point that minimises this action surface in the vicinity of the true minimum we want to tunnel to.

Before moving on, we need to make sure we are able to calculate the S_t action values of our discretised $V_t(\underset{\sim}{\phi})$ approximations. This requires us to introduce a new variable, α, parameterising the field space path so that we can discretise our expression for the S_t action in Eq. (4.16). Following [17],

$$\begin{aligned} S_t &= 54\pi^2 \int_{\alpha_0}^{\alpha_{fv}} \frac{(V-V_t)^2}{\left(\frac{dV_t}{d\alpha}\right)^3} \left(\frac{d\underset{\sim}{\phi}}{d\alpha}\cdot\frac{d\underset{\sim}{\phi}}{d\alpha}\right)^2 d\alpha \\ &= 54\pi^2 \int_{V_{t0}}^{V_{tfv}} \frac{(V-V_t)^2}{\left(\frac{dV_t}{dV_t}\right)^3} \left(\frac{d\underset{\sim}{\phi}}{dV_t}\cdot\frac{d\underset{\sim}{\phi}}{dV_t}\right)^2 dV_t \\ &= \frac{27\pi^2}{2} \sum_{i=0}^{n} \left[V(\underset{\sim}{\phi}_i) + V(\underset{\sim}{\phi}_{i+1}) - V_{t,i} - V_{t,i+1}\right]^2 \frac{[(\underset{\sim}{\phi}_{i+1}-\underset{\sim}{\phi}_i)\cdot(\underset{\sim}{\phi}_{i+1}-\underset{\sim}{\phi}_i)]^2}{(V_{t,i+1}-V_{t,i})^3} \end{aligned} \tag{4.20}$$

where i's represent specific points along the field space path, $\underset{\sim}{\phi}$, of $n+1$ points and we have set the variable α that parameterises the path to be the tunnelling potential V_t. This is something we are entitled to do due to the properties of V_t outlined in Sec. 4.3.3, namely,

that it is monotonic and only is defined between the false vacuum $\underset{\sim}{\phi}_{fv}$ and the release point $\underset{\sim}{\phi}_0$.

In Sec. 4.4.1 and Sec. 4.4.2 we outline the respective Newton's method and gradient descent components of the overall iteration scheme to minimise the functional $S_t[\phi_0]$, in a single field scenario.

4.4.1 Newton's method step for a single field

As discussed above, using Newton's optimization method we can find the $V_t(\phi)$ configuration with minimum action for a fixed ϕ_0 release point of the path. Newton's method is conceptually the same as applying the Newton-Raphson method which we use to find the root of a function. But instead of trying to find the root of a function we want to find the root of the function's derivative thus giving us its extremum.

Taking the single field case as an example, we first fix an initial guess for the release point ϕ_0 and choose our naive initial path through field space to this location using a fixed number of equidistant points that make a straight line between the chosen ϕ_0 and the fixed false vacuum $\phi_{fv} = \phi_n$. Thus we discretise ϕ as a 1-dimensional column array,

$$\phi = \begin{bmatrix} \phi_0 \\ \vdots \\ \phi_n \end{bmatrix} \tag{4.21}$$

The end points are fixed throughout the Newton's method part of the numerical procedure, whilst all the remaining ϕ grid points that reside between these two values are free to vary according to the Newton numerical scheme.

Our next task is to construct a V_t grid that satisfies the boundary conditions in Eq. (4.13) and remains fixed throughout this Newton's method step of our numerical scheme. Following [17], we define

$$V_{t,i} = V(\phi_{fv}) + x_i^2(3-2x_i)(V(\phi_0) - V(\phi_{fv})) \tag{4.22}$$

where i represents the chosen point along the path and the x_i are equidistant points in the range [0,1] that are distributed non-linearly using $x_i^2(3-2x_i)$ and then scaled up to reside in the interval $[V(\phi_0), V(\phi_{fv})]$, so that they satisfy the boundary conditions in Eq. (4.13). We have chosen the function Eq. (4.22) as it distributes most of the points at the beginning and ends of the path where resolution of its trajectory will be important for the solution's overall accuracy.

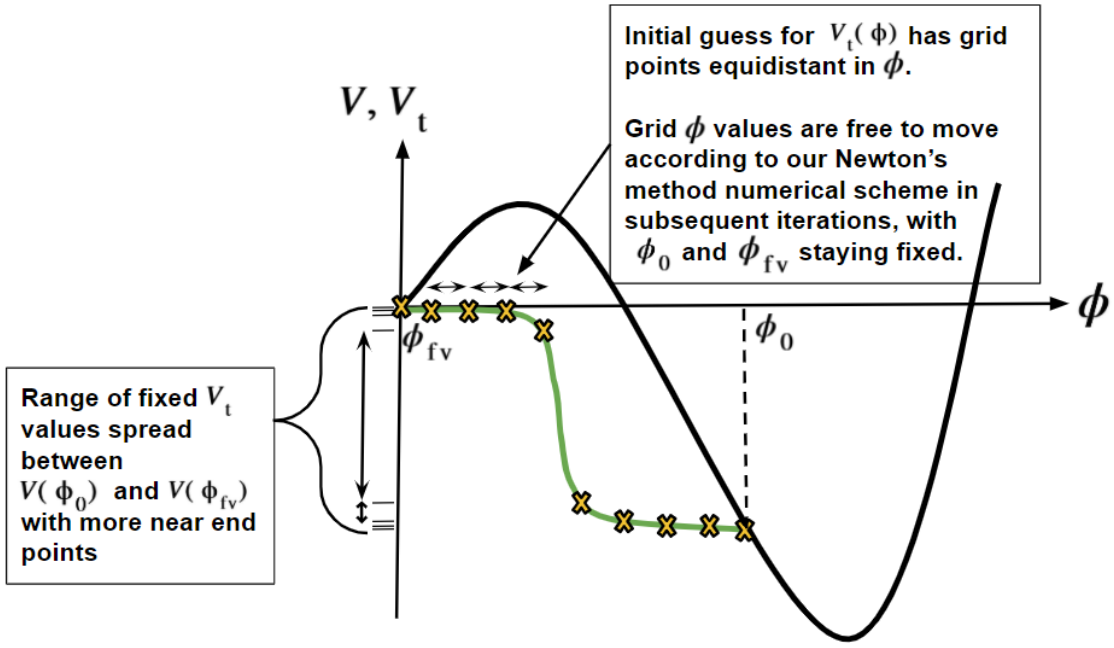

Fig. 4.2 *Setting up the Newton's method step for a single field.*

Having chosen an initial ϕ guess grid and also defined a fixed V_t grid with the same dimensions, we point-wise associate the two grids to define an initial guess for the function $V_t(\phi)$ as is shown heuristically for the 1D case in Fig. 4.2. We can then plug our $V_t(\phi)$ guess into Eq. (4.20) to obtain an approximation for its $S_t[\phi_0]$ action value.

Next, we calculate the gradient and Hessian of the S_t tunnelling action for our initial $V_t(\phi)$ guess for the ϕ_0 release value concerned. Both the gradient vector and Hessian matrix will consist of an array of partial derivatives with respect to each non-boundary point $\phi_i \in [\phi_1, \phi_{n-1}]$ along the initial guess curve. This will provide us with slope and curvature information of S_t that will inform us in which direction we should move each non-boundary ϕ point to get a new $V_t(\phi)$ curve that has largest decrease in S_t.

In the single field example the gradient column array is

$$\nabla S_t = \begin{bmatrix} \frac{\partial S_t}{\partial \phi_1} \\ \vdots \\ \frac{\partial S_t}{\partial \phi_{n-1}} \end{bmatrix}, \tag{4.23}$$

whilst the Hessian takes the form

$$H = \frac{\partial^2 S_t}{\partial\phi_i \partial_j \phi} = \begin{pmatrix} \frac{\partial^2 S_t}{\partial\phi_1\partial\phi_1} & \cdots & \frac{\partial^2 S_t}{\partial\phi_1\partial\phi_{n-1}} \\ \frac{\partial^2 S_t}{\partial\phi_2\partial\phi_1} & & \frac{\partial^2 S_t}{\partial\phi_2\partial\phi_{n-1}} \\ \vdots & \ddots & \vdots \\ \frac{\partial^2 S_t}{\partial\phi_{n-2}\partial\phi_1} & \cdots & \frac{\partial^2 S_t}{\partial\phi_{n-2}\partial\phi_{n-1}} \\ \frac{\partial^2 S_t}{\partial\phi_{n-1}\partial\phi_1} & & \frac{\partial^2 S_t}{\partial\phi_{n-1}\partial\phi_{n-1}} \end{pmatrix} \tag{4.24}$$

The Hessian matrix physically describes local curvature information of the S_t action at each ϕ point along the $V_t(\phi)$ guess curve. From Eq. (4.20), the curvature at a given point ϕ_i can only be affected by changes of the point itself or its neighbouring points; changes in far away points on the other hand can have no effect. Therefore the second partial derivatives of the action that make up the Hessian are only non-zero for entries where derivatives are with respect to the same or neighbouring points. For this reason the Hessian is a tri-diagonal matrix as follows

$$H = \begin{pmatrix} \frac{\partial^2 S_t}{\partial\phi_1\partial\phi_1} & \frac{\partial^2 S_t}{\partial\phi_1\partial\phi_2} & 0 & & 0 & 0 & 0 \\ \frac{\partial^2 S_t}{\partial\phi_2\partial\phi_1} & \frac{\partial^2 S_t}{\partial\phi_2\partial\phi_2} & \frac{\partial^2 S_t}{\partial\phi_2\partial\phi_3} & \cdots & 0 & 0 & 0 \\ 0 & \frac{\partial^2 S_t}{\partial\phi_3\partial\phi_2} & \frac{\partial^2 S_t}{\partial\phi_3\partial\phi_3} & & 0 & 0 & 0 \\ 0 & 0 & \frac{\partial^2 S_t}{\partial\phi_4\partial\phi_3} & & 0 & 0 & 0 \\ & \vdots & & \ddots & & \vdots & \\ 0 & 0 & 0 & & \frac{\partial^2 S_t}{\partial\phi_{n-2}\partial\phi_{n-3}} & \frac{\partial^2 S_t}{\partial\phi_{n-2}\partial\phi_{n-2}} & \frac{\partial^2 S_t}{\partial\phi_{n-2}\partial\phi_{n-1}} \\ 0 & 0 & 0 & \cdots & 0 & \frac{\partial^2 S_t}{\partial\phi_{n-1}\partial\phi_{n-2}} & \frac{\partial^2 S_t}{\partial\phi_{n-1}\partial\phi_{n-1}} \end{pmatrix} \tag{4.25}$$

After computing [3] H and $\nabla S_t[\phi]$ for our initial ϕ grid we can feed this into the Newton's update rule to get a new ϕ grid

$$\phi_{new} = \phi_{old} - \upsilon H^{-1}[\phi_{old}]\nabla S_t[\phi_{old}] \tag{4.26}$$

where $0 < \upsilon \leq 1$ is the variable step size and $H^{-1}\nabla S_t$ is a column array detailing the co-ordinate updates in path required from one iteration to the next. As ϕ_0 and thus the V_t grid remains fixed throughout this Newton's method portion of the algorithm, ϕ_{new} amounts to a new and improved guess for the V_t curve that has minimum S_t action for the input ϕ_0 release value.

[3] In our code we compute all partial derivatives used in our algorithm using analytic expressions we calculated by hand as outlined in Appendix A.1. We initially tried to calculate them via numerical differencing schemes but found issues with accuracy in certain scenarios that motivated us to compute them precisely.

We can calculate the action value of this $V_t(\phi_{new})$ guess using Eq. (4.20) and compare it to the previous action value by computing the 'error',

$$Error = \frac{S_{t,old} - S_{t,new}}{0.5(S_{t,old} + S_{t,new})} \tag{4.27}$$

If we get a positive error, corresponding to a decrease in the action, we complete the first iteration of our Newton's method and repeat the process with the new set of points, ϕ_{new}, first calculating its Hessian and gradient following the variational rules outlined above and again feeding it into the update rule Eq. (4.26) to iterate the $V_t(\phi)$ approximation once again. We continue this procedure until the absolute action error from one iteration to the next changes by less than 1% in which case we can be confident we have converged to the minimum action for the chosen ϕ_0 release point.

However, if at the end of any given iteration we get a negative error, corresponding to an increase of S_t, we know we have overshot the minimum action and so opt to go back two steps in our iteration scheme and repeat the Newton method from that point but with a reduced step size, υ, to avoid overshooting the minimum again. [4]

4.4.2 Gradient descent step for a single field

Performing the above Newton's method based algorithm independently for a grid of ϕ_0 release values would allow us to map out the minimum $S_t[\phi_0]$ surface. However, as discussed in Sec. 4.3.2, only at the minimum of this surface does the S_t action value coincide with the Euclidean bounce action value that describes tunnelling. Thus accurately finding the minimum of the $S_t[\phi_0]$ surface without having to map out the whole action space is a critical task if we want to efficiently find the solution that has an interpretation in terms of false vacuum decay.

We implement a simple gradient descent algorithm to find this minimum. This involves computation of the gradient of the $S_t[\phi_0]$ action with respect to the ϕ_0 release point to inform us in which ϕ_0 direction we need to step to get closer to the minimum. In the single field case we simply need to calculate the derivative $\frac{dS_t}{d\phi_0}$, giving an iterative update scheme as follows,

$$\phi_{0,new} = \phi_{0,old} - \delta \frac{dS_t[\phi_0]}{d\phi_0}. \tag{4.28}$$

Here $\delta \in [0,1]$ is a scalar quantity that controls the size of the step we take towards the minimum. In a similar manner to that outlined in our Newton's method scheme, we

[4] Technically the Newton method should be able to over-shoot the minimum and still converge due to the structure of the algorithm but we found this was not always the case and so found our code to be more reliable when enforcing this condition on the code implementation.

implement our gradient descent algorithm with a variable step size that starts off large but we reduce δ and go back two iterations each time we overshoot the minimum.

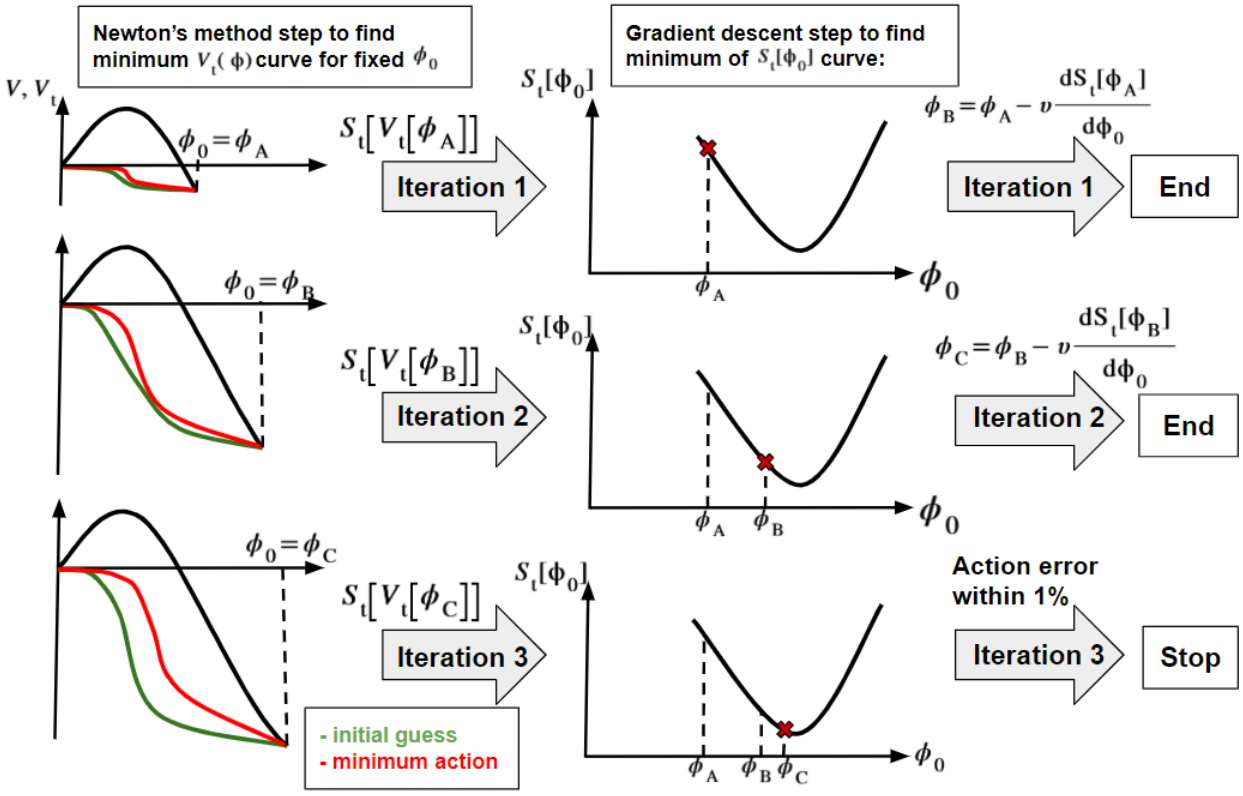

Fig. 4.3 *Summary of numerical algorithm for a single field.*

In Fig. 4.3 we show a heuristic box diagram of the overall numerical routine. From this it is clear that the gradient descent algorithm described above sits on top of the Newton method based algorithm (Sec. 4.4.1) that seeks to the find minimum action for a fixed ϕ_0.

4.4.3 Generalising to multi-field scenarios

Our numerical scheme is sufficiently flexible that it can be easily generalised from the single field scenario described above to a potential landscape with many fields. To demonstrate how this is done we will go through a concrete two field example, in the knowledge that one can generalise in a similar way to any number of fields providing one has the computing resources required.

Whilst in the single field scenario our ϕ points are constrained to live in only one dimension, in scenarios with more than one field the arrangement of our $\underset{\sim}{\phi}$ points map out a path in our multi-dimensional field space. The aim of our numerical scheme then becomes trying to find the path through field space that has $V_t(\varphi)$ with minimum action, where φ is the distanced travelled along the path. This again requires us to split our numerical scheme

into a Newton's method part and a gradient descent path in a similar way to as was done in the single field case.

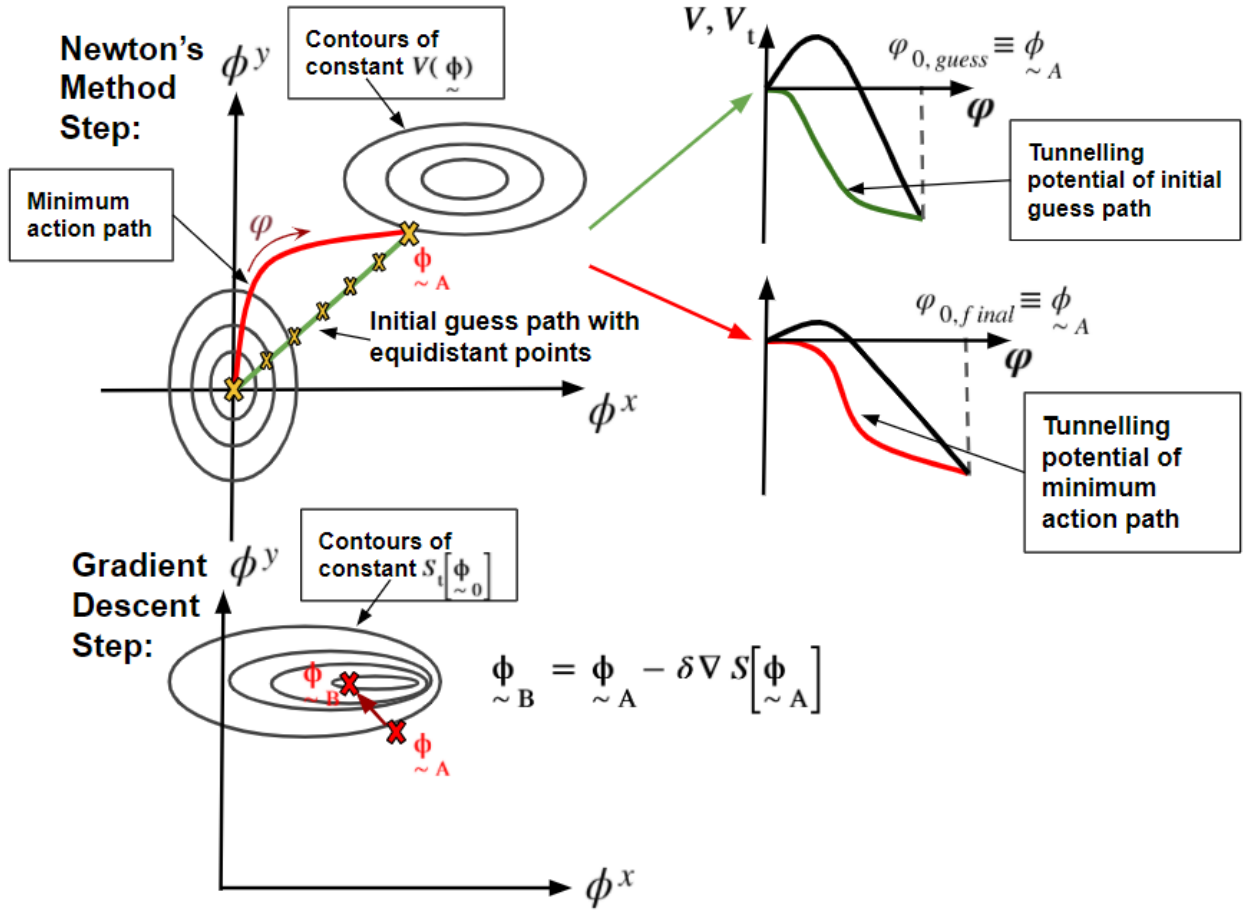

Fig. 4.4 *Summary of numerical algorithm for two fields.*

In Fig. 4.4 we show a summary of the multi-field numerical algorithm where we have taken the two field case as a demonstrative example. In the Newton's method portion of the algorithm this means again using Eq. (4.22) to fix a V_t grid based on the boundary conditions in Eq. (4.13) for a particular $\underset{\sim}{\phi}_0$ release point. We then pick an initial guess path of equidistant ϕ points between $\underset{\sim}{\phi}_0$ and $\underset{\sim}{\phi}_{fv}$ which we point-wise associate to our V_t grid to obtain an initial guess for V_t.

Generalising the Newton's method update scheme in Eq. (4.26) to its multi-dimensional form

$$\underset{\sim}{\phi}_{new} = \underset{\sim}{\phi}_{old} - \upsilon H^{-1}[\underset{\sim}{\phi}_{old}]\underset{\sim}{\nabla} S_t[\underset{\sim}{\phi}_{old}] \tag{4.29}$$

We must iterate this to find the optimum configuration of ϕ points which map to the fixed V_t grid values to define a $V_t(\varphi)$ curve with minimum action for the chosen ϕ_0 release value. In general the path through field space is not straight and so we parameterise our V_t curve as a function of its distance travelled in field space, φ.

Taking the two field case as an example, this path can be described using a 1D column vector as follows

$$\underset{\sim}{\phi} = \begin{pmatrix} \phi_0^x & \phi_0^y \\ \phi_1^x & \phi_1^y \\ \vdots & \vdots \\ \phi_{n-1}^x & \phi_{n-1}^y \\ \phi_n^x & \phi_n^y \end{pmatrix} = \begin{bmatrix} \phi_0^x \\ \vdots \\ \phi_n^x \\ \phi_0^y \\ \vdots \\ \phi_n^y \end{bmatrix}. \tag{4.30}$$

The overall Hessian matrix is a symmetric matrix of second partial derivatives, which in this scenario describes changes in the action when different pairs of points are perturbed in different pairs of field space directions. For us it is constructed using individual Hessian matrices, H_{ij}, arranged into a block super matrix where each H_{ij} block represents changes in the action when points along the path are perturbed in a fixed pair of field space directions. Using the 2D case as an illustrative example we have,

$$H = \left[\begin{array}{c|c} H_{xx} & H_{xy} \\ \hline H_{yx} & H_{yy} \end{array}\right] = \left[\begin{array}{c|c} \frac{\partial^2 S_t}{\partial\phi^x\partial\phi^x} & \frac{\partial^2 S_t}{\partial\phi^x\partial\phi^y} \\ \hline \frac{\partial^2 S_t}{\partial\phi^y\partial\phi^x} & \frac{\partial^2 S_t}{\partial\phi^y\partial\phi^y} \end{array}\right] \tag{4.31}$$

where

$$H_{xy} = \frac{\partial^2 S_t}{\partial\phi^x\partial\phi^y} = \begin{pmatrix} \frac{\partial^2 S_t}{\partial\phi_1^x\partial\phi_1^y} & \cdots & \frac{\partial^2 S_t}{\partial\phi_1^x\partial\phi_{n-1}^y} \\ \frac{\partial^2 S_t}{\partial\phi_2^x\partial\phi_1^y} & & \frac{\partial^2 S_t}{\partial\phi_2^x\partial\phi_{n-1}^y} \\ \vdots & \ddots & \vdots \\ \frac{\partial^2 S_t}{\partial\phi_{n-2}^x\partial\phi_1^y} & \cdots & \frac{\partial^2 S_t}{\partial\phi_{n-2}^x\partial\phi_{n-1}^y} \\ \frac{\partial^2 S_t}{\partial\phi_{n-1}^x\partial\phi_1^y} & & \frac{\partial^2 S_t}{\partial\phi_{n-1}^x\partial\phi_{n-1}^y} \end{pmatrix} \tag{4.32}$$

The overall Hessian Eq. (4.31) is symmetric so that in the 2-field case for example $H_{xy} = H_{yx}$, whilst each individual Hessian block should be a tri-diaganol matrix as follows

$$H_{xy} = \frac{\partial^2 S_t}{\partial \phi^x \partial \phi^y} = \begin{pmatrix} \frac{\partial^2 S_t}{\partial \phi_1^x \partial \phi_1^y} & \frac{\partial^2 S_t}{\partial \phi_1^x \partial \phi_2^y} & 0 & & & 0 & 0 & 0 \\ \frac{\partial^2 S_t}{\partial \phi_2^x \partial \phi_1^y} & \frac{\partial^2 S_t}{\partial \phi_2^x \partial \phi_2^y} & \frac{\partial^2 S_t}{\partial \phi_2^x \partial \phi_3^y} & \cdots & & 0 & 0 & 0 \\ 0 & \frac{\partial^2 S_t}{\partial \phi_3^x \partial \phi_2^y} & \frac{\partial^2 S_t}{\partial \phi_3^x \partial \phi_3^y} & & & 0 & 0 & 0 \\ 0 & 0 & \frac{\partial^2 S_t}{\partial \phi_4^x \partial \phi_3^y} & & & 0 & 0 & 0 \\ & \vdots & & \ddots & & \vdots & & \\ 0 & 0 & 0 & & \frac{\partial^2 S_t}{\partial \phi_{n-2}^x \partial \phi_{n-3}^y} & \frac{\partial^2 S_t}{\partial \phi_{n-2}^x \partial \phi_{n-2}^y} & \frac{\partial^2 S}{\partial \phi_{n-2}^x \partial \phi_{n-1}^y} \\ 0 & 0 & 0 & \cdots & 0 & \frac{\partial^2 S_t}{\partial \phi_{n-1}^x \partial \phi_{n-2}^y} & \frac{\partial^2 S_t}{\partial \phi_{n-1}^x \partial \phi_{n-1}^y} \end{pmatrix} \tag{4.33}$$

We also express the gradient of the action as a column vector, so that in the two field case we would have,

$$\underset{\sim}{\nabla} S_t = \begin{bmatrix} \nabla_x S_t \\ \nabla_y S_t \end{bmatrix} = \begin{bmatrix} \frac{\partial S_t}{\partial \phi_1^x} \\ \vdots \\ \frac{\partial S_t}{\partial \phi_{n-1}^x} \\ \frac{\partial S_t}{\partial \phi_1^y} \\ \vdots \\ \frac{\partial S_t}{\partial \phi_{n-1}^y} \end{bmatrix}. \tag{4.34}$$

We compute the above quantities at each new step of the Newton's method to iterate Eq. (4.29), until the S_t action error in Eq. (4.27) converges to within 1%.

In a similar manner to the single field case we implement a gradient descent algorithm that sits on top of our Newton's Method algorithm and seeks to find the minimum of the $S_t[\phi_0]$ surface without having to map out the whole multi-dimensional action space. This involves computation of the the gradient of the action with respect to the $\underset{\sim}{\phi}_0$ release point at which the algorithm resides. [5] In the 2D case this would look like

$$\underset{\sim}{\nabla} S_t = \begin{bmatrix} \frac{\partial S_t}{\partial \phi_0^x} \\ \frac{\partial S_t}{\partial \phi_0^y} \end{bmatrix} \tag{4.35}$$

This quantity specifies the field space direction in which a change in $\underset{\sim}{\phi}_0$ provides the steepest increase in action. Thus by stepping in the opposite direction to this we step down the slope towards the minimum always in the steepest direction, using an iterative update

[5] We calculate this quantity analytically in our code, see Appendix A.1 & A.2.

scheme

$$\underset{\sim}{\phi}_{0,new} = \underset{\sim}{\phi}_{0,old} - \delta \underset{\sim}{\nabla} S_t[\underset{\sim}{\phi}_0]. \tag{4.36}$$

where $\delta \in [0,1]$ is again a scalar quantity that controls the size of the step we take towards the minimum and $S_t[\underset{\sim}{\phi}_0]$ is a functional that takes as input a path between $\underset{\sim}{\phi}_{fv}$ and $\underset{\sim}{\phi}_0$.

4.5 Single Field Examples: False Vacuum Decay to Non-adjacent Minima

In this section we look to use our code to investigate false vacuum decay in single field potential scenarios with multiple true minima as is expected to be present in the string landscape and where, in some regions, comparatively large decay rates could occur for tunnelling routes to far away vacua [43]. One could then compare the false vacuum decay rates to far away minima in the landscape to those of adjacent minima and explore the relationship between the 'distance' (in quantum number) of the destination minima from the false vacuum and the false vacuum decay rate to it.

Rather than exclusively focusing on potentials that have a direct physical interpretation, we will rather look to categorise the types of potentials for which our code succeeds in finding multi-minima false vacuum decay solutions and those for which it fails. These findings could form the initial basis of future investigations seeking to definitively identify specific potential landscapes that admit multi-minima tunnelling solutions.

4.5.1 Potential landscapes with equal vacuum energy difference

Considerations of the string landscape in the context of cosmology in Sec. 4.1, as well as some chain inflation scenarios [50], motivate us to first study tunnelling for a single field sine wave potential with a linear shift of the form

$$V(\phi) = -\cos\phi - \gamma\phi \tag{4.37}$$

where $\gamma \in [0,1]$ is a parameter that controls the barrier height and the difference in vacuum energy between the true and false vacua. We implement our tunnelling potential numerical algorithm to find the tunnelling action to the first minimum of Eq. (4.37) in both a thin and thick wall situation. We then compare it to the solution found using the usual 'overshoot/undershoot' approach (Sec. 3.2.1) to verify our numerical algorithm works.

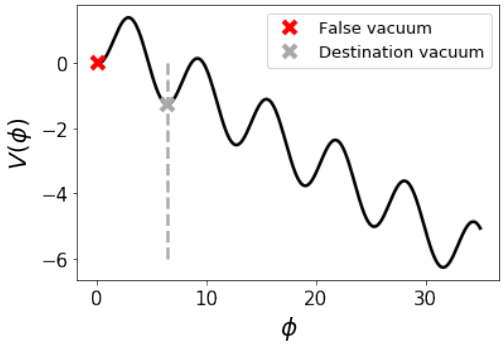

(a) *Destination vacuum for tunnelling.*

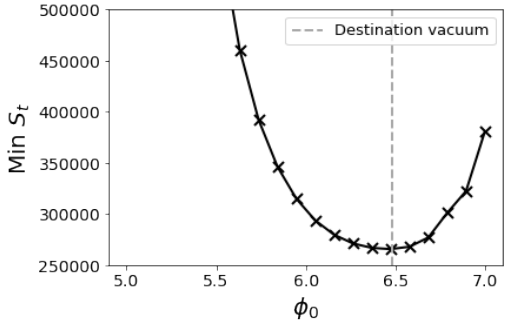

(b) *Minimum values of functional* $S_t[\phi_0]$.

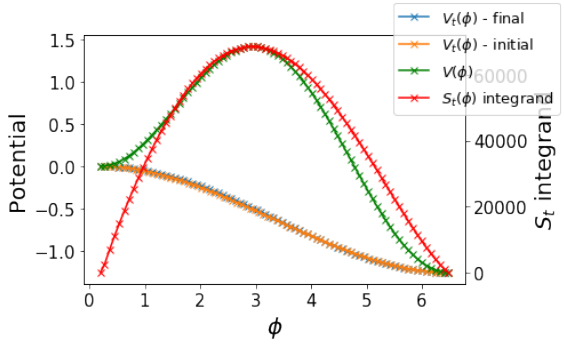

(c) *Tunnelling solution at* $\phi_0 \approx 6.47$.

Fig. 4.5 *Large barrier tunnelling to 1st minimum of potential in Eq.* (4.37), $\gamma = 0.2$, *80 pts.*

Fig. 4.5a shows the potential from Eq. (4.37) with $\gamma = 0.2$. The false vaccuum is marked with a red cross and the destination 'true vacuum' marked with a grey cross. Fig. 4.5b shows the minimum tunnelling potential action, S_t, as a function of the ϕ_0 release point. The destination true vacuum we want to tunnel to is marked with a grey dashed line.

We know from Sec. 4.3.2 that the solution that lies at the minimum of the $S_t[\phi_0]$ curve should coincide with the bounce solution that describes tunnelling between our false vacuum and the destination minimum. Thus in Fig. 4.5c we plot the tunnelling potential (blue curve) as it journeys through the potential barrier $V(\phi)$ (green curve) for the solution associated with the release point $\phi_0 = 6.47$ which has minimum $S_t[\phi_0]$ action of all the release points in Fig. 4.5b. We can see that this V_t solution possess the properties defined in Sec. 4.3.3, namely that between the boundary points ϕ_{fv} and ϕ_0 at which $V_t = V$, the solution must be monotonic and satisfy $V_t < V$. On the same graph we plot the initial $V_t(\phi)$ guess (orange) that we fed into our algorithm for this ϕ_0, and also the the contribution to the tunnelling potential action S_t (red) as a function of its journey through the potential ϕ, which we can see is a smooth and well-behaved curve.

We can also see that the minimum of the S_t surface in Fig. 4.5b lies very close to the true minimum of the potential that we want to tunnel to and thus our solution should correspond to a bubble profile with a relatively thin wall. We show that this is indeed the

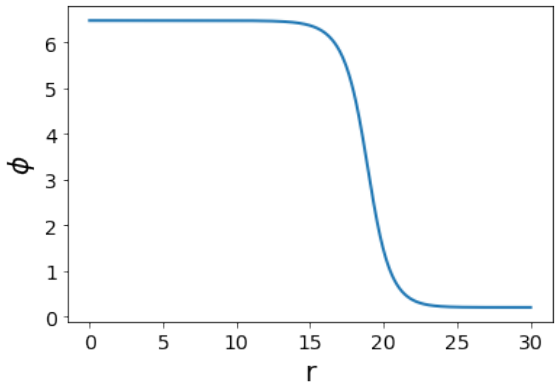

Fig. 4.6 *Bounce profile to first minimum of potential in Eq.* (4.37) *for* $\gamma = 0.2$ *found using 'overshoot-undershoot' method.*

case in Fig. 4.6 by plotting the profile of the bounce solution obtained using a shooting method.

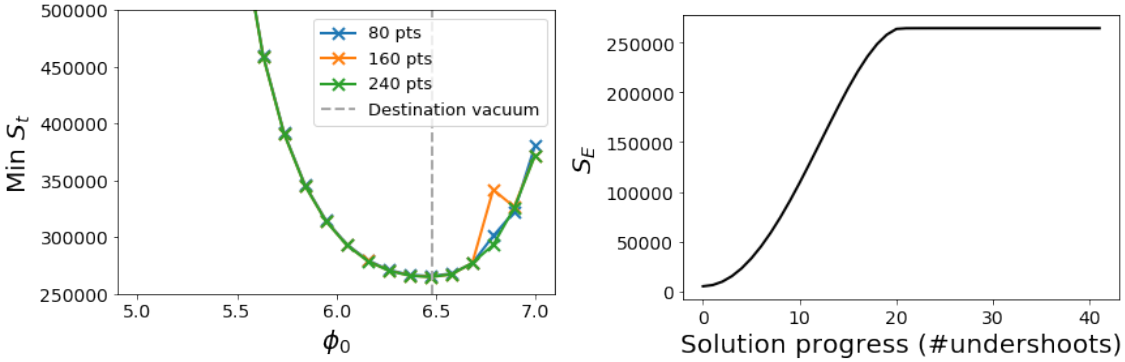

(a) *Tunneling action convergence* ***(b)*** *Bounce action convergence*

Fig. 4.7 *Convergence plots to first minimum of potential in Eq.* (4.37) *for* $\gamma = 0.2$.

In Fig. 4.7 we compare convergence of the Euclidean bounce action for this scenario found using a 'overshoot/undershoot' method to convergence of the minimum of the S_t action found using the tunnelling potential algorithm. We can see from Fig. 4.7a that the minimum value of S_t converges with increasing number of path points to a figure that is approximately the same as the value the Euclidean action converges to (see Fig. 4.7b) using a shooting method, $S_E \approx 264580.23$. Therefore we can be confident our code implementing the tunnelling potential algorithm works as expected.

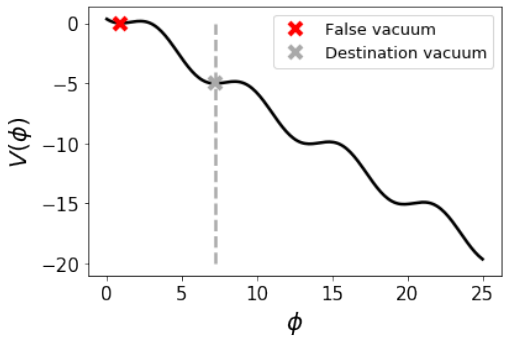

(a) *Destination vacuum for tunnelling.*

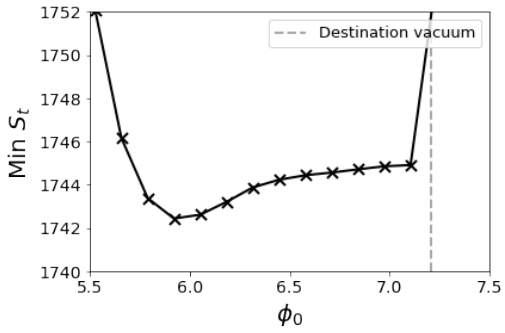

(b) *Minimum values of functional $S_t[\phi_0]$.*

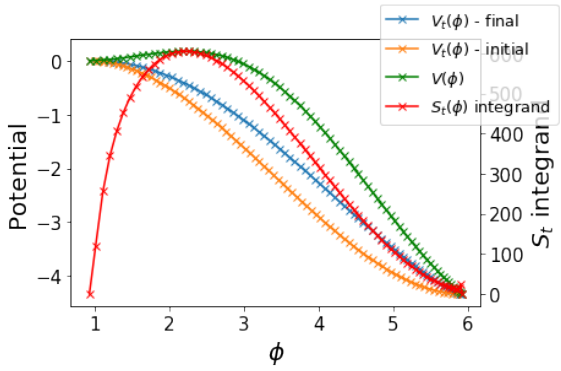

(c) *Tunnelling solution at $\phi_0 \approx 5.92$.*

Fig. 4.8 *Small barrier tunnelling to 1st minimum of potential in Eq.* (4.37)*, $\gamma = 0.8$, 80 pts.*

In Fig. 4.8 we show similar plots obtained from using the tunnelling potential algorithm again for the case of tunnelling to the first true minimum of the potential (grey cross in Fig. 4.8a), but this time when $\gamma = 0.8$. Contrary to the previous case with $\gamma = 0.2$, we can see that the difference in vacuum energy between true and false minima is large when compared to the size of the barrier. Using our intuition of a pseudo-particle rolling down an inverted potential from ϕ_0 to ϕ_{fv}, one would expect such a potential to result in a bounce solution with a thick wall profile where the release point is far from the destination true minima. Fig. 4.8b suggests that this is indeed the case given that the minimum of the $S_t[\phi_0]$ curve with which the bounce solution should coincide is at $\phi_0 \approx 6.05$ which is far from the destination true minimum (grey dashed line) which lies at $\phi_0 \approx 7.2$. In Fig. 4.8c we plot the form of the $V_t(\phi)$ solution (blue) at the minimum of the $S_t[\phi_0]$ curve in Fig. 4.8b, as well as its contribution to the S_t action (red) as a function of ϕ, noting that V_t has the desired properties and both curves are smooth and well behaved.

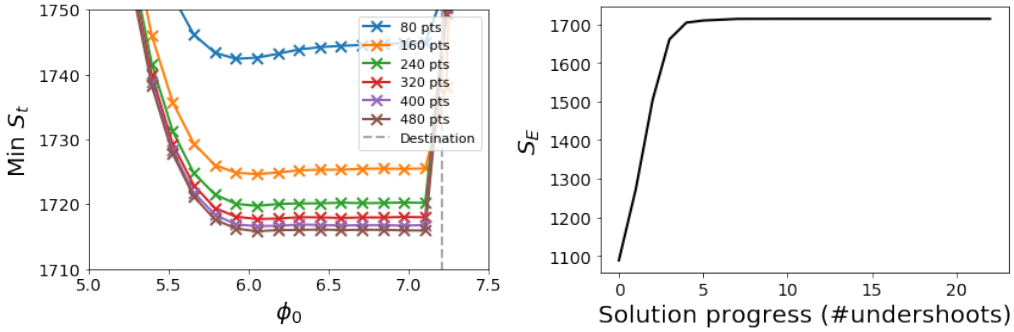

(a) Tunneling action convergence *(b) Bounce action convergence*

Fig. 4.9 *Convergence plots to first minimum of potential in Eq.* (4.37) *for* $\gamma = 0.8$.

In Fig. 4.9 we compare convergence of the minimum of S_t using the tunnelling potential algorithm to convergence of the bounce action using the 'undershoot/overshoot' method, when $\gamma = 0.8$. Fig. 4.9a shows increasing the number of path points results in S_t converging to the same value as the Euclidean bounce action, $S_E \approx 1713.81$, seen in Fig. 4.9b. In

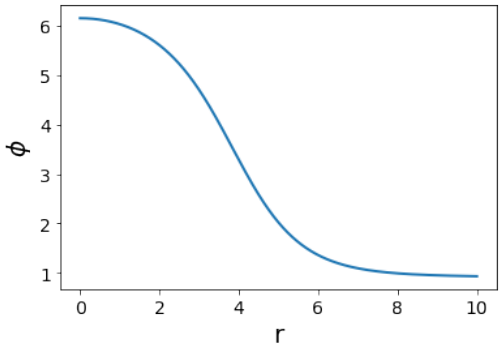

Fig. 4.10 *Bounce profile for tunnelling to first minimum of potential in Eq.* (4.37) *for* $\gamma = 0.8$ *found using 'overshoot-undershoot' method.*

Fig. 4.10 we show the thick wall bounce profile found using a shooting method.

Safe in the knowledge that our numerical tunnelling potential algorithm works as expected, we now explore the possibility of tunnelling to the second true minimum of our potential, as shown in Fig. 4.11a where we set $\gamma = 0.8$. However, when we map out the $S_t[\phi_0]$ curve on a fixed ϕ_0 we find that we get a jagged and non-smooth function with no clear minimum as shown in Fig. 4.11b. When we plot the form of V_t as a function of ϕ for an example ϕ_0 release point as done in Fig. 4.11c we see the source of the problem, in that the $V_t(\phi)$ curve (blue) briefly goes above the $V(\phi)$ (green) curve in the vicinity of the intermediate minima of the potential. This invalidates the whole solution as we know V_t cannot be greater than V in any of the solution's domain, also explaining the non-continuous change in the S_t action (red curve in Fig. 4.11c) around this intermediate minimum.

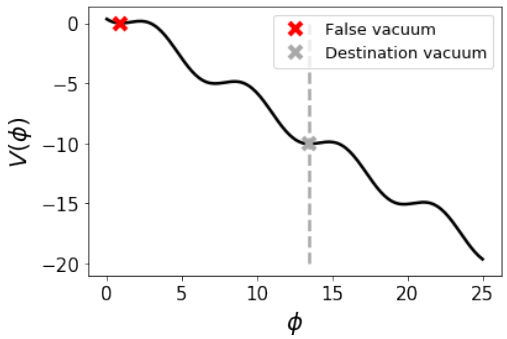

(a) *Destination vacuum for tunnelling.*

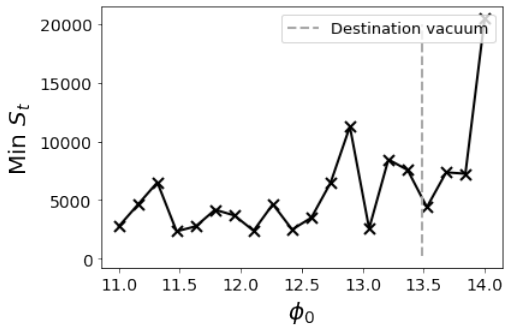

(b) *Minimum values of functional* $S_t[\phi_0]$.

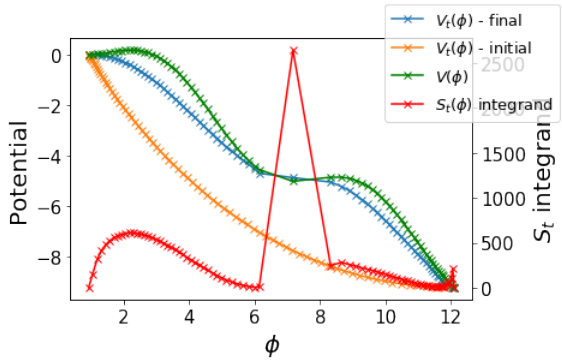

(c) *Tunnelling solution at* $\phi_0 \approx 12.11$.

Fig. 4.11 *Small barrier tunnelling to 2nd minima of potential in Eq.* (4.37), $\gamma = 0.8$, *80 pts.*

We found a similar issue when trying to compute a tunnelling solution using our code to any of the further away true minima across the whole range of values, $\gamma \in [0,1]$, that control the barrier height. We found that in each case, the V_t curve clips the potential curve in the vicinity of the intermediate minima of the potential as shown in Fig. 4.11c, so that $V_t > V$ and the solution is not a valid tunelling solution. This suggests that no direct tunnelling solutions exist to minima that are further on than the first true minima for this type of linearly shifted sin wave potential. Instead the field would have to tunnel to the far away minima indirectly, via a series of separate tunnelling events to each intermediate minima in turn. However, the source of the issue could also simply be due to numerical instability of the solution space that makes finding a solution extremely challenging and so a claim that no solution exists would require further investigation to be substantiated. There may be some formal analytical argument one could construct, perhaps using the mechanical rolling analogy, to demonstrate whether a bounce solution exists in this scenario and we leave this task for further work.

4.5.2 Potential landscapes with decreasing vacuum energy difference

Having considered single field, multi-vacua potential landscapes with equal vacuum energy difference between neighbouring minima, we now study situations where the energy difference decreases. Such potentials are often seen in chain inflation scenarios [44, 45] where the universe starts in a high energy false vacuum and rapidly tunnels through a series of sequentially lower minima until it reaches the vacuum we reside in today where the cosmological constant takes on the small value we measure. During the time spent in each intermediate minimum the universe inflates by some fraction of an e-fold and when all these contributions are summed they should equal the ≈ 60 e-folds required to solve the cosmological constant problem. Following [44] we use a toy model potential to describe this situation

$$V(\phi) = -\cos\phi + \gamma\phi^2 \tag{4.38}$$

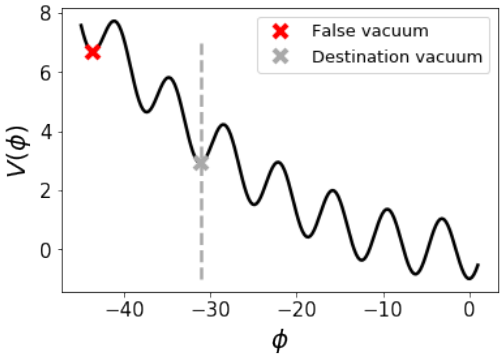

(a) Destination vacuum for tunnelling.

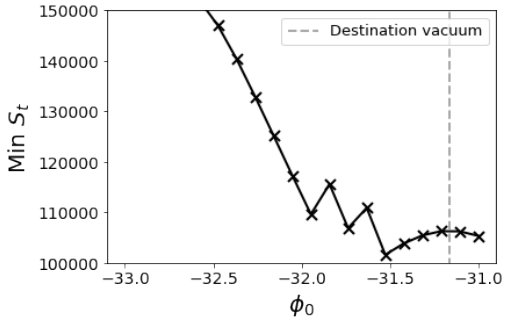

(b) Minimum values of functional $S_t[\phi_0]$.

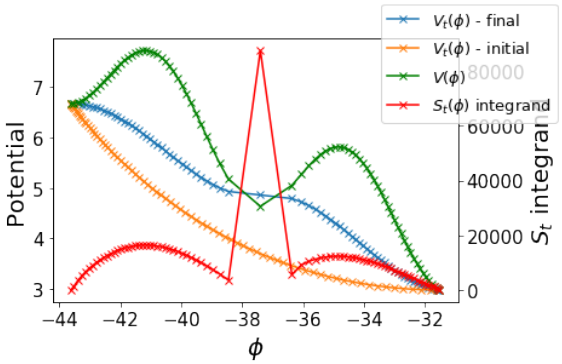

(c) Tunnelling solution at $\phi_0 \approx -31.53$.

Fig. 4.12 *Large barrier tunnelling to 2nd minima of potential in Eq.* (4.38)*, $\gamma = 0.004$, 80 pts.*

In Fig. 4.12 we use our code to try and calculate tunnelling solutions for this potential when $\gamma = 0.004$ (see Fig. 4.12a) and we are tunnelling from the false vacuum shown with a red cross in Fig. 4.12a to the second true minima marked with a grey cross. In Fig. 4.12b we show the S_t action curve as a function of the ϕ_0 release point which demonstrates some

suspicious jagged behaviour near its minimum. In Fig. 4.12c we plot both the final $V_t(\phi)$ solution (blue) and $S_t(\phi)$ action curve (red) for the minimum $\phi_0 \approx 31.53$ release value shown in Fig. 4.12b, with the expectation that if tunnelling is possible the solution here should coincide with the bounce solution. We can see, infact, that $V_t > V$ in the region of the intermediate minima and thus the solution is not a valid one. The discontinuous behaviour of the S_t action curve around the intermediate minima reinforces this view.

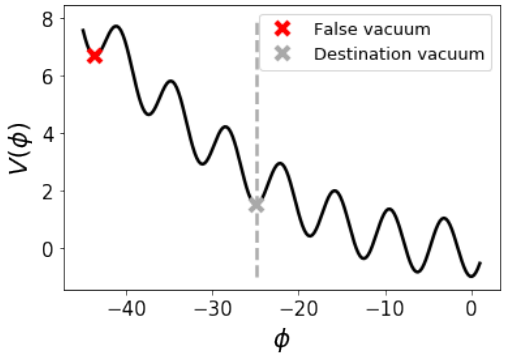

(a) *Destination for tunnelling.*

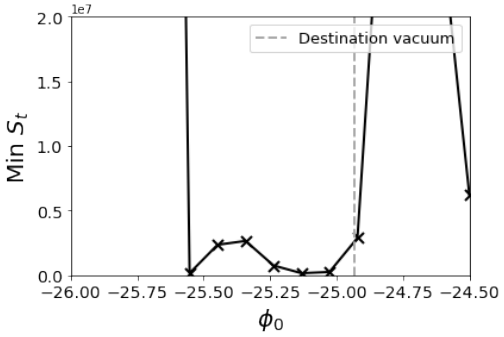

(b) *Minimum values of functional $S_t[\phi_0]$.*

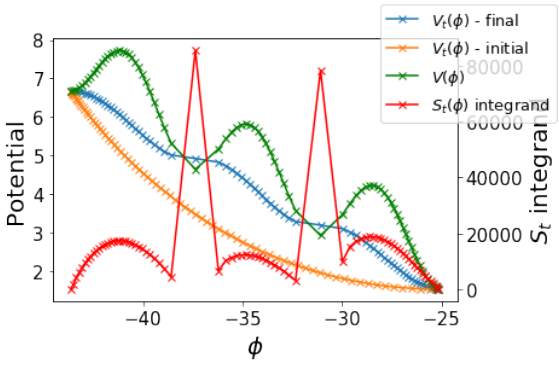

(c) *Tunnelling solution at $\phi_0 \approx -25.13$.*

Fig. 4.13 *Large barrier tunnelling to 3rd minima of potential in Eq.* (4.38)*, $\gamma = 0.004$, 80 pts.*

In Fig. 4.13 we compute tunnelling solutions for the same potential ($\gamma = 0.004$) but this time tunnell to the third true minimum. In Fig. 4.13c we again plot the $V_t(\phi)$ and $S_t(\phi)$ curves corresponding to the ϕ_0 with minimum $S_t[\phi_0]$ value shown in Fig. 4.13b and can see that $V_t > V$ in the vicinity of both intermediate minima so the V_t solution is not valid. We continued to look at tunnelling to increasingly further away minima and found the same issue persisting with the $V_t(\phi)$ solution going above $V(\phi)$ around each of the intermediate minima.

To see if this behaviour of not finding a valid solution changes when we adjust the size of the barrier, we also ran our code for a range of γ values which control the height of the barrier and still found no valid V_t solutions due to the aforementioned issues at the intermediate minima.

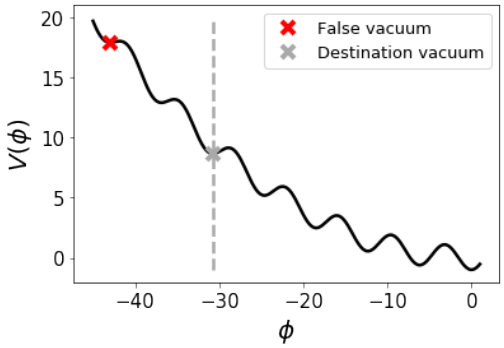

(a) Destination vacuum for tunnelling.

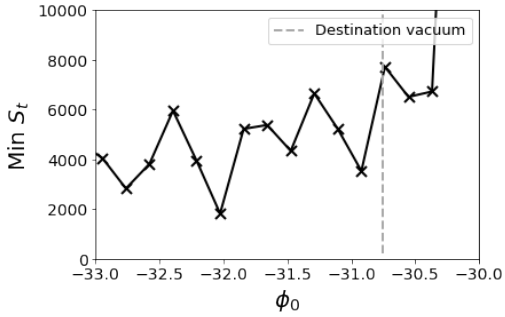

(b) Minimum values of functional $S_t[\phi_0]$.

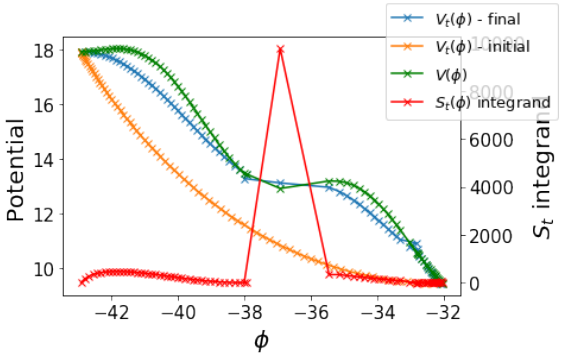

(c) Tunnelling solution at $\phi_0 \approx -32.03$.

Fig. 4.14 *Small barrier tunnelling to 2nd minima of potential in Eq.* (4.38)*, $\gamma = 0.01$, 80 pts.*

In Fig. 4.14 we show another concrete example for tunnelling to the second true minimum but this time with a small barrier height ($\gamma = 0.01$) and find similar difficulties with obtaining a well behaved solution. The fact that our code fails to find a tunnelling solution at all for the potential in Eq. (4.38) warrants further investigation as to whether this is due to some numerical shortcomings with our approach that can possibly be resolved or whether it points to something more fundamental. Indeed, in the latter scenario this solution may suggest that tunnelling must proceed in a step-wise fashion between successive adjacent minima for this potential shape.

4.5.3 Potential landscapes with increasing vacuum energy

To conclude our categorisation of tunnelling in single field potential landscapes with multiple minima, we finally consider a potential where the vacuum energy difference between neighbouring minima increases as you move away from the false vacuum. Such scenarios are considered in [43] and a toy model potential we suggest that could perhaps model such a situation is

$$V(\phi) = -\cos\phi - \gamma\phi^2 \tag{4.39}$$

Investigating this case will also gives us a handle on whether our code can find any potential shapes in a single field setting, that permit false vacuum decay solutions to non-adjacent minima.

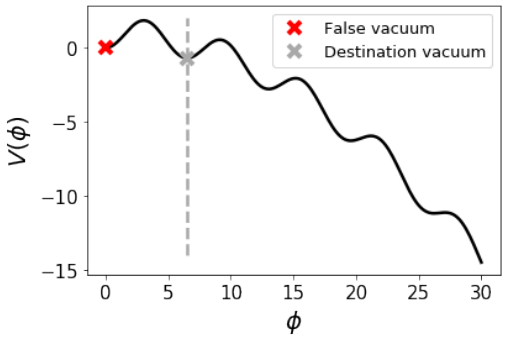

(a) *Destination vacuum for tunnelling.*

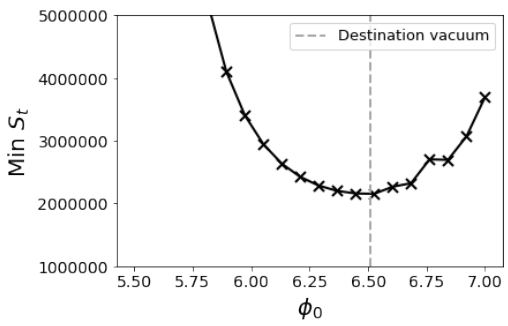

(b) *Minimum values of functional $S_t[\phi_0]$.*

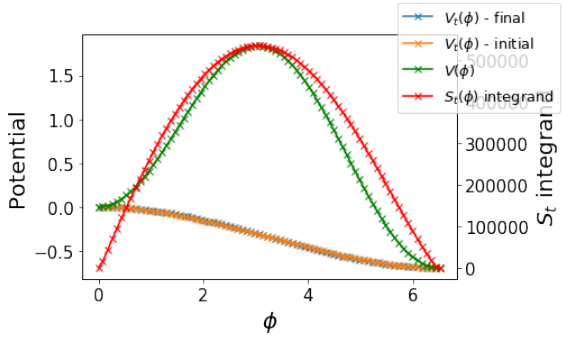

(c) *Tunnelling solution at $\phi_0 \approx 6.53$.*

Fig. 4.15 *Tunnelling to 1st minima of potential in Eq.* (4.39)*, $\gamma = 0.017$, 80 pts.*

In Figs. 4.15-4.18 we successfully use our code to calculate false vacuum decay solutions to successive true minima when $\gamma = 0.017$, where the potential is shown in the sub figures labelled with an (a). In the (b) sub figures we show how the $S_t[\phi_0]$ action curve varies with the ϕ_0 release value and see that it behaves relatively smoothly up to tunnelling to the third true minima and even the curve describing tunnelling to the fourth true minima has consistent behaviour after ruling out the clearly problematic ϕ_0 release values.

This smooth behaviour of the $S[\phi_0]$ curve already gives us some indication that our code is not struggling to find false vacuum decay solutions to non-adjacent minima for

this potential. Choosing the ϕ_0 release values with minimum $S_t[\phi_0]$, we can see that sensible tunnelling solutions are indeed found for all four scenarios, as shown in Fig. 4.15c-4.18c where we plot smooth final $V_t(\phi)$ solutions (blue) with its smooth accompanying contributions to the $S_t(\phi)$ action integrand (red). In Fig. 4.19 we plot the action value of the true tunnelling solution against the destination vacuum being tunnelled to and can see that the probability of vacuum decay to far away minima is larger than to the adjacent minima for potentials of this shape.

This concludes our investigation into false vacuum tunnelling to far away minima in the single field case. In the next section we will apply our code to the more challenging case of finding false vacuum tunnelling solutions to far away minima in a specific coupled two-field potential landscape example.

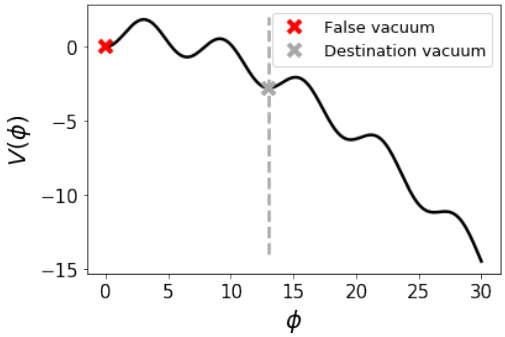

(a) *Destination vacuum for tunnelling.*

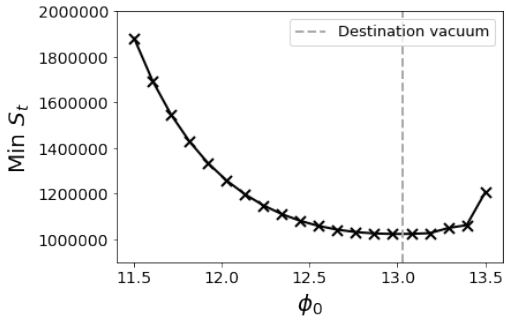

(b) *Minimum values of functional $S_t[\phi_0]$.*

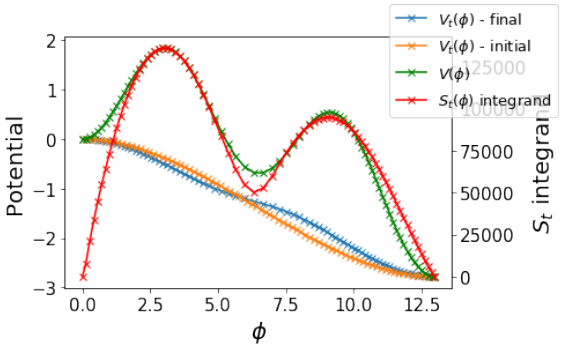

(c) *Tunnelling solution at $\phi_0 \approx 12.97$.*

Fig. 4.16 *Tunnelling to 2nd minima of potential in Eq.* (4.39)*, $\gamma = 0.017$, 80 pts.*

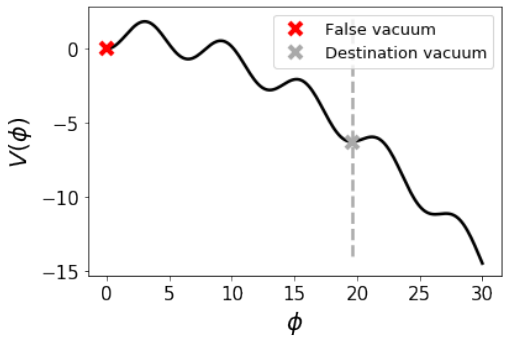

(a) *Destination vacuum for tunnelling.*

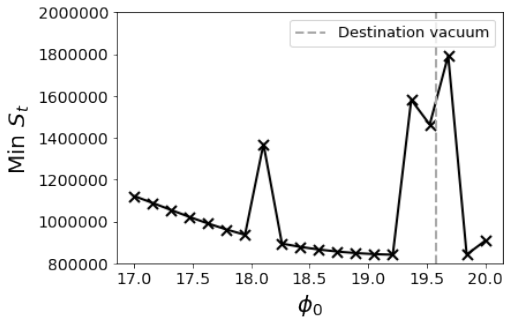

(b) *Minimum values of functional $S_t[\phi_0]$.*

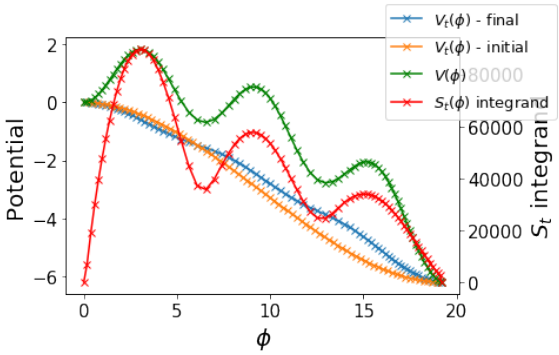

(c) *Tunnelling solution at $\phi_0 \approx 19.21$.*

Fig. 4.17 *Tunnelling to 3rd minima of potential in Eq.* (4.39)*, $\gamma = 0.017$, 80 pts.*

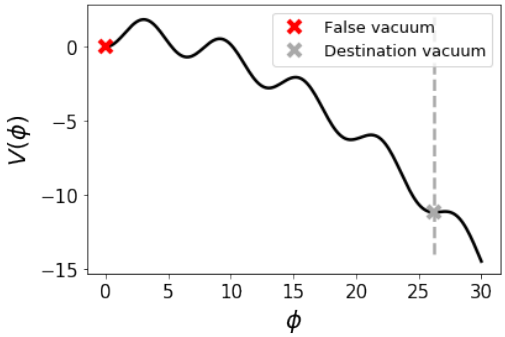

(a) Destination vacuum for tunnelling.

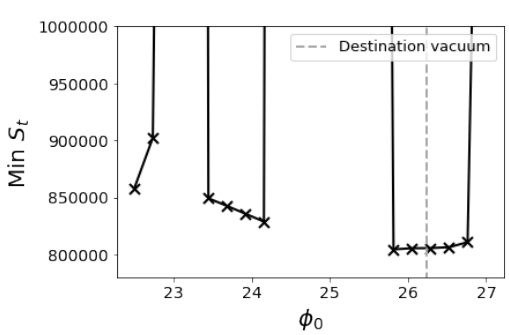

(b) Minimum values of functional $S_t[\phi_0]$.

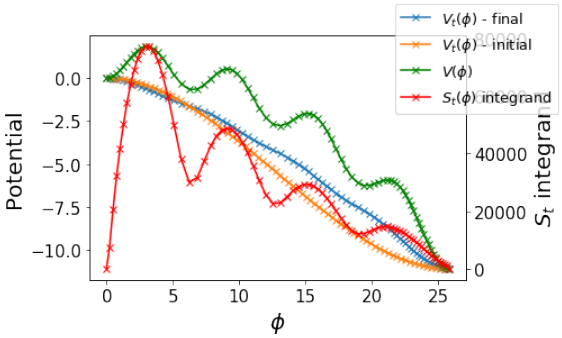

(c) Tunnelling solution at $\phi_0 \approx 25.82$.

Fig. 4.18 *Tunnelling to 4th minima of potential in Eq.* (4.39)*, $\gamma = 0.017$, 80 pts.*

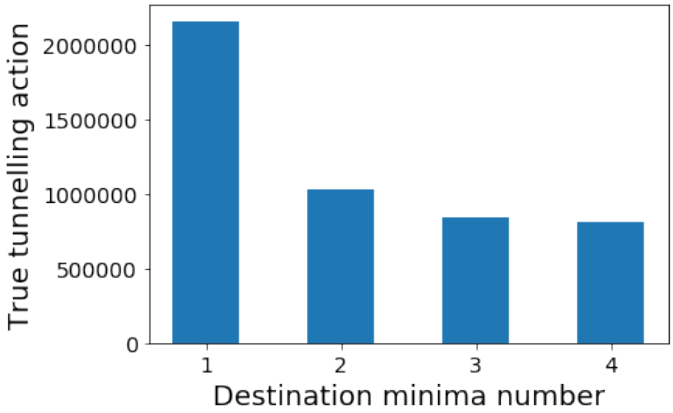

Fig. 4.19 *Tunnelling action to increasingly far minima of potential in Eq.* (4.39)*, $\gamma = 0.017$, 80 pts. See Figs. 4.15 - 4.18 for individual solutions.*

4.6 Multi-field Example: False Vacuum Decay to Non-adjacent Minima

We know that the string landscape not only consists of many minima but also many moduli fields. In this section we seek to demonstrate that our code can also be used to find false vacuum decay solutions to non-adjacent minima in multi-field scenarios by applying it to a coupled two field example potential with multiple minima. We only explore the two field case in this thesis as it is easiest to depict graphically and we seek to only give a flavour of the sorts of multi-field potentials that could be studied. However, our code is written so that it is easily generalised to cases with > 2 fields by simply adding additional block matrices to the Hessian in Eq. (4.31) associated with all possible new field combinations and also additional rows to the S_t gradient column vector in Eq. (4.34).

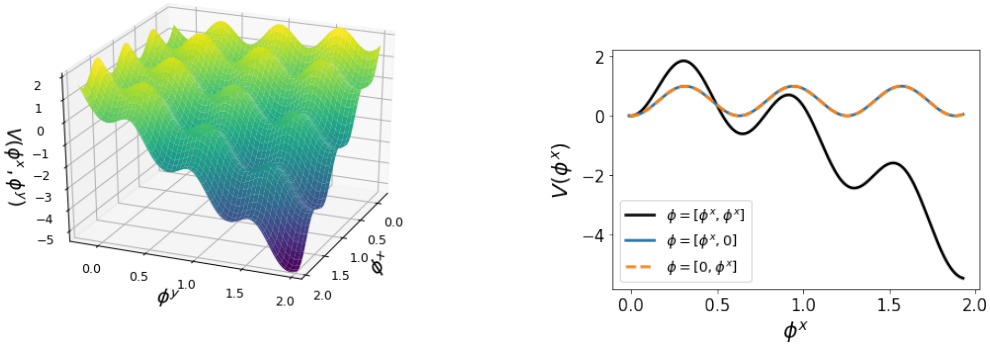

(a) *3D view.* ***(b)*** *2D projection.*

Fig. 4.20 *The two field potential of Eq.* (4.40) *with* $\gamma_{xy} = 1.5$ *and a=5.*

In Fig. 4.20 we plot the potential we will study for two scalar fields ϕ^x and ϕ^y which takes the analytical form

$$V(\phi^x, \phi^y) = -\cos^2(a\phi^x) - \cos^2(a\phi^y) - \gamma_{xy}\phi^x\phi^y, \tag{4.40}$$

for $\gamma_{xy} = 1.5$ and a=5. We label each vacua with integer numbers representing their horizontal and vertical position relative to the false vacuum which we label as minimum (0,0). For example the successive minima in the diagonal direction would be labelled (1,1), (2,2) etc. whilst the minima in the ϕ^x direction would be labelled (1,0), (2,0) etc.

4.6.1 False vacuum decay solutions

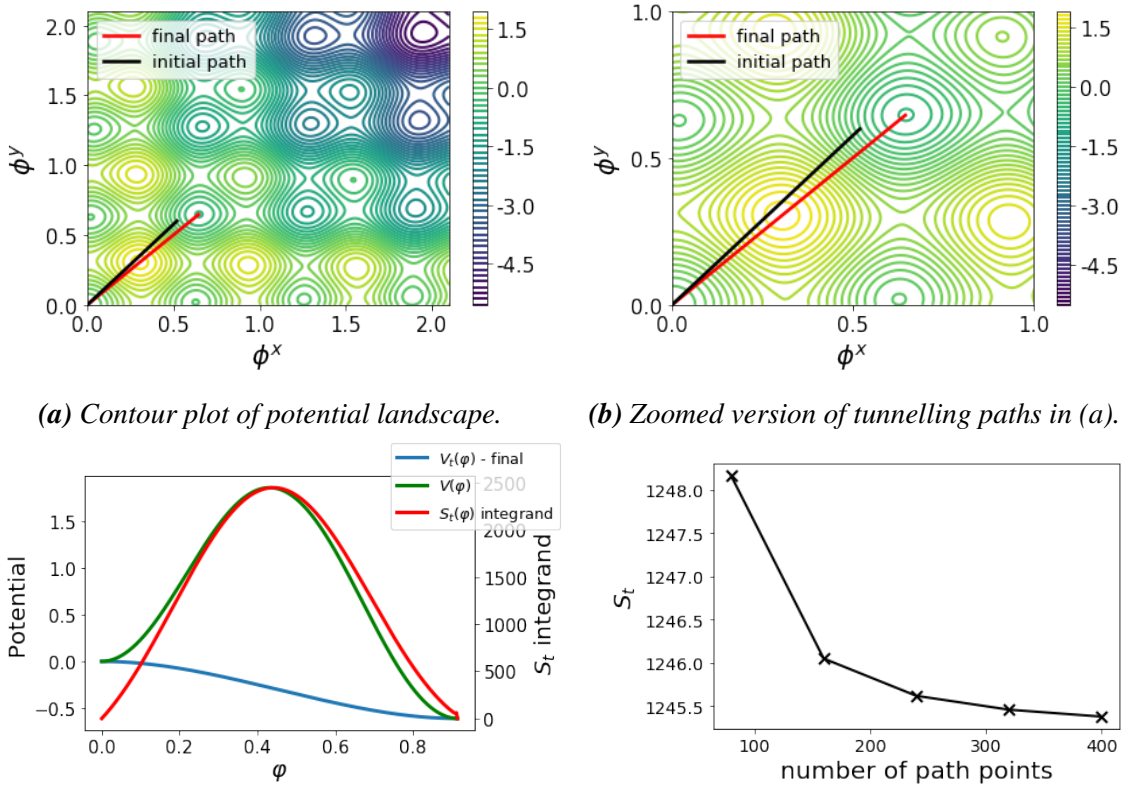

(a) *Contour plot of potential landscape.*

(b) *Zoomed version of tunnelling paths in (a).*

(c) *Tunnelling solution, $S_t \approx 1245$, 400 pts.*

(d) *Convergence of minimum S_t value.*

Fig. 4.21 *Tunnelling to the (1,1) minimum of Eq.* (4.40) *with $\gamma_{xy} = 1.5$ and a=5.*

In Fig. 4.21 we show the false vacuum decay solution for tunnelling to minimum (1,1). As shown in Fig. 4.21a we choose an initial tunnelling path (black line) and run our algorithm described in Sec. 4.4 to find the path (red line) with minimum $S_t[\tilde{\phi}_0]$ action. In this case the minimum path is simply a straight line going through $\phi^x = \phi^y$ in field space which can be explained by the symmetry of the potential surface in this direction.

In Fig. 4.21c we show the V_t curve (blue) associated with the path of minimum action, where we have taken 560 points along the path and φ is a parameter describing the distance travelled along the path, which in general takes a curved trajectory through field space. We also show the value of the potential V (green) and the contributions to the total S_t action (red) as a function of the path parameter φ. All these curves seem well behaved and we also note that $V_t < V$ at all φ values along the path which gives us some level of confidence that our numerical algorithm has indeed found the solution with minimum S_t action for the $(1,1)$ minimum. Given this coincides with the bounce, we can conclude that it describes the false vacuum decay tunnelling solution to this minimum. This view is further reinforced by Fig. 4.21d which shows that the S_t action converges as we increase the number of points along the path.

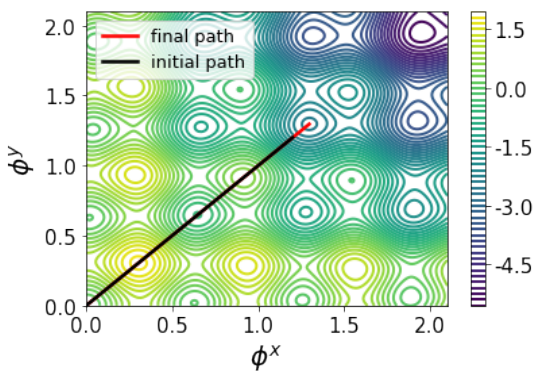

(a) *Contour plot of potential landscape.*

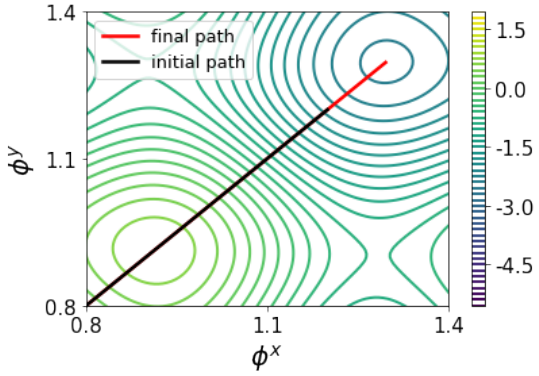

(b) *Zoomed version of tunnelling paths in (a).*

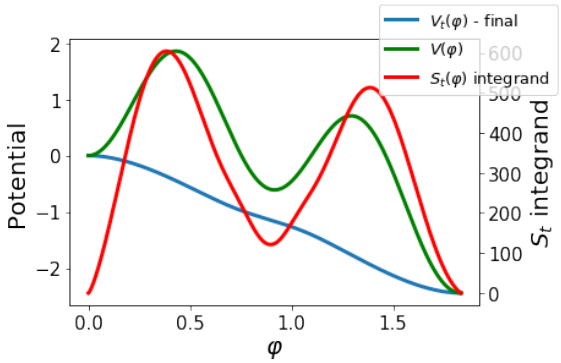

(c) *Tunnelling solution, $S_t \approx 582$, 800 pts.*

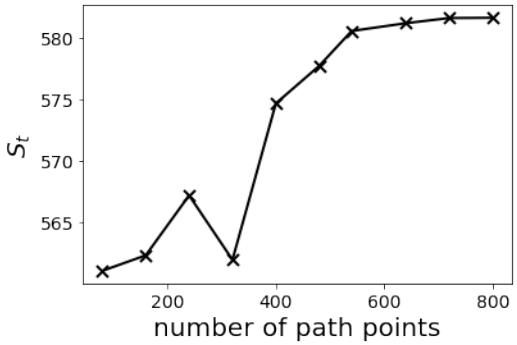

(d) *Convergence of minimum S_t value.*

Fig. 4.22 *Tunnelling to the (2,2) minimum of Eq.* (4.40) *with $\gamma_{xy} = 1.5$ and a=5.*

In Fig. 4.22 we show the solution we obtain when running our code to find the tunnelling solution to the (2,2) minimum. Similar to the (1,1) solution we find that the path with minimum $S_t[\underset{\sim}{\phi}_0]$ is along the $\phi^x = \phi^y$ symmetry axis as shown in Fig. 4.22a. The associated $V_t(\varphi)$, $V(\varphi)$ and $S_t(\varphi)$ curves are smooth with $V_t(\varphi) < V(\varphi)$ for all φ along our 800 point path as seen in Fig. 4.22c. Furthermore, the S_t action value converges with the number of points along the path, as seen in Fig. 4.24d, which if you take with the aforementioned sanity checks allows us to be confident that the approximate minimum S_t value has been found and we can interpret this solution as one that coincides with the bounce and thus describes false vacuum decay to this minimum.

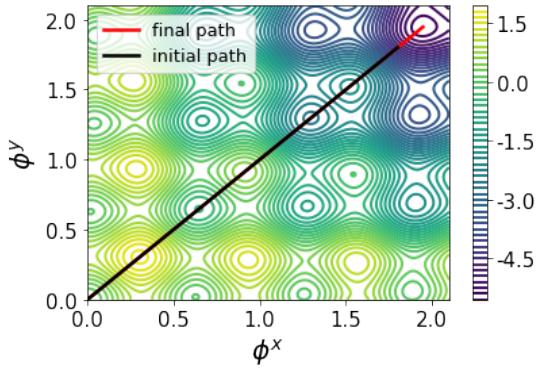

(a) Contour plot of potential landscape.

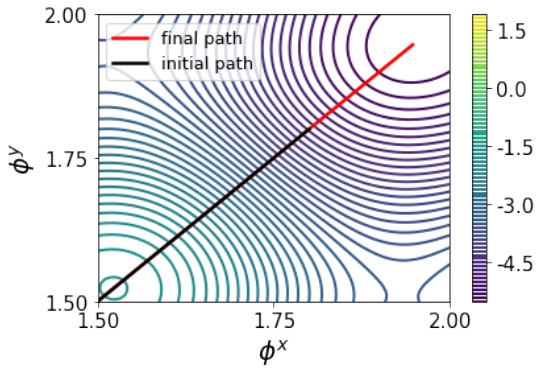

(b) Zoomed version of tunnelling paths in (a).

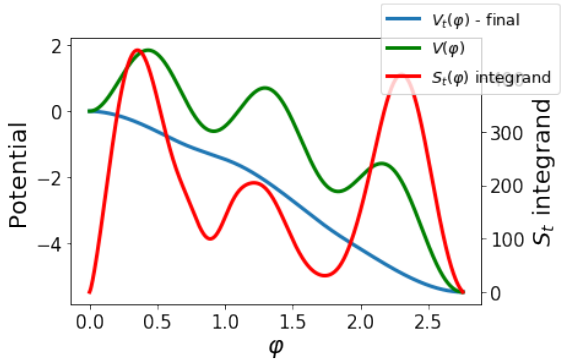

(c) Tunnelling solution, $S_t \approx 551$, 960 pts.

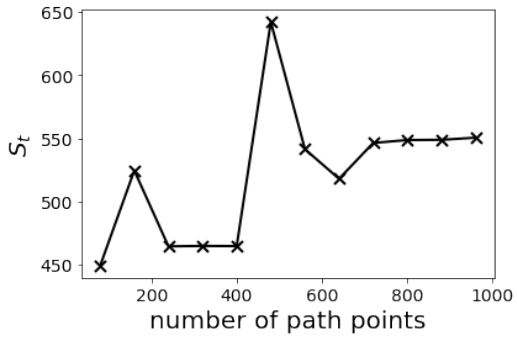

(d) Convergence of minimum S_t value.

Fig. 4.23 *Tunnelling to the (3,3) minimum of Eq.* (4.40) *with* $\gamma_{xy} = 1.5$ *and a=5.*

In Fig. 4.23 we show the false vacuum decay solution to the (3,3) diagonal minimum, finding that the $V_t(\varphi)$ and $S_t(\varphi)$ profiles (shown in Fig. 4.23c for 960 path points) are consistent with the expected behaviour discussed above when enough points are taken along the path. In Fig. 4.23d we see that the S_t action broadly converges with the number of points, though we do see some numerical instability creeping into the solution for $n \approx 500$ path points that subsequently disappears when $n > 700$.

In Figs. 4.24, 4.25 & 4.26 we show the false vacuum decay tunnelling solutions to the (2,1), (3,1) and (3,2) off-diagonal minima respectively. These will perhaps provide a sterner test that our code works as expected in multi-field scenarios because these minima lie off the $\phi^x = \phi^y$ symmetry axis and so in general we would expect the paths to follow curved paths through field space. We can see this is indeed the case from the solution paths in field space shown in Fig. 4.24a, Fig. 4.25a & Fig. 4.26a for each of the minima.

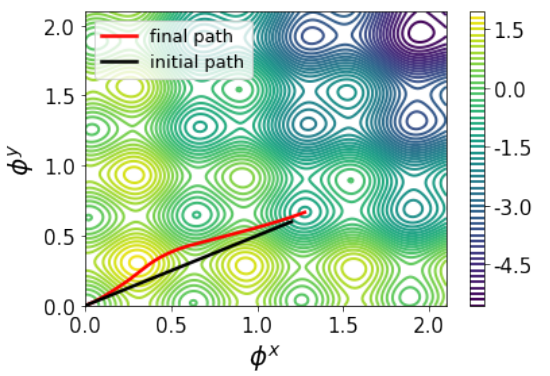

(a) *Contour plot of potential landscape.*

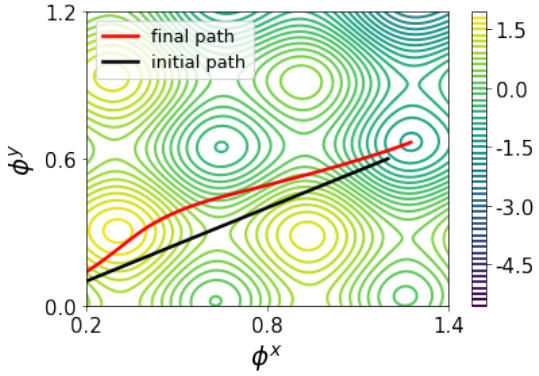

(b) *Zoomed version of tunnelling paths in (a).*

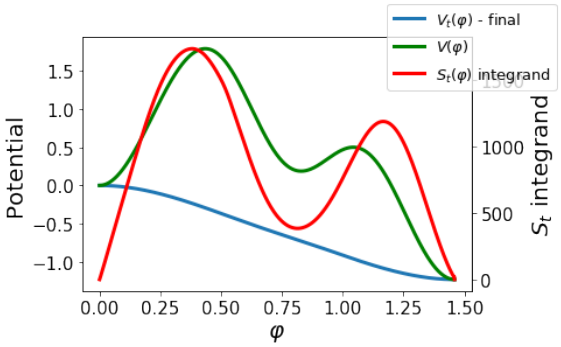

(c) *Tunnelling solution, $S_t \approx 1322$, 1040 pts.*

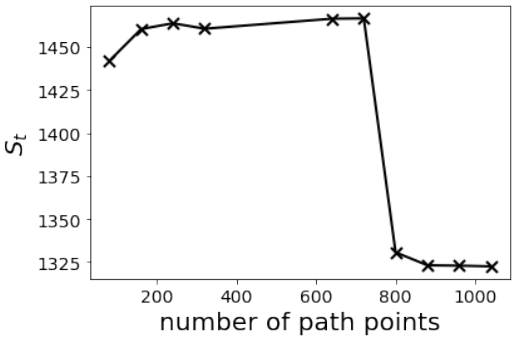

(d) *Convergence of minimum S_t value.*

Fig. 4.24 *Tunnelling to the (2,1) minimum of Eq.* (4.40) *with $\gamma_{xy} = 1.5$ and a=5.*

In Fig. 4.24 we show the tunnelling solution to the (2,1) minimum. It exhibits the desired properties for $n \geq 800$ points as can be seen in Fig. 4.24c where we plot the minimised V_t solution for 1040 points along the path. Looking at the plot of path points against S_t value in Fig. 4.24d we can see that, in a similar but more pronounced manner to the (3,3) tunnelling solution, numerical instability in our algorithm is introduced when the number of path points is below 800 which causes it to find the wrong solution. However, when $n \geq 800$ the sensitive regions of the path are sufficiently resolved that the correct solution is found and this solution converges with the number of points hereafter.

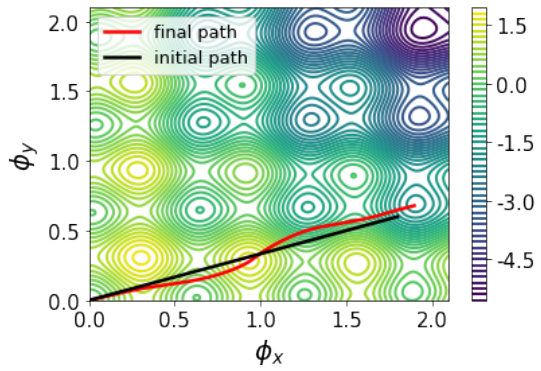

(a) *Contour plot of potential landscape.*

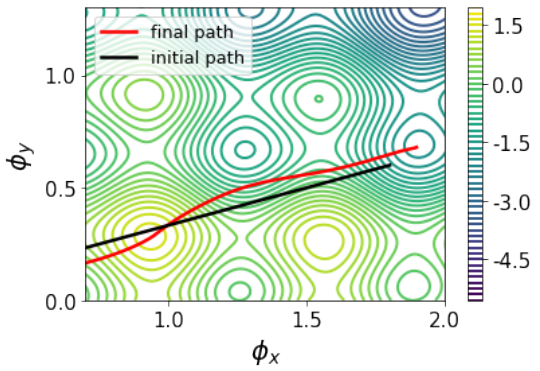

(b) *Zoomed version of tunnelling paths in (a).*

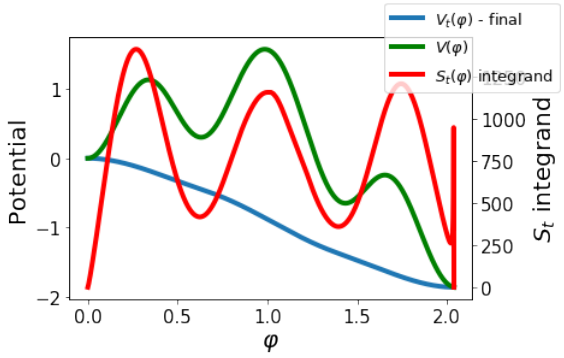

(c) *Tunnelling solution, $S_t \approx 1631$, 960 pts.*

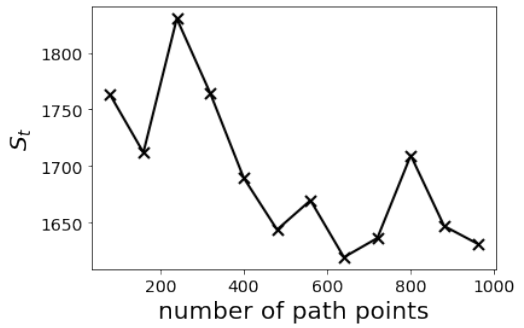

(d) *Convergence of minimum S_t value.*

Fig. 4.25 *Tunnelling to the (3,1) minimum of Eq.* (4.40) *with $\gamma_{xy} = 1.5$ and a=5.*

In Fig. 4.25 we show the solution found with minimum $S_t[\underset{\sim}{\phi}_0]$ action in the vicinity of the (3,1) vacuum. From Fig. 4.25c we can see this has some non-smooth behaviour in its associated $S_t(\varphi)$ action curve. Despite the fact that the S_t value of the minimum $V_t[\underset{\sim}{\phi}_0]$ solution seems to converge up to the number of points we tested it with, the presence of the non-smooth behaviour makes us less confident in the accuracy of our solution. Further investigation of the source of this instability is required and with more time it is likely one could identify the cause and remedy the numerical algorithm to deal with it. Given what happened in the case of the (2,2) minimum perhaps we might expect that if we increase the number of points further the correct solution would eventually be found. However, computing resources and time would eventually limit how many points we could check for and so it would be better to try and fix the source of the instability in our algorithm to improve its overall efficiency.

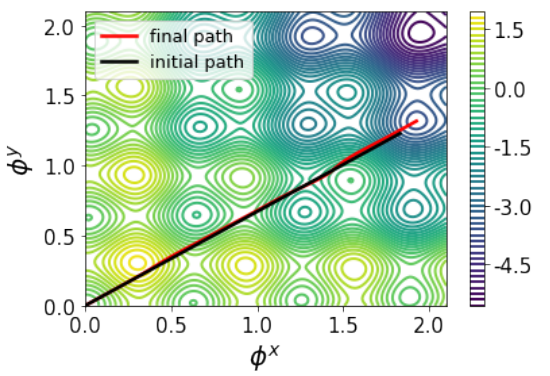

(a) *Contour plot of potential landscape.*

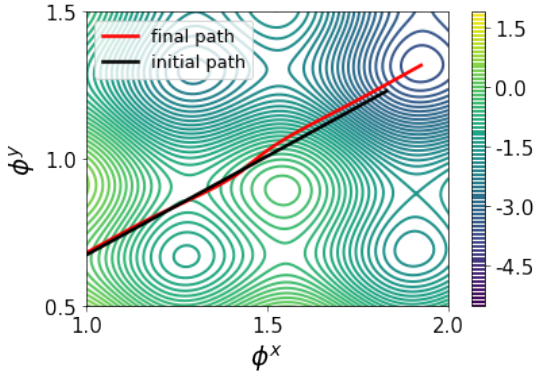

(b) *Zoomed version of tunnelling paths in (a).*

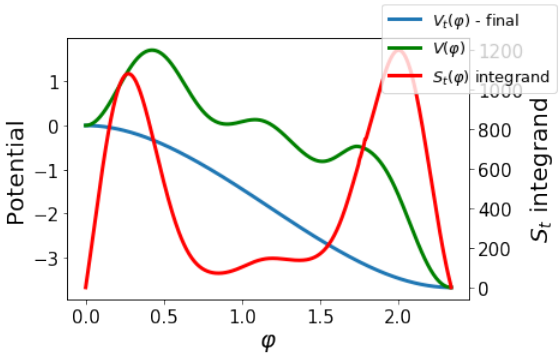

(c) *Tunnelling solution, $S_t \approx 1095$, 560 pts.*

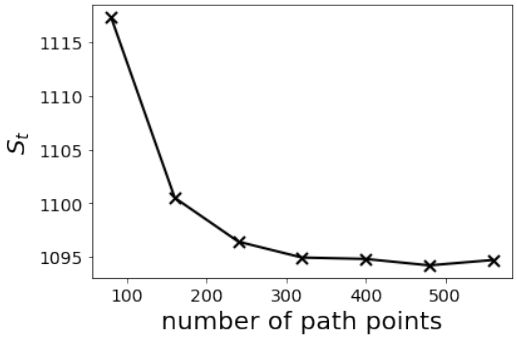

(d) *Convergence of minimum S_t value.*

Fig. 4.26 *Tunnelling to the (3,2) minimum of Eq.* (4.40) *with $\gamma_{xy} = 1.5$ and a=5.*

Finally, in Fig. 4.26 we show the tunnelling solution to the (3,2) off-diagonal minimum. Fig. 4.26c demonstrates the required properties of the $V_t(\varphi)$ curve for the case of 560 path points, whilst Fig. 4.26d shows convergence of the action with increasing number of points. Thus we can confidently conclude that the minimum V_t solution has been found that describes tunnelling from the false vacuum at (0,0) to the minimum at (3,2).

4.7 Areas of Further Work

We have verified that our tunnelling potential algorithm can successfully calculate false vacuum decay tunnelling solutions to non-adjacent minima in some specific single field and multi-field potential landscape examples. However there are many potential avenues for further work. One immediately obvious task is to track down and remedy the source of numerical instabilities in specific solutions, such as the (2,1) and (3,1) minima results in Fig. 4.24 and Fig. 4.25 respectively. Such issues are probably due to singularities in the computation of the Hessian entries close to the boundary points, where the discretised S_t action in Eq. (4.20) becomes particularly sensitive. Such singularities can possibly be remedied by some form of numerical regularisation method [37], that once implemented should allow the algorithm to more efficiently compute false vacuum decay solutions to increasingly far away minima.

If such improvements to our numerical algorithm were made, one could start to tackle areas of further work with wider implications. For example, a study that sought to definitively categorise the types of potential landscapes that permit tunnelling solutions to far away minima and those that do not. For the landscapes where solutions do exist one could then use the improved algorithm to confidently calculate how the false vacuum decay rate varies with the quantum number of the destination vacuum being considered. Such analysis could then be used to better understand various string theory landscape models where the cosmological constant becomes a dynamical variable e.g. chain inflation scenarios [44].

Chapter 5

First Order Phase Transitions in Cosmology

Moments after the Big Bang we expect the universe to have undergone a series of phase changes as it cooled due to the breaking of various high energy symmetries in the underlying particle physics Lagrangian as fundamental fields of the universe took on new values. One commonly referenced example is the electroweak phase transition where the electromagnetic and weak nuclear force become differentiated but other examples include the QCD phase transition and any phase transition arising from symmetry breaking in a Grand Unified Theory (GUT).

In this chapter we will first discuss the different mechanisms by which a phase transition could have taken place in the early universe (see Sections 5.1 and 5.2) whether it be via quantum tunnelling through the potential barrier or thermal fluctuations over it. We will then go on to discuss the dynamics of the bubble wall as it expands in the primordial plasma (see Sections 5.3 and 5.4) which ultimately governs the form of any ensuing gravitational wave or magnetic field signal produced. We will conclude the chapter in Sec. 5.5 by outlining some specific particle physics models that admit first order phase transitions which we will come back to later in our analysis of cold hidden sector phase transitions (Chapter 6) and the gravitational waves they can produce (Chapter 7), and primordial magnetic field generation (Chapter 9).

5.1 Tunnelling at Finite Temperature

The formalism developed in the previous chapters concern how one can calculate the rate that bubbles of a new phase ($\phi \neq 0$) of a quantum field can nucleate purely via the process of quantum tunnelling through a potential barrier when the system is at zero temperature. However, when temperature is turned on it becomes possible for the field to make use of thermal fluctuations to jump over the barrier and into the true minima. This process would

again ultimately manifest itself via bubbles of the broken phase nucleating in the symmetric phase but these bubbles would have been nucleated by a purely thermal mechanism. After recognising that false vaccum decay can take place via either a purely quantum tunnelling process or a purely thermal process one is naturally led to a third mechanism that is a mixture of both: false vacuum decay via thermally assisted tunnelling. In this scenario thermal fluctuations allow the field to get into an excited state where the barrier penetration action integral is smaller and thus the field can tunnel more easily [26]. Fig. 5.1 summarises

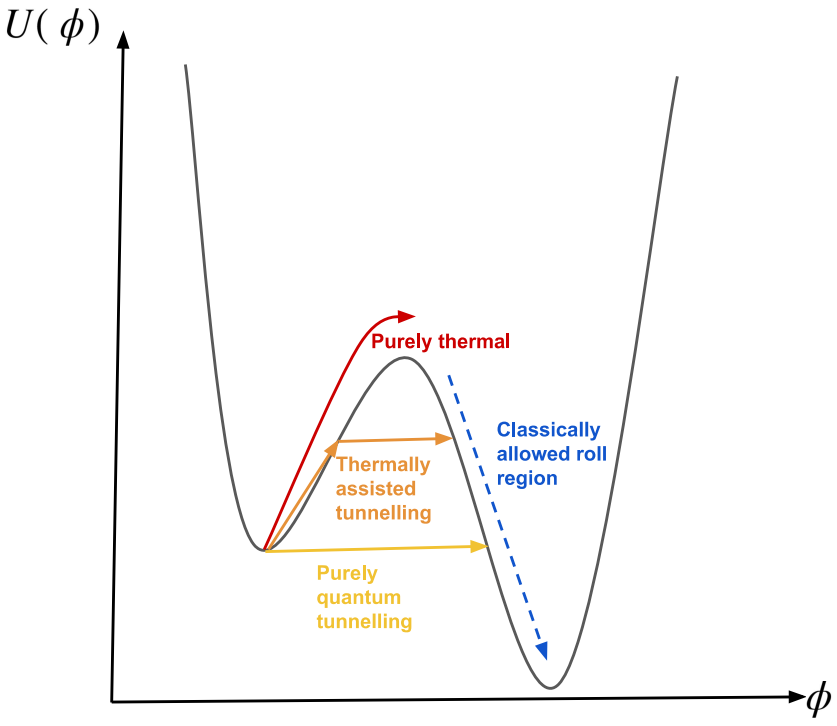

Fig. 5.1 *Three different false vacuum decay mechanisms in yellow, orange and red as based on Fig. 2.19 of [36]. The classically allowed region where the field can roll down the potential is shown with a blue dashed line. Here $U[\phi]$ is the total potential of the Euclidean system as defined in Eq.* (3.6).

the different mechanisms available for false vacuum decay of a quantum field.

A nucleation rate of bubbles from quantum tunnelling, $\Gamma_4(T)$, can in principle be calculated at any given temperature, T, using Eq. (3.13) as it purely depends on the size of the barrier at the time of the transition. However, one can also independently calculate a nucleation rate of bubbles from thermal fluctuations,

$$\Gamma_3 \simeq T^4 \left(\frac{S_3}{2\pi T}\right)^{3/2} e^{-S_3/T} \tag{5.1}$$

where S_3 is the action value of an $\mathrm{O}(3)$ symmetric bounce solution. Whilst we expect the $\Gamma_4(T)$ tunnelling rate to be a maximum at $T = 0$ when the size of the barrier is minimised

and exponentially suppressed at high temperatures when the barrier is large, we expect the converse of the $\Gamma_3(T)$ thermally induced nucleation rate.

At finite temperature, the bounce solution is deformed in the τ direction from its O(4) symmetric form to a solution that is periodic in τ with period $\beta = T^{-1}$. This follows from the fact that the quantum statistics of bosons at finite temperature is formally equivalent to QFT in Euclidean space-time where the time direction is periodic [2, 51].

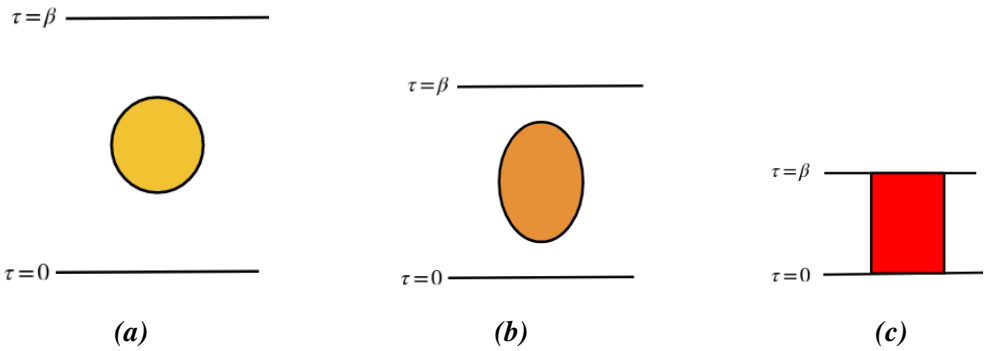

Fig. 5.2 *Thermal bounce solutions with increasing temperature from left to right as based on Fig. 12.10 of [26]*

.

Fig. 5.2 illustrates how the bounce deformation takes place with increasing temperature, from the nearly O(4) symmetric bounce solution in Fig. 5.2a describing thermally assisted tunnelling at low temperatures, to the τ deformed O(3) symmetric bounce solution in Fig. 5.2b describing thermally assisted tunnelling at higher temperatures. Finally, in Fig. 5.2c we show the form of the high temperature, τ independent, O(3) symmetric bounce solution that describes a fully thermal transition. Each horizontal slice of this cylindrical bounce is made up of a 3-dimensional bubble of true vacuum separated from the false vacuum exterior with a wall, represented by the vertical boundary lines of the box, that connects these two vacuum field values.

The S_3 thermal tunnelling action is calculated by solving

$$\frac{d^2\phi}{dr^2} + \frac{2}{r}\frac{d\phi}{dr} = \frac{dV(\phi,T)}{d\phi} \tag{5.2}$$

for the O(3) symmetric bounce solution, with boundary conditions $\phi \to 0$ at $r \to \infty$, $d\phi/dr = 0$ at $r = 0$ and substituting this into the three dimensional version of the Euclidean action in Eq. (3.2).

5.2 False Vacuum Decay and First Order Phase Transitions

After accepting that it is highly probable that at least one phase transitions took place in the early universe, it is natural to next explore the mechanism by which such a transition happens. Fortunately phase transitions are a phenomenon that pervade physics and their study in thermodynamics helps us classify them into two broad categories.

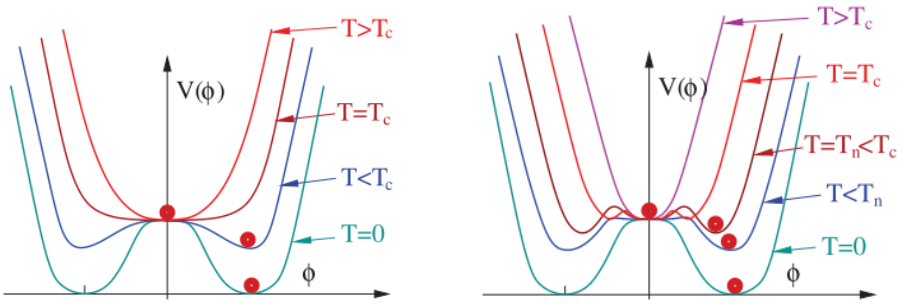

(a) *Admits a cross-over transition* ***(b)*** *Admits a first order transition*

Fig. 5.3 *Two example thermal effective potentials with different phase transitions as taken from Fig. 47 and Fig. 48 of [52].*

In Fig. 5.3 we illustrate these two mechanisms in terms of a thermal effective potential $V(\phi,T)$ which describes our particle physics model at any given temperature T. The shape of the potential and position of the true vacuum vary depending on the value of T but we enforce that $V(\phi,T=0)$ must coincide with the zero temperature particle physics potential, $V_0(\phi)$ from QFT i.e. $V(\phi,T=0)=V_0(\phi)$.

First and perhaps more commonly one can have a cross-over (or second order transition) as shown in Fig. 5.3a where the universe transitions smoothly in time from one phase to the next as the relevant field smoothly transitions from the value of the symmetric phase to the value of the broken phase. At sufficiently large temperatures, nominally much larger than any of the mass parameters of the underlying theory, the potential has a single stable minimum that is symmetric around $\phi=0$. As the temperature of the universe drops to a value that is close to the mass scale of the theory, the shape of the potential changes and the minimum becomes increasingly flat until the universe reaches a critical temperature $T=T_c$ where a minimum develops at $\phi\neq 0$ and the original symmetric minimum of $V(\phi,T)$ becomes a maximum. The field value of the universe, currently at $\phi=0$, is now unstable and thus different casual patches of the universe can spontaneously roll down the potential into the new vacuum at $\phi\neq 0$. The crucial thing to note about such a cross-over transition is that a given causal patch of the universe smoothly transitions from $\phi=0$ to $\phi\neq 0$ as it rolls down the potential to the broken minimum.

The other mechanism by which a phase transition can take place and that which we will be exclusively interested in for the rest of this thesis is known as a first order phase transition and is illustrated using the $V(\phi,T)$ effective potential shown in Fig. 5.3b. At large temperatures the potential again has a single stable minimum at $\phi = 0$. However, when the temperature drops in this scenario a *second* minimum develops in the potential at $\phi \neq 0$. This second minimum will initially be at a potential value that is higher than the symmetric minimum i.e. $V(\phi \neq 0,T) \geq V(\phi,T)$, but after some time the temperature will drop to a critical value, T_c, such that the second minimum and the symmetric minimum become degenerate $V(\phi \neq 0,T_c) = V(0,T_c)$. Below T_c the minimum at $\phi \neq 0$ becomes the true minimum of the potential, $V(\phi \neq,T) < V(0,T)$ when $T < T_c$, and the symmetric minimum becomes meta-stable. This means the false vacuum at $\phi = 0$ can begin to decay via the appearance of bubbles nucleated via either a thermal or quantum tunnelling mechanism as outlined in the previous section.

There is one additional essential condition that needs to be met before a first order phase transition can complete and the universe can fully transition into the broken phase: the bubbles need to percolate. Whilst after nucleation a given bubble will expand up to very large speeds, sometimes close to the speed of light (see Sec. 5.3 & Sec. 5.4), percolation of the bubbles is impossible if the universe is expanding at a faster rate than the bubbles are being produced. Thus for a first order transition to complete we need the nucleation rate of bubbles at a given temperature, whether they be nucleated via a thermal or quantum tunnelling mechanism, to be greater than the rate of Hubble expansion of the universe at that temperature. Whilst the tunnelling rate is exponentially suppressed when the barrier is large, as the barrier becomes smaller one would expect the nucleation rate to increase. Eventually the universe will reach a temperature $T_n < T_c$, as shown in Fig. 5.3b, where the rate of bubble nucleation is equal to the Hubble rate of expansion of the universe i.e. $\Gamma(T_n) \approx H(T_n)^4$. We call this temperature the 'nucleation temperature' and take it to be the time at which the first order phase transition completes. T_n is often referred to as simply the temperature of the first order phase transition because the duration of a typical PT is expected to be negligible compared to the age of the universe at the time it occurs.

Note that whilst both effective potentials shown in Fig. 5.3a and Fig. 5.3b end up at exactly the same $T = 0$ shape, the sequence of intermediate forms of the potential through which they arrive here are vastly different and control whether the phase transition takes place via a cross-over or whether it can be first order. Mathematically speaking, one models such behaviour by adding a thermal correction term $V_T(\phi,T)$ to the zero temperature potential $V_0(\phi)$ so that the full temperature dependent effective potential can be written as $V(\phi,T) = V_0(\phi) + V_T(\phi,T)$. Later on in Sec. 5.5.3 we will study a potential where the zero temperature form of the effective potential still has a barrier present and we will find this has interesting consequences in terms of our ability to detect such scenarios.

5.3 Bubble Wall Dynamics in the Primordial Plasma

After nucleation it is energetically favourable for the bubble walls to expand as discussed in Sec. 3.1.5. In the early universe we typically expect there to be some coupling between the wall and the primordial plasma which manifests itself as a frictional effect on the wall, impeding its expansion and transferring energy to the plasma.

In all of the models that we consider in this thesis the phase transition is relatively strong, so the bubble walls expand faster than the speed of sound. As we will see later, this is a typical feature of theories that produce observable gravitational wave (or magnetic field) signals, since a fairly strong transition is required for significant gravitational wave emission (or magnetic field production). Consequently, the number density of states $n_{\rm h}$ in front of the bubble wall is determined by the temperature of the plasma immediately prior to the transition (the situation is more complicated in subsonic transitions where information can travel ahead of the wall into the plasma).

The dynamics of bubble walls can be described in terms of a driving pressure, sourced by the difference in energy densities between the meta-stable and true vacua, and a frictional pressure $P_{\rm fr}$ acting against the expansion of the bubble walls. The velocity of a given bubble wall, $v_{\rm w}$, changes with time as

$$\frac{dv_{\rm w}}{dt} = \frac{1}{\sigma\gamma_{\rm w}^3}\left(\rho_{\rm vac} - P_{\rm fr}\right) \ , \tag{5.3}$$

where $\gamma_{\rm w}$ is the relativistic Lorentz factor of the bubble walls, and σ is their energy per unit area (i.e. their tension). After series expanding the friction in terms of its leading-order (LO) and next-to-leading order (NLO) contributions to the gauge coupling we obtain the equation of motion for the wall

$$p = \Delta V - \Delta P_{\rm LO} - \gamma_{\rm w}\Delta P_{\rm NLO} \tag{5.4}$$

At leading order the friction on the bubble walls is [53]

$$\Delta P_{\rm LO} \sim \frac{\Delta m^2 T^2}{24} \tag{5.5}$$

and so arises due to states having different masses in the two phases. This means there is a mismatch between the thermal distribution of states crossing the bubble walls and the equilibrium configuration in the true vacuum, and evolving to the equilibrium distribution transfers energy into the plasma. This friction is independent of $\gamma_{\rm w}$ when $\gamma_{\rm w} \gg 1$ and so is a constant value. If, in the limit $\gamma_{\rm w} \to \infty$, the friction from this source is greater than the driving force then the right hand side of Eq. (5.3) becomes zero and the bubble walls reach a finite terminal velocity.

On the other hand, if the friction is smaller than the driving force then this source of friction will not prevent the bubble walls accelerating indefinitely and they are said to 'runaway' where they accelerate without bound right up until the point they collide with each other. Although our discussion so far would seem to permit runaway bubble walls in thermal transitions in some parts of parameter space, there can be other sources of friction that do not lead to a constant pressure in the limit $\gamma_w \to \infty$. In particular, if a gauge boson changes mass across the wall, splitting radiation leads to a next-to-leading order friction term that grows $\propto \gamma_w$ [54]. Consequently, the bubble walls generally have a maximum velocity if there is a thermal bath of particles present.

There is still uncertainty on the exact parametric dependence of the friction from splitting radiation. [54] proposes that it scales as

$$\gamma w \Delta P_{\rm NLO} \sim \gamma_w g^3 w T^3 \ , \tag{5.6}$$

where w is the scale of symmetry breaking, although they also discuss a possible weaker dependence on γ_w. The exact scaling of this friction deserves further study, and will affect our quantitative determination of the boundaries between regimes, but it does not affect the qualitative possibilities that we identify.

It is currently unknown whether models which have no gauge boson masses change across the phase transition can have runaway bubbles, or if there is another source of friction that scales as γ_w^n with $n > 0$. Given that γ_w reaches extremely large values in runaway transitions, $\sim 10^{14}$, such a contribution could prevent runaway walls even if it has an extremely suppressed coefficient, e.g. from multiple loop factors. [1] This is a major source of uncertainty on the dynamics of the bubble walls in such models, and it is an important topic to resolve in the future.

5.4 Runaway Walls

In thermal transitions with finite bubble wall speeds, the terminal values of γ_w are not too far from $\mathcal{O}(1)$ regardless of which source of friction dominates. [2] The bubble walls reach such speeds very quickly after nucleating, long before they typically collide. The energy density in bubble walls is $\simeq \gamma_w \sigma R_*^2$, where R_* is the average bubble size at collision, and the energy released by the region of space now inside the bubble is $\sim \rho_{\rm vac} R_*^3$. Therefore, since the average bubble size when they collide is $\sim H_*^{-1}$, the energy in the bubble walls is negligible compared to that in the plasma when the bubbles percolate. [3] We will study one

[1] A $\propto \log \gamma_w$ dependence might not be enough to stop the bubble walls accelerating before the transition completes.

[2] This is why we do not study the boundary between these two regimes in detail.

[3] This assumes that ε is not tiny. If ε is extremely small a thermal transition is less likely, and even if one occurs the gravitational wave signal will be unobservable.

such model that resides in this regime, described in Sec. 5.5.1, in the context of Intergalatic Magnetic field generation (see Sec. 9.6.2).

Even if models without gauge bosons can have thermal transitions with runaway bubbles, part of the energy released by such phase transitions will be transferred to the plasma in this case, through the leading order friction Eq. (6.22). For an explicit model, assuming that only the γ_w independent friction is present, the proportion of the released energy transferred to the plasma can be found by considering the hydrodynamic solutions of the bubble wall [55]. Apart from extremely strong thermal transitions with significant supercooling as we study in Sec. 5.5.2, or tunnelling transitions that take place in cold hidden sectors as studied in Chapter 6, at least $\sim 10\%$ of the energy goes into the plasma, with the remainder localised in the bubble walls.

5.5 Particle Physics Models with First Order Phase Transitions

Classifying which particle physics models admit a first order phase transition is a particularly interesting task due to the possibility that GWs can be emitted from these early universe events and propagate freely until today. Thus if a transition were to take place that was sufficiently violent, the signal could potentially be observed today with upcoming GW detectors giving us an unprecedented means to probe the high energy particle physics models that were so crucial to the early stages of the universe. We study GW detection scenarios from first order phase transitions in a cold hidden sector in Chapter 7. Additionally, first order phase transitions could also be the origin of magnetic fields that are currently measured on galactic scales and are proving difficult to explain using astrophysical mechanisms. We study this possibility in detail in Chapter 9.

Whilst detecting a first order phase transition in the early universe is a viable prospect, detecting a smooth cross-over transition would be impossible as no GW emission is expected from such an event. Unfortunately, calculations have been done that find the electroweak phase transition in the SM to have taken place via a crossover [56, 57]. However, we know that the SM needs modifications if it is to explain many crucial observed quantities such as dark matter, neutrino masses and the baryon asymmetry of the universe. Encouragingly, many of the models that have been proposed, such as the Two-Higgs-Doublet Model [58] and various other BSM (beyond the Standard Model) theories, could provide scenarios where the electroweak phase transition could be first order and thus potentially detectable. In the remainder of this section we detail three specific BSM models that admit first order phase transitions which we will be selectively utilising as toy model examples in our study of cold hidden sector phase transitions in Chapter 6 and intergalactic magnetic fields from phase transitions in Chapter 9.

5.5.1 Standard Model with $|H|^6$ term

Perhaps the simplest possible extension to the Standard Model one might envisage is the SM (Standard Model) supplemented by a non-renormalisable dimension 6 self interacting Higgs operator $|H|^6/\Lambda^2$ [59]. We use this model in Chapter 5.5.1 in the context of primordial magnetic field generation. The scalar potential for this theory is

$$V(H) = -m^2 H + |H|^4 + \frac{1}{\Lambda^2}|H|^6 \tag{5.7}$$

where H is the single electroweak Higgs doublet of the Standard Model $H^T = (\chi_1 + i\chi_2, +i\chi_3)/\sqrt{(2)}$. Only the real part of the neutral component obtains a vacuum expectation value (VEV) leading to a tree level potential after symmetry breaking

$$V(h)^{\text{tree}} = -\frac{m^2}{2}h^2 + \frac{\lambda}{4}h^4 + \frac{1}{8}\frac{h^6}{\Lambda^2} \tag{5.8}$$

Using the observed Higgs Boson mass of $m_h = 125\text{GeV}$ with the observed Higgs VEV of $v = 246\text{GeV}$ in the renormalisation conditions,

$$V'(h=v) = 0, \quad V''(h=v) = m_h^2 \tag{5.9}$$

we can write the mass and coupling parameters seen in the potential in Eq. (5.8) as

$$m^2 = \frac{m_h^2}{2}\frac{3v^4}{4\Lambda 2}, \quad \lambda = m_h^2 2v^2 - \frac{3v^2}{2\Lambda^2} \tag{5.10}$$

Zero temperature one-loop corrections and thermal corrections must also be added to this potential as outlined in the appendix of [59]. Further details studying the viable parameter space that allows a strongly first order phase transition for this theory are also found in [59].

5.5.2 Standard Model with $U(1)_{B-L}$ hidden sector

A new hidden sector is a well motivated extension of the Standard Model (SM), both from top down considerations of string theory [60] and from a phenomenological perspective e.g. because it could contain the dark matter (DM) [61]. However, any hidden sector present might be extremely weakly coupled to the visible sector, in which case it would be challenging or even impossible to directly probe [62]. One signal that could be observed even in the limit of a vanishing coupling to the SM is a background of gravitational waves left over from a first order phase transition in the hidden sector which occurred early in the universe's cosmological history.

One simple hidden sector extension to the SM is called the $U(1)_{B-L}$ model [63] and involves the addition of a single hidden scalar field φ that couples to the Higgs field via a 'portal' interaction, $\lambda_p h^2\varphi^2/4$. We will consider this SM extension in the context of primordial magnetic field generation in Sec. 9.6.3. The tree level potential is

$$V = \lambda_H(H^\dagger H)^2 + \lambda_\phi(\phi^\dagger\phi)^2 - \lambda_p(H^\dagger H)(\phi^\dagger\phi) \tag{5.11}$$

where ϕ is a complex scalar carrying $U(1)_{B-L}$ charge and quarks and leptons have a B–L charge of $+1/3$ and 1 respectively. H is the SM Higgs doublet that transforms as a singlet under $U(1)_{B-L}$.

In this theory, radiative corrections to the tree level potential result in an effective minimum of the potential developing in the φ direction which means the $U(1)_{B-L}$ symmetry can be spontaneously broken when the φ develops a non-zero vacuum expectation value v_φ. The VEV of φ subsequently becomes manifest in the Higgs sector via the portal coupling by inducing a negative mass term for the Higgs field which results in the EW symmetry being broken and the Higgs field obtaining a VEV v_h. Thus the primary symmetry breaking pattern of this theory in most of the parameter space consists of first $(0,0) \to (v_\varphi, 0)$, followed by $(v_\varphi, 0) \to (v_\varphi, v_h)$.

It is the first step of this symmetry breaking process that is of particular interest for our purposes as when thermal corrections to the potential are accounted for, a barrier is generated between the $B-L$ symmetric and $B-L$ broken minima through which a first order phase transition could have taken place. The size of the barrier is controlled by the relative size of the g_{B-L} gauge coupling and the $B-L$ guage boson mass $m_{Z'}$ as it is this gauge boson that dominates the thermal loop corrections. The full thermal effective scalar potential in the φ direction for this scenario can be approximately expressed as

$$V(\varphi, T) \approx \frac{3g_{B-L}^4\varphi^4}{4\pi^2}\left[\log\left(\frac{\varphi^2}{v_\varphi^2}\right) - \frac{1}{2}\right] + g_{B-L}^2 T^2 \tag{5.12}$$

where v_φ is the VEV of φ.

In some regions of the parameter space the symmetry breaking pattern of the theory can be different to that described above. For example if the hidden φ phase transition happens at sufficiently low temperatures, $T_* \lesssim 140$ GeV, then the Higgs field and the hidden φ field obtain a VEV simultaneously in which case the symmetry breaking pattern is $(0,0) \to (v_\varphi, v_h)$. In this scenario there is a single scalar field wall localised in space but it is made up of two components: a hidden φ part and a Higgs h part. As the VEV of the Higgs is typically much smaller than the VEV of the hidden scalar, $v_h \ll v_\varphi$, we typically expect the ratio, κ_h of energy going into the Higgs component of the bubble wall compared to the hidden φ component to be small i.e. $\kappa_h = \frac{\Delta_h}{\Delta_\varphi} \ll 1$ where $\frac{\Delta_h}{\Delta_\varphi} = \frac{V(v_\varphi,0)-V(v_\varphi,v_h)}{V(0,0)-V(v_\varphi,0)}$.

Provided kinetic mixing between the $U(1)_Y$ and $U(1)_{B-L}$ gauge fields is present, some fraction of the energy deposited into the hidden plasma could be transferred back into the SM fields which could be used for subsequent GW generation as considered in [59, 63, 64] or magnetic field generation as we consider in Sec. 9.6.3. However, one has to be very careful when making such an assumption as in Ref. [65] it was shown that the magnetic field transfer from a dark U(1) to the visible U(1) through kinetic mixing is not efficient.

A further symmetry breaking pattern, first pointed out in [66], can take place if the φ PT percolates after the QCD phase transition i.e. $T_* \leq T_{QCD}$. In this scenario the Higgs field obtains a small VEV, $v_{h,QCD}$, prior to the transition so that the first order phase transition is from $(0, v_{QCD}) \to (v_\varphi, v_h)$ where $v_{QCD} \sim T_{QCD} \ll v_h$. Upon the Higgs taking on this small v_{QCD} VEV prior to the transition, this induces a negative mass term for φ, $\frac{\lambda_p(t) v_{QCD}^2 \varphi^2}{4}$, which makes the potential barrier between $\varphi = 0$ and $\varphi = v_\varphi$ smaller which subsequently reduces the overall strength of the first order phase transition.

For further details on this model and in depth study into the viable parameter space that admits a strongly first order phase transition see [63, 64].

5.5.3 SU(2) hidden sector

The other example hidden sector we consider in this thesis, consists of an SU(2) gauge group with coupling constant g and a dark scalar field Φ, the "hidden sector Higgs", which is in the fundamental of the gauge group and has a tree level potential

$$V = -m^2 |\Phi|^2 + \lambda |\Phi|^4 \ . \tag{5.13}$$

We will consider this model when discussing cold hidden sectors in Chapter 6 and the GW signals that can arise from them in Chapter 7.

A similar hidden sector, albeit with large couplings to the visible sector, has been studied in the context of baryogenesis [67]. As we discuss in Sec. 6.1 such a sector also leads to a viable DM candidate in parts of parameter space, and related models have been considered in [68–73]. The gravitational wave signals from classically scale invariant hidden sectors (at the same temperature as the visible sector) have also been studied in [74]. We consider models that are close to the scale invariant limit and share some features with those in [74] and also that seen in Sec. 5.5.2.

In some parts of parameter space Φ gets a vacuum expectation value (VEV). We parameterise $\Phi = \left(0, \frac{1}{\sqrt{2}}\phi\right)$, where ϕ is the hidden sector field that gets a VEV $\langle\phi\rangle$, so the resulting hidden sector gauge boson masses are $m_A = \frac{1}{2} g \langle\phi\rangle$.

We consider theories with $g^2 \gg \lambda$ and further assume that the tree level mass squared in Eq. (5.13) satisfies $\left|m^2\right| \ll \langle\phi\rangle^2$. In this part of parameter space the 1-loop Coleman-Weinberg potential is comparable to the tree level potential [75]. We make this choice

because the combination of the tree and 1-loop potentials can lead to a first order phase transition but also to induce a barrier in the potential at zero temperature between a metastable vacuum and the true vacuum. Neither of these features are possible if the tree level potential Eq. (5.13) dominates. In the regime we consider, it is convenient to write the mass squared parameter in Eq. (5.13) in terms of a dimensionless parameter $\tilde{m}^2$ and a renormalisation group (RG) scale w

$$m^2 \equiv \tilde{m}^2 \frac{9g^4}{1024\pi^2} w^2 \ . \tag{5.14}$$

We choose the RG scale to coincide with the VEV $\langle\phi\rangle = w$ (in parts of parameter space in which a symmetry breaking vacuum exists).

It is straightforward to evaluate the 1-loop correction to the potential in Eq. 5.13. Given the assumption of a small quartic coupling we can neglect loops of ϕ itself, and the result comes only from the hidden sector gauge bosons. After adding appropriate counterterms, the total zero temperature potential is

$$V_0(\phi) = \frac{9g^4}{1024\pi^2}\left[\frac{1}{2}\tilde{m}^2 w^2\phi^2 + \phi^4\left(\log\left(\frac{\phi^2}{w^2}\right) - \frac{\left(2+\tilde{m}^2\right)}{4}\right)\right] \ . \tag{5.15}$$

As usual the quartic coupling has been replaced with the renormalisation scale w and renormalisation conditions by dimensional transmutation. [4]

If $\tilde{m}^2 \leq 0$ the point $\langle\phi\rangle = 0$ is unstable at zero temperature, if $0 < \tilde{m}^2 < 2$ it is a metastable minimum, and if $\tilde{m}^2 > 2$ this is the true vacuum. If $0 < \tilde{m}^2 < 2$ the difference in energy density between the true vacuum at $\langle\phi\rangle \neq 0$ and the metastable vacuum at $\langle\phi\rangle = 0$ at zero temperature is

$$\rho_{\rm vac} = \frac{9g^4}{1024\pi^2}\frac{\left(2-\tilde{m}^2\right)}{4} w^4 \ , \tag{5.16}$$

and the mass of ϕ in the symmetry breaking vacuum is

$$m_\phi^2 = \frac{9}{512\pi^2}\left(4-\tilde{m}^2\right) g^4 w^2 \ . \tag{5.17}$$

Phase transitions in the early universe depend on ϕ's potential at finite temperature. The simplest estimate of this is obtained by combining the zero temperature potential, Eq. (5.15), with the naive one loop finite temperature correction V_T [76]

$$V(\phi) = V_0(\phi) + V_T(\phi) \ . \tag{5.18}$$

[4] The contribution to the zero temperature potential from ϕ itself is of the form $V = \frac{1}{64\pi^2}\left(V''(\phi)\right)^2 \log(\frac{V''(\phi)}{w^2})$. Since $V'' \sim 9g^4w^2/(64\pi^2)$ our analysis is consistent for $g \sim 1$.

The contribution to $V_T(\phi)$ from the hidden sector gauge bosons is

$$V_T(\phi) \supset \frac{n_i T^4}{2\pi^2} \int_0^\infty q^2 \log\left(1 - \exp\left(-\sqrt{q^2 + m_A^2(\phi)/T^2}\right)\right) dq \,, \tag{5.19}$$

where $n_i = 9$ and $m_A(\phi) = \frac{1}{2} g\phi$. The one loop correction from ϕ loops has a similar form and at temperatures around the time of the phase transition is subleading to Eq. (5.19), as is the case with the zero temperature potential. [5]

Although it demonstrates the existence of a phase transition, the simple one-loop thermal potential is known to lead to significant inaccuracies in many models and can even lead to incorrect predictions of the order of a transition. Different approaches have been proposed to capture the effects missed by Eq. (5.19) (a recent discussion can be found in [77]). In our present work we are interested in phenomenological possibilities rather than precise demarcation of the parameter space. It is therefore sufficient to only improve Eq. (5.19) by resumming an infinite set of daisy diagrams. This fixes the most severe shortcoming of Eq. (5.19) by removing IR divergences that would otherwise spoil the perturbative loop expansion [78, 79]. In practice the daisy resummation can be performed by simply replacing the masses in Eq. (5.19)

$$m_i^2(\phi) \to m_i^2(\phi) + \Pi_i \,, \tag{5.20}$$

where Π_i is the finite temperature self energy of the species i. At leading order in T^2 the longitudinal components of the hidden sector gauge bosons have $\Pi_{\text{long}} = \frac{11}{6} g^2 T^2$ and the transverse gauge bosons have no dependence at this order, and $\Pi_\phi = \frac{1}{2}\left(g^2 + \lambda\right) T^2$ [80].

[5] This can be seen directly by expanding the integral analogous to that in Eq. (5.19).

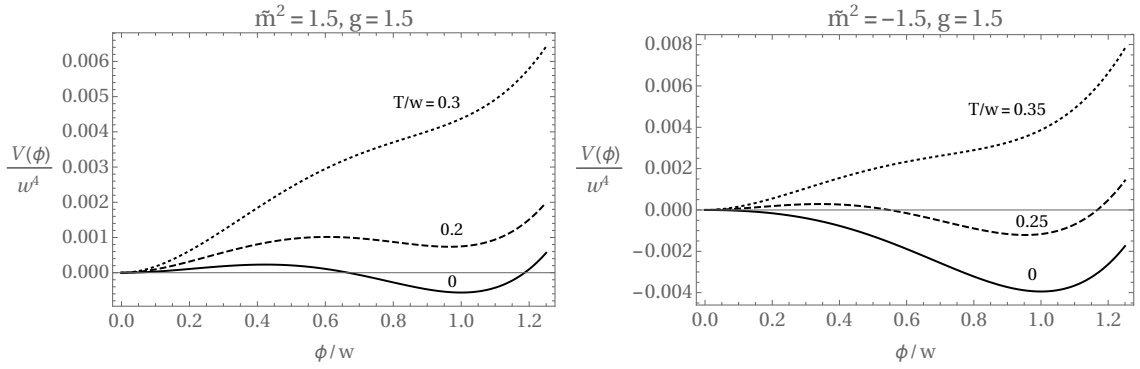

Fig. 5.4 *The scalar potential $V(\phi)$ of the hidden sector that we consider, at different points in parameter space (left and right), at zero temperature (solid) and increasing temperature (dashed, dotted). The model plotted in the left panel has a barrier between the two vacua that remains at zero temperature, and the barrier disappears at zero temperature in the model in the right panel.*

In Fig. 5.4 we show examples of ϕ's finite temperature potential for different points in parameter space, computed after making the modifications in Eq. (5.20). The RG scale w is the only dimensionful parameter in the hidden sector and fixes the overall scale. At high temperatures $\phi = 0$ is always favoured and if this field value remains as a stable minimum there will be no phase transition, but if it persists as a metastable minimum there could be a first order phase transition. Further, if $\phi = 0$ becomes a local maximum by the time the temperature reaches zero, the phase transition could be second order if the barrier disappears before the $\phi \neq 0$ minimum has lower energy than $\phi = 0$. Conversely the transition could be first order if this happens while a barrier remains. [6]

[6] In contrast if $\lambda \gtrsim g$ so that the tree-level potential dominates over the 1-loop potential any phase transition will be second order, unless there are additional hidden sector degrees of freedom.

Chapter 6

First Order Phase Transitions in Cold Hidden Sectors

If a hidden sector is extremely weakly coupled to the visible sector there is no reason to expect that the two should be at the same temperature in the early universe. Indeed, as we will discuss, if a hidden sector contains relatively light degrees of freedom it might need to be cold to be compatible with constraints on the effective number of additional relativistic degrees of freedom at the time of Big Bang nucleosynthesis (BBN) and at the formation of the cosmic microwave background (CMB). A hidden sector that contains stable heavy states without efficient annihilation channels may also need to be cold to avoid these overclosing the universe (e.g. this is the case for pure gauge hidden sectors that contain stable glueballs).

In this Chapter we will study the properties of a possible first order phase transition taking place in a hidden sector that is cold relative to the visible sector. To do this we adopt the SU(2) hidden sector model that we outlined in Sec. 5.5.3 and first discuss the mechanisms and conditions for it to be cold relative to the visible sector in Sec. 6.1. This discussion of cosmological bounds provides us with the necessary basis to explore the nature of the phase transitions in different regions of the viable parameter space in later sections.

We will be particularly interested in the qualitatively different behaviour of the first order phase transition when the hidden sector is very cold and a barrier remains in the potential at zero temperature, which is a distinctive feature possible in the type of model we consider (see Sec. 5.5.3). We will see in Chapter 7 that such scenarios can lead to an observable GW signal with a frequency dependence that may allow such cold hidden sectors to be distinguished from models in which the hidden and visible sector temperatures are similar.

6.1 Cosmological Constraints

A hidden sector can affect the cosmological history of the universe, and the requirement that its effects do not lead to contradictions with observations can exclude large regions of parameter space. In particular, the energy density in a hidden sector should not destroy the successful predictions of BBN or leave an imprint in the CMB, while any stable relics it contains that potentially could make up the dark matter must not overclose the universe. The resulting constraints depend on when the hidden sector phase transition happens relative to events in the visible sector. In Chapter 7 we will see that hidden sector phase transitions can take place at hidden sector temperatures $T_{\rm h} \sim w$ or when the hidden sector is much colder $T_{\rm h} \ll w$.

In this section we summarise the cosmological constraints, laid out in detail in Appendix B, on scenarios where there exists a temperature ratio between the hidden and visible sectors. We will use these to lead us in the rest of this chapter when we study possible first order phase transitions that could have taken place in cold hidden sectors and also the ensuing gravitational wave signals that could be generated from such events (see Chapter 7).

The class of hidden sectors that we consider has many potentially viable parts of parameter space, and rather than fully explore all of these we simply argue that cosmologically acceptable models can easily be found. For simplicity, we consider theories in which the hidden sector Higgs is lighter than the gauge bosons $m_\phi < m_A$ (c.f. Eq. (5.17)). In this case there are no decay or annihilation channels for ϕ unless it has a coupling to the visible sector. Further, the hidden sector gauge bosons are stable through the analogue of the SM's custodial symmetry. Both ϕ and the gauge bosons can be made unstable by introducing new light hidden sector fermions, and we will see that this is necessary to evade cosmological bounds in some parts of parameter space.

We define a parameter characterising the amount of energy released by the hidden sector phase transition

$$\alpha = \frac{\rho_{\rm vac}}{\rho_{\rm v}} \,, \tag{6.1}$$

where $\rho_{\rm vac}$ is the energy density released by the phase transition, and $\rho_{\rm v}$ is the energy density in the visible sector thermal bath when it occurs. We also introduce a similar parameter measuring the energy released relative to that in the hidden sector thermal bath, $\rho_{\rm h}$, immediately prior to the transition

$$\alpha_{\rm h} = \frac{\rho_{\rm vac}}{\rho_{\rm h}} \,. \tag{6.2}$$

We will see in Chapter 7 that $\alpha \lesssim 10$ and both $\alpha_{\rm h} \sim 1$ and $\alpha_{\rm h} \gg 1$ are possible, depending on the type of transition.

6.1.1 Generating a temperature hierarchy

In this section we explore possible mechanisms to generate a temperature difference between a hidden and visible sector in the early universe. We define the temperature ratio between the hidden and visible sectors to be

$$\varepsilon \equiv \frac{T_{\rm h}}{T_{\rm v}} \,, \tag{6.3}$$

where $T_{\rm h}$ and $T_{\rm v}$ are the hidden and visible sector temperatures at some time prior to the phase transition.

If there is no energy exchange between the visible and hidden sectors and no entropy injection into either sector, ε is approximately constant during the evolution of the universe. In this case it only evolves due to changes in the number of relativistic degrees of freedom in the two sectors and

$$\frac{g_{\rm h} T_{\rm h}^3}{g_{\rm v} T_{\rm v}^3} = \frac{g_{\rm h,RH} T_{\rm h,RH}^3}{g_{\rm v,RH} T_{\rm v,RH}^3} \,, \tag{6.4}$$

where $g_{\rm h}$ and $g_{\rm v}$ are the number of relativistic degrees of freedom in the hidden and visible sectors respectively, and RH indicates that a quantity is defined immediately after reheating completes. The resulting changes in ε are relatively small and do not matter when considering extreme temperature hierarchies. However, only a mild temperature difference is needed to satisfy observational constraints from BBN and the CMB so the effects of Eq. (6.4) are relevant when considering these bounds.

The universe might enter its final period of radiation domination when the inflaton decays at the end of inflation. Alternatively, in many string theory models the universe goes through a period of matter domination after inflation. This is due to the presence of relatively light and long lived moduli that are initially displaced from the minimum of their potentials, before being reheated for a final time when the longest lived of these decays. In both of the above cases the initial value of ε is set by the partial decay rates to the visible and hidden sectors ($\Gamma_{\rm v}$ and $\Gamma_{\rm h}$, respectively) of the state responsible for reheating the universe for the final time. Then assuming the energy density in the two sectors is negligible prior to reheating, the temperature ratio just after this is

$$\varepsilon_{\rm RH} = \left(\frac{g_{\rm v} \Gamma_{\rm h}}{g_{\rm h} \Gamma_{\rm v}} \right)^{1/4} \,, \tag{6.5}$$

where $g_{\rm v}$ and $g_{\rm h}$ are the effective number of relativistic degrees of freedom in the visible and hidden sectors immediately after reheating. It is plausible that $\Gamma_{\rm h}$ and $\Gamma_{\rm v}$ could differ dramatically leading to a significant temperature ratio. For example, this could occur if the longest lived modulus in a string compactification comes from a cycle associated with the visible sector, and the hidden sector is localised elsewhere.

Having obtained a hierarchy in their initial values, we also require that the temperature ratio between the hidden and visible sectors persists until the hidden sector phase transition occurs. This can be achieved simply by assuming that the two sectors are completely decoupled. [1]

On the other hand, it is interesting to consider the size of interactions between the two sectors that are allowed without the temperature hierarchy being destroyed. The presence of such a coupling would affect the cosmological history of a hidden sector, for example by allowing otherwise stable hidden sector states to decay, and could potentially also lead to observable signals of a hidden sector.

In Appendix B.1 we show that maintaining a large temperature hierarchy requires parameterically smaller portal couplings than the well known conditions for a hidden sector to remain out of thermal equilibrium with the visible sector. For example, the constraint on the Higgs portal coupling,

$$\mathscr{L} \supset -\frac{1}{2}\lambda_p |\Phi|^2 |H|^2 \ , \tag{6.6}$$

where H is the SM Higgs doublet, to maintain a temperature hierarchy is found to be

$$\lambda_p \lesssim 10^{-10}\varepsilon^2 \ . \tag{6.7}$$

6.1.2 The viable parameter space

Summarising the results in Appendix B, we identify two regions of our model's parameter space that are cosmologically safe and in which it is out of thermal equilibrium with the visible sector. These serve as a basis for our subsequent study of hidden sector phase transitions and their gravitational wave signals.

In the first region, the hidden sector is at a relatively high scale such that $m_\phi \gg m_h$ and its temperature is not too different to that of the visible sector, so the hidden sector phase transition happens before EW symmetry breaking. The introduction of a small Higgs portal coupling allows ϕ to decay to the visible sector before BBN, and this does not destroy the temperature asymmetry provided $\varepsilon \gtrsim 10^{-3}$. Meanwhile, since ε is not too small the annihilation of hidden sector gauge bosons is reasonably efficient compared to the Hubble parameter at the time of the phase transition and the relic abundance of these can easily be viable.

A second possibility is that the hidden sector has no portal coupling to the visible sector. In this case, by introducing light hidden sector fermions, hidden sector models at any scale are viable provided the values of ε and α are such that BBN and CMB constraints

[1] There is still the possibility of thermalisation via the inflaton if this has relatively large couplings, however if it decays via non-renormalisable operators this effect is negligible [81, 82].

are satisfied (assuming the hidden sector fermions are sufficiently light that their relic abundance is small).

We compare the phase transitions that happen in cold hidden sectors to those in hidden sectors that are at the same temperature as the visible sector. It is therefore useful to briefly discuss the parameter space in which such sectors are not excluded.

First we note that any hidden sector at the same temperature as the visible sector is excluded by BBN constraints if it goes through a phase transition at a temperature $T \lesssim 10$ MeV. For the hidden sector that we consider, this is the case if $w \lesssim 50$ MeV.

If the example SU(2) hidden sector that we consider has a portal coupling $\lambda \gtrsim 10^{-7}$ at a scale $w \gtrsim 10$ GeV, it reaches thermal equilibrium with the visible sector and is cosmologically safe. ϕ decays safely before BBN and the relic abundance of hidden sector gauge bosons can easily be viable. Such a model is also not excluded by collider bounds, e.g. on invisible Higgs decays, provided that λ is not too large.

It is hard, but not impossible, to accommodate the hidden sector that we consider if 50 MeV $\lesssim w \lesssim 5$ GeV and it is at the same temperature as the visible sector. ϕ must decay to evade the relic density constraint, however light hidden sector fermions cannot be introduced due to BBN limits. Instead ϕ must decay to the visible sector before BBN, which most easily happens through a Higgs portal operator. There are numerous strong constraints on such operators, and such a model is only viable in small parts of parameter space (e.g. if ϕ has a mixing angle with the Higgs $\sin^2\theta \simeq 10^{-8}$) [83].

More generally, we expect that there are relatively few viable models of hidden sectors that are thermalised with the visible sector and which go through transitions at temperatures 10 MeV $\lesssim T \lesssim 5$ GeV. Such a sector must have a relatively strong interaction with the visible sector for its energy to be transferred to the visible sector before BBN. However, portal interactions at low scales are strongly constrained by, for example, observations of supernovae and beam dump experiments.

6.2 Thermal Transitions vs. Tunnelling Transitions

A first order phase transition in a hidden sector begins when hidden scalar field bubbles of the true vacuum start to be nucleated at a significant rate and completes when these have expanded and engulfed the universe. In the process, the difference in energy density between the two hidden sector vacua, including the finite temperature contribution to the potential, is released. This drives the expansion of the bubbles and heats the hidden thermal bath behind the bubble walls. [2]

Bubbles of the true vacuum can be nucleated by thermal fluctuations or by quantum tunnelling through the energy barrier (see Sec. 5.1). Given the scaling of the volume and

[2] In transitions with subsonic walls speeds, the plasma ahead of the bubble walls is also heated.

surface energies of a bubble with its radius, there is a minimum bubble size above which it will expand. The probability of nucleating such a bubble is set by an action, determined from the field profile of a critical bubble. The action depends on whether the bubble is nucleated through a thermal fluctuation or quantum tunnelling and is denoted S_3 or S_4 respectively. [3]

The probability of nucleating a critical hidden scalar bubble via a thermal fluctuation per unit time and volume, Γ_3, is approximately

$$\Gamma_3 \simeq T_{\rm h}^4 \left(\frac{S_3}{2\pi T_{\rm h}}\right)^{3/2} e^{-S_3/T_{\rm h}} , \tag{6.8}$$

where $T_{\rm h}$ is the temperature of the hidden sector [51]. The analogous expression for the rate of nucleations by tunnelling, Γ_4, is

$$\Gamma_4 \simeq w^4 \left(\frac{S_4}{2\pi}\right)^2 e^{-S_4} , \tag{6.9}$$

where w is the VEV that ϕ gets after the transition [84, 85]. As well as the explicit temperature dependence in $S_3/T_{\rm h}$, both S_3 and S_4 implicitly depend on the hidden sector temperature, since they are determined by the finite temperature potential. Both S_4 and $S_3/T_{\rm h}$ tend to infinity for temperatures approaching that at which the high temperature phase is energetically favoured and go to 0 if the barrier disappears.

The critical actions can sometimes be estimated with one of several analytic approximations [86]. The simplest of these, appropriate if the barrier between the vacua is large compared to the energy difference between them, is the thin wall approximation outlined in Sec. 3.1.6. This treats the actions as a sum of independent contributions from the bubble's volume and from its surface. However, the assumption of a thin wall is not valid for the close to conformal models that we consider and leads to significant inaccuracies [74] (other analytic approaches are also inaccurate in such models [87]). [4]

Instead, we calculate the critical actions numerically by varying the field configurations to minimise the actions. [5] We also note that Eqs. (6.8) and (6.9) are only approximations to the nucleation rates. Their accuracy can be improved by replacing the factors in front of the exponentials with a function that includes the determinant of fluctuations around the

[3] The S_4 action is exactly equivalent to the S_E Euclidean action discussed in previous Chapters. For the remainder of the thesis we refer to S_4 for notational convenience.

[4] Calculating the predicted thickness of the bubble walls in our model assuming the thin wall approximation shows that this is not self consistent, and the results for the critical actions that we obtain numerically also deviate significantly from the thin wall predictions.

[5] This can be done efficiently using an overshoot/undershoot method. We use the publicly available code CosmoTransitions [35], which we have validated with our own implementation.

critical field configuration [88–91]. However, the error introduced by Eqs. (6.8) and (6.9) is typically relatively mild, so they are sufficient for our present purposes. [6]

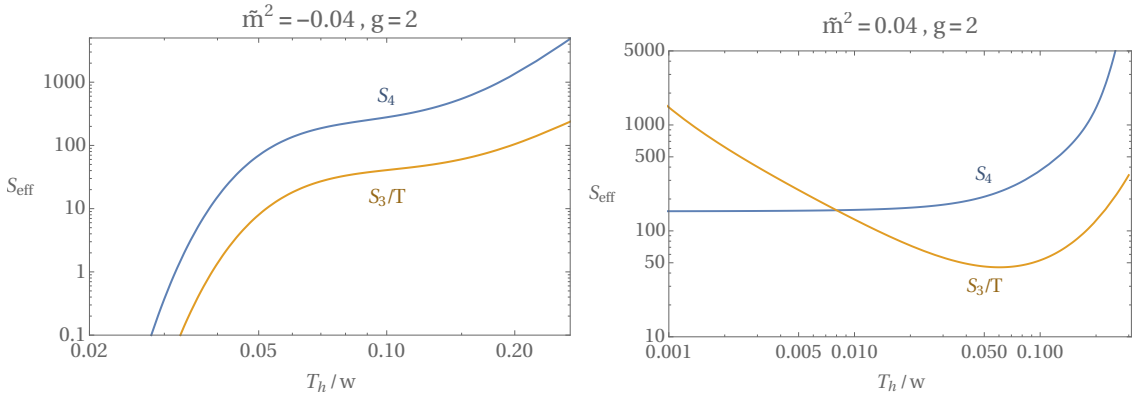

Fig. 6.1 *Examples of the dependence of the critical bubble nucleation actions S_3/T_h and S_4 on the hidden sector temperature T_h. The parameters g and $\tilde{m}^2$ define the model via Eq.* (5.15)*. The left panel corresponds to a hidden sector for which the energy barrier between the two minima vanishes at zero temperature, so both S_3/T_h and S_4 go to zero. The right panel corresponds to a model in which a barrier remains at zero temperature, so S_4 asymptotes to a constant and $S_3/T_\mathrm{h} \to \infty$.*

In Fig. 6.1 we show examples of the critical bubble actions for two points in the parameter space of the hidden sector model described in Sec. 5.5.3. As seen in the left panel of Fig. 6.1, a transition is guaranteed to complete if the hidden sector potential is such that the barrier between the two minima disappears at low temperatures. Provided that the true vacuum is energetically favoured before the barrier vanishes (and internal thermal equilibrium is maintained), the transition happens through bubble nucleation before the barrier vanishes completely due to the rapid increase in the Γ_3 and Γ_4 at such times [93, 94]. The temperatures at which the symmetry breaking vacuum is energetically favoured, that at which nucleation becomes efficient, and that at which the barrier disappears completely are typically not dramatically different.

As seen in the right panel of Fig. 6.1, in the parts of the parameter space in which a barrier remains between the two vacua at zero temperature, the behaviour of S_3/T_h and S_4 are qualitatively different from each other. S_3/T_h initially decreases at large hidden sector temperatures because small decreases in T_h result in comparatively large decreases in the height of the barrier meaning thermal fluctuations in the thermal bath have greater chance of jumping over the barrier and into the true vacuum. Conversely, at low hidden sector temperatures S_3/T_h increases with decreasing temperature, since the energy available from the thermal bath to fluctuate into a bubble decreases whilst the barrier approaches a constant shape in the $T_\mathrm{h} \to 0$ limit. Thus a minimum value of S_3/T_h exists at

[6] Alternative, more accurate, non-perturbative methods to calculate the nucleation probabilities have also been developed [92].

a hidden temperature between these extremes for which the energy available for thermal flucatuations is maximised relative to the barrier height.

The S_4 action has no such dependence on the energy in the thermal bath and only depends on the hidden sector temperature through the shape of the potential. Therefore, at high T_h, S_4 rapidly drops with deceasing temperature due to the quickly reducing barrier height, before asymptoting to a non-zero value as the barrier approaches a constant shape in the $T_{\rm h} \to 0$ limit.

The time when a phase transition begins can be estimated as the point when one critical bubble is nucleated per Hubble volume per Hubble time, so that the true vacuum starts to permeate, i.e. when

$$\max\left[\Gamma_3\left(T_{\rm h}\right), \Gamma_4\left(T_{\rm h}\right)\right] = H\left(T_{\rm v}\right)^4 \ . \tag{6.10}$$

If a hidden sector is at the same temperature as the visible sector, this condition is satisfied if $S_3/T_{\rm h} \simeq 120$ or $S_4 \simeq 120$ for a phase transition at temperatures around the EW scale.

Although Eq. (6.10) is useful to get a rough idea of when a transition happens, it is not accurate enough to reliably determine whether a transition successfully completes if a barrier remains at zero temperature. Further, the gravitational wave signal that is produced depends on how long a transition takes and the average bubble size. To extract these properties, we evaluate $S_3/T_{\rm h}$ and S_4 as a function of temperature for a given point in hidden sector parameter space. Another required physical input is the speed of the bubble walls throughout the transition $v_{\rm w}$. Over all of the parameter space that we consider the phase transitions are fairly strong so that $v_{\rm w} \simeq 1$ and for tracking the progress of the transition and the average size of bubbles it is sufficient to fix $v_{\rm w} = 1$. [7] Then we track the proportion of the universe that is in the low temperature phase and the distribution of bubble sizes throughout the phase transitions, accounting for bubbles only forming in regions of space that are in the false vacuum and allowing for the expansion of bubbles. This calculation is standard (see e.g. Sec. 3.2 of [95] for a clear summary).

6.3 Transitions in Hot and Cold Hidden Sectors

We start by assuming that the hidden sector reheating temperature is high enough that the high temperature phase ($\langle\phi\rangle = 0$) is initially favoured. As before the temperature of the visible and hidden sectors are allowed to differ by a ratio ε, and we assume there is no energy transfer between the sectors. [8]

[7] When we study the gravitational wave signals produced, the difference between bubble walls with Lorentz factors $\gamma_{\rm w} = \mathcal{O}(1)$ and those with $\gamma_{\rm w} \to \infty$ will be important.

[8] When presenting results we quote ε at the time of the hidden sector phase transition.

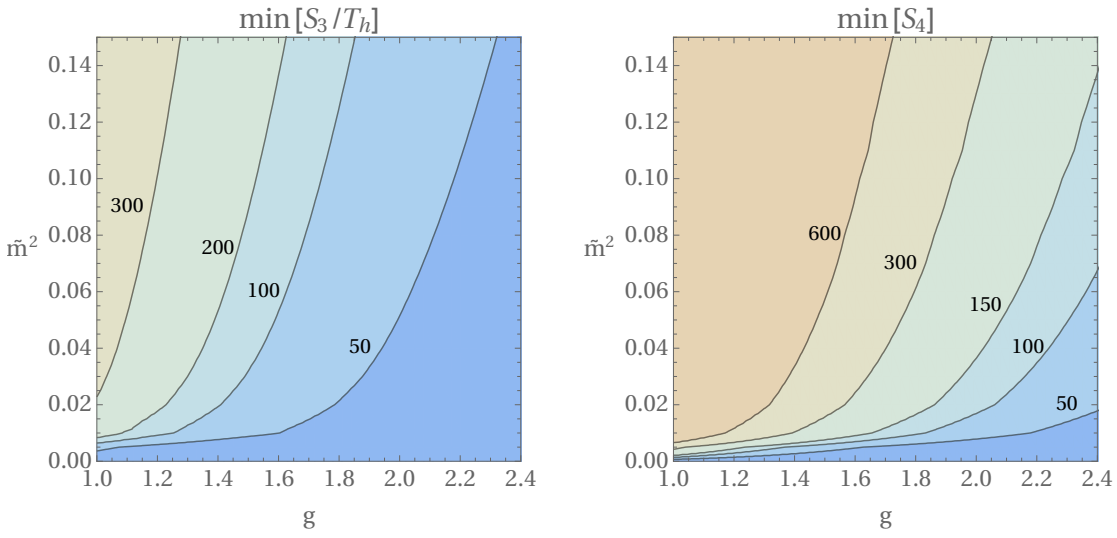

Fig. 6.2 *Contours of the minimum values of S_3/T_h (left) and S_4 (right) as a function of the parameters of the hidden sector (defined in Sec. 5.5.3).*

In Fig. 6.2 we plot contours of the minimum values of S_4 and S_3/T_h as a function of the dimensionless parameters of the hidden sector, for models such that a barrier persists at zero temperature. The value of w does not affect these results, since it is the only relevant scale in the calculation. We consider relatively large gauge couplings $1 \gtrsim g \gtrsim 2.5$. Towards the upper end of this range the accuracy of our perturbative calculations may be compromised, however since $g < \sqrt{4\pi}$ we do not expect the qualitative dynamics to change significantly. Therefore, despite this source of potential numerical imprecision, we regard our hidden sector as a useful toy model to explore the phenomenological possibilities that can arise more generally.

The minimum value of S_3/T_h is smaller than that of S_4 over all of the parameter space in Fig. 6.2. Further, S_3/T_h is also smaller than S_4 at hidden sector temperatures $T_\mathrm{h} \sim w$ (as is the case for the points in parameter space shown in Fig. 6.1). These features are not surprising. As discussed in [96], in the thin wall approximation the actions scale as

$$S_3/T_\mathrm{h} \sim \frac{w}{T_\mathrm{h}} \left(\frac{w^4}{\Delta V} \right)^2 , \tag{6.11}$$

and

$$S_4 \sim \left(\frac{w^4}{\Delta V} \right)^3 , \tag{6.12}$$

where ΔV is the difference in energy density between the two vacua. Even though the thin wall approximation often does not give precise numerical results, the feature that if $S_3/T_\mathrm{h} \gg 1$ then $S_4 \gg S_3/T_\mathrm{h}$ is typical across many classes of models (although it would be interesting to find theories for which it does not hold). As a result, if a first order phase

transition happens at a temperature $T_\mathrm{h} \sim w$, this will be through nucleation of bubbles by thermal fluctuations (including in the case that no barrier remains at zero temperature).

In a model for which a barrier remains at zero temperature, if a transition does not complete when $T_\mathrm{h} \sim w$ then S_3/T_h subsequently increases as the temperature drops further, while S_4 only changes slightly. This raises the possibility that a hidden sector might fail to complete a thermal transition but could later undergo a tunnelling transition once the Hubble parameter has dropped, despite Γ_4 remaining smaller than the largest value of Γ_3. However, if the hidden and visible sectors are at the same temperature this is not possible in generic models, for a reason related to the problems faced by old inflation [97]. If a transition is to occur, the total vacuum energy density at the true minimum must be tuned to (approximately) zero, so the vacuum energy density of the false minimum is $\sim w^4$. Once $T_\mathrm{h} = T_\mathrm{v} \ll w$ this will dominate the energy density of the universe. As a result H remains $\sim w^2/M_\mathrm{Pl}$, and the universe enters a new inflationary phase. Therefore, the proposed tunnelling transition, which requires much smaller values of H since $S_4 \gg \min(\mathrm{S_3/T_h})$, cannot occur.

Consequently, for the model we consider, a first order phase transition in a hidden sector at the same temperature as the visible sector will only ever happen through nucleation of bubbles by thermal fluctuations, at a time when the hidden sector temperature is $T_\mathrm{h} \sim w$. We also believe that this is a typical feature across generic models, although it would be interesting to study other calculable models further.

This conclusion does not hold if the hidden sector is cold relative to the visible sector. If there is barrier between the two vacua that remains at zero temperature, the Hubble parameter when S_3/T_h is minimised is $H \sim \varepsilon^{-2} w^2/M_\mathrm{Pl}$. For a transition to occur through thermal fluctuations requires

$$H\left(T_\mathrm{v}\right)^4 \lesssim T_\mathrm{h}^4 \left(\frac{S_3}{2\pi T_\mathrm{h}}\right)^{3/2} e^{-S_3/T_\mathrm{h}} \,. \tag{6.13}$$

If this is ever satisfied, it happens when $T_\mathrm{h} \sim w$, and requires

$$\left(\frac{S_3}{T_\mathrm{h}}\right) < \left(\frac{S_3}{T_\mathrm{h}}\right)_0 - 8\log\left(\frac{1}{\varepsilon}\right) \,, \tag{6.14}$$

where $(S_3/T_\mathrm{h})_0$ is the value necessary for a transition to complete when the two sectors are at equal temperatures (e.g. $(S_3/T_\mathrm{h})_0 \sim 120$ for an EW scale transition). A cold hidden sector requires a smaller value of S_3/T_h because the universe is expanding faster when S_3/T_h reaches its minimum, so the condition for the true vacuum to permeate is stronger.

On the other hand, the vacuum energy of a cold hidden sector still starts dominating the expansion of the universe when $H_{\rm min} \simeq \sqrt{\rho_{\rm vac}}/\left(3M_{\rm Pl}\right)$, and provided

$$\Gamma_4\left(T_{\rm h} \simeq 0\right) \gtrsim H_{\rm min}^4 \,, \tag{6.15}$$

the transition can complete through tunnelling. This is independent of whether the hidden sector is colder than the visible sector (apart from the variation of Γ_4 with temperature, which is negligibly small for the relevant temperatures $T_{\rm h} \ll w$).

Eq. (6.15) is a weaker condition than Eq. (6.14), so for sufficiently small ε a hidden sector can fail to undergo a thermal transition at $T_{\rm h} \sim w$, but later goes through a tunnelling transition. Even though the minimum value of $S_3/T_{\rm h}$ is smaller than that of S_4, the tunnelling transition happens later when the visible sector temperature has dropped and the Hubble parameter is smaller.

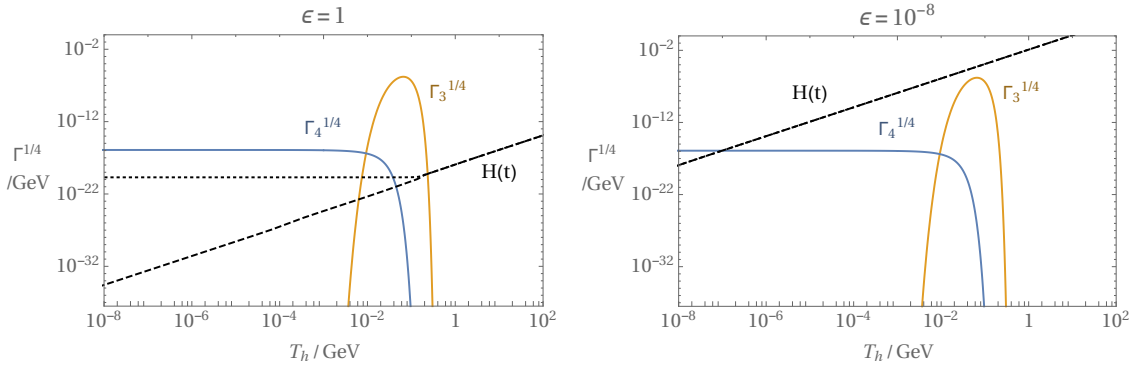

Fig. 6.3 *The bubble nucleation rate as a function of the hidden sector temperature for a model with $g = 2$ and $\tilde{m}^2 = 0.04$ (as in the right panel of Fig. 6.1) and $w = 1$ GeV. Results are shown for a hidden sector at the same temperature as the visible sector ($\varepsilon = 1$, left) and for a hidden sector that is much colder ($\varepsilon = 10^{-8}$, right). The Hubble parameter in the two cases is also plotted, assuming that the transition occurs prior to the hidden sector false vacuum energy dominating the energy density of the universe (dashed black), and assuming the phase transition does not complete prior to this (dotted black). If $\varepsilon = 1$ (left panel) the hidden sector false vacuum energy begins to dominate at $T_{\rm v} = T_{\rm h} \simeq 0.2$ GeV when the two Hubble curves diverge. A transition happens when $H(t)$ is first smaller than one of $\Gamma_3^{1/4}$ or $\Gamma_4^{1/4}$. Therefore the warm hidden sector (left) undergoes a thermally nucleated transition, while the cold hidden sector (right) misses a thermal transition, but subsequently goes through a tunnelling transition.*

In Fig. 6.3 we show this by plotting the nucleation rates via thermal fluctuations and tunnelling as a function of the hidden sector temperature, for a model with $\varepsilon = 1$ and $\varepsilon = 10^{-8}$. The hidden sector is the same as in the right panel of Fig. 6.1 with $w = 1$ GeV. We also plot the Hubble parameter assuming the transition occurs prior to the hidden sector false vacuum energy density dominating the universe and assuming that the transition

never occurs, with the cosmological constant tuned to zero in the true vacuum. However, in both models plotted the transition will complete and the dotted Hubble dependence is not realised. As expected, for $\varepsilon = 1$ the transition happens through thermal nucleation. [9] For $\varepsilon = 10^{-8}$, the larger value of the Hubble parameter when $T_{\rm h} \sim w$ prevents a thermal transition occurring, and a tunnelling transition happens later once H is smaller.

For a tunnelling transition to happen this way, $\log \varepsilon$ must be comparable to the difference between the minimum values of $S_3/T_{\rm h}$ and S_4. Since this is typically $\mathcal{O}(10)$ a huge temperature hierarchy is required, indeed, in the model that we consider $\varepsilon \lesssim 10^{-7}$. Such small values are compatible with our assumed cosmological history, provided that the visible sector reheating temperature $T_{\rm RH} \gtrsim w/\varepsilon$ (so that the hidden sector is reheated above w). The visible sector temperature when the phase transition takes place is fixed by

$$\Gamma_4 \simeq H \left(T_{\rm v}\right)^4 \ , \tag{6.16}$$

i.e. when

$$T_{\rm v} \simeq \frac{S_4^{1/4} e^{-S_4/8}}{g_v^{1/4}} \sqrt{w M_{\rm Pl}} \ , \tag{6.17}$$

where S_4 is approximately temperature independent at the relevant times. The exponential dependence on S_4 in Eq. (6.17) means that $T_{\rm v}$ changes by orders of magnitude as the parameters of the hidden sector vary.

[9] If the hidden sector parameters are altered to increase the height of the barrier, Γ_3 and Γ_4 decrease by approximately the same factor. So if the maximum value of Γ_3 is small enough that a thermal transition does not occur, the hidden sector false vacuum energy density dominates the universe before a tunnelling transition is possible.

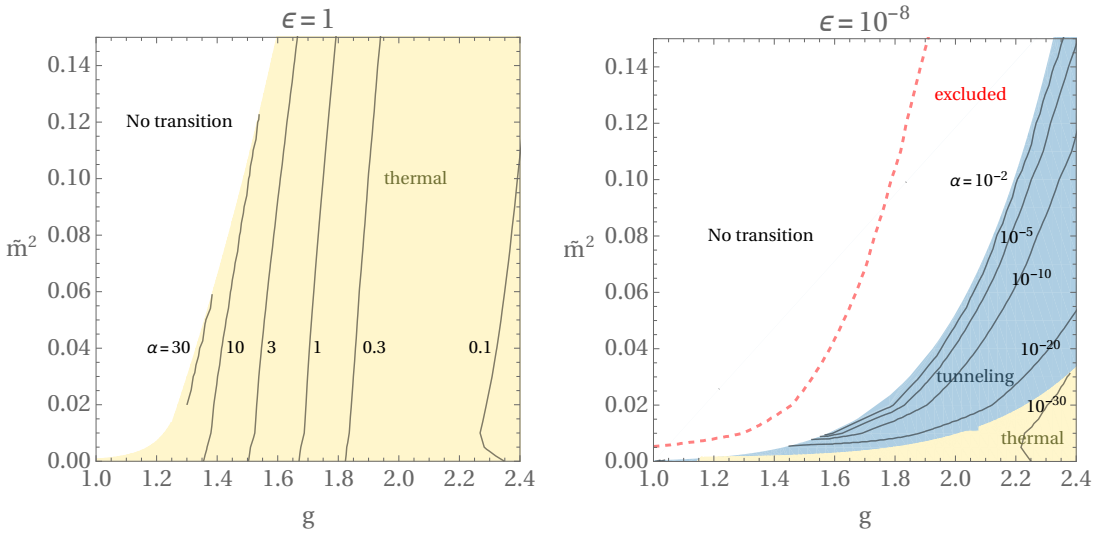

Fig. 6.4 *The type of phase transition that occurs (yellow: thermal, blue: tunnelling) over the hidden sector parameter space for $w = 1$ GeV, when the hidden sector is at the same temperature as the visible sector (left) and when the hidden sector is much colder with $\varepsilon = 10^{-8}$ (right). The contours give the values α for the transitions. In the white region no phase transition takes place. For cold hidden sectors there are models that cannot lead to an acceptable cosmological history, as described in the text.*

In Fig. 6.4 we plot the type of phase transition that occurs over our example hidden sector parameter space for $\varepsilon = 1$ and $\varepsilon = 10^{-8}$. Only the region in which a barrier remains at zero temperature is shown, since in the converse case a thermal transition always occurs.

Some models in Fig. 6.4 right are incompatible with the cosmological history of the universe regardless of how the vacuum energy is tuned, despite the hidden sector being extremely cold. For example, both tuning the vacuum energy of the universe to zero when the hidden sector is in the false vacuum and tuning it to zero in the true minimum lead to an unacceptable cosmology when the thermal transition window is missed. In the former case, the tunnelling nucleation rate must be small compared to the present day value of the Hubble parameter, which is not always the case, whilst in the latter case the universe can become dominated by the false minimum and subsequently trapped in this phase. A significant region of the parameter space of models with $\varepsilon = 10^{-8}$ fail in both scenarios and are always problematic. [10]

Finally we note that models with a low reheating temperature, below that at which the hidden sector temperature is restored, do not evade our argument that tunnelling transitions only occur in cold hidden sectors. We do not consider such theories further, and details of the dynamics in this case may be found in Appendix B.4.

[10] If $\varepsilon = 1$ the difference between S_3/T_h and S_4 is sufficiently large that if a thermal transition is missed, a tunnelling transition will be slow compared to the age of the universe, so this issue does not arise.

6.4 Transition Properties

If a hidden sector is colder than the visible sector this will affect the properties of its phase transition, even if the transition still happens through thermal fluctuations; and if a transition happens through tunnelling rather than thermal fluctuations this will also affect its dynamics.

One crucial quantity for determining the gravitational wave signal produced that will be of interest in Chapter 7, is the amount of energy released by the phase transition relative to that in the thermal bath. This is the quantity α defined in Eq. (6.1).

First we consider transitions that happen through thermal fluctuations. Suppose there are two identical hidden sectors, at the same scale w, that both go through thermal transitions, one of which is at the same temperature as the visible sector and the other much colder. Both transitions happen when their respective hidden sector temperatures are $T_\mathrm{h} \sim w$, with only an $\mathcal{O}(1)$ difference due to the increased Hubble parameter when there is a hotter visible sector present (c.f. Eq. (6.14)). Therefore the visible sector temperature at the time of the phase transition is approximately

$$T_\mathrm{v} \propto \frac{w}{\varepsilon} \,, \tag{6.18}$$

and

$$\alpha = \frac{g_\mathrm{h}}{g_\mathrm{v}} \alpha_\mathrm{h} \varepsilon^4 \,. \tag{6.19}$$

In thermal transitions the relative energy released into the hidden sector is $\alpha_\mathrm{h} \lesssim 10$ and α is strongly suppressed when the hidden sector is cold.

The situation is different if a hidden sector transition happens through tunnelling. In this case the visible sector temperature at the time of the transition, and therefore α, is fixed by Eq. (6.17), which is independent of ε. Unlike for thermal transitions, α can span a wide range of values for different models. It still cannot be orders of magnitude larger than 1 since this would mean that the hidden sector vacuum energy dominated the universe prior to the transition, leading back to the problems of old inflation. Since tunnelling transitions always happen at temperatures $T_\mathrm{h} < w$ we also know that $\alpha \gtrsim \varepsilon^4$.

Contours of α as a function of the hidden sector parameters are plotted in Fig. 6.4. In the left panel $\varepsilon = 1$, so the phase transition is always via thermal fluctuations and α is roughly $\mathcal{O}(1)$. As the value of g increases the hidden sector potential favours the true vacuum at higher temperatures, so the transition happens slightly earlier and α decreases. Relatively large values of $\alpha \simeq 30$ are possible close to the boundary at which the transition only just manages to complete, corresponding to significant supercooling. This is due to the almost conformal nature of our hidden sector, which results in the energy barrier between the two vacua remaining temperature dependent down to temperatures significantly below

w. For example, Fig. 5.4 shows the barrier changing at temperatures around $T \simeq 0.1w$. [11] The possibility that conformal models could lead to significant supercooling has previously been studied in [87, 98–100] and we study one such model, outlined in Sec. 5.5.2, in the context of magnetic field generation in Sec. 9.6.3.

In the right panel of Fig. 6.4 the hidden sector is cold, with $\varepsilon = 10^{-8}$, and over the majority of this parameter space a phase transition happens through tunnelling. As expected, α takes a wide range of values 10^{-25} – 1 and it is fairly large only close to the boundary at which a transition fails to complete. In the part of parameter space for which a thermal transition takes place α is extremely small, roughly ε^4.

Another parameter that is important in determining the gravitational wave signal is the time taken for the phase transition to complete relative to the Hubble parameter when the transition occurs. This is also approximately inversely proportional to the average size of bubbles when they collide compared to the Hubble distance.

If a thermal transition takes place relatively fast, and at a temperature such that S_3/T_h decreases approximately linearly with temperature, it will complete once S_3 decreases by an order 1 amount after nucleation first becomes efficient (since its exponential dependence means the nucleation rate will be extremely fast at this point). The duration of such a phase transition can be estimated as β^{-1} where

$$\beta = -\frac{\partial S_3}{\partial t} \,, \tag{6.20}$$

evaluated at the time of the phase transition (see e.g. [101]). Eq. (6.20) can be rewritten in the more useful form

$$\begin{aligned} \frac{\beta}{H_*} &= T_{\mathrm{v}*} \frac{\partial}{\partial T_\mathrm{v}} \left(\frac{S_3}{T_\mathrm{h}} \right) \\ &= T_{\mathrm{h}*} \frac{\partial}{\partial T_\mathrm{h}} \left(\frac{S_3}{T_\mathrm{h}} \right) \,, \end{aligned} \tag{6.21}$$

where a $*$ indicates a quantity at the time of the phase transition, and the derivative is evaluated at this time as well. The right hand side of Eq. (6.21) is not far from $\mathcal{O}(1)$ even if the hidden sector is cold, so the duration of such a phase transition is always approximately set by the Hubble parameter.

More generally the duration of a transition can be defined as the time between e.g. 90% and 10% of the universe being in the high temperature phase (the qualitative features of our results are not sensitive to these particular choices). Unlike the estimate from β, this is applicable to tunnelling transitions, and also thermal transitions that happen when S_3/T_h is close to its minimum (additionally, Eq. (6.21) requires modification in the case of significant supercooling, as can occur in our model).

[11] In that figure $\tilde{m}^2$ is relatively large so that the presence (or absence) of the barrier is visible. Models with smaller values of $\tilde{m}^2$ are more phenomenologically interesting, and in this case the suppression of the critical temperature is more pronounced.

In tunnelling transitions the duration of a phase transition is also approximately set by the Hubble parameter. Once nucleation is efficient enough that 10% of the universe reaches the low temperature phase, existing bubbles expand at close to the speed of light and further bubbles continue to form, so the rest of space goes through the transition within approximately a Hubble time. This is also the case in the previously mentioned classes of thermal transitions for which β is not a good measure of the duration.

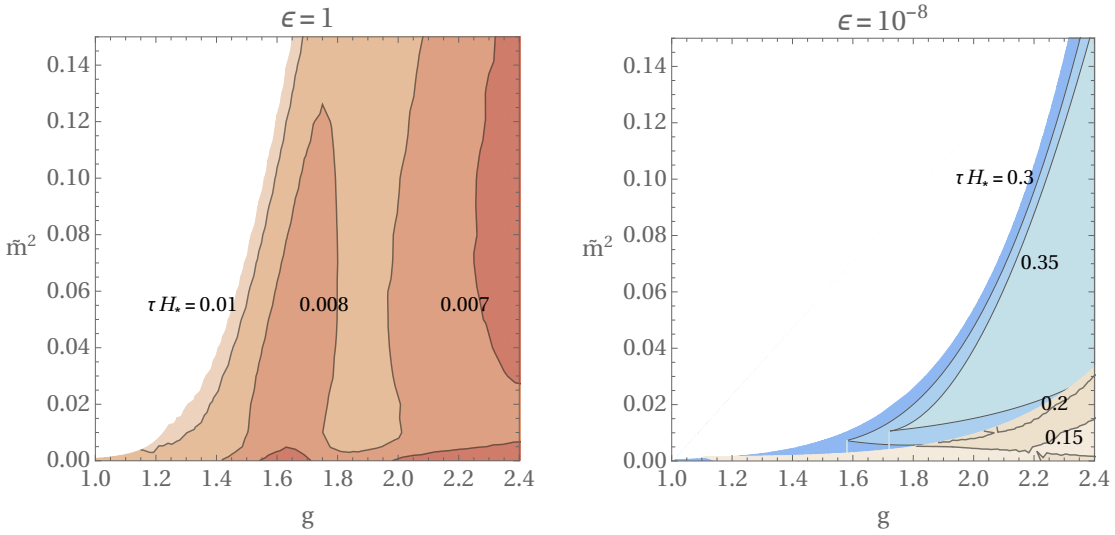

Fig. 6.5 *Contours of phase transition duration τ relative to the Hubble parameter for a hidden sector at the same temperature as the visible sector (left panel) where transitions happen via thermal fluctuations (red shading) and for a cold hidden sector (right panel) with $\varepsilon = 10^{-8}$ where most transitions happen via quantum tunnelling (blue shading).*

In Fig. 6.5 we plot the duration of the hidden sector phase transition as a function of the model's parameters, for $\varepsilon = 1$ and 10^{-8}. As expected the duration of a transition is $\sim H_*^{-1}$ up to a numerical factor $\lesssim 100$, regardless of whether the hidden sector is cold. The average bubble radius can also be calculated and is similarly parametrically given by H_*^{-1}, even if the hidden sector is cold (with a numerical factor $\sim 0.001 - 0.1$, as expected from [102]).

Despite having the same parametric dependence on H_*, there is a mild difference between the duration of a thermal and tunnelling transitions. In typical thermal transitions the critical action decreases fast once it first becomes small enough for a significant number of bubbles to form, and the transition usually completes within $\simeq 1/100$ of a Hubble

time.[12] Tunnelling transitions typically take slightly longer, leading to a slightly larger average bubble radius, since the nucleation rate is constant in this case. [13]

6.5 Bubble Wall Velocities in Hot and Cold Transitions

We now study the velocities of bubble walls in hidden sector models with thermal and tunnelling transitions where much of the analysis in Sec. 5.3 and Sec. 5.4 still applies. Specifically, we explore first order phase transitions of the hidden scalar field to a lower minimum of its potential meaning the ensuing bubbles that are nucleated are made up of this hidden scalar. Due to the vanishing coupling between the hidden sector and visible sector, the hidden scalar wall can only couple with the hidden sector plasma as it expands which results in a frictional pressure impeding the bubble walls expansion and transferring energy into the hidden plasma. Therefore the speed the walls reach is related to the proportion of the energy released by the hidden phase transition that is concentrated in the bubble walls compared to the proportion being dissipated into the surrounding hidden plasma. As we discuss in the next section, this has a significant effect on the spectrum of gravitational waves that is produced by a phase transition.

The leading order friction on the bubble walls is independent of γ_w when $\gamma_w \gg 1$ and arises from hidden states having different masses in the two phases. The total effective pressure on the bubble walls can be obtained by making the approximation

$$(\rho_{\rm vac} - \Delta P_{\rm LO}) \to \left(V_0(0) - V_0(\phi_{\rm min}) + \frac{T_h^2}{24} \sum_i m_i^2(0) - m_i^2(\phi_{\rm min}) \right) , \tag{6.22}$$

in Eq. (5.3), where $\phi_{\rm min}$ is the position of the true vacuum of the full finite temperature potential, and V_0 is the zero temperature potential. [14] In our example model the right hand side of Eq. (6.22) is

$$V_0(0) - V_0(\phi_{\rm min}) + \frac{T_h^2}{24} \sum_i m_i^2(0) - m_i^2(\phi_{\rm min}) = \frac{9g^4}{1024\pi^2} \frac{2-\tilde{m}^2}{4} w^4 - \frac{3g^2 w^2 T_h^2}{32} , \tag{6.23}$$

where we have consistently neglected the subleading contribution from ϕ itself, as in Sec. 5.5.3.

[12] The small non-monotonic dependence on g that is visible in Fig. 6.5 left is because exact dependence of S_3/T_h on time throughout the phase transition varies across the parameter space (e.g. transition might begin closer or further away from the minimum of S_3/T_h).

[13] For $\varepsilon = 10^{-8}$ thermal transitions are slightly slower than when ε is larger. This is because such transitions only just complete, and happens when S_3/T_h is close to its minimum and approximately temperature independent.

[14] More accurate expressions in terms of integrals over particle occupation numbers are given in [53].

Not surprisingly, the friction and driving forces in Eq. (6.22) depend only on the temperature of the hidden sector and its microscopic properties. Therefore, if a hidden sector goes through a thermal transition, the friction on the bubble walls is approximately independent of whether it is cold relative to the visible sector. There are only order 1 changes in the friction due to bubble nucleation becoming efficient at slightly different hidden sector temperatures, as a result of the larger value of the Hubble parameter at this time if the hidden sector is cold. We find that this source of friction leads to finite bubble wall speeds over some, but not all, of the parameter space of the model that we consider. The region with finite bubble walls speeds approximately coincides with those parts of Fig. 6.4 for which $\alpha \lesssim 0.5$, and the value of ε only changes the boundary of this region of parameter space slightly. [15]

As discussed in Sec. 5.3, there is a further source of friction that arises due to the splitting radiation that takes place when hidden gauge bosons gain mass across the wall. This next-to-leading order contribution to the friction depends on the γ_w factor and we take it to be [54]

$$\Delta P_{\rm NLO} \sim \gamma_{\rm w} g^3 w T_{\rm h}^3 \,, \tag{6.24}$$

6.6 Runaway Walls in Cold Hidden Sectors

Assuming we are not considering a very strong transition with a high degree of supercooling (Sec. 5.3) we expect most of the energy released during a thermal hidden sector phase transition to be transferred into the hidden plasma. This is because in thermal transitions the bubbles typically reach terminal velocity long before they collide so most of the energy in the wall is efficiently dumped into the hidden plasma. We now argue that, in contrast, tunnelling transitions can lead to the vast majority of the energy density going into bubble walls with a negligible proportion transferred to the plasma via friction. This is possible because the hidden sector can be arbitrarily cold compared to the scale that sets the driving force.

The hidden sector temperature at the time of a tunnelling transition is $T_{\rm h} = \varepsilon T_{\rm v} \simeq (\varepsilon g w)/\alpha^{1/4}$. Therefore the $\gamma_{\rm w}$ independent contribution to the friction Eq. (6.22) is suppressed by $T_{\rm h}^2 \simeq \varepsilon^2 g^2/\alpha^{1/2}$. For small ε, and not too small α, this does not transfer a significant fraction of the released energy to the plasma, and it is never sufficient to prevent the bubble walls running away. This is intuitively due to the low hidden sector temperature compared to the scale of the driving force $T_{\rm h} \ll w$ suppressing the number density of the hidden sector particles that the walls pass through, and also reducing the mismatch in the thermal distributions ahead of and behind the bubble walls.

[15] Other conditions for this source of friction to prevent bubble walls accelerating without bound have been given in the literature, sometimes differing slightly from Eq. (6.22). The small differences are of no consequence for our present work.

The γ_w dependent contribution to the friction has a different effect to the γ_w independent piece, since it grows arbitrarily large as the bubble walls gain speed. However, for a sufficiently cold hidden sector the bubble walls will not have reached sufficiently high speeds for this friction to become relevant before they collide. If they are still accelerating at the time of the collision, the friction will be suppressed by γ_*/γ_t where γ_* is the Lorentz factor of the bubble walls when they collide and γ_t is the value corresponding to the bubble wall's terminal velocity. Apart from models close to the boundary $\gamma_* = \gamma_t$, such a suppression is sufficient to prevent any significant energy transfer to the plasma. On the other hand, if the bubble walls reach their terminal velocity before colliding, at least an $\mathcal{O}(1)$ fraction of the released energy goes into the plasma, and if they reach terminal speeds long before they collide the vast majority of the energy goes into the plasma.

In the model that we consider the γ_w dependent frictional force is parametrically $n_h \gamma_w g^3 w$, and the driving force on the bubble walls per unit area is approximately $g^4 w^4$ (ignoring numerical factors). The terminal value of γ_w is therefore roughly

$$\gamma_t \simeq \frac{w^3}{n_h} \simeq \frac{w^3}{\varepsilon^3 T_{v*}^3} \simeq \frac{\alpha^{3/4}}{g^2 \varepsilon^3} \,. \tag{6.25}$$

As expected, the terminal velocity is large if ε is small and α is not too small.

We compare γ_t to what the wall's Lorentz factor would be in the absence of friction as a function of a bubble's radius, which we denote $\gamma_0(R)$. In the thin wall approximation, which is accurate up to order 1 factors in our model, this is simply

$$\gamma_0(R) \simeq \frac{R\rho_v}{\sigma} \simeq g^2 R w \,. \tag{6.26}$$

The typical bubble radius at the time of collisions R_* is to be set by the Hubble parameter at the time of transition

$$R_* \simeq 10^{-2} H_*^{-1} \simeq \alpha^{1/2} \frac{M_{Pl}}{g^2 w^2}. \tag{6.27}$$

As a result, the bubble walls are still accelerating at the time they collide if

$$\alpha^{1/2} \frac{M_{Pl}}{w} \lesssim \frac{\alpha^{3/4}}{g^2 \varepsilon^3} \,, \tag{6.28}$$

that is

$$\varepsilon < 10^{-6} \alpha^{1/12} \left(\frac{w}{\text{GeV}}\right)^{1/3} g^{-2/3} \,. \tag{6.29}$$

Thus a hidden sector must be extremely cold for the bubble walls to effectively runaway.

For a particular hidden sector, the energy density in the bubble walls when they collide is

$$\frac{\gamma_*}{\gamma_0} = \min\left[1, R_t/R_*\right] = \min\left[1, \frac{\alpha^{1/4}}{g^2 \varepsilon^3} \frac{w}{M_{Pl}}\right] \,, \tag{6.30}$$

where $\gamma_*/\gamma_0 = 1$ corresponds to runaway bubble walls. The proportion of the energy density released into the fluid is $\sim 1 - \gamma_*/\gamma_0$, which is negligible for runaway bubbles and $\simeq 1$ for bubbles that reach terminal velocity.

Chapter 7

Gravitational Waves from Cold Hidden Sectors

We now consider the gravitational wave spectra produced by first order transitions, in hot and cold hidden sectors. Rather than focusing exclusively on the particular SU(2) hidden sector that we have studied, we aim to study the effect of those features identified above that apply to large classes of hidden sectors.

Gravitational waves from phase transitions can be produced by different processes, and excellent reviews on the development of the literature can be found in [103–107]. Depending on the type of transition, and the dynamics of the bubble walls, the overall spectrum is made up of contributions from a subset of the following sources:

- **Colliding scalar field shells**. Depending on the nature of the phase transition, a significant fraction of the energy released can be concentrated in the bubble walls. When these collide they lead to quadrupole moments, which efficiently emit gravitational waves.

- **Acoustic waves in the plasma**. If a transition happens in a thermal bath, some of the energy in the wall will be deposited into the plasma via friction. This produces acoustic wave fronts in the plasma which, when they collide, can source gravitational waves.

- **Turbulence in the plasma**. After the acoustic sound shells collide, some portion of their energy is transferred into turbulent flows, which could act as a relatively long lasting source of gravitational waves.

- **Long lived field oscillations after collisions**. When bubble collision take place they can establish long lived oscillations of the field, which can emit gravitational waves.

The gravitational wave spectrum emitted by each of these sources can be studied using numerical simulations and theoretical models. Although both of these approaches have shortcomings, a reasonably good understanding of the expected signal from each source has been reached in the literature, as a function of the physical parameters of a transition. [1] For our present work, gravitational waves from bubble collisions and sound waves are the most important, while turbulence and long lived field oscillations give negligible contributions to the overall signal. We therefore focus on these effects, utilising standard parameterised fits to predict the signals produced. In Appendix C, we collect results from different parts of the literature that support this approach.

7.1 Bubble Collisions

The gravitational wave signal from colliding bubbles during a first order phase transition was first proposed in [108, 109] and was carefully studied in [110–112], where the 'envelope' approximation was developed. This approximates the gravitational waves from collisions as being sourced by an expanding infinitely thin bubble of stress energy, and neglects regions in which the bubbles have previously overlapped. In this context the thickness of a bubble wall is judged relative to e.g. bulk motions of any plasma present, and the thin wall assumption was shown to be valid for relatively strong transitions in [113]. [2] In cold hidden sectors the profile of the bubble walls is determined by $\alpha_{\rm h} = \frac{\rho_{\rm vac}}{\rho_{\rm h}}$ rather than $\alpha = \frac{\rho_{\rm vac}}{\rho_{\rm v}}$, where here, $\rho_{\rm vac}$, $\rho_{\rm h}$ and $\rho_{\rm v}$ are the vacuum energy released in the transition, the energy density in the hidden sector and the energy density in the visible sector respectively. Also, the thin wall assumption is valid for all the models that we consider.

Various predictions, both analytical [111, 114, 115] and numerical [116–118], have been made regarding the form of the frequency dependence of the gravitational wave spectrum emitted by bubble collisions. We use the fit of the gravitational wave power spectrum from bubble collisions given in [104]. After redshifting to the present day, this takes the form

$$\Omega_{\rm coll}(f) \equiv \frac{1}{\rho_{\rm crit}} \frac{d\rho_{\text{GW-coll}}}{d\ln f}, \tag{7.1}$$

where $\rho_{\rm crit}$ is the critical density of the Universe, and

$$h^2\Omega_{\rm coll}(f) = 1.67\times 10^{-5}\,\Delta \left(\frac{H_*}{\beta}\right)^2 \left(\frac{\kappa_{\rm col}\alpha}{1+\alpha}\right)^2 \left(\frac{100}{g_{\rm v*}}\right)^{\frac{1}{3}} S_{\rm env}(f) \tag{7.2}$$

[1] In this Sec., we denote the transition time by β, regardless of the type of transition (even though we previously defined β in Eq. (6.21) in a way that was only appropriate to particular classes of thermal transitions).

[2] This is a weaker condition than that involved in the thin walled approximation for calculating the critical bubble actions.

where $h \simeq 0.7$ is the dimensionless present day Hubble parameter. As before, $*$ indicates the value of a quantity at the time of the phase transition, and α is the ratio between the energy density released during the transition and the background radiation density in the visible sector defined in Eq. (6.1).

The remaining parameters in Eq. (7.2) are: $\kappa_{\rm col}$, which is the efficiency with which the vacuum energy released is deposited in the bubble wall; Δ, which is the amplitude of the gravitational wave signal in the limit $\kappa_{\rm col} \to 1$ and $\alpha \gg 1$; and $S_{\rm env}(f)$, which is the spectral shape, normalised to have maximum value 1.

Δ can be fitted by

$$\Delta = \frac{0.48 v_{\rm w}^3}{1 + 5.3 v_{\rm w}^2 + 5 v_{\rm w}^4} \,. \tag{7.3}$$

Using the envelope approximation, the peak energy density in gravitational waves from thin walled bubble collisions scales like $h^2\Omega_{env} \propto \kappa_{\rm col}^2$. The dependence of the peak energy density on $\kappa_{\rm col}$ in Eq. (7.2) can be derived in the envelope approximation, and is also supported by numerical simulation. The overall amplitude, i.e. the prefactor in Eq. (7.2), is set by theory [114] and agrees fairly well with simulations [116]. We can approximate

$$\kappa_{\rm col} \simeq \frac{\gamma_{\rm w}\sigma}{R_* \rho_{vac}} \,, \tag{7.4}$$

where σ is the surface tension of the wall and R_* is the average bubble separation length at collision, $R_* = v_{\rm w}\beta^{-1}$. This is precisely the quantity that we calculated when analysing the finite bubble wall speeds, leading to the result Eq. (6.30).

Finally, the frequency dependence of the gravitational wave spectrum $S_{\rm env}(f)$ takes the form (for $v_{\rm w}$ close to 1)

$$S_{\rm env}(f) = \left[c_l \left(\frac{f}{f_{\rm env}} \right)^{-3} + (1 - c_l - c_h) \left(\frac{f}{f_{\rm env}} \right)^{-1} + c_h \left(\frac{f}{f_{\rm env}} \right) \right]^{-1} \tag{7.5}$$

where fits to numerical simulations give rise to the values $c_l = 0.064$ and $c_h = 0.48$. We are assuming here that the high frequency tail drops like f^{-1}, which as discussed may not be precisely the case. The peak frequency f_* is given by

$$f_{\rm env} = 16.5\,\mu{\rm Hz} \left(\frac{f_*}{\beta} \right) \left(\frac{\beta}{H_*} \right) \left(\frac{T_{v*}}{100\,{\rm GeV}} \right) \left(\frac{g_*}{100} \right)^{\frac{1}{6}} \,, \tag{7.6}$$

which has a dependence on $v_{\rm w}$ via [3]

$$\frac{f_*}{\beta} = \frac{0.35}{1 + 0.069 v_{\rm w} + 0.69 v_{\rm w}^4} . \tag{7.7}$$

[3] This has a slightly different form to that adopted in [119] due to the fact they are using results from the earlier analysis of [116].

7.2 Sound Waves

If a significant proportion of the energy released by a phase transition is transferred to the plasma through friction, sound waves in the plasma form. These propagate through the primordial plasma either behind the wall, as deflagrations, or in front of it as detonations (hybrid regimes are also possible). As mentioned, the model that we consider is always in the supersonic detonation regime for both thermal and tunnelling transitions. The collision of these acoustic shells causes a stirring of the plasma, which provides a long lasting source of gravitational waves.

A combination of numerical simulations [120–122] and analytical models [123, 124] suggest that sound waves are an important source of gravitational waves if a significant fluid component exists. The spectrum obtained peaks at a wavelength approximately set by the average bubble separation at collision, R_*, and at high frequencies, the signal falls off $\propto f^{-3}$ for detonations, and it seems to be even steeper for deflagrations. This is in stark contrast to the shape of signals arising from phase transitions occurring in vacuum, which fall off in the range f^{-1} to $f^{-1.5}$ at high frequencies.

For our present work, we use the fit of the gravitational wave spectrum given in [104], based on the simulations in [122]. This is

$$h^2\Omega_{\rm sw}(f) = 8.5\times10^{-6}\left(\frac{100}{g_*}\right)^{\frac{1}{3}}\kappa_{\rm sw}^2(v_w,\alpha)\alpha^2\left(\frac{H_*}{\beta}\right)v_{\rm w}\,S_{\rm sw}(f)\,, \tag{7.8}$$

where the spectral shape is

$$S_{\rm sw}(f) = \left(\frac{f}{f_{\rm sw}}\right)^3\left(\frac{7}{4+3(f/f_{\rm sw})^2}\right)^{7/2}\,, \tag{7.9}$$

with approximate peak frequency

$$f_{\rm sw} = 8.9\,\mu{\rm Hz}\,\frac{1}{v_{\rm w}}\left(\frac{\beta}{H_*}\right)\left(\frac{T_{v*}}{100\,{\rm GeV}}\right)\left(\frac{g_*}{100}\right)^{\frac{1}{6}}\,, \tag{7.10}$$

and we have fixed the simulation derived factor $z_{\rm p}$ which appears in [122] to take what is estimated to be its usual value of 10.

The fit in Eq. (7.8) is based on simulations in which $v_{\rm w}$ is not too close to 1. However, in the model that we consider, $\gamma_{\rm w}$ is typically at least $\mathcal{O}(1)$ in thermal transitions since the bubble walls only reach a terminal velocity due to the loop suppressed $\gamma_{\rm w}$ dependent friction. Meanwhile, in tunnelling transitions the terminal value of $\gamma_{\rm w}$ can be huge and the sound wave contribution to the gravitational wave spectrum is only significant if this is reached. This difference in dynamical regimes introduces some unavoidable uncertainty into our analysis. Directly studying systems with extremely large $\gamma_{\rm w}$ appears impossible in

simulations, however further theoretical developments might be possible and such progress could potentially be combined with extrapolations of results from simulations. [4]

The parameter $\kappa_{\rm sw}$ in Eq. (7.8) is the proportion of the vacuum energy transferred to kinetic energy in the plasma. If the bubble walls reach a constant velocity, $\kappa_{\rm sw}$ can be determined from a hydrodynamical analysis of the wall and plasma system. Since this depends only on the properties of the hidden sector, we can adapt results calculated for visible sector phase transitions [55], and if $v_{\rm w} \simeq 1$

$$\kappa_{\rm sw} \simeq \frac{\alpha_{\rm h}}{0.73 + 0.083\sqrt{\alpha_{\rm h}} + \alpha_{\rm h}} \ . \tag{7.11}$$

In the model we consider α_h is typically ~ 1 in thermal transitions, which corresponds to efficient conversion to kinetic energy in the plasma and little energy going into directly heating it. In tunnelling transitions, α_h is $\gg 1$, so if the bubble walls reach a terminal velocity long before colliding then $\kappa_{\rm sw}$ is basically 1. As argued, if the bubble walls are still accelerating when they collide, the energy transfer to the plasma is negligible and we can simply set $\kappa_{\rm sw} = 0$. In the intermediate regime for which the bubble walls reach a terminal velocity not long before colliding, we can estimate

$$\kappa_{\rm sw} = 1 - \gamma_*/\gamma_0 \ , \tag{7.12}$$

which also takes the correct values in the other regimes.

7.3 Gravitational Wave Signals

We are now ready to study the gravitational wave signal produced by a particular phase transition, and analyse its detectability in future experiments [101, 125–129]. To do this we use the standard sensitivity curves corresponding to the noise power spectral density (see [130]) which are widely used in the phase transition literature.

First we note that the amplitude of a gravitational wave signal is strongly suppressed if $\alpha \ll 1$, regardless of which source dominates, and only models with relatively large α have a chance of being observed. In Sec. 6.4 we saw that $\beta/H_* \sim 10$ in tunnelling transitions and $\beta/H_* \sim 10$ – 100 in thermal transitions, regardless of whether the hidden sector is cold or at the same temperature as the visible sector. Combined with Eqs. (7.6) and (7.10), this means that a signal's peak frequency is always parameterically set by the Hubble parameter at the time of the transition. Tunnelling transitions usually have a slightly smaller peak frequency than thermal transitions for a given value of the Hubble parameter, due to having smaller β/H_*. However, there are likely to exist models with

[4] We also note that the amplitude of the fit that we use differs from that in [101], which was based on earlier simulations.

thermal transitions for which $\beta/H_* \simeq 10$ as well, for example due to a nucleation rate that is only weakly temperature dependent, so this is not a sharp prediction.

In thermal transitions $\alpha \simeq \varepsilon^3 \alpha_h$, where $0.1 \gtrsim \alpha_h \gtrsim 10$ in typical models (c.f. Eq. (6.19)). As discussed in Sec. 6.5, the bubble wall velocity is always finite in thermal transitions in the model that we consider, so the vast majority of the energy is transferred to the plasma. The gravitational wave spectrum is therefore dominantly produced by sound waves, and has a high frequncy fall off $\propto f^{-3}$. The amplitude of the gravitational wave signal produced by bubble collisions is suppressed by

$$\kappa_{\rm col} \simeq \gamma_w \sigma/(R_* \rho_{\rm vac}) \,, \tag{7.13}$$

and is negligible as expected.

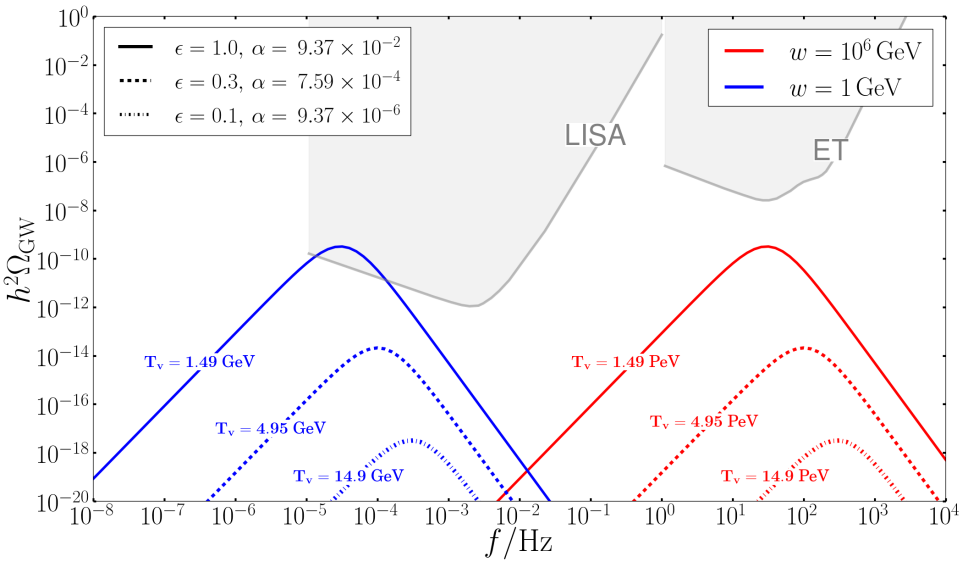

Fig. 7.1 *Example gravitational wave spectra from thermal transitions in the model described in Sec. 5.5.3. Results are shown for different hidden and visible sector temperature ratios ε, and scales w which determine the hidden sector temperature that the transition occurs at. We fix $g = 2$, and adjust $\tilde{m}^2$ such that $\alpha_h = 1$ remains fixed. As ε decreases, the thermal energy in the visible sector is increasingly greater than the energy released by the phase transition. Thus with decreasing ε the amplitude of the gravitational wave spectrum becomes heavily supressed and rapidly moves out of sensitivity of any upcoming searches. Somewhat larger values of $\alpha_h \lesssim 50$ are possible in some parts of parameter space, which would increase the detection possibilities slightly.*

In Fig. 7.1 we plot example spectra from thermal transitions with different values of ε, and fixed $\alpha_h = 1$ (so that α varies). We see that, in this frequency range, observable signals are only possible in such models for $\varepsilon \simeq 1$, corresponding to a hidden sector at almost the same temperature as the visible sector prior to the transition. The closeness of the hidden

and visible sector temperatures required for a detectable signal is slightly relaxed for larger α_h, and values $\alpha_h \simeq 50$ are possible in parts of the hidden sector parameter space that we consider, corresponding to significant super cooling. However, the minimum ε that leads to an observable signal only scales approximately as $\propto \alpha_h^{1/3}$, so sectors with parametrically small ε remain unobservable even in this case.

Unlike in thermal transitions, the gravitational wave signal from a tunnelling transition can be dominated either by emission from sound waves or from bubbles collisions, depending on whether the bubble walls reach a terminal velocity, or not, respectively. The boundary between the two regimes is determined by Eq. (6.30), via the factors κ_{col} and κ_{sw} in Eqs. (7.4) and (7.12) (we study the change in spectral shape moving between these two regimes shortly). Regardless of which dominates, the amplitude of the signal is again strongly suppressed if $\alpha \ll 1$.

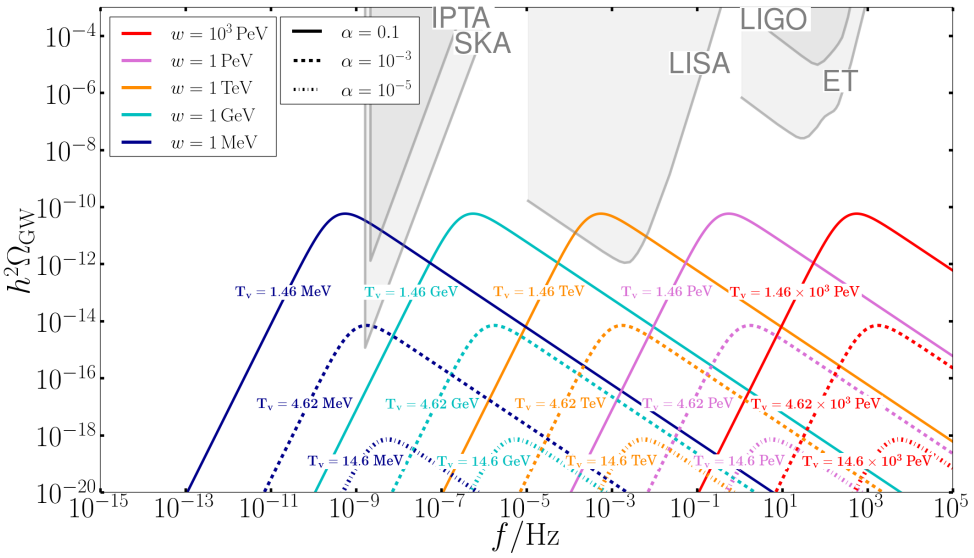

Fig. 7.2 *Examples of the gravitational wave spectra emitted by tunnelling transitions in the absence of friction (due to the hidden sector being extremely cold, with $\varepsilon \approx 0$). We show results for different values of the relative energy released by the transition compared to that in the visible sector: α, as well as for different hidden sector scales w, and we fix $g = 2$. For a fixed α the scale w determines the visible sector temperature at the time of the transition. In such models the bubbles walls runaway and gravitational waves are dominantly produced by the collision of bubbles. A signal is only observable for models in which α is relatively large.*

In Fig. 7.2 we show the GW spectrum from a tunnelling transition in the absence of any hidden sector thermal bath, i.e. if $\varepsilon = 0$, for different values of α. This corresponds to all the released energy going into the bubble walls, and the signal from a model with any ε that is significantly less than the boundary value between effective runaway and

terminal wall velocities will also look almost identical. It can be seen that only transitions for which $\alpha \gtrsim 10^{-4}$ have a chance of being detected in currently proposed experiments, and this is also the case for tunnelling transitions with larger ε for which the signal comes dominantly from sound waves. In tunnelling transitions α varies from $\sim \varepsilon^3$ to ~ 1, with a roughly logarithmic distribution of models in this range, so detectable signals only occur in relatively small parts of parameter space.

The amplitude of a gravitational wave signal from a phase transition in a sector at the same temperature as the visible sector can easily vary by orders of magnitude across different models. For example, a transition with relatively small bubble walls speeds, significantly below the speed of light, will produce a strongly suppressed signal. Hence, observation of a signal with a small amplitude would not be sufficient to claim discovery of a sector that is not thermalised with the visible sector. Similarly the peak frequency of the gravitational wave signal from a sector at the same temperature as the visible sector can be adjusted by altering the scale of the hidden sector. This flexibility in the signals from thermalised sectors seems unpromising for discriminating between thermalised and non-thermalised hidden sectors. However, we now describe two possibilities that might provide an insight into the source of a gravitational wave signal, were one to be discovered.

7.3.1 Runaway vs non-runaway transitions

The high frequency fall off of a measured gravitational wave spectrum could give a clear indication that it arose from a transition in which the bubble walls runaway with negligible energy transfer to the plasma, rather than a transition in which a significant proportion of the released energy is transferred to the plasma. The spectrum emitted by the former will have a fall off $\propto f^{-1} - f^{-1.5}$ since it is dominantly produced by bubble collisions (allowing for the uncertainty between simulations and theoretical predictions), which is significantly different to the $\propto f^{-3}$ fall off in transitions with finite bubble wall speeds. [5]

A transition with negligible energy transfer to the plasma can arise in a cold hidden sector that goes through a tunnelling transition at a time when the number density of the hidden sector thermal bath is sufficiently small (see Sec. 6.6).

[5] As mentioned previously, we assume that the contribution from turbulence is sub-leading.

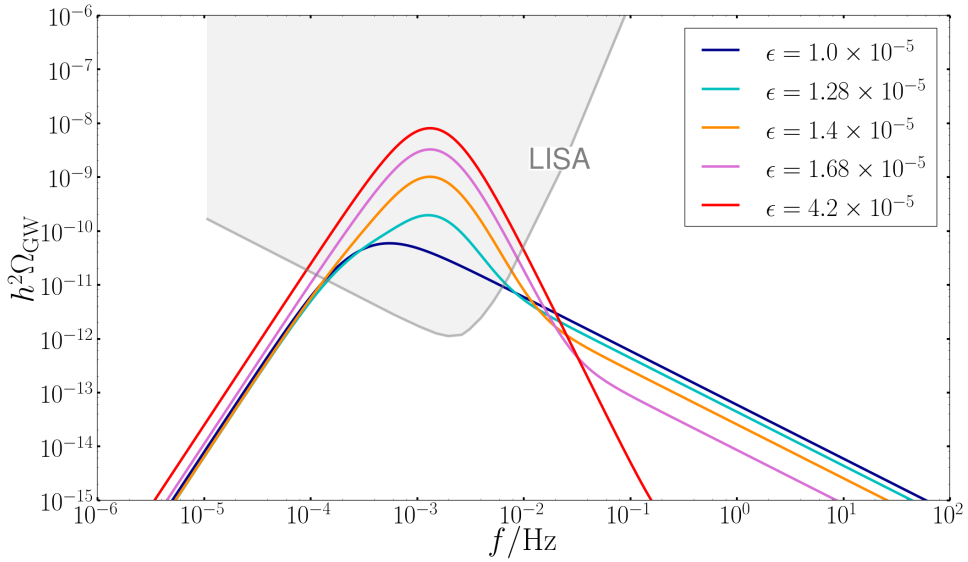

Fig. 7.3 *The gravitational wave spectrum emitted by tunnelling transitions for different values of the hidden sector temperature (via different ε). We fix the visible sector temperature at the time of transition $T_{v*} = 1461$ GeV, $w = 10^3$ GeV, $\alpha = 0.1$, and $g = 2$ across the different spectra. As ε is increased from 1×10^{-5} to 4.2×10^{-5}, the hidden sector temperature at the transition increases, so the friction on the bubble walls increases. For $\varepsilon \gtrsim 1.2 \times 10^{-5}$, the bubble walls reach a terminal velocity before they collide, and the gravitational wave spectrum goes from being dominated by bubble collisions (with a $\propto f^{-1}$ high frequency fall off) to being dominated by sound waves (with a $\propto f^{-3}$ fall off).*

In Fig. 7.3 we show the change in the gravitation wave spectrum emitted by a tunnelling transition in the hidden sector that we consider, for different values of ε. As ε increases, the friction grows and the bubble walls reach their terminal velocity prior to collisions. The fast drop in $\kappa_{\rm col}$ after ε passes the boundary between regimes, Eq. (6.29), results in a sharp transition in the signal's shape. [6]

As discussed, it is unclear if runaway bubbles are possible in thermal transitions in models without gauge bosons. Even if this can occur, at least $\simeq 10\%$ of the released energy is transferred to the plasma through the γ_w independent friction in typical models. The amplitude of the gravitational wave signal from sound waves Eq. (7.8) appears to be larger than that from bubble collisions, fit by Eq. (7.2), in the limit $v_w \simeq 1$, and the peak frequencies of the signals from sound waves and bubble collisions differ by a factor $\simeq 2$. Therefore, it seems plausible that a sound wave contribution could usually be distinguished in most such cases. It would be interesting to study the shape of the spectra produced in

[6] These results are calculated using fits from simulations with much smaller values of γ_w than will occur in the regime plotted, which introduces some uncertainty. However, based on theoretical models, we still expect a significantly less steep fall off of the spectrum in a bubble dominated collision.

this case in more detail, especially if further results from large scale numerical simulations become available. [7]

This difference in gravitational wave spectral shape between a runaway tunnelling, and a non-runaway tunnelling or non-runaway thermal transition could be experimentally distinguished, provided that the signal is detected over a reasonably wide frequency range. Although it may not be possible to exclude a runaway thermal transition that is completely dominated by bubble walls, the unusual model building requirements for this to arise mean that detection of such a spectral shape would still be extremely interesting. From Fig. 7.3 we see that a f^{-1} fall off, which would be enough to show that emission from bubble walls dominates, could be observed at e.g. LISA if α is close to $\mathcal{O}(1)$. Discovery of a signal would also prompt further targeted experimental investigation with increased sensitivity, which would allow for more detailed analysis of the frequency dependence of the spectrum.

7.3.2 Phase transitions around BBN

Another potentially observable possibility is that a thermal transition in a hidden sector that is slightly colder than the visible sector, or a tunnelling transition, could lead to a detectable gravitational wave signal in a frequency range that is not possible from a hidden sector at the same temperature as the visible sector, due to cosmological constraints. [8]

The constraint on the effective number of relativistic degrees of freedom in the hidden sector at the time of BBN, Eq. (B.20), means that a phase transition at a temperature $T_{v*} \lesssim 10$ MeV is not possible in a hidden sector at the same temperature as the visible sector. The corresponding peak frequencies of gravitational wave spectra emitted at around such temperatures are (assuming sound wave domination, and $v_w \simeq 1$)

$$f_{sw} = 6.1 \times 10^{-8}\ \text{Hz} \left(\frac{\beta/H_*}{100}\right) \left(\frac{T_{v*}}{10\ \text{MeV}}\right) , \tag{7.14}$$

where β/H_* is typically 50 – 100, but might plausibly be as small as 10 in some models. As discussed in Sec. 6.1.2 transitions $T_{v*} \gtrsim 10$ MeV are possible in hidden sectors at the same temperature as the visible sector, although the parameter space is quite strongly constrained unless the transition is at a much higher temperature $T_{v*} \gg 10$ MeV.

In contrast, a cold hidden sector can have a transition at any visible sector temperature, and therefore emit gravitational waves with any peak frequency. It needs only satisfy

[7] Additionally, an intermediate f^{-1} dependence could arise in transitions with v_w close to the speed of sound [122], confirming the need for careful analysis of the spectral shape after initial discovery for models to be discriminated.

[8] This has also been carefully considered in [119], which was posted on the arXiv as we were preparing our manuscript. Our results are compatible with theirs, and the reader is refereed there for an alternative very nice discussion of this possibility.

the constraints, outlined in Sec. 6.1.2, on its energy density ($\varepsilon < 0.2$ and $\alpha < 0.015$) and contain light hidden sector states that avoid the universe being over closed, none of which restrict the allowed time of a transition. [9]

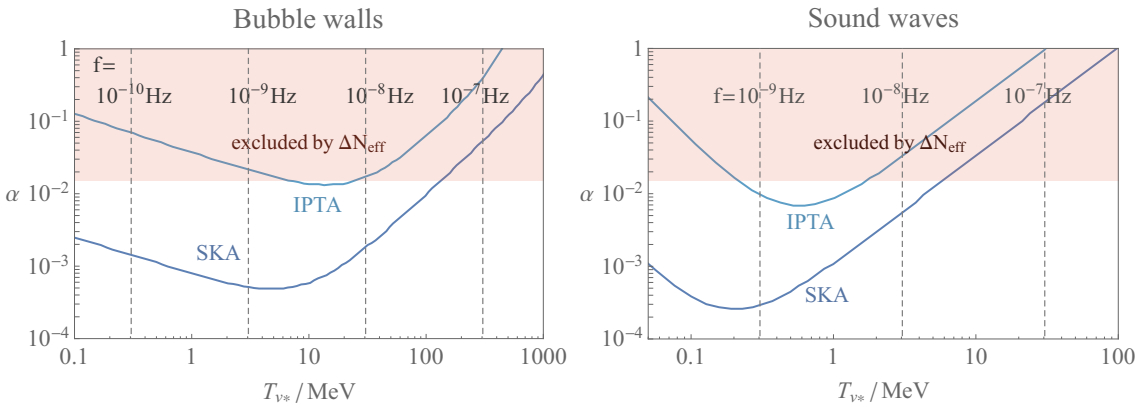

Fig. 7.4 *The minimum value of α that leads to a gravitational wave signals that can be detected at SKA and IPTA as a function of the visible sector temperature at the time of the transition T_{v*}. Results are shown for runaway bubble walls in an effective vacuum with $\beta/H_* = 10$ (left) and sound waves from a phase transition that is strong (but without runaway bubble walls) with $\beta/H_* = 100$ (right). The corresponding peak frequencies of the emitted gravitational wave signal are also indicated. We assume the hidden sector states decay to light hidden sector states, and the effects of these on the number of relativistic degrees of freedom constrains $\alpha < 0.015$. Once parameterised in terms of β/H_*, α, and T_{v*} the results are independent of the particular hidden sector considered. Constraints from BBN mean we do not expect to see a signal from a hidden sector at the same temperature as the visible sector for $T_{v*} \lesssim 10$ MeV, which means that a signal with a peak frequency $\lesssim 10^{-9}$ Hz would be a strong indication of a signal originating in a cold hidden sector (even allowing for freedom in β/H_*).*

In Fig. 7.4 we plot the minimum values of α that could be detected in the upcoming experiments IPTA and SKA, for runaway tunnelling transitions and non-runaway thermal transitions with $v_w \simeq 1$. The results are shown as a function of the visible sector temperature at the time of the transition, and the corresponding peak frequencies of the signals are also given. For our purposes a model is detectible if any part of its gravitational wave spectrum crosses the sensitivity curve of an experiment.

In these plots we assume $\beta/H_* = 10$ and $\beta/H_* = 100$ for the tunnelling and thermal cases respectively, although the results are not too sensitive to these choices. We also show the constraint on α from CMB observations, assuming that all of the energy released by the phase transition ends up in light hidden sector states (the previously mentioned model dependent opening up of the allowed values of α at $T_{v*} \gtrsim 10$ MeV is not shown).

[9] We impose the slightly stronger constraints on ε and α from the CMB rather than BBN so that the light hidden sector states can definitely evade the relic abundance bound, however the difference is only small.

Although the hidden sector that we have studied provides an example of a model that can lead to the signals we consider here, the results in Fig. 7.4 are general to any cold sector, once its phase transition is parameterised in terms of α and β/H_* (and the dominant source of gravitational waves is determined).

We see that there are significant regions of parameter space in which a cold hidden sector has a phase transition at a visible sector temperature $T_{\mathrm{v}*} \lesssim 10$ MeV that leads to a gravitational wave signal that is detectable at SKA, without being excluded by cosmological constraints. There is also a small region of parameter space in which the same is true of IPTA. In these parts of parameter space the peak frequencies of the gravitational wave signals are in the range $\lesssim 10^{-9}$ Hz and $\lesssim 10^{-8}$ Hz for runaway bubbles and sound waves respectively.

There is no sharp lower bound on the peak frequency of a gravitational wave signal from a hidden sector at the same temperature as the visible sector, since there is some freedom in the value of β/H_*, and the fit Eq. (7.9) may not be precisely correct for all transitions. However, it seems extremely unlikely that such a sector would produce a signal with a peak frequency $\lesssim 10^{-9}$ Hz.

As a result, the discovery of a signal with a sufficiently small peak frequency would be a strong sign of the existence of a cold hidden sector that was out of thermal equilibrium with the visible sector. The first observation of a signal is likely to be through integration over frequencies, which might not be sufficient to exclude the possibility that the observed signal is the low frequency tail of a spectrum peaked at higher frequencies. However, with further observation, combined with much more careful analysis of experimental uncertainties than we attempt, the location of the spectrum's peak could be reliably determined.

Chapter 8

Gravitational Waves from Helical MHD Turbulence

In this chapter we study in detail the epoch following the phase transition during which we expect magnetohydrodynamic (MHD) turbulence to be generated in the primordial plasma from which a significant emission of Graviational Waves could take place. In particular we focus on the case where there is some initial magnetic helicity in the plasma immediately after the transition and see how this can boost the gravitational wave signal compared to the case where there is no helicity present. As we will see, this scenario could leave an imprint on the stochastic gravitational wave background (SGWB) in the form of a circular polarisation that could be detectable by the up-coming LISA experiment. [1]

The subject of helical MHD turbulence in the primordial plasma from a first order phase transition has been extensively discussed in the literature [15, 131–133] and is often looked at in the context of its impact on any potential primordial magnetic field [15, 134, 135] as studied in detail in Chapter 9. However, more recently some effort has been put into understanding the potential effects it could have on the period of GW generation expected after a first-order phase transition and whether this could be imprinted on the GW spectrum [136–142].

The turbulent regime develops over time after the phase transition due to a system of eddy currents that are first generated at the scale of the bubble radius, R_*, and subsequently extend over a range of both larger and smaller length scales. This network of eddies allows for plasma and magnetic energy, both initially concentrated at the scale R_*, to be spread throughout the MHD system in a 'cascade' of energy, as discussed in [143]. Once MHD turbulence has fully developed at a given scale it decays freely, and we expect equipartition between the plasma and magnetic energy densities, $\rho_M \sim \rho_K \sim \rho_{\rm eq}$.

[1] Only future experiments with one or more triangular sets of interferometers, such as LISA, would be sensitive to polarisation in the SGWB [14], as discussed further in Appendix D.

As we discuss further in Sec. 8.4, the behaviour of the turbulence can be dramatically changed if the initial magnetic field left over after the phase transition has a non-zero helical component [144]. In this scenario the non-helical component of the field gets dissipated away leaving a fully helical field that induces an inverse cascade in the turbulence where energy is transferred to increasingly larger scales resulting in an increase in the fields strength and correlation length of the field. This process could result in a significant boost to any potential gravitational wave signal and could even result in emission of circularly polarised GW, a manifestation of the helicity imprinted on the signal.

Such initial magnetic helicity could be generated via a variety of mechanisms including bubble collisions at the electroweak [145, 146] or QCD [147, 148] phase transitions, baryon-number-violating processes such as decaying non-perturbative field configurations, e.g. electroweak sphalerons [149], or even via inflation [150]. We do not discuss further the possible origin of this helical turbulence, but parametrise it by the initial helicity fraction of the magnetic field left over after the transition, ζ_*.

8.1 Sourcing Gravitational Waves and Computing the Spectrum

We consider statistically homogeneous and isotropic turbulence, which sources GW lasting for a limited time $\tau_T < H_*^{-1}$, so that the expansion of the universe may be ignored during the period in which the gravitational radiation is produced. Furthermore, following [151, 152], we make the additional simplifying assumption that direct cascade MHD turbulence decaying on a time scale $\tau_{\rm direct}$ is equivalent to stationary turbulence with duration $\tau_{\rm direct}/2$, as justified by the argument for unmagnetised turbulence in [153]. For the inverse cascade period we also consider stationary turbulence [152], but this time with a scale-dependent duration time as outlined in Sec. 8.4. There has been some debate in the literature [139, 151] regarding the extent to which assuming a stationary source is a valid simplification. [2] However, whilst such an approximation has limitations, it is currently the only available model that has a complete treatment of helicity and inverse cascade turbulence, and hence the potential polarisation signal. Thus, our results may be considered as a demonstration of principle, which may be used as a prototype for other, more sophisticated calculations. We expect that our results will be refined as many unknowns in the simulation and modelling of turbulence are clarified.

As shown in [151], in order to find the total GW energy density at a point in space and time we integrate over a spherical shell centered at that point that contains all GW

[2] This debate is especially relevant in the case of direct cascade turbulence where no attempt has been made to account for the decay of the source by considering scale dependent turbulence, in contrast to inverse cascade tubulence.

sources with a light-like distance from such an observer. The thickness of the shell would then correspond to the duration of the phase transition, and its radius would correspond to the proper distance between observer and source along a light-like trajectory. Following [151, 152] we can estimate the ensuing GW signal strength with $\pm 25\%$ accuracy by working in the aero-acoustic approximation ($\mathbf{k} \to 0$). Using our premise that the source is homogeneous and isotropic and making the aforementioned simplifying assumption that the source is stationary, the integral for the total GW energy density finally simplifies to

$$\rho_{\rm GW}(\omega_*) = \frac{d\rho_{\rm GW}}{d\ln\omega_*} = 16\pi^3\omega_*^3 G{\rm w}^2\tau_T H_{ijij}(0,\omega_*)\,, \tag{8.1}$$

where $\omega_* = \omega(t_*)$ is the angular frequency measured at the time of the phase transition and w is the enthalpy density.[3] The scalar quantity $H_{ijij}(0,\omega_*)$ is the double trace of the four-dimensional power spectrum of the energy density tensor describing stationary turbulence in the $\mathbf{k} \to 0$ approximation [152]. The quantity H_{ijij} controls both the peak frequency and shape of the resulting GW signal, and its functional form varies depending on whether one is considering direct cascade or inverse cascade turbulence, as we outline in the following sections.

In order to calculate the spectrum of GW radiation measured today, we redshift Eq. (8.1) to now and normalise it to the critical energy density required to make the universe flat ($k=0$), namely $\rho_c = 3H_0^2/(8\pi G)$, defining the fraction of energy density in GWs today as

$$\Omega_{\rm GW,0} = \left(\frac{a_*}{a_0}\right)^4 \frac{\rho_{\rm GW,*}}{\rho_{c,0}} = \left(\frac{a_*}{a_0}\right)\frac{128\pi^4}{3H_0^2}\omega^3 G^2{\rm w}^2\sum\nolimits_{m=1,2}\tau_T^{(\text{stage } m)}H_{ijij}^{(\text{stage } m)}(0,\omega_*)\,, \tag{8.2}$$

where $\omega = (a_*/a_0)\omega_*$, the enthalpy density ${\rm w} = 4\rho_*/3 = 2\pi^2 g_* T_*^4/45$, $H_*^2 = 8\pi G\rho_*/3 = 8\pi^3 G g_* T_*^4/90$ and $m = 1,2$ corresponding to the direct and inverse cascade stages of the turbulent epoch respectively. Rearranging this relation, we obtain $G^2{\rm w}^2 = H_*^4/4\pi^2$, and substituting this back into the Eq. (8.2) we get

$$\begin{aligned}\Omega_{\rm GW,0} &= \left(\frac{a_*}{a_0}\right)\frac{32\pi^2}{3H_0^2}\omega^3 H_*^4\sum\nolimits_{m=1,2}\tau_T^{(\text{stage } m)}H_{ijij}^{(\text{stage } m)}(0,\omega_*) \\ &= \left(\frac{a_*}{a_0}\right)\frac{1\times 10^{37}}{{\rm Hz}^2}\omega^3 H_*^4\sum\nolimits_{m=1,2}\tau_T^{(\text{stage } m)}H_{ijij}^{(\text{stage } m)}(0,\omega_*)\,,\end{aligned} \tag{8.3}$$

where we have used $H_0 = h_0 \times 100\,{\rm km\,sec^{-1}\,Mpc^{-1}}$ with $h_0 = 0.67$ [154].

[3] This definition of w is in contrast to previous chapters where it was defined as the vacuum expectation value of the field studied.

8.2 Our Stationary Direct Cascade Model

Collisions of bubbles at the end of the phase transition cause stirring of the primordial plasma on scales close to the average radius R_* of the bubbles. In order to compute the characteristic velocity of such turbulent motions at the beginning of the turbulent period, we first identify two distinct forms in which the liberated vacuum energy, typically quantified by $\alpha = \rho_{\rm vac}/\rho_{\rm rad}$, is initially deposited. We express these forms quantitatively via GW efficiency factors κ_i equivalent to those described in Chapter 7.

First, a fraction of the available vacuum energy goes into accelerating the bubble wall, which is expressed using the GW efficiency factor $\kappa_{\rm col}$. This fraction should generally be subtracted from the total energy subsequently deposited into the plasma. However, we will be dealing with transitions that are not strong enough to produce the runaway scenario described in Sec. 5.4, meaning that the bubble walls will reach a terminal velocity long before collision due to the high friction on them from the surrounding plasma. Therefore, it is valid to assume that essentially all the energy is transferred to the plasma, so that $\alpha_{\rm eff} = \alpha\,(1-\kappa_{\rm col}) \approx \alpha$ [64].

The vacuum energy deposited into the plasma can either be transferred into bulk fluid motion that sources GWs or can be used in heating up the plasma itself. Thus, as is common in the literature and we also employed in Sec. 7.2, we finally express the fraction of vacuum energy in our GW source as the fraction transferred into fluid motion [55, 64, 101]:

$$\kappa_{\rm sw} = \frac{\alpha}{0.73 + 0.083\sqrt{\alpha} + \alpha}\,, \tag{8.4}$$

where we have assumed for simplicity that the speed of expansion of the walls is relatively fast, with $v_w \approx 1$. We can then express the RMS fluid velocity as [121, 143]

$$U_f = \sqrt{\frac{3}{4}\frac{\alpha}{1+\alpha}\kappa_{\rm sw}}\,. \tag{8.5}$$

Given that we only consider scenarios where the sound wave period is relatively short, we can assume that not much energy in the plasma is lost and make the approximation that all the energy left in the bulk fluid motion when the flow becomes nonlinear is converted into vortical turbulent motions of the plasma, $\kappa_{\rm turb} \approx \kappa_{\rm sw}$ [64]. We also assume that the characteristic velocity of the plasma at the beginning of the turbulent period is as shown in Eq. (8.5).

This initial vortical fluid motion drives the formation of a hierarchy of eddy currents, first on scales around the bubble radius and subsequently on scales $\lambda \leq R_*$. This is known as the 'direct energy cascade'. We parameterise the turbulent system with the quantity $\xi_M(t)$, known as the magnetic correlation length which describes the maximum scale at which the magnetic field is correlated and thus physically represents the size of the largest

magnetic eddy. During the direct cascade period energy is transferred from the initial correlation scale of the turbulence $\xi_M(t_*) \simeq R_*$, to increasingly smaller scales until it is viscously dissipated as heat at the dissipation scale of the plasma, λ_d.

The distribution of magnetic and plasma energy at different scales in a direct cascade is known to follow a Kolmogorov decay law $\rho_{*,i}(\lambda, t_*) \approx \rho_{*,i}\lambda^{-2/3}$ where $i = K, M$ for kinetic and magnetic components, respectively [138, 152]. We assume that this direct cascade period of turbulence lasts for a few times longer than the characteristic turn-over time of the largest eddy, $\tau_0 = R_*/U_f$, so that the hierarchy of eddy currents have time to equilibrate. [4] Thus the duration of this stage of turbulence is $\tau_{\rm direct} = s_0\tau_0$, where in this work we make the representative choice $s_0 = 3$ [152].

In the case of direct cascade turbulence, the quantity H_{ijij} from Eq. (8.2) takes the form [152]

$$H_{ijij}^{(\text{stage 1})}(0,\omega) \approx \frac{7C_k^2\varepsilon}{6\pi^{3/2}}\int_{k_0}^{k_d}\frac{dk}{k^6}\exp\left(-\frac{\omega^2}{\varepsilon^{2/3}k^{4/3}}\right)\text{erfc}\left(-\frac{\omega}{\varepsilon^{1/3}k^{2/3}}\right), \tag{8.6}$$

where $\varepsilon = k_0U_f^3 = k_0M^3$ is the energy dissipation rate per unit enthalpy, $M = U_f < 1$ is the turbulent Mach number and C_k is a constant that is $\mathcal{O}(1)$. We assume that in the above integral $k_0 \ll k_d$, where k_0 is the wavenumber associated with the average bubble radius that sets the characteristic scale of the turbulence, and k_d is the wavenumber associated with the scale at which the turbulence is dissipated by viscosity. As we are considering MHD turbulence, we take the prefactor of Eq. (8.6) as $7/6$, after doubling the result for pure hydrodynamic turbulence given in [151] to account for approximate equipartition between the magnetic and kinetic energy components. The integral (Eq. (8.6)) for direct cascade turbulence is dominated by large-scale contributions at wavenumbers close to k_0, corresponding to the average bubble radius and, as such, we expect the GW signal for this stage of turbulence to peak at frequencies close to this scale.

After normalising Eq. (8.6), we can express the peak frequency of the GW signal due to direct cascade turbulence at the time of the transition as

$$f_{\text{peak},*} = 1.48M/R_*\,, \tag{8.7}$$

which after red-shifting gives a peak frequency today of

$$f_{\text{peak},0} = \frac{a_*}{a_0}f_{\text{peak},*} = 2.45\times10^{-5}\,\text{Hz}\left(\frac{T_*}{100\,\text{GeV}}\right)\left(\frac{g_*}{100}\right)^{1/6}\frac{M}{R_*H_*}\,, \tag{8.8}$$

[4] The eddy turn-over time is defined as the time it takes for an eddy at a given plasma scale to complete one full revolution.

where we have used the relation

$$\frac{a_*}{a_0} \approx 8 \times 10^{-16} \left(\frac{100\text{GeV}}{T_*}\right) \left(\frac{100}{g_*}\right)^{1/3} . \tag{8.9}$$

The peak amplitude of the direct cascade GW signal can then be written as

$$\Omega_{\text{GW},0}^{(\text{stage 1})} = 7.357 \times 10^{-6} \left(\frac{100}{g_*}\right)^{1/3} (R_* H_*) \big(\tau_T H_*\big) C_k^2 M^6 , \tag{8.10}$$

where $\tau_T H_* \leq 1$ is the duration of the Stage 1 direct cascade turbulence normalised to the Hubble time, $R_* H_*$ is the average bubble radius at percolation normalised to the Hubble radius, M is the Mach number and C_k is a constant of order unity.

The $\tau_T H_*$ factor in Eq. (8.10) tells us that, as expected, the longer lasting the period of direct cascade turbulence the larger the abundance of GW emitted during this direct cascade stage. The average bubble size $R_* H_* < 1$ sets the characteristic length scale of the problem, and thereby controls the peak frequency of the GW spectrum arising from direct cascade turbulence, as seen in Eq. (8.8). A larger bubble radius $R_* H_*$ also implies fewer bubbles per Hubble horizon, which in turn means a higher energy concentration as the bubbles convert vacuum energy from their volume into the walls. After the bubble collisions this results in a more inhomogeneous energy distribution centred around the scale R_*, and thus a higher abundance of GWs as exhibited by the factor $\propto R_* H_*$ seen in (8.10).

8.3 Alternative Direct Cascade Models

Several other models for approximating the GW signal from direct cascade turbulence have been proposed in the literature. Generalising Eq. (8.7), they may be characterised by the peak frequency at the time of the phase transition:

$$f_{\text{peak},*} = \frac{A}{R_*} , \tag{8.11}$$

which is redshifted to the following generalisation of (8.8) today,

$$f_{\text{peak},0} = B\,\text{Hz} \, \frac{T_*}{100\text{GeV}} \left(\frac{g_*}{100}\right)^{\frac{1}{6}} \frac{1}{R_* H_*} , \tag{8.12}$$

where A and B are constants that depend on the way the turbulent GW source is modelled. They take the following values in some commonly-used source models:

- The stationary approximation discussed above yields $A = 1.48M$, $B = 2.45 \times 10^{-5} M$, and the spectra shown as black curves in Figs. 8.1 & 8.2 below;

- The top-hat approximation yields $A = 5.1$, $B = 8.46 \times 10^{-5}$ (see Eq. (85) of [139]), and the spectra shown as dark grey curves in Figs. 8.1 & 8.2 below;
- The coherent approximation yields $A = 0.586$, $B = 9.728 \times 10^{-6}$ (see Eq. (80) of [139]);
- The incoherent approximation yields $A = 8.64$, $B = 1.43 \times 10^{-4}$ (see Eq. (76) of [139]).

In the LISA phase transitions working group review paper [101], which we use for our analysis of gravitational waves from hidden sectors in Chapter 7, the main source of GW signal from plasma flow is associated with sound waves. Repeating the details of this model here, the GW spectrum for this source is [155, 122, 123, 121]

$$h^2\Omega_{\rm sw,0} = 0.9 \times 10^{-6} \, (R_* H_*) \, (\tau_{\rm sw} H_*) \left(\frac{\kappa_{\rm sw} \alpha}{1+\alpha} \right)^2 \left(\frac{100}{g_*} \right)^{\frac{1}{3}} S_{\rm sw}(f) \,, \tag{8.13}$$

where $\kappa_{\rm sw}$ is the efficiency with which vacuum energy is transformed into bulk motion of the fluid (and can be easily expressed for fast bubble walls, see Eq. (8.4)), and the spectral shape is

$$S_{\rm sw}(f) = (f/f_{sw})^3 \left(\frac{7}{4+3(f/f_{sw})^2} \right)^{7/2} . \tag{8.14}$$

Finally, there is an additional suppression factor that depends on fluid velocity (see Eq. (8.5))

$$\tau_{\rm sw} H_* = \min \left(1, \frac{R_* H_*}{U_f} \right) , \tag{8.15}$$

which is associated with the time at which shocks develop in the flow [122], and is much less than one for most models [59, 64, 143, 156]. The peak frequency of the sound wave source at the time of the phase transition reads

$$f_{\rm sw,*} = \frac{3.38}{R_*} \tag{8.16}$$

which becomes

$$f_{\rm sw,0} = 5.61 \times 10^{-5} \, {\rm Hz} \, \frac{T_*}{100 {\rm GeV}} \left(\frac{g_*}{100} \right)^{\frac{1}{6}} \frac{1}{R_* H_*} \tag{8.17}$$

when redshifted to the present day. This contribution provides the light grey curves in Figs. 8.1 & 8.2 below.

In order to model the GWs sourced from turbulence, Ref. [101] used the top-hat approximation to estimate the signal (dark grey curves in Figs. 8.1 & 8.2) for reasons outlined in [139]. Assuming Kolmogorov-type turbulence, they calculate the associated

GW spectrum arising from this model to be

$$h^2\Omega_{\rm turb,0} = 1.14\times10^{-4}\,(R_*H_*)\left(\frac{\kappa_{\rm sw}\alpha}{1+\alpha}\right)^{\frac{3}{2}}\left(\frac{100}{g_*}\right)^{\frac{1}{3}} S_{\rm turb}(f)\,, \tag{8.18}$$

where v_w is the wall velocity, [5] R_*H_* is the amplitude suppression factor discussed in the previous section and we have also used $\kappa_{\rm sw}$ as the efficiency for conversion of the latent heat released during the phase transition into MHD turbulence. This comes from our optimistic assumption that when the flow becomes non-linear and the sound wave period ends, the remaining energy is readily converted into turbulence. Given that we discuss scenarios in which the sound wave period lasts a relatively short time, very little energy is lost and we expect this to be a reasonable approximation. However, in principle there can be an extra damping factor due to, for example, loss of sound wave energy into reheating the plasma. The corresponding spectral shape is

$$S_{\rm turb}(f) = \frac{(f/f_{\rm turb})^3}{[1+(f/f_{\rm turb})]^{\frac{11}{3}}(1+8\pi f/h_*)}\,, \tag{8.19}$$

where

$$h_* = 16.5\times10^{-6}\,{\rm Hz}\left(\frac{T_*}{100{\rm GeV}}\right)\left(\frac{g_*}{100}\right)^{1/6} \tag{8.20}$$

is the inverse Hubble time at GW production redshifted to today. This contribution provides the dark grey curves in Figs. 8.1 & 8.2 below.

8.4 Modelling Inverse Cascade Turbulence

We expect helicity to be conserved in a highly conductive plasma. Thus, if there is some initial helicity left over in the magnetic field after the phase transition, which we parameterise with the initial magnetic helicity fraction ζ_* as defined in [152], we expect it to be approximately conserved during the direct cascade period of turbulence. After this stage the turbulence, with the plasma and the magnetic field both in equipartition, relaxes to a fully helical state, since the non-helical turbulent energy is fully dissipated away at small scales in contrast to the conserved helical component [143].

This results in a second period of 'inverse cascade' turbulence following the direct cascade stage, during which the remaining fully helical turbulence can only be transferred to scales that are increasingly larger than the bubble radius. For large enough initial helicity fractions, this can result in a rapid increase in the magnetic correlation length of

[5] We assume $v_w \sim 1$ in this work.

the turbulence, $\xi_M(t)$, which corresponds physically to a large increase in the size of the largest eddy, compared with the direct cascade period.

Adopting Model B outlined in detail in [152] and originally based on the work of [157, 158], we take the following evolution law for the magnetic eddy correlation scale

$$\xi_M(t) \simeq R_* \left(1 + \frac{t}{\tau_1}\right)^{2/3}, \tag{8.21}$$

where $\tau_1 \simeq R_*/v_1 = \tau_0/\zeta_*^{1/2}$ is the characteristic eddy turn-over time of the largest eddy at the beginning of the inverse cascade stage, $v_1 \simeq \zeta_*^{1/2} U_f$ is the associated characteristic plasma velocity, and we have used the relation $R_* = \tau_0 U_f$. Furthermore, the evolution of the magnetic and kinetic energy densities are given by

$$\begin{aligned} \rho_M(t) &\simeq \mathrm{w} b_1^2 \left(1 + \frac{t}{\tau_1}\right)^{-2/3}, \\ \rho_K(t) &\simeq \mathrm{w} v_1^2 \left(1 + \frac{t}{\tau_1}\right)^{-2/3}, \end{aligned} \tag{8.22}$$

where $v_1 \simeq \zeta_*^{1/2} U_f$ and $b_1 \simeq \zeta_*^{1/2} b_0$ are, respectively, characteristic velocity and magnetic field perturbations at the beginning of the inverse cascade stage, and $v_1 \simeq b_1$ due to equipartition of the two components. The turnover time at the correlation scale of the turbulence (τ_ξ) and the inverse cascade timescale ($\tau_{\rm inverse}$) then evolve as

$$\tau_\xi \simeq \tau_{\rm inverse} \simeq \frac{\xi_M(t)}{v_k(t)} = \tau_1 \left(1 + \frac{t}{\tau_1}\right), \tag{8.23}$$

where we have used that $v_k(t) \propto v_1 (1 + \frac{t}{\tau_1})^{-1/3}$ from Eq. (8.22). Putting Eq. (8.21) together with Eq. (8.23), we obtain the time when turbulence exists on the scale $\xi_M(t)$ as

$$\tau_{\rm inverse} \simeq \tau_1 \left(\frac{\xi_M(t)}{R_*}\right)^{3/2} = \tau_1 \left(\frac{k_0}{k_\xi(t)}\right)^{3/2}, \tag{8.24}$$

where the wavenumber of the largest eddy is defined as $k_\xi(t) \equiv 2\pi/\xi_M(t)$.

Based on the approach used in [159], we compute the GW output during the inverse cascade period by adopting a stationary turbulence model wherein, rather than considering freely-decaying turbulence, we consider stationary turbulence with a duration time that depends on the scale, k, being considered, i.e.,

$$\tau_{\rm inverse}(k) \approx \tau_1 \left(\frac{k_0}{k}\right)^{3/2}. \tag{8.25}$$

Thus we can express the turn-over time associated with the largest scale, k_s, when the inverse casade stops as

$$\tau_s \approx \tau_1 \left(\frac{k_0}{k_s}\right)^{3/2}. \tag{8.26}$$

In the absence of any effective mechanisms for dissipating the turbulence at the largest scales, an inverse cascade can cause the correlation length of the magnetic field to increase greatly during this period, limited only by the Hubble expansion of the universe. Thus, the inverse cascade stops either at a scale, λ_s, when the correlation length of the turbulence reaches the Hubble radius,

$$\lambda_s \leq H_*^{-1}, \tag{8.27}$$

or the inverse cascade stops after a time, τ_s, when the turn-over time of the largest eddy reaches the expansion timescale,

$$\tau_s = \tau_1 \left(\frac{k_0}{k_s}\right)^{3/2} = \frac{\lambda_s^{3/2}}{U_f \zeta_*^{1/2} R_*^{1/2}} \leq H_*^{-1}. \tag{8.28}$$

Since $R_* H_*$, U_f and ζ_* are all less than unity, we see that the inequality Eq. (8.28) gives a stronger condition than (8.27). Thus we obtain an expression for the scale at which the inverse cascade stops by saturating the inequality

$$\frac{\lambda_s}{R_*} \leq \left(\frac{U_f}{R_* H_*}\right)^{2/3} \zeta_*^{1/3}. \tag{8.29}$$

For the period of freely-decaying inverse cascade MHD turbulence we adopt the 'Model B' introduced in Sec. 8.4 and outlined in [152]. [6] The form of the $H_{ijij}(0,\omega)$ quantity from Eq. (8.2) that is associated with the inverse cascade period is then expressed as

$$H_{ijij}^{(\text{stage 2})}(0,\omega) \approx \frac{7 C_1^2 M^3 \zeta_*^{3/2}}{6\pi^{3/2} k_0^{3/2}} \int_{k_s}^{k_0} \frac{dk}{k^{7/2}} \exp\left(-\frac{\omega^2 k_0}{\zeta_* M^2 k^3}\right) \text{erfc}\left(-\frac{\omega k_0^{1/2}}{\zeta_*^{1/2} M k^{3/2}}\right), \tag{8.30}$$

where ζ_* is the fraction of magnetic helicity left over at the end of the phase transition, and C_1 is a $\mathcal{O}(1)$ constant that links the magnetic energy and helicity densities with their respective power spectra.

In contrast to the direct cascade, the length scale providing the largest contribution to the $H_{ijij}^{(\text{stage 2})}(0,\omega)$ quantity used to calculate the GW signal arising from the inverse cascade period of turbulence is model-independent, being simply set by the Hubble scale. This is because the majority of the turbulent energy is found around the Hubble scale at the end of the inverse cascade before it is dissipated due to the expansion of the universe

[6] If we had used the 'Model A' also outlined in [152], which was originally based on the work of [160, 161], we would have found the same peak frequency but a mild suppression of the GW peak amplitude.

as outlined in Sec. 8.4. Taking the value of the Hubble parameter at the phase transition and red-shifting it to today, we find that the characteristic frequency of the inverse cascade GW spectrum today is

$$f_{\text{horizon},0} = 1.65 \times 10^{-5}\,\text{Hz} \left(\frac{T_*}{100\text{GeV}}\right)\left(\frac{g_*}{100}\right)^{1/6}. \tag{8.31}$$

As we will see in the examples in the next section, at this frequency the power-law of abundance of GWs changes from $\Omega_{\text{GW}} \propto f^3$ as expected beyond the horizon scale [162] to a flatter plateau composed of contributions from both the direct cascade turbulence and the helicity fraction dependent inverse cascade turbulence. The size of the plateau depends on the magnitude of the helicity fraction: for small ζ_* the signal briefly levels off before reverting to its original $\Omega_{\text{GW}} \propto f^3$ growth rate; whilst for sufficiently large ζ_* the plateau continues all the way up to the scale associated with the bubble size at the transition (see Eq. (8.12)).

8.5 Graviational Wave Spectra

Fig. 8.1 and Fig. 8.2 compare our calculated GW spectra (black) for representative choices of the model parameters α, R_* and T_* with the LISA [101] and AEDGE [163] sensitivity curves (shown in orange and green, respectively). The value of M is not an independent quantity, being related to the magnitude of α (see Eq. (8.5)). Our calculations are for four values of the helicity fraction $\zeta_* = 0.05$ (solid), 0.1 (dashed), 0.5 (dash-dotted) and 1 (dotted).

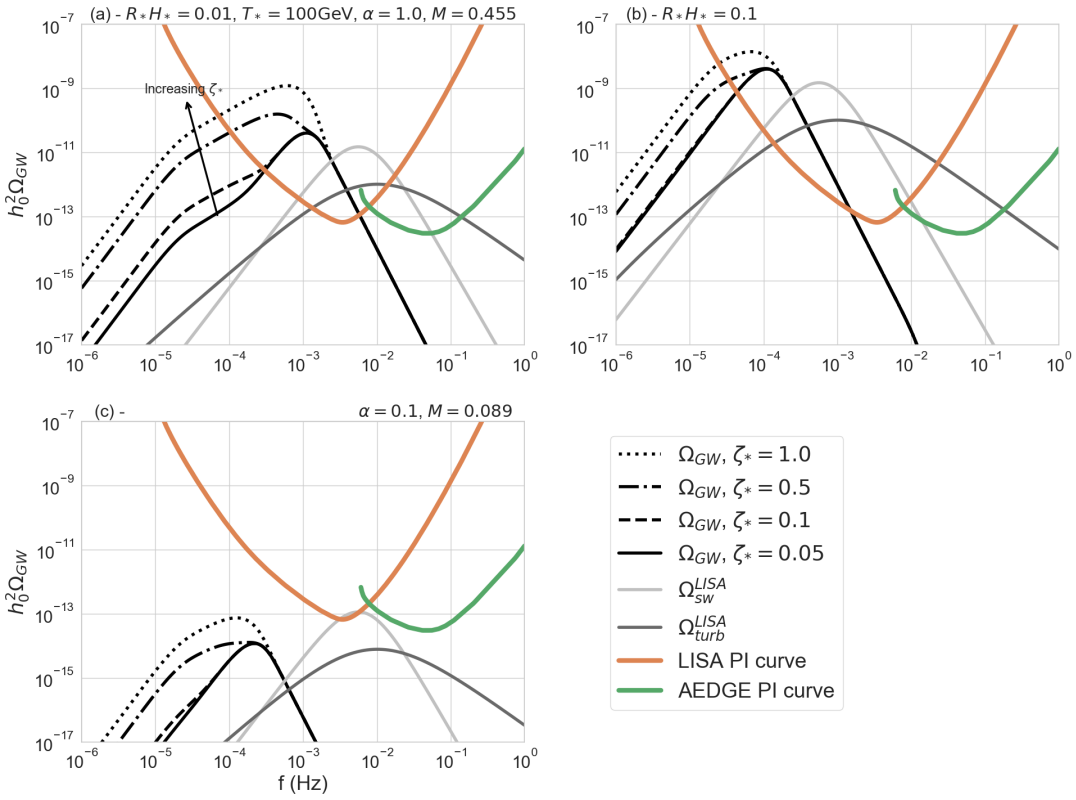

Fig. 8.1 *Calculations of GW spectra for fixed $T_* = 100$ GeV and $\zeta_* = 0.05$ (solid black), 0.1 (dashed black), 0.5 (dash-dotted black) and 1.0 (dotted black), compared with the spectra from sound waves (light grey) and turbulence (dark grey) taken from [101]. R_*H_* increases from left to right and α decreases from top to bottom. The parameter values are the same as in panel (a) unless specified. The power-law integrated LISA [101] (orange) and AEDGE [163] (green) sensitivity to the total SGWB spectrum, each for a 4-year integration time.*

Fig. 8.1 shows comparisons for fixed $T_* = 100$ GeV and different choices of the parameters α (going down) and R_*H_* (going across), describing the strength of the first-order transition and the bubble size R_* respectively. We recall that α sets the value of the turbulent Mach number M through Eq. (8.5). The value of M affects the peak frequency

and amplitude of the direct cascade GW signal through Eq. (8.8) & Eq. (8.10), respectively, whilst the characteristic amplitude of the inverse cascade GW signal is given by Eq. (8.30).

Fig. 8.1(a) shows that, as ζ_* increases, the size of the low-frequency plateau in the GW spectrum arising from the inverse cascade period of turbulence, which was discussed in Sec. 8.4, also increases. Indeed, for large enough ζ_* where the contribution to the GW spectrum from the inverse cascade period is sufficiently sizeable, the plateau transitions into a distinct new peak at a frequency slightly below the frequency of the direct cascade peak. Similar features are seen in Fig. 8.1(b) and 8.1(c).

Comparing Fig. 8.1(a) with Fig. 8.1(b), we see that decreasing the value of $R_*H_* \leq 1$ both suppresses the amplitude of the GW signal and pushes it to higher frequencies. This is to be expected from the analysis in Sec. 8.2. Furthermore, we see that the relative contribution of the low-frequency inverse cascade turbulence to the overall GW amplitude decreases with increasing R_*H_*, because for larger values of R_* the inverse cascade turbulence has less time to develop before being washed out by the Hubble expansion.

Comparing Fig. 8.1(a) with Fig. 8.1(c) where the value of α (and thus the value of M) has been decreased, we see that for smaller values of α the peak frequency of the GW spectrum is shifted to lower frequencies and the amplitude is suppressed.

Comparing our predictions with the top-hat approximation favoured in the LISA phase transitions working group review paper [101] (dark grey curves), we see that the peak frequencies are closer for larger α (and M). The heights of our peaks increase with ζ_* and are generally higher than the top-hat peaks for $\alpha = 1.0$, but lower for $\alpha = 0.1$. Both our calculations and the top-hat approximation for the choices $\alpha = 1.0$ and $R_*H_* = 0.01$ (Fig. 8.1(a)) and 0.1 (Fig. 8.1(b)) yield spectra peaking well within the sensitivity of LISA, whereas for $\alpha = 0.1$ and $R_*H_* = 0.01$ (Fig. 1(c)) both peaks lie below the LISA sensitivity.

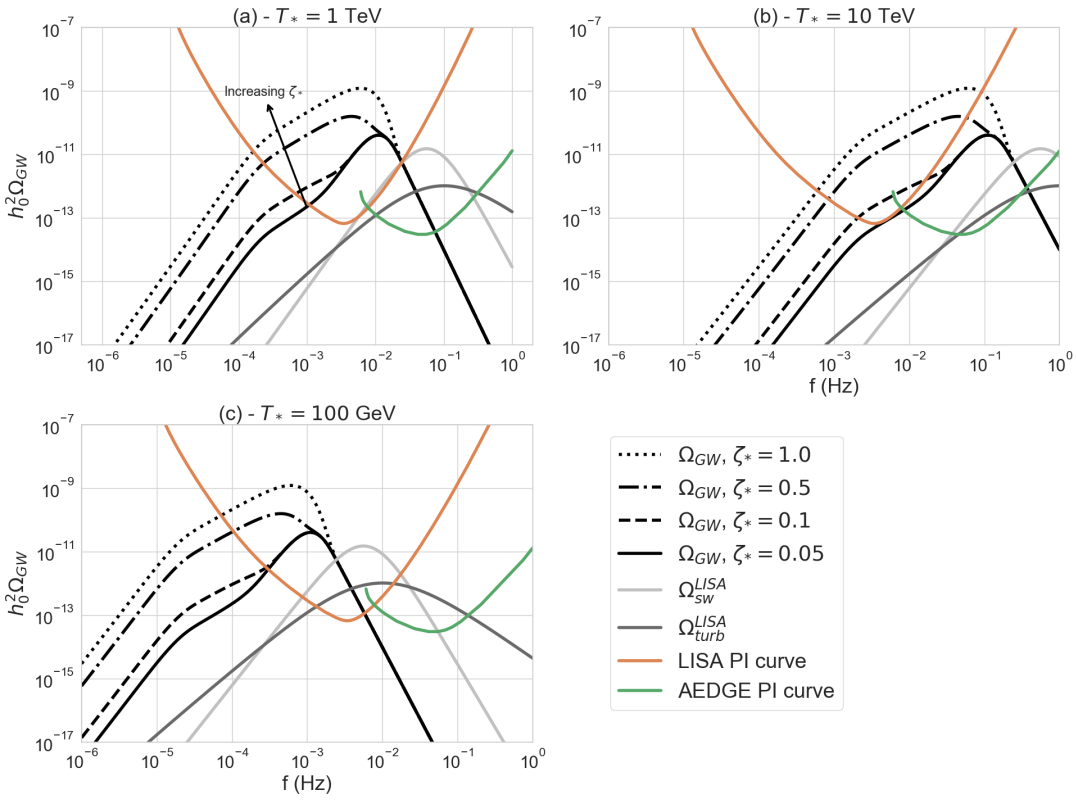

Fig. 8.2 *Similar to Fig 8.1 but for fixed $\alpha = 1.0$, $R_*H_* = 0.01$ and varying T_*, which increases from left to right and decreases from top to bottom.*

In Fig. 8.2 we display comparisons similar to Fig. 8.1, but now fixing $\alpha = 1.0$ and $R_*H_* = 0.01$ and choosing different transition temperatures T_*. (Fig. 8.1(a) is repeated here as panel (c)). The peaks of the calculated spectra shift to larger frequencies for larger T_*. We can see from Fig. 8.2(a) that our calculations for $T_* = 1$ TeV peak within the LISA [101] sensitivity, whereas the peak of the top-hat calculation peaks within the AEDGE [163] sensitivity. Fig. 8.2(b) shows that for $T_* = 10$ TeV our peak reaches within the AEDGE sensitivity, whereas the peak of the top-hat calculation peaks at higher frequency.

Our calculations indicate that LISA and AEDGE have complementary capabilities to detect the SGWB from a first-order phase transition, with the higher frequency range of AEDGE extending the detectable range of T_* to higher values.

8.6 Circular Polarisation of the Stochastic Gravitational Wave Background

One of the most interesting scientific targets for upcoming gravitational-wave (GW) detectors is the stochastic gravitational-wave background (SGWB) [106, 164]. This

SGWB could come from many sources including primordial inflation [165] astrophysical sources [166] and of course strong phase transitions in the early Universe [108, 139, 167].

The most easily measurable characteristic of a SGWB is its frequency spectrum, but this provides limited insight into its origin. Further valuable information could be provided by its intrinsic circular polarisation, which is due to a difference between the amplitudes of GWs with left and right polarisations. A SGWB generated by astrophysical sources would have negligible net polarisation, since it arises from multiple uncorrelated sources. However, a cosmological SGWB could be generated coherently over large scales, and might exhibit net circular polarisation if interactions that violate parity were important in the early Universe. Indeed, polarisation of the SGWB could in principle arise from a variety of physical mechanisms in the early Universe, for example gravitational chirality and modifications of gravity at high energies [168–170], pseudoscalar-like couplings between the inflaton and gauge fields [171–173] and helical turbulence created during a first-order phase transition [140, 174]. Thus the polarisation of the SGWB could be an important diagnostic tool for probing fundamental physical processes in the early Universe.

For the purpose of our work we are particularly interested in assessing the detectability of a potential net circular polarisation of the SGWB arising from helical MHD turbulence after a first-order phase transition, following on from work in [140, 151, 152].

8.6.1 Detecting polarised gravitational wave signals

The circular polarisation of a GW signal is given by [140, 174]

$$\mathscr{P}_{\rm GW}(k) = \frac{\langle h^{+\star}(\mathbf{k})h^{+}(\mathbf{k}') - h^{-\star}(\mathbf{k})h^{-}(\mathbf{k}')\rangle}{\langle h^{+\star}(\mathbf{k})h^{+}(\mathbf{k}') + h^{-\star}(\mathbf{k})h^{-}(\mathbf{k}')\rangle} = \frac{\mathscr{I}_A(K)}{\mathscr{I}_S(K)}\,, \tag{8.32}$$

where h^+ and h^- are the states corresponding to right- and left-handed circularly polarised GWs, and $K = k/k_0$ is a wavenumber normalised to the wavenumber associated with the bubble radius at collision, k_0. The explicit calculation of the polarisation of the GW spectrum using Eq. (8.33) is only required for the direct cascade period of turbulence where $\zeta_* < 1$. For the GW spectrum emitted during the inverse cascade period, on the other hand, we simply assume that the emitted GW spectrum is fully polarised, on the premise that $\zeta_* \simeq 1$ at the beginning of the inverse cascade stage.

In the particular case of helical turbulence the relevant functions can be approximated as [140]

$$\begin{aligned}
\mathscr{I}_S(K) &\simeq \int dP_1\, P_1 \int dP_2\, P_2\, \bar{\Theta}\left[\left(1+\gamma_p^2\right)\left(1+\beta_p^2\right) P_1^{n_S} P_2^{n_S} + 4h^2\gamma_p\beta_p P_1^{n_A} P_2^{n_A}\right]\,, \\
\mathscr{I}_A(K) &\simeq 2h \int dP_1\, P_1 \int dP_2\, P_2\, \bar{\Theta}\left[\left(1+\gamma_p^2\right)\beta_p P_1^{n_S} P_2^{n_A} + \left(1+\beta_p^2\right)\gamma_p P_1^{n_A} P_2^{n_s}\right]\,,
\end{aligned} \tag{8.33}$$

where

$$\gamma_p = \frac{K^2 + P_1^2 - P_2^2}{2KP_1}, \qquad \beta_p = \frac{K^2 + P_2^2 - P_1^2}{2KP_2}, \tag{8.34}$$
$$\bar{\Theta} = \theta\left(P_1 + P_2 - K\right)\theta\left(P_1 + K - P_2\right)\theta\left(P_2 + K - P_1\right),$$

and θ is the Heaviside step function. The parameter h is the fraction of helicity dissipation as defined in [140], which is related to the magnetic helicity fraction. Indeed, these two parameters coincide in the helical Kolmogorov turbulence model: $\zeta_* \simeq h$ [140]. Following the approach in [140], which seeks to generalise the polarisation degree calculation for helical hydrodynamic turbulence given in [174] to the case of helical MHD turbulence, in this paper we determine the polarisation degree of the direct cascade period by modelling the source as stationary [7] and using the symmetric and helical spectral indices, $n_S = -11/3$ and $n_A = -14/3$, consistent with a helical Kolmogorov spectrum. [8] We take the integration limits in Eq. (8.33) to range from 1 to k_d/k_0, and simply discard scales larger than the bubble radius, i.e., $k < k_0$, which are only relevant to the inverse cascade period of turbulence.

Using $\Omega_{\rm GW}(k) \propto k^5 \langle h(k)^2 \rangle$, we can rearrange Eq. (8.32) to obtain

$$\Omega_{\rm GW}(k)\,\mathscr{P}_{\rm GW}(k) = \Omega^{+}_{\rm GW}(k) - \Omega^{-}_{\rm GW}(k), \tag{8.35}$$

where $\Omega_{\rm GW}(k) = \Omega^{+}_{\rm GW}(k) + \Omega^{-}_{\rm GW}(k)$. Then, for the helical turbulence model we consider in this work, we have

$$\Omega^{+}_{\rm GW}(k) = \frac{1 + \mathscr{P}^{\text{stage 1}}_{\rm GW}(k)}{2}\Omega_{\text{stage 1}}(k) + \Omega_{\text{stage 2}}(k),$$
$$\Omega^{-}_{\rm GW}(k) = \frac{1 - \mathscr{P}^{\text{stage 1}}_{\rm GW}(k)}{2}\Omega_{\text{stage 1}}(k), \tag{8.36}$$

where we have assumed $\mathscr{P}^{\text{stage 2}}_{\rm GW}(k) \approx 1$, on the basis that by the beginning of the second stage $\zeta_* \approx 1$ and we are in a regime of strong helical turbulence that can be well approximated by a helicity transfer spectrum [140, 174] where $\mathscr{P}_{\rm GW}(k) \approx 1$ across the range of k relevant to inverse cascade turbulence. In the large wave-number limit where this approximation could no longer hold, the contribution of Stage 2 to the GW abundance is negligible.

[7] Debate regarding the validity of modelling the direct cascade source as stationary is of less importance when the helicity fraction is large given our results shown later demonstrate that in this regime the inverse cascade spectrum, which attempts to account for the turbulent decay through scale dependent decorrelation, dominates the overall signal.

[8] If the helicity fraction is large, strong helical turbulence modelling [174] could be more appropriate, and would result in a larger helicity fraction from the first stage of turbulence. However, as we demonstrate later and have explicitly checked for all our results, the contribution from the second stage of turbulence is always clearly dominant in the case of a large helicity fraction, and for simplicity we use here the Kolmogorov spectrum also for the first stage.

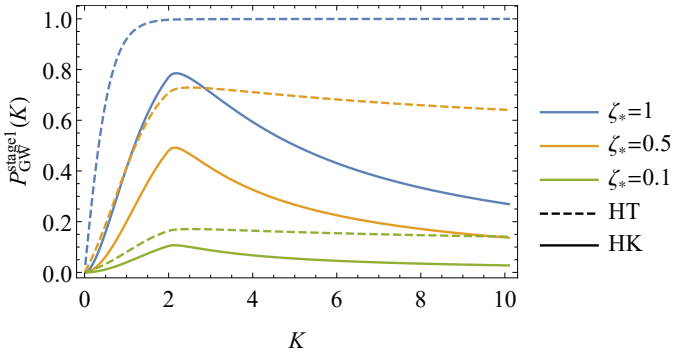

Fig. 8.3 *Degree of polarisation of Stage 1 direct cascade GWs as a function of the normalised wavenumber $K = k/k_0$, assuming indicated values of the helicity dissipation parameter h. Value of h coincides with initial magnetic helicity fraction ζ_* for helical Kolmogorov turbulence (HK) model considered in this paper (solid lines). We also show the polarisation fraction for Stage 1 turbulence driven by the Helicity Transfer (HT) model (dashed lines) whose use may be more appropriate in the large helicity regime.*

In Fig. 8.3 we plot the degree of polarisation of GWs emitted during Stage 1 direct cascade turbulence. We see that $\mathscr{P}_{\rm GW}^{\rm stage\ 1}$ reaches a peak at $K \sim 2$, whose height increases with $h = \zeta_*$, and then falls for larger K.

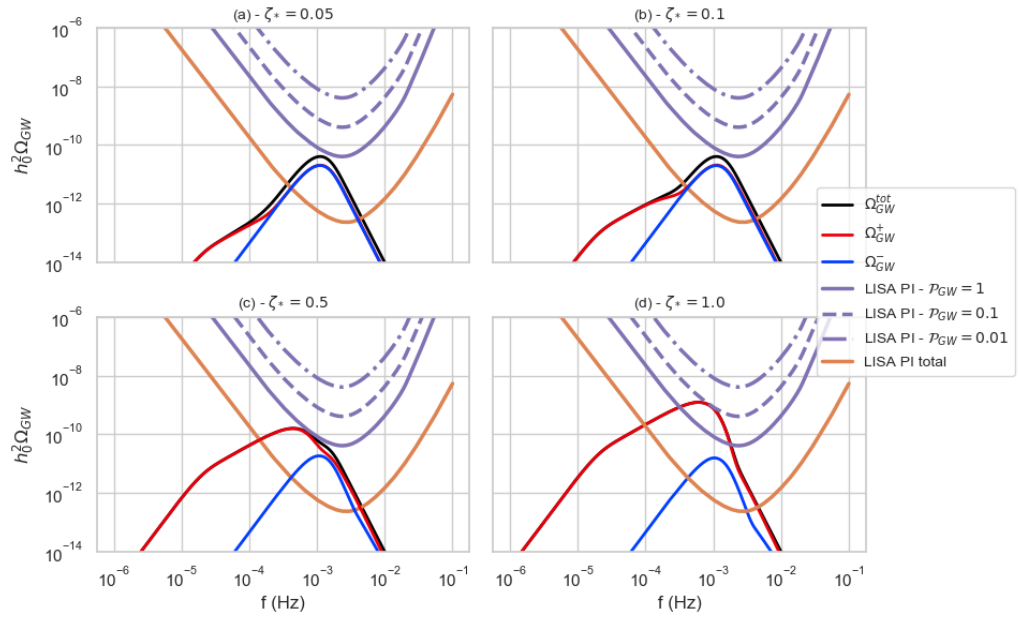

Fig. 8.4 *Strengths of polarised $\Omega_{GW,\pm}$ signals for different initial helicity fractions, ζ_* and fixed $\alpha = 1.0$, $T_* = 100$ GeV and $R_*H_* = 0.01$. Power-law integrated sensitivity of LISA to total GW signal (orange) and polarised signal (purple) are also shown assuming polarisation fractions (Eq. (8.35)) $\mathscr{P}_{GW} = 1$ (solid), 0.1 (dashed) and 0.01 (dot-dashed).*

Fig. 8.4 displays the strengths of the signals for different GW polarisations $\Omega_{\rm GW}^{\pm}$ for fixed $T_* = 100$ GeV, $R_*H_* = 0.01$, $\alpha = 1.0$, and various choices of the initial helicity

fraction, ζ_*. We see in Fig. 8.4(a) that for small $\zeta_* \lesssim 0.05$ the total GW signal $\Omega_{\rm GW}^{\rm tot}$ is dominated by the contribution from direct cascade turbulence with negligible net polarisation, i.e., $\Omega_{\rm GW}^{+} \simeq \Omega_{\rm GW}^{-}$. Conversely, the small low-frequency inverse cascade plateau in the signal emits fully-polarised GW, $\Omega_{\rm GW}^{+} \simeq \Omega_{\rm GW}^{\rm tot}$, as expected from our previously-stated assumption that $\zeta_* \simeq h$. Moving to Fig. 8.4(b), we see that raising ζ_* to 0.1 increases the size of the fully-polarised inverse cascade plateau in the GW signal, an effect that continues until $\zeta_* \sim 0.5$ (Fig. 8.4(c)) where it begins to dominate and transitions from being a plateau into a distinct new peak of the total GW signal. We see in the lower two panels of Fig. 8.4 that for $\zeta_* \gtrsim 0.5$ the contribution of the fully-polarised inverse cascade GW increasingly dominates that of the total GW signal, $\Omega_{\rm GW}^{\rm tot}$.

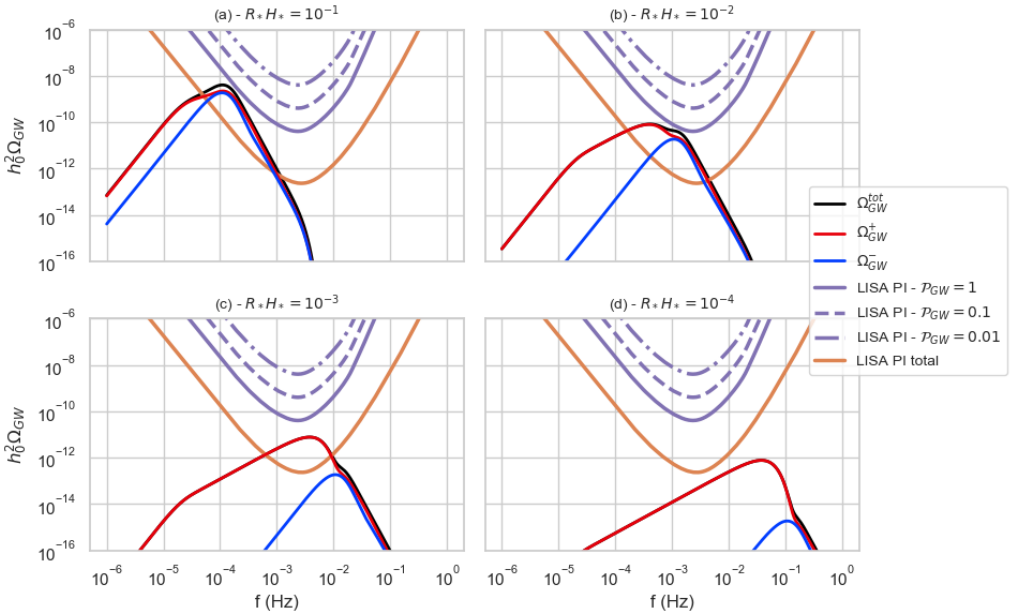

Fig. 8.5 *The strengths of the polarisation of the $\Omega_{GW,\pm}$ signals for various values of the average bubble radius, R_*H_*, ζ_* and fixed $\zeta_* = 0.4$ $\alpha = 1.0$ and $T_* = 100$ GeV. The orange and purple sensitivity curves are the same as in Fig 8.4.*

Fig. 8.5 shows the $\Omega_{\rm GW}^{\pm}$ signal strengths for fixed $T_* = 100$ GeV, $\zeta_* = 0.4$, $\alpha = 1.0$, and various choices of R_*H_*. We can see that as R_*H_* decreases the total GW amplitude decreases, as expected from the discussion in the previous section. However, the net polarisation of the signal increases as R_*H_* decreases. This is because inverse cascade turbulence is more important at smaller R_*H_* since the turnover time of the largest eddy, τ_s, takes longer to reach the Hubble timescale for phase transitions with smaller average bubble radius. Thus the duration of the inverse cascade stage where fully-polarised GWs are emitted increases, resulting in a GW signal with larger net polarisation.

Figs. 8.4 and 8.5 also feature power-law integrated sensitivities for LISA: the orange curves are the usual PI sensitivity for the total gravitational wave signal [130], while in

purple we show PI curves for a polarisation signal. We refer the reader to Appendix D for a formal derivation. The interpretation is the same as in the unpolarised case, i.e., a power law with a polarisation fraction $\mathscr{P}_{GW}$ (see Eq. (8.35)) crossing a purple line with the same $\mathscr{P}_{GW}$ gives SNR≥ 10 for a polarisation measurement with LISA.

As can be seen in Fig. 8.2, the effect of increasing T_* would be to shift the $\Omega_{\rm GW}$ signal to higher frequencies, without changing the relative amounts of $\Omega^{\pm}_{\rm GW}$ or their dependences on ζ_* and R_*H_*.

8.6.2 LISA sensitivity

We now assess the sensitivity of LISA to both the SGWB and to its circular polarisation, as would be generated by helical turbulence following a first-order phase transition. To do this we take an approach with the least possible sensitivity to the underlying particle physics model, calculating the transition strengths and temperatures, bubble sizes, and helicity fractions required to obtain a LISA SNR value greater than or equal to 10. This requires us to draw upon much of the analysis in the previous sections, first calculating the contributions to the total GW spectrum (Eq. (8.3)) from both direct cascade (Eq. (8.6)) and inverse cascade (Eq. (8.30)) turbulence for a particular point in parameter space and then computing the associated circularly-polarised spectrum (Eq. (8.36)). Finally, we translate both signal types into the LISA SNR values associated with the total GW spectra (Eq. (D.11)) and its polarised counterpart (Eq. (D.12)).

The left panels of Fig. 8.6 display reaches in the (R_*H_*, α) plane for a LISA measurement of the overall strength of the total SGWB signal with a signal-to-noise ratio $\mathrm{SNR}_{\rm tot} = 10$, with larger values of SNR found in the shaded regions above these lines. The panels from top to bottom correspond to $T_* = 10\,\mathrm{GeV}$, $1\,\mathrm{TeV}$ and $10\,\mathrm{TeV}$, and the various contours correspond to different values of the initial helicity fraction ζ_*. Thus, if a parameter point is enclosed within the shaded area of a given ζ_* contour, one can infer that a GW signal with this value of ζ_* would be detectable by LISA with an SNR ≥ 10. The red crosses correspond to sample frequency spectra plotted in the indicated previous Figures for fixed R_*H_*, α and T_*, which exemplify the spectral sensitivity of LISA to the GW signal.

As expected, the largest detectable signals in all three panels come from larger values of R_*H_*, where the number of bubbles per horizon is smaller and thus the average bubble radius at collision is larger. As R_*H_* decreases we see that increasingly large values of the helicity fraction, ζ_*, are required to obtain a signal with $\mathrm{SNR}_{\rm tot} \gtrsim 10$. Thus GW emission from the inverse cascade turbulent period is increasingly important for LISA to be sensitive to the total GW signal for smaller values of R_*H_*. This can be traced back to the R_*H_* suppression of the GW amplitude produced in a direct cascade that is a general feature of the models used to describe GW emission from turbulence (see Sec. 8.2).

We see from the different contours that increasing the initial helicity fraction increases the total SNR, in agreement with the increasing strength of the GW signal shown for different values of ζ_* in Fig. 8.1. In general, the GW signal should be detectable at a level of $\mathrm{SNR}_{\mathrm{tot}} \gtrsim 10$ for $\alpha \gtrsim 1$ and $R_*H_* \gtrsim 10^{-3}$ for a transition at $T_* = 100\,\mathrm{GeV}$. For larger values of T_*, larger values of R_*H_* are needed for $\mathrm{SNR}_{\mathrm{tot}} = 10$ measurements, though smaller values of α are sufficient.

We also see in the left panels of Fig. 8.6 that for large values of R_*H_* the position of the $\mathrm{SNR}_{\mathrm{tot}} = 10$ contours are approximately independent of ζ_* and depend only on α, whereas for smaller values of R_*H_* the contour lines have a greater dependence on the value of ζ_* associated with the contour. This is explained by the fact that for large R_*H_* the contribution of inverse cascade period is minimised as the large average bubble radius at collision means inverse cascade turbulence cannot operate for very long before being washed out by the Hubble expansion. Thus increasing ζ_* does relatively little to increase the amplitude of the signal (see Fig. 8.1(b)) and has minimal effect on its sensitivity to LISA. Conversely, for small R_*H_* the inverse cascade can operate for far longer before being washed out by the expansion, and thus the potential contribution from the inverse cascade to the total GW signal can be much larger (see Fig. 8.1(a)). As larger values of ζ_* result in greater importance of the inverse cascade period for the total GW signal, it follows that in the low-R_*H_* region of the parameter space, the $\mathrm{SNR}_{\mathrm{tot}}$ is much more sensitive to the value of ζ_*. [9]

The right panels of Fig. 8.6 display the corresponding reaches in the (R_*H_*, α) plane for a LISA measurement of the circular polarisation of the SGWB with $\mathrm{SNR}_{\mathrm{pol}} = 10$. As expected the reach is smaller than for the total GW signal, but we see that many of the qualitative features of the plots of $\mathrm{SNR}_{\mathrm{tot}}$ described above are also present in the polarised case. Whilst detection prospects for circular polarisation in the SGWB are strongest for large R_*H_* where the suppression in the amplitude of the spectra is minimised (see Fig. 8.5), in order for LISA to be able to probe a circularly-polarised signal at small R_*H_*, larger values of ζ_* are required to compensate for the suppression R_*H_* introduces into the total GW signal. Larger ζ_* means fully-polarised GWs from the inverse cascade period make an increasingly important contribution to the total GW signal, raising the amplitude of Ω^{+}_{GW} relative to Ω^{-}_{GW} and increasing the prospects for detection by LISA of circular polarisation in the SGWB from a phase transition.

Comparing the right panels of Fig. 8.6, we see that for smaller values of the helicity fraction, $\zeta_* \lesssim 0.2$, LISA is most sensitive to polarisation of the GW signal when the transition temperature is $T_* = 1\,\mathrm{TeV}$. This can be understood by looking at Fig. 8.2 and noting that, of the three transition temperatures, the $T_* = 1\,\mathrm{TeV}$ spectrum peaks at the

[9] We note that new simulations suggest that the f^1 plateau at low frequencies could also develop in cases with small initial helicity [142]. This would improve detection prospects for low-ζ_* scenarios and reduce the dependence of the total SNR on that parameter.

optimal frequency for LISA to be sensitive to the fully-polarised low-frequency inverse cascade plateau that develops in the signal for small ζ_*.

As seen in the right hand panels of Fig. 8.6, in the polarised case the positions of the $\mathrm{SNR}_{\mathrm{pol}} = 10$ contours exhibit a larger relative dependence on ζ_* at large R_*H_* than their $\mathrm{SNR}_{\mathrm{tot}}$ counterparts. Whilst in the $\Omega_{\mathrm{GW}}^{\mathrm{tot}}$ case the low-frequency inverse cascade contribution was less important for larger R_*H_*, in the polarised case it has a larger impact. Even when considering the case of a low-frequency plateau in the signal associated with relatively low helicity inverse cascade turbulence (see Fig. 8.4(a)), fully-polarised GW are still being emitted, implying that relatively small changes in the value of ζ_* can have a larger effect on the net polarisation of the SGWB and the ability of LISA to probe it.

As seen in the top right panel of Fig. 8.6, for larger values of the helicity fraction, $\zeta_* \gtrsim 0.3$, the parameter space in which $\mathrm{SNR}_{\mathrm{pol}} > 10$ expands significantly in the $T_* = 100\mathrm{GeV}$ case, allowing a larger range of small R_*H_* values to be probed by LISA. This can be understood by referring to the $T_* = 100\mathrm{GeV}$ spectrum plot in Fig. 8.1(a) and noting that for intermediate values of the helicity fraction, $0.1 \lesssim \zeta_* \lesssim 0.5$ the low-frequency, fully-polarised inverse cascade plateau transitions into a new, distinct peak, and in so doing becomes rapidly more sensitive to the frequency band where LISA is most sensitive.

Similar behaviour is seen for the $T_* = 1\,\mathrm{TeV}$ case shown in the middle panel of Fig. 8.6, though less pronounced, because the GW spectra for this transition temperature peak at higher frequencies where LISA is already more sensitive to the fully-polarised inverse cascade plateau.

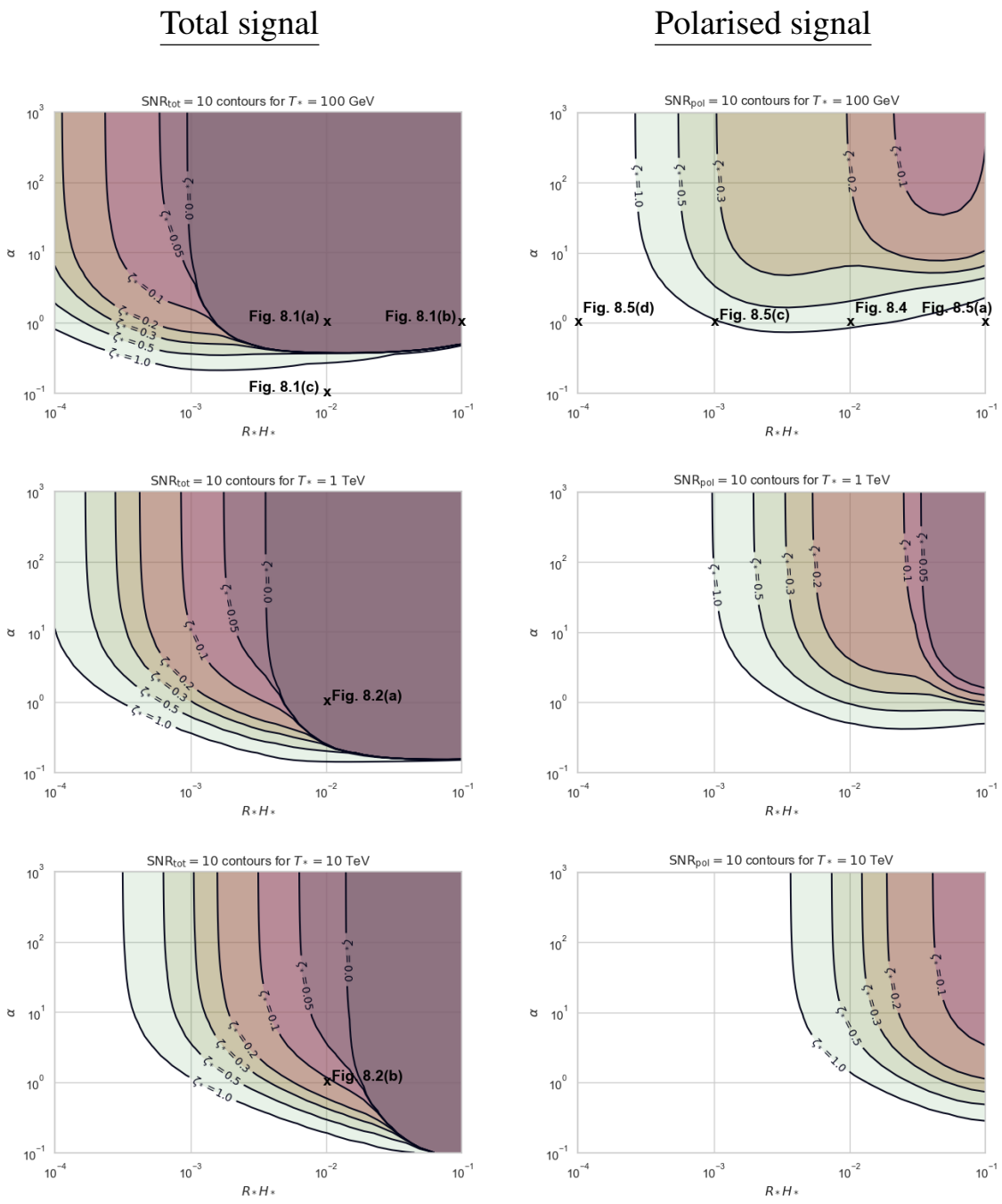

Fig. 8.6 *Signal-to-noise (SNR)* $= 10$ *contours in the* (R_*H_*, α) *plane for* $T_* = 100$ *GeV (top),* $T_* = 1$ *TeV (middle) and* $T_* = 10$ *TeV (bottom), for a LISA measurement with a 4-year observation time. In the left panels the SNR is shown for the total SGWB signal and in the right panels for observing the polarisation of the SGWB. The different contours correspond to various values of the initial helicity fraction* ζ_**, as shown in the plots. The red crosses correspond to sample GW spectra for fixed* α*,* R_*H_* *and* T_* *plotted in the indicated previous Figures, which allow comparison of the LISA sensitivity to the GW signal for ranges of* ζ_* *values.*

Chapter 9

Intergalactic Magnetic Fields from First Order Phase Transitions

The existence, magnitude and origin of an intergalactic magnetic field (IGMF) have long been topics for debate. Until relatively recently there were only upper limits on its possible magnitude coming from Big-Bang Nucleosynthesis (BBN) [175, 176], and measurements of the spectrum and anisotropies of the cosmic microwave background (CMB) [177–184]. However, for some years now lower limits on the magnitude of the IGMF have been reported [185–189], in particular in a recent analysis by the *Fermi*-LAT collaboration [190], based on their observations of blazars in conjunction with measurements of very-high-energy (VHE) γ emissions by imaging air Čerenkov telescopes (IACTs). In combination, these provide evidence for electromagnetic cascades interpreted as being due to the processes of pair production via the IGMF: $\gamma + \mathbf{B} \rightarrow e^+e^-$ followed by γ emission during $e^\pm$ scattering off the magnetic field: $e^\pm + \mathbf{B} \rightarrow e^\pm + \gamma$. The inferred magnitude of the IGMF depends on its unknown coherence length λ and on the unknown duration of blazar emissions. Making the very conservative assumption that the blazars studied have been active at a similar level for at least 10 years, the *Fermi*-LAT collaboration established the lower limit $|\mathbf{B}| > 3 \times 10^{-16}$ Gauss over a large range of $\lambda > 10^{-2}$ Mpc [190], increasing at smaller λ, rising to $|\mathbf{B}| > 10^{-14}(3 \times 10^{-13})$ Gauss for plausible active periods of $10^4(10^7)$ years.

The origin of such a field on large scales does not yet have a satisfactory explanation. There are several astrophysical scenarios for the generation of magnetic fields on cluster and galaxy scales which involve battery effects creating seed fields [191–193] which are subsequently amplified to the observed strength in galaxies and clusters by dynamo action [194–196]. Such mechanisms have difficulty in explaining magnetic fields in the large voids which would be required to explain the constraints from gamma rays outlined above, so one is led to envisage possible primordial sources originating from processes involving particle physics. Natural sources include non-adiabatic episodes in the early

universe such as cosmological inflation [167, 197–199] or some phase transition, e.g., the QCD or electroweak phase transition [131, 200, 201]. The QCD phase transition is well understood and thought to have been rather smooth, and hence unlikely to have generated large primordial magnetic fields. The electroweak phase transition would also have been quite smooth in the Standard Model (SM), but there is scope for extensions of the SM that could have generated a first-order phase transition that might have created significant primordial magnetic fields [202].

Here we study IGMF generation in two possible extensions of the SM, outlined in Sec. 5.5, that have been used previously in the literature to explore the possible magnitudes of GW signatures. One is the SM supplemented by an $|H|^6$ operator (SM+H^6) [59], and the other is a classically scale-invariant extension of the SM with an extra gauged U(1) $B-L$ symmetry (SM$_{B-L}$) [64].

In exploring the possible generation of the IGMF in these models, we consider two contributions arising from non-adiabatic processes during a first-order phase transition: bubble collisions and turbulence in the primordial plasma. These were both already found to make significant contributions to the GW signals produced in these two models [59, 64]. We also consider two different sources that lead to significant amplification of the magnetic field via an inverse cascade process: primordial helical field configurations [144, 203] and kinetic helicity [204–206].

9.1 Primordial Magnetic Field Generation

In this section we discuss possible sources of magnetic fields generated during a first-order phase transition, using an approach similar to that used previously [59, 64] for gravitational wave production (see Chapter 7). We expect that some fraction of the energy released during the phase transition would generically be available for the production of magnetic fields, and can divide the sources into two main sub-classes:

- energy stored in the bubble walls, which source **B**-fields upon collision,
- turbulent kinetic energy in the charged plasma that is available for later **B**-field generation via magnetohydrodynamic (MHD) mechanisms.

At any given time $t \geq t_*$ after the phase transition, we can describe both the magnetic field and the turbulent plasma using their respective energy density spectra, $\rho_i(\lambda,t) = \mathrm{d}\rho_i(t)/\mathrm{d}\log\lambda$, $i = B,K$, and the corresponding magnetic field spectrum is then given by

$$B(\lambda,t) = \sqrt{2\rho_B(\lambda,t)}\,. \tag{9.1}$$

The mean energy densities of the two components at this time are $\rho_i(t) = \int \rho_i(\lambda,t)\mathrm{d}\log\lambda$. We define $v_i^2(t) = 2\rho_i(t)/\rho_0$, so that v_B and v_K are, respectively, the Alfvèn velocity

associated with the magnetic field and the root-mean-square plasma velocity, while ρ_0 describes the initial plasma energy density.

Magnetic fields sourced from bubble collisions were recently revisited in [207], where it was found that about 10% of the energy of the transition was expended on production of magnetic fields, mostly as the field oscillates around the minimum of the potential after the transition has been completed. In this simulation all the energy from vacuum conversion was used to accelerate the bubble walls. In order to use these results in the more realistic setting of a transition taking place in a plasma-filled background, we need to include the appropriate efficiency factor

$$\kappa_{\rm col} = \frac{\rho_{\rm wall}}{\rho_{\rm V}}\,, \tag{9.2}$$

which describes the fraction of energy used to accelerate the bubbles, just as in the case of GW generation (see Sec. 7.1 for details).

For the plasma-related sources the efficiency factor is

$$\kappa_{\rm sw} = \frac{\alpha_{\rm eff}}{\alpha}\frac{\alpha_{\rm eff}}{0.73+0.083\sqrt{\alpha_{\rm eff}}+\alpha_{\rm eff}}\,, \quad \text{with} \quad \alpha_{\rm eff} = \alpha(1-\kappa_{\rm col})\,, \tag{9.3}$$

which describes the fraction of the energy converted into bulk fluid motion [55, 101], including also through $\alpha_{\rm eff}$ the fraction of energy used for bubble acceleration [64]. Here $\alpha = \rho_{vac}/\rho_{rad}$ is the usual quantity that parameterises the strength of the phase transition. We assume that the efficiency for converting bulk fluid motion of the plasma into magnetic fields via MHD turbulence is 10% [132, 208, 209]. This value is an order-of-magnitude estimate at best, but it will be very simple to re-scale our estimates below with more accurate results once more detailed estimates are available. This assumption leads to a simple final expression for the energy density of the magnetic field after the phase transition:

$$\rho_{B,*} = \frac{0.1\kappa\,\alpha}{1+\alpha}\rho_*\,, \tag{9.4}$$

where κ is the efficiency factor for the source in question (either $\kappa_{\rm col}$ or $\kappa_{\rm sw}$) and $\rho_* = 3M_p^2H_*^2$ is the total energy density at the time of percolation.

Taking the Fourier transform of the mean magnetic and kinetic energy densities, we obtain a power spectrum for each of these components $P_B(\lambda)$ and $P_K(\lambda)$. These power spectra can then be expressed in terms of their associated energy density spectra as

$$P_i(\lambda,t) = \frac{\lambda^3}{4\pi}\rho_i(\lambda,t), \tag{9.5}$$

where $i = B,K$ describe quantities related to the magnetic and turbulent plasma fields respectively. We can represent the initial configuration of the two fields in terms of their

power spectra, both of which peak at the average bubble size at collision, $\lambda_* = R_*$:

$$P_{*,i}(\lambda, t_*) \approx P_{*,i}\lambda^{-n_i(\lambda)} \tag{9.6}$$

where we have approximated each initial power spectrum with a separate power law.

At scales $\lambda > \lambda_*$, causality and the divergence-free condition on the initial magnetic field require that $n_B \geq 2$ [210], whilst in the case of the plasma the requirement is less stringent, with $n_K \geq 0$, where $n_K = 0$ and 2 correspond to compressible and incompressible plasmas, respectively, both of which are feasible scenarios in an MHD system.

We do not consider the slope of the initial spectrum at length scales smaller than λ_*, as we generically expect turbulence, driven by the turbulent eddies at the coherence scale, to fully develop relatively quickly on these smaller length scales, due to the smaller eddy turnover times involved. Once the turbulent eddies have developed on all scales $\lambda < \lambda_*$, magnetic and kinetic energy is subsequently transferred to increasingly smaller scales via a direct energy cascade, [1] until the energy is eventually lost as heat at the dissipation scale of the plasma, λ_d. When a turbulent eddy develops on a particular distance scale, we expect the power spectrum of the initial magnetic or plasma field to be 'processed' into an independent spectrum following a global turbulent decay law. In our work we assume that the form of any processed turbulent spectrum follows a Kolmogorov decay law [211] with $n_i = -11/3$, as argued on dimensional grounds in [212].

Assuming the power $n_B = 2$ at large scales, the initial magnetic field energy density spectrum is then given by

$$\rho_B(\lambda, t_*) = \frac{17}{10}\rho_{B,*}\begin{cases}\left(\frac{\lambda}{\lambda_*}\right)^{-5} & \text{for} \quad \lambda \geq \lambda_*\,, \\ \left(\frac{\lambda}{\lambda_*}\right)^{2/3} & \text{for} \quad \lambda < \lambda_*\,. \end{cases} \tag{9.7}$$

In the following we discuss how this spectrum evolves. The evolution changes only the amplitude and the coherence scale of the spectrum, but does not change its shape.

9.2 Direct Cascade Evolution of the Magnetic Field

The initial power in the magnetic field subsequently spreads over a variety of different length scales, due to the non-zero coupling between the magnetic and plasma components. To study the evolution of the magnetic field in the turbulent plasma we need to track how key quantities, such as the comoving magnetic coherence length, λ_B, [2] and the comoving magnetic field strength, B, change with time from their initial values set immediately after

[1] This direct energy cascade arises due to the non-linear terms in the fluid equations that facilitate interactions between the different wavelength modes.

[2] Here λ_B is the equivalent quantity to that denoted ξ_M in Chapter 8.

the phase transition completes, at $t = t_*$. Properties related to both the turbulent plasma and inherent to the magnetic field itself, e.g., non-zero magnetic helicity, can significantly impact this evolution, as we discuss below, broadly following the approach in [208].

It is important to emphasize that the scaling laws of the magnetic field quoted in this section apply only in the presence of a plasma background. As such, we assume they are relevant only until the time of recombination, $t_{\rm rec}$, and that subsequently the magnetic field strength simply dilutes as normal due to redshift, $B \sim a^{-2}$.

Immediately after the phase transition, turbulent eddies have only had time to develop fully [3] on scales $\lambda < \lambda_*$. At subsequent times after the transition, turbulent eddies begin to develop on increasingly larger scales $\lambda > \lambda_*$, and the power spectrum on these scales is processed from its initial slope to one characterised by a Kolmogorov decay law. Thus the maximum comoving distance on which the field is correlated, known as the comoving coherence scale, λ_i, increases with time. We can approximate the time evolution of λ_i by a power law

$$\lambda_i \sim t^{\zeta_i}\,, \qquad i = B, K\,, \tag{9.8}$$

where $\zeta_i > 0$. Assuming Kolmogorov turbulent decay, the direct energy cascade transfers both magnetic energy and turbulent plasma energy to increasingly smaller scales before it is eventually dissipated into heat. Thus the comoving energy density of both the magnetic field, ρ_B, and the turbulent plasma, ρ_K, can be assumed to decay with time.

These energy densities define characteristic velocities for the respective magnetic and turbulent plasma field components, describing the rate at which changes in the relevant field can propagate. We can subsequently use these velocities to describe the maximum length scale on which each of the fields are correlated at any given time $t \gg t_*$ after the transition:

$$\lambda_i \sim v_i t\,. \tag{9.9}$$

Once MHD turbulence has fully developed at a given scale, we expect equipartition between the plasma and magnetic energy densities, $\rho_B \sim \rho_K \sim \rho_{\rm eq}$. Using Eq. (9.5) in conjunction with Eq. (9.6), we can write

$$v_{\rm eq} \sim \sqrt{2\rho_{\rm eq}} \sim \lambda_{\rm eq}^{-\frac{3+n}{2}}\,, \tag{9.10}$$

where $\lambda_{\rm eq} \sim \lambda_B \sim \lambda_K$ and $v_{\rm eq} \sim v_B \sim v_K$ from the equipartition condition, and $n = \min(n_B, n_K)$ corresponds to the spectral decay law of the field that initially dominates, whether it be the magnetic field or the turbulent plasma. The size of the largest 'processed'

[3] By 'develop fully' we mean that the plasma eddy needs to have completed one rotation on the scale of interest.

eddy can then be expressed using Eq. (9.10) as

$$\lambda_{\rm eq} \sim v_{\rm eq} t \sim t^{\frac{2}{5+n}} . \tag{9.11}$$

Using Eqs. (9.1) and (9.11) we obtain the following scaling laws based on dimensional arguments:

$$B(\lambda_{\rm eq}) \sim \sqrt{2\rho_{\rm eq}} \sim t^{\frac{3+n}{5+n}} , \tag{9.12}$$

and

$$B(\lambda_{\rm eq}) \sim \lambda_{\rm eq}^{-\frac{3+n}{2}} . \tag{9.13}$$

9.3 Inverse Cascade Evolution of the Magnetic Field in a Helical Plasma

As shown in [213, 214], the behaviour of the field evolution can be changed dramatically in the presence of non-zero average magnetic helicity, $\langle \mathbf{A}\cdot\mathbf{B} \rangle$, where $\mathbf{B} = \nabla \times \mathbf{A}$, a quantity describing the twisting of magnetic field lines. We considered this in the context of gravitational wave generation in Chapter 8. We expect some fraction of magnetic helicity to be left over after the phase transition from baryon-number-violating processes such as decaying non-perturbative field configurations, e.g., electroweak sphalerons [215]. Furthermore, we expect some amount of helicity to be generated as the swirling plasma results in twisted field lines, due to the coupling between magnetic field and plasma components in an MHD system [214].

In a highly conductive plasma we expect magnetic helicity to be conserved: $\langle \mathbf{A}\cdot\mathbf{B} \rangle \propto \rho_B \lambda_B = \text{const}$, and thus $B \sim \sqrt{\rho_B} \sim 1/\sqrt{\lambda_B}$, which we can use with Eq. (9.13) to deduce that this corresponds to the case $n = -2$. Thus from Eq. (9.11) and (9.12) the time evolution of the comoving coherence scale λ_B and the comoving magnetic field strength B in the presence of magnetic helicity can be argued to be [213]

$$\lambda_{\rm eq} \sim t^{\frac{2}{3}} , \qquad B(\lambda_{\rm eq}) \sim t^{-\frac{1}{3}} . \tag{9.14}$$

Assuming some initial fractional magnetic helicity immediately after the transition, we expect the field to reach a maximally helical state some time later [200], due to the direct energy cascade, which results in the conversion of the large-scale non-helical field component to heat [179].

More recently, numerical simulations in [216] have shown that inverse cascade behaviour also takes place when a non-helical magnetic field is in the presence of a plasma with initial kinetic helicity. The scalings of the comoving coherence scale and comoving

magnetic field amplitude with time in this scenario are then found to be

$$\lambda_{\rm eq} \sim t^{\frac{1}{2}}\,, \qquad B(\lambda_{\rm eq}) \sim t^{-\frac{1}{2}}\,. \tag{9.15}$$

9.4 Magnetic Field Spectrum Today

Using the above results for the evolution of the comoving magnetic field spectrum, we can calculate the spectrum today. The scaling laws (9.14) and (9.15) hold until recombination, which happens only shortly after matter-radiation equality, so it is a good approximation that the scale factor behaves as $a \sim t$. So, redshifting the initial spectrum (9.7) while assuming a decay law $\sim a^{-q_B}$ of the comoving magnetic field until recombination gives the following magnetic field spectrum today:

$$B_0(\lambda) \equiv B(\lambda, t_0) = \left(\frac{a_*}{a_{\rm rec}}\right)^{q_B} \left(\frac{a_*}{a_0}\right)^2 \sqrt{\frac{17}{10}\rho_{B,*}} \begin{cases} \left(\frac{\lambda}{\lambda_0}\right)^{-5/2} & \text{for} \quad \lambda \geq \lambda_0\,, \\ \left(\frac{\lambda}{\lambda_0}\right)^{1/3} & \text{for} \quad \lambda < \lambda_0\,, \end{cases} \tag{9.16}$$

where the initial magnetic field energy density $\rho_{B,*}$ is given by Eq. (9.4). Similarly, assuming that the comoving field coherence scale evolves as $\sim a^{q_\lambda}$ until recombination, the field coherence scale today is

$$\lambda_0 \equiv \lambda_B(t_0) = \left(\frac{a_{\rm rec}}{a_*}\right)^{q_\lambda} \left(\frac{a_0}{a_*}\right) \lambda_*\,, \tag{9.17}$$

where the initial coherence scale is given by the bubble size at percolation, $\lambda_* = R_*$. Assuming fast reheating to a temperature $T_{\rm reh}$ after the phase transition, the factor a_*/a, where a is either $a_{\rm rec}$ or a_0, can be expressed as

$$\frac{a_*}{a} = \left(\frac{h_{\rm eff}(T)}{h_{\rm eff}(T_{\rm reh})}\right)^{\frac{1}{3}} \frac{T}{T_{\rm reh}}\,, \tag{9.18}$$

where $h_{\rm eff}(T)$ is the effective number of entropy degrees of freedom at temperature T.

9.5 Experimental Constraints on the IGMF

The strength of an IGMF can be constrained in a variety of different ways, both from above and from below. Additionally, the maximum size of an IGMF can be constrained by the horizon size today.

We expect upper bounds arising from the BBN and the CMB. Strong magnetic fields are expected to affect BBN in a variety of different ways as summarised in [175, 176],

a primary example of which is a significant increase in the neutron decay rate which suppresses the relic abundance of helium as after the neutron to proton ratio has been frozen the neutrons can decay before they can be bounded into composite nuclei.

CMB constraints arise from measurements of the spectrum and anisotropies of the cosmic microwave background that we would expect would imprint itself on the CMB in the presence of a strong, largescale magentic field [177–184].

As mentioned at the beginning of the chapter, very-high-energy gamma rays emitted by TeV blazars will Thompson scatter with the photons in the Extragalatic Background Light (EBL) to produce highly-relativistic e^+e^- pairs. These pairs are subsequently expected to lose energy via inverse Compton scattering with CMB photons, finally producing a significant emission of secondary cascade photons in the GeV band.

A lower bound on the IGMF can be inferred from the non-observation of such GeV cascade photons. In the presence of an IGMF, e^+e^- pairs produced during the cascade process would be deflected from the trajectory expected in the absence of the magnetic field. Thus the total emission in the GeV band would be reduced for increasing IGMF strength, as the initial incoming photon flux is distributed over a greater solid angle. Additionally, a stronger IGMF would also result in an increasing time delay between the cascade GeV and direct TeV emissions. Both these effects provide mechanisms for suppressing the flux of GeV cascade photons, which can then be re-expressed in terms of a lower bound on the strength of the IGMF.

Refs. [185–187, 190, 217] analysed *Fermi* data from blazars possessing hard TeV spectra with negligible GeV cascade emission, under the assumption that this suppression was due to the large angular size of the cascade emission. They each derived a constraint, later verified by [218] using simultaneous GeV/TeV energy band observation data, on the minimum value of the IGMF. The constraints reported varied in the range $B_0 \gtrsim 10^{-16} - 10^{-15}$ G for $\lambda_0 \gtrsim 1$ Mpc depending on the adopted EBL and source model. For our purposes we adopt the *Fermi*-LAT constraint in [190], $B_0 > 3 \times 10^{-16}$ G, corresponding to the blue solid line of the plots in Sec. 9.6. Their analysis shows that the high-latitude sources detected by the *Fermi*-LAT do not have significant spatial extension.

Independently, Refs. [218, 219] considered explaining the suppressed GeV emission by an IGMF-induced time delay in the GeV cascade signal compared to the TeV direct signal. Using simultaneous multi-band observation data from *Fermi* and ground-based Cherenkov telescopes, and assuming that the blazars had not been firing for a long period, so that the cascade signal had not yet reached the detectors, these authors were able to deduce lower bounds on the IGMF lying in the range $B_0 \gtrsim 10^{-18} - 10^{-17}$ G for $\lambda_0 \gtrsim 1$ Mpc. The difference between the values obtained by the two investigations can be explained by the method used to model the cascade signal, and in our work we take the constraint from [218], $B_0 > 10^{-17}$ G, shown as the dashed blue line in the plots in Sec. 9.6.

The above constraints on the IGMF are independent of the magnetic coherence scale for $\lambda_0 \gtrsim 1$ Mpc, because the length scales on which e^+e^- pairs undergo inverse Compton cooling are much smaller than those over which the underlying field is correlated. In this scenario the pairs can be approximated as moving through a homogeneous magnetic field. However, for scales $\lambda_0 \lesssim 1$ Mpc this simplifying approximation is no longer valid and the e^+e^- pairs may experience changes in their deflection trajectory as they journey through uncorrelated patches of the IGMF. Thus an uncertainty in the final deflection angle and time delay of the signal is introduced at these scales. To account for this, the strength of the magnetic field should increase like $B_0 \sim \lambda_0^{-1/2}$ at scales $\lambda_0 \lesssim 1$ Mpc, in order to ensure that the trajectories of the e^+e^- pairs are deflected to the degree required to explain the absence of the GeV emission in the experimental data.

For our plots in Sec. 9.6 we take the IGMF constraint associated with the extended angular cascade emission from Ref. [190], where the bound is taken to be flat for $\lambda_0 \gtrsim 10\,\mathrm{kpc}$ and increases like $B_0 \sim \lambda_0^{-1/2}$ below such scales. On the other hand, for the IGMF constraint associated with the time delay of the cascade signal we take the result from Ref. [217], where the bound is taken to be flat for $\lambda_0 \gtrsim 100\,\mathrm{kpc}$.

9.6 Results in Illustrative Examples

In order to calculate the IGMF generated by a particular phase transition, we need to be more specific about the scenario that we consider. Here we follow closely the two scenarios outlined in Secs. 5.5.1 and 5.5.2, the first being a Higgs sector with an additional non-renormalizable $|H|^6$ operator (SM+H^6), and the second being a classically scale-invariant extension of the SM with an extra gauged U(1) $B-L$ symmetry (SM$_{B-L}$).

The generation of GWs in these models has been analyzed previously in [59, 64] and we follow the procedure described there in the current analysis. The GW signal produced by turbulence could be enhanced due to the inverse cascade occurring during the evolution of MHD turbulence with a helical magnetic field [14, 152], as considered in Chapter 8. The impact of this modification, however, depends on the modelling of the evolution of the turbulence and will not change the experimental reach into the models at hand, as turbulence is usually not the dominant source of GWs. Still, observation of the tail of the signal produced by turbulence could probe the helicity of the source through polarisation of the GW signal [140].

9.6.1 Template plot components

Before moving on to analysing our concrete examples of Magnetic field generation from a first order phase transition we first will build up and briefly explain the different components

of the template Magnetic field plot that we will generate and analyse for each of the examples.

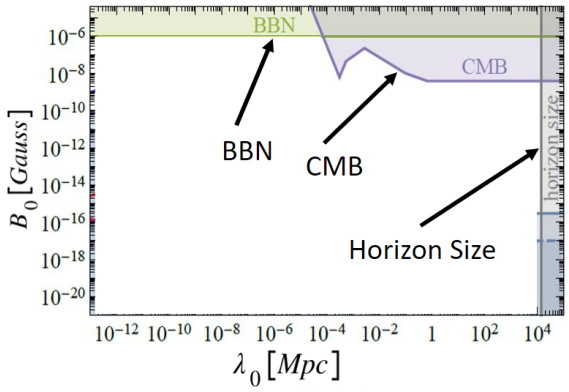

(a) *Upper bounds on:*
- B_0 from BBN (green) and CMB (purple),
- λ_0 from horizon size (grey)

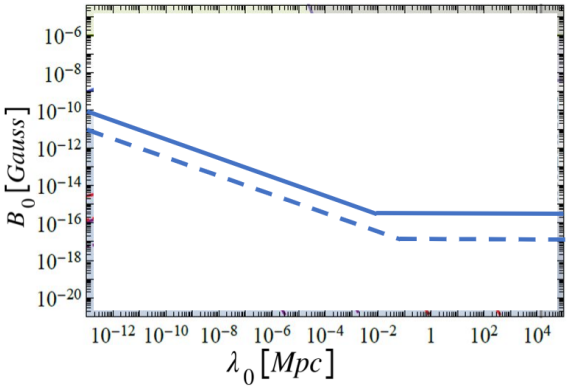

(b) *Lower bounds on B_0 from non-observation of GeV Blazar cascade due to:*
- angular size (solid blue line)
- time delay (dashed blue line).

Fig. 9.1 *Experimental constraints on the IGMF*

In Fig. 9.1 we plot the constraint curves we discussed in Sec. 9.5. Fig. 9.1a shows the upper bounds on the field strength of an IGMF at a given coherence length λ_0, where the green curve is from Big Bang Nuclesynthesis and the purple curve is from the CMB. The grey vertical curve is a constraint on the maximum size of any IGMF from the measured size of the cosmological horizon today.

The blue curves in Fig. 9.1b are lower bounds on the strength of an IGMF from the non-observation of a secondary GeV cascade emission from TeV blazars, as discussed in Sec. 9.5. The solid blue line represents the bound that arises from the assumption that the negligible GeV cascade emission is due to it being spread over a large angular size due to deflection by the IGMF. The dashed blue line, on the other hand, represents the bound that

arises from assuming there is a IGMF-induced time-delay of the signal that explains the non-observation of the GeV cascade signal.

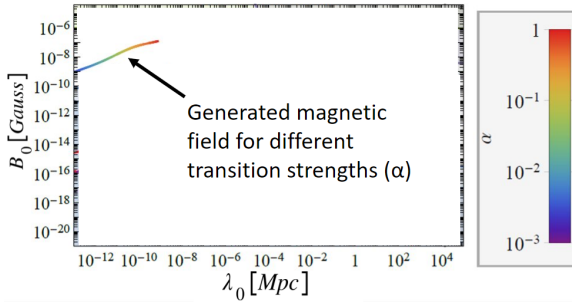

(a) *Generated B_0*

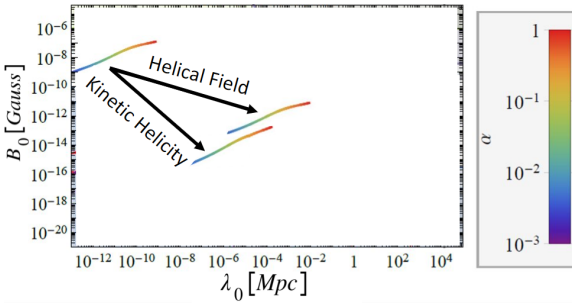

(b) *Evolution of B_0*

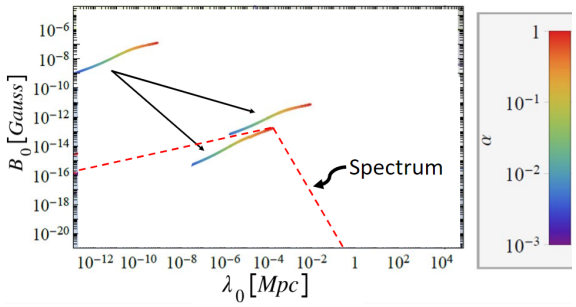

(c) *Example spectrum of B_0 today*

Fig. 9.2 *Components of template plot related to generation and evolution of the field*

In Fig. 9.2 we show the components of the template plot related to generation and evolution of the magnetic field to today. The rainbow curve in Fig. 9.2a shows the strength of the magnetic field generated from a first order phase transition at a given coherence length where we have used Eq. (9.1) with Eq. (9.4) and assumed that the coherence length of the field is dictated by the size of the average bubble radius at collision, i.e. $\lambda_* \approx R_*$. Each point on the curve has a colour of the rainbow assigned to it which corresponds to the strength of the phase transition, α. The shape of this rainbow curve should reveal a lot about the dynamics of the PT in the individual theories we consider when we come to analyse them.

In Fig. 9.2b we use Eq. (9.16) to show an example of how such a range of primordial fields generated from a phase transition might have evolved to today in the presence of an

initial helical component seeded in either the gauge field or the plasma. The resulting field strengths today for each of these cases are shown by the two lower rainbow curves, each of which are labelled with an arrow denoting the case it corresponds to. In both scenarios we assume the initial helical component induces an inverse cascade shortly after, which increases the field strength and correlation length of the field via Eq. (9.14) for the helical field case and Eq. (9.15) for the kinetic helicity case, up until recombination when the plasma disappears and after which time the magnetic field is simply red-shifted as normal like a^2 till today.

In Fig. 9.2c we use Eq. (9.16) to show an example magnetic field spectra (red dashed line) that might be present today for a field with coherence length today, λ_0, in the case of a magnetic field that was generated with initial kinetic helicity. The spectrum peaks at the predicted value of the present day field strength after fixing the coherence length of the field to one of the range of possible values. The red colour of the spectral line matches the color of the PT strength, α, assigned to this parameter point.

9.6.2 Standard Model with $|H|^6$ term

This model, discussed in Sec. 5.5.1, serves as a minimal and natural extension of the SM in which to explore the consequences of a possible first-order electroweak phase transition which could have been the source of the intergalactic magnetic field. The dynamics of the phase transition in this model is quite generic, and it has features typical of many simple modifications of the SM featuring polynomial potentials as might be generated, for instance, by a new neutral scalar. Specifically, the field cannot remain in the metastable vacuum too long without spoiling percolation. As a result, the strength of the phase transition is bounded by $\alpha \lesssim 1$ for all feasible transitions in this model.

Large couplings with the plasma result in a large leading-order plasma friction on the wall that arises from particles gaining mass as they cross the scalar field boundary (see Sec. 5.3). The impossibility of cooling in order to decrease this friction means that the bubbles reach their terminal velocity very quickly, and most of the energy of the transition is dumped into plasma shells surrounding the bubbles. In principle, these models could be mapped onto the recent simulations of first-order SM phase transitions [207]. However, in those simulations, interaction of the wall with the plasma background was neglected and the source of the magnetic field was oscillations of the scalar field.

Since we find that most of the energy is transferred into the plasma, we would only expect a very small residual magnetic field to be produced - the fraction of energy transferred directly into the bubble walls is very small $\kappa_{\rm col} \approx 10^{-10}$ [64]. Instead, just as in the GW case [64], the bulk of our results come from plasma-related sources, specifically turbulence developing in the plasma after the transition. The sound-wave period in these models

lasts less than a Hubble time [59], and the nonlinear dynamics following it may lead to a significant amount of bulk fluid motion which could be converted into turbulence [64, 101].

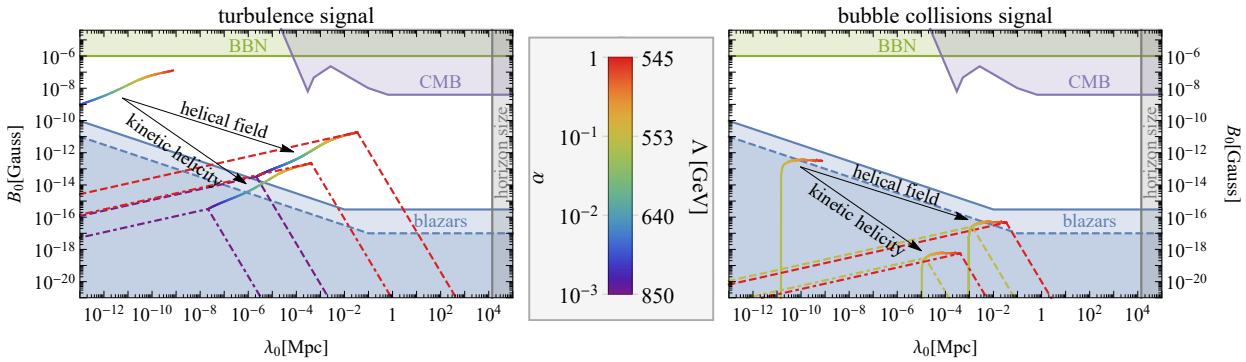

Fig. 9.3 *Magnetic field strength B_0 as a function of its coherence length λ_0. Phase transition model: SM+H^6. Panels: left turbulence, right bubble collisions. Colour coding: strength of transition, $\alpha(\Lambda)$. Arrows: B_0 evolution due to inverse cascade. Dashed lines: final B_0 spectra for selected transitions.*

In Fig. 9.3 we show the results for both bubble collisions and plasma-related sources for all of the SM+H^6 parameter space with a reasonably strong transition. We see that the calculated field strength generically exhibits a peak at a coherence scale λ_0 given by Eq. (9.17), which originates from the break in the initial magnetic field energy density shown in Eq. (9.7). The value of λ_0 at the peak and the corresponding value of B_0 depend on the strength α of the transition, which depends in turn on the scale Λ of the $|H|^6$ operator, as indicated by the colour coding. The left panel of Fig. 9.3 shows the possible contribution to the magnetic field spectrum from turbulence, and the right panel shows that from bubble collisions. In each panel we also exhibit the evolution of the field due to the inverse cascade in the plasma background under the hypotheses that the primordial field is due to helical field configurations or kinetic helicity.

We see that the magnetic field strength due to turbulence may well exceed the blazar lower limit, peaking at a coherence scale $\sim 10^{-5}$ to $\sim 10^{-2}$ Mpc. On the other hand, it is not possible to explain the blazar data with a magnetic field produced by bubble collisions in the plasma after the phase transition in this model, even when the transition is rather strong and the field becomes fully helical quickly after it is produced.

The parameter region where the phase transition is strong offers other possible experimental probes. We consider first the GWs produced by the same phenomena responsible for magnetic field production [220–222].

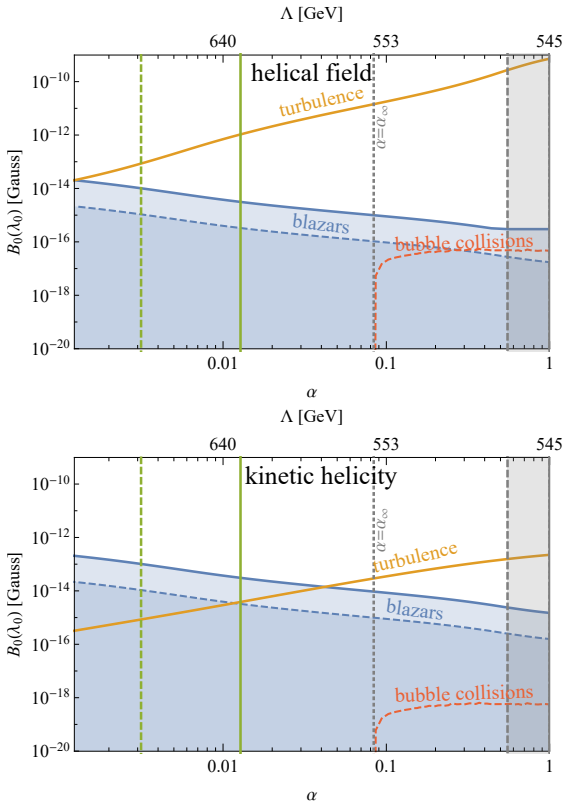

Fig. 9.4 *Magnetic field strength B_0 as a function of transition strength α. Phase transition model: SM+H^6. Panels: top magnetic helcity, bottom kinetic helicity. Axes: bottom transition strength α, top cut-off scale Λ. Curve colours: orange B_0 from turbulence, red B_0 from bubble collisions Green vertical lines (RHS): sensitive to HL-LHC signal (dashed 2-σ, solid 3-σ). α_∞ grey vertical line (RHS): bubble wall overcomes leading-order plasma friction.*

In Fig. 9.4 we show the strength of the magnetic field and in Fig. 9.5 the signal-to-noise ratio (SNR) in the planned GW experiments most relevant for this model: LISA [165], MAGIS [223, 224] and AION [225]. [4] As we can see, the strength of both magnetic field and GW signal produced grows with the strength of the transition. Both the signals are also produced predominantly by plasma related sources with bubble collisions predicting a contribution too weak to explain the observed IGMF. The conclusion here is that, as expected, the GW signals and magnetic field production are correlated and, in the case of purely kinetic helicity, future GW experiments will be able to probe all of the parameter space in which the resulting magnetic field is strong enough to satisfy the blazar bounds. [5]

Another promising avenue for testing such scenarios is in collider experiments, although here the details depend a lot more on the underlying particle physics model [226–228]. In our particular case of a single non-renormalisable H^6 operator the only such probe is through the modification of the triple-Higgs coupling [59], and we indicate the reach of

[4] See [64] for more details on the GW spectra.

[5] This is not necessarily the case if the field becomes fully helical at some point.

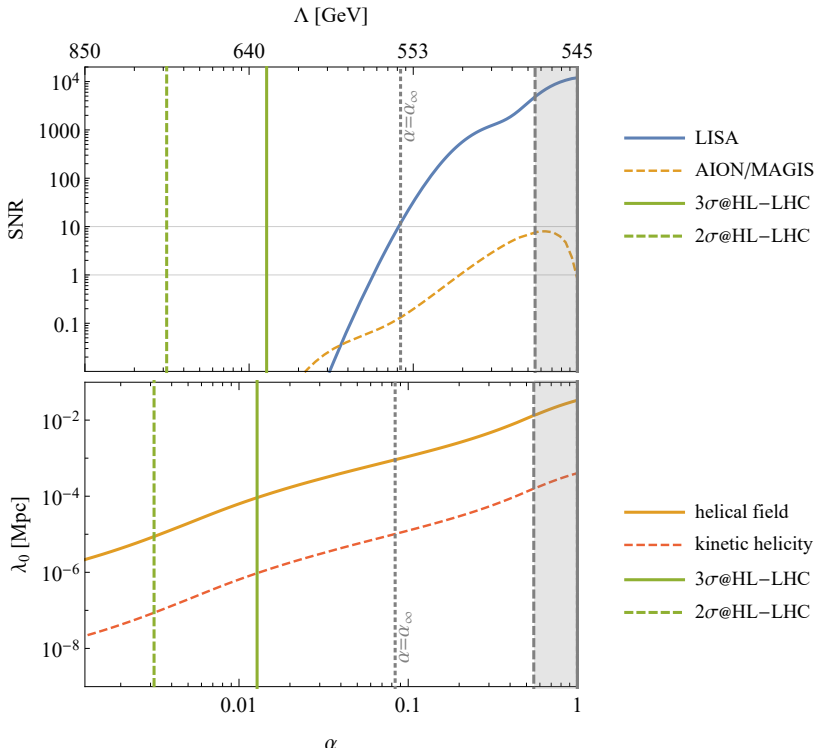

Fig. 9.5 *The top panel shows SNR of the GW signal from the phase transition in the SM+H^6 model for different experiments, while the lower panel indicates the magnetic field coherence scale. The solid and dashed lines in the lower panel correspond to evolution assuming a helical magnetic field or kinetic helicity, as shown in Fig. 9.3.*

HL-LHC in Fig 9.4 and Fig 9.5, expressed as the scale Λ associated with the $|H|^6$ operator. We see that HL-LHC will also be able to probe all of the parameter space relevant from the point of view of magnetic field production. However, this is a model-dependent statement that would not necessarily be true in other SM extensions e.g. singlet scalar [229, 230].

9.6.3 Classically scale invariant $U(1)_{B-L}$

In the classically scale-invariant U$(1)_{B-L}$ extension of the SM (Sec. 5.5.2) the transition can be very strong, $\alpha \gg 1$. The breaking of the U$(1)_{B-L}$ gauge symmetry is triggered by a new hidden scalar field φ. The thermal corrections to its scalar potential induce a barrier between the $B-L$-symmetric and $B-L$-breaking minima, so that the transition is first-order. These corrections are dominated by the $B-L$ gauge boson Z'. Therefore, the $B-L$ gauge coupling g_{B-L} and the Z' mass $m_{Z'}$ determine the dynamics of the transition. As the hidden φ field acquires a non-zero vacuum expectation value, it triggers electroweak symmetry breaking via the portal coupling $-\lambda_p h^2\varphi^2/4$. We show results for $m_{Z'} = 4\,\text{TeV}$ (LHC energies) and $m_{Z'} = 40\,\text{TeV}$ (100 TeV circular collider energies). [6]

[6] Using the latest constraints from the ATLAS collaboration [231], we find that the 95% confidence level constraints on the gauge coupling g_{B-L} are $\{0.11, 0.40, 0.83\}$ for $m_{Z'} = \{3\,\text{TeV}, 4\,\text{TeV}, 5\,\text{TeV}\}$ respectively.

Production of magnetic fields in this model is less trivial than in SM extensions that modify the Higgs potential to feature a first-order phase transition. The reason is that most of the transition energy is carried by bubbles of the new scalar field φ, or is transferred to the dark sector Z' plasma, neither of which contribute to magnetic fields directly.

If the transition proceeds at sufficiently low temperatures $T_* \lesssim 140\,\mathrm{GeV}$ (Sec. 5.5.2) the bubble wall is made up of the usual hidden scalar φ and an additional Higgs component h. In this scenario a small fraction of bubble wall energy is stored in the Higgs component of the bubble wall, proportional to $\kappa_h \equiv \Delta V_h/\Delta V_\varphi$, which is small due to the large ratio between the vacuum expectation values of the fields. Provided that kinetic mixing between the $\mathrm{U}(1)_Y$ and $\mathrm{U}(1)_{B-L}$ gauge fields is present, part of the energy deposited into the dark plasma is expected to be transferred to the SM fields. However [65] showed that magnetic field transfer from a dark $\mathrm{U}(1)$ to the visible $\mathrm{U}(1)$ through kinetic mixing is not efficient and the transferred magnetic field is weaker than that generated directly.

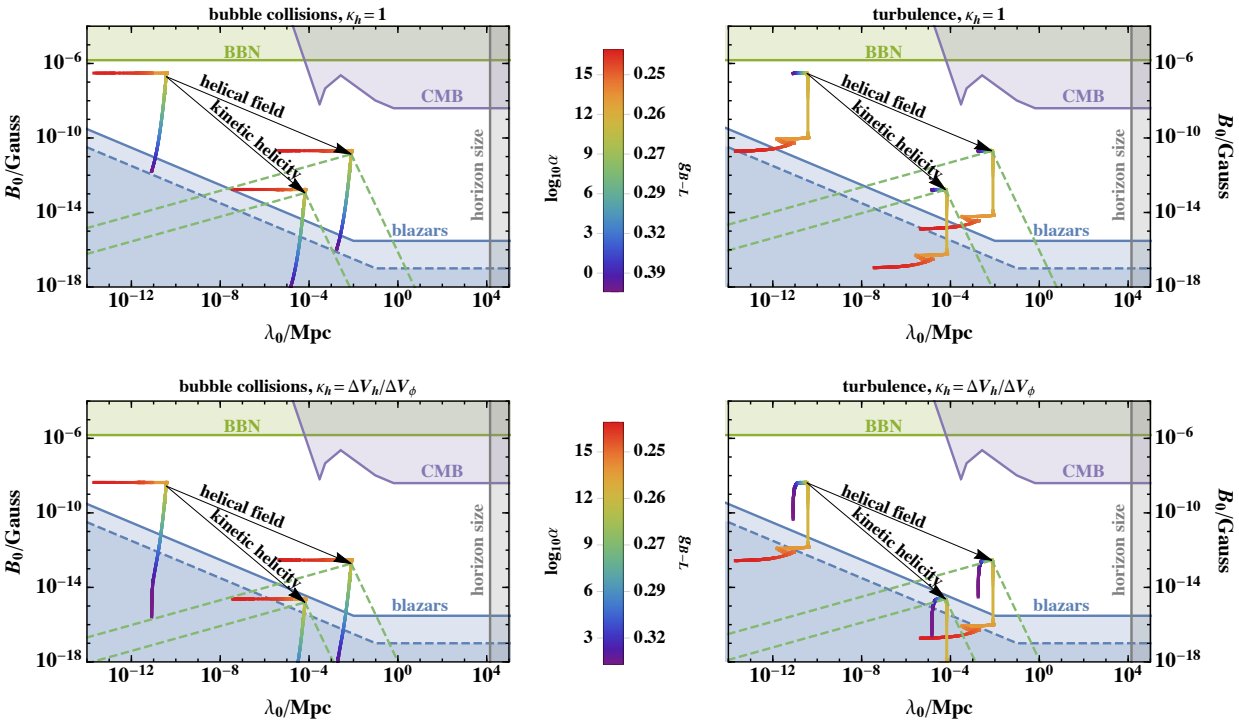

Fig. 9.6 *Results as in Fig. 9.3 computed for SM_{B-L} model with $m_{Z'} = 4\,\mathrm{TeV}$. The upper panels show optimistic results assuming all phase transition energy is transferred into the visible sector, and lower panels are for realistic cases in which only the Higgs field bubbles produce magnetic fields, with no contribution from heavy fields beyond the SM.*

In Fig. 9.6 we show the predicted magnetic field strengths today for a range of possible coherence lengths of the field, generated from a first order $U(1)_{B-L}$ phase transition. Magnetic fields that are generated predominantly by bubble collisions are shown in the left panels whilst those generated by turbulence are shown in the right panels. In the bottom panels we show our results for fields that are generated with $\kappa_h = \Delta V_h/\Delta V_\varphi$ which

corresponds to the more realistic case where the magnetic field are produced purely by the Higgs component of the bubble wall with negligible kinetic mixing between the hidden and visible sectors. For comparison, in the top panels we also show the overly optimistic case with no suppression, $\kappa_h = 1$, that would correspond to the case where the transfer of the magnetic field from the dark U(1) to the visible one would be very efficient.

Summarising our findings from Fig. 9.6, we see that both bubble collisions and turbulence may yield a peak above the blazar lower limit if the primordial field was seeded by magnetic helicity even when including the $\kappa_h = \Delta V_h/\Delta V_\varphi$ suppression but this is not always true in the case of initial kinetic helicity.

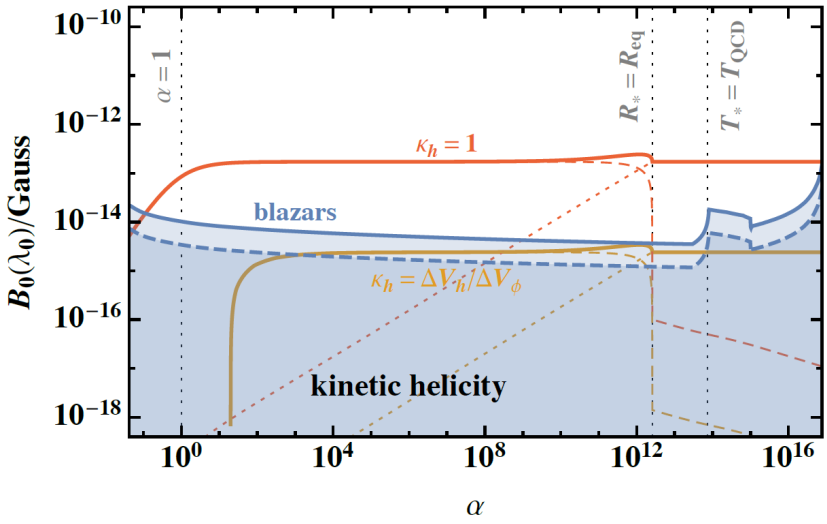

Fig. 9.7 *The red and yellow lines show the magnetic field strength B_0 at the coherence scale λ_0 with and without the $\Delta V_h/\Delta V_\varphi$ suppression. The short and long dashed lines show separately the contributions from bubble collisions and turbulence in the plasma. The upper and lower panels correspond respectively to evolution assuming a helical magnetic field or kinetic helicity, as shown in Fig. 9.6.*

In Fig. 9.7 we show the total strength of the magnetic field as a function of the phase transition strength α for a transition with initial kinetic helicity where the mass of the Z' boson is $M_{Z'} = 4$ Tev. The case with the $\kappa_h = \Delta V_h/\Delta V_\varphi$ supression is shown in yellow whilst the overly optimistic case with no suppression, $\kappa_h = 1$, is shown in orange. In each of these scenarios we show the individual contributions from bubble collisions (coloured short dashed lines) and turbulence (coloured long dashed lines) to the overall magnetic field strength (coloured thick lines). Which of these two source dominate the magnetic field generation is clearly dictated by whether the α value of the PT is to the left (turbulence dominated) or right (bubble collisions dominated) of the $R_* = R_{eq}$ line (grey dashed vertical line) which we will explain the meaning of presently.

In the $U(1)_{B-L}$ model the phase transition tends to be very strong with $\alpha \gg 1$, as can be seen in Fig. 9.7 where most of the observable parameter space lies to the right of the

grey $\alpha = 1$ line. This results in the γ_w factors, which parameterise the bubble wall speed, tending to be very large and the γ_w dependent next-to-leading order friction term arising from transition radiation in the plasma becomes important (see Sec. 5.3).

In these scenarios one can calculate the γ_w factor at which the vacuum energy driving the bubble wall forward balances both the leading order and the γ_w dependent next-to-leading order friction. At this speed, $\gamma_w = \gamma_{eq}$, the wall reaches terminal velocity. This can be expressed in terms of a bubble radius at which the bubble wall reaches terminal velocity, $R_* = R_{eq}$, marked as a grey dashed vertical line on Fig. 9.7.

For α values to the left of this line, the next-to-leading order friction term successfully balances the pressure driving the walls expansion and the bubble walls reach terminal velocity before collision i.e. $R_* > R_{eq}$. This results in there being a significant period of time where the vacuum energy is deposited into the plasma so that the plasma ends up being the dominant source of magnetic fields.

For α values to the right of the $R_* = R_{eq}$ line, the PT is so strongly super-cooled that that the vacuum energy released outweighs the next-to-leading order plasma friction and the bubbles are said to run away (see Sec. 5.4). In this case, the bubble walls do not reach terminal velocity before percolation, $R_* < R_{eq}$, which means most of the energy released in the PT is stored in the bubble wall at collision and so bubble collisions are the dominant source of magnetic field generation.

As explained in Sec. 5.5.2, if the hidden φ transition percolates below the scale of the QCD phase transition then the φ field takes on a small VEV, v_{QCD}, prior to the transition. This subsequently induces a small negative mass term in the φ field that acts to reduce the size of the barrier between $\varphi = 0$ and $\varphi = v_\varphi$. A reduction in the size of the barrier height means it is easier for the field to thermally jump over the barrier which leads to a larger nucleation rate of bubbles of the new phase. This means there are more bubbles nucleated per Hubble horizon and each bubble has less time to get large before it collides, which results in a reduction in R_* and, ultimately, a reduction in the coherence length of the magnetic field. We see this effect in Fig. 9.7, where at $T_* = T_{QCD}$ (grey vertical dashed line) there is an increase in the blazar bounds for transitions that happen at temperatures $T_* < T_{QCD}$ shown to the right of this $T_* = T_{QCD}$ line, owing to the fact that there is a decrease in the correlation length of the field for transitions happening around these temperature. This effect is seen more clearly later on in the lower panels of Fig. 9.9 where we plot the coherence length of the magnetic field as a function of α and also in the upper panels of Fig. 9.9 where we plot the GW SNR as a function of α for a $U(1)_{B-L}$ phase transition.

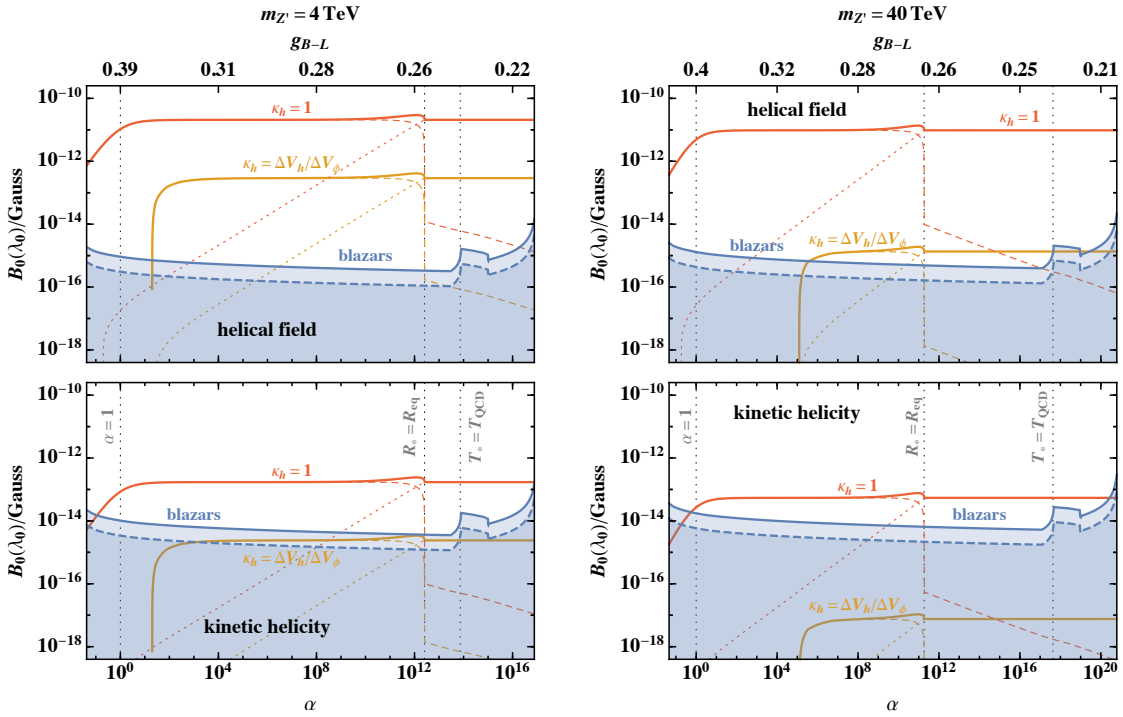

Fig. 9.8 *The red and yellow lines show the magnetic field strength B_0 at the coherence scale λ_0 with and without the $\Delta V_h/\Delta V_\varphi$ suppression. The short and long dashed lines show separately the contributions from bubble collisions and turbulence in the plasma. The upper and lower panels correspond respectively to evolution assuming a helical magnetic field or kinetic helicity, as shown in Fig. 9.6.*

In Fig. 9.8 we show a repeat of the Fig. 9.7 but as part of a comparison of the cases of $m_{Z'} = 4\,\mathrm{TeV}$ (left panels) and $m_{Z'} = 40\,\mathrm{TeV}$ (right panels) for a transition with initial magnetic helicity (upper panels) and initial kintetic helicity (lower panels). In these plots we additionally include the strength of the g_{B-L} gauge coupling on the top axis which dictates much of the phase transition dynamics. Most of the previous analysis holds for each of these plots, in particular we note that the total strength of the magnetic field for $\alpha \gg 1$ is roughly independent of the strength of the transition, with bubble collisions making the dominant contribution when the average radius of the bubbles at percolation is $R < R_{\mathrm{eq}}$ (corresponding to $\alpha \lesssim 10^{12}$), and turbulence dominating at larger α. We see that a magnetic field generated during a first order $U(1)_{B-L}$ phase transition with initial magnetic helicity could well lie above the Blazar bounds but find that the observation prospects are significantly less optimistic when the helicity is seeded kinetically.

After the phase transition, the plasma is reheated to a high temperature where the electroweak symmetry is restored. Then, as the plasma cools, the electroweak symmetry becomes broken again but this time the transition is a smooth crossover. The results of Ref. [232] indicate that in the presence of a helical magnetic field that could explain the blazar observations, an overabundance of baryons is produced in the crossover transition

which would place additional constraints on the helical field case shown in the upper panels of Fig. 9.8. The impact depends on the evolution of the weak mixing angle during the crossover, which has considerable uncertainty. However, it seems that a transition faster than in the SM case [233] is required in order to avoid the baryon overproduction.

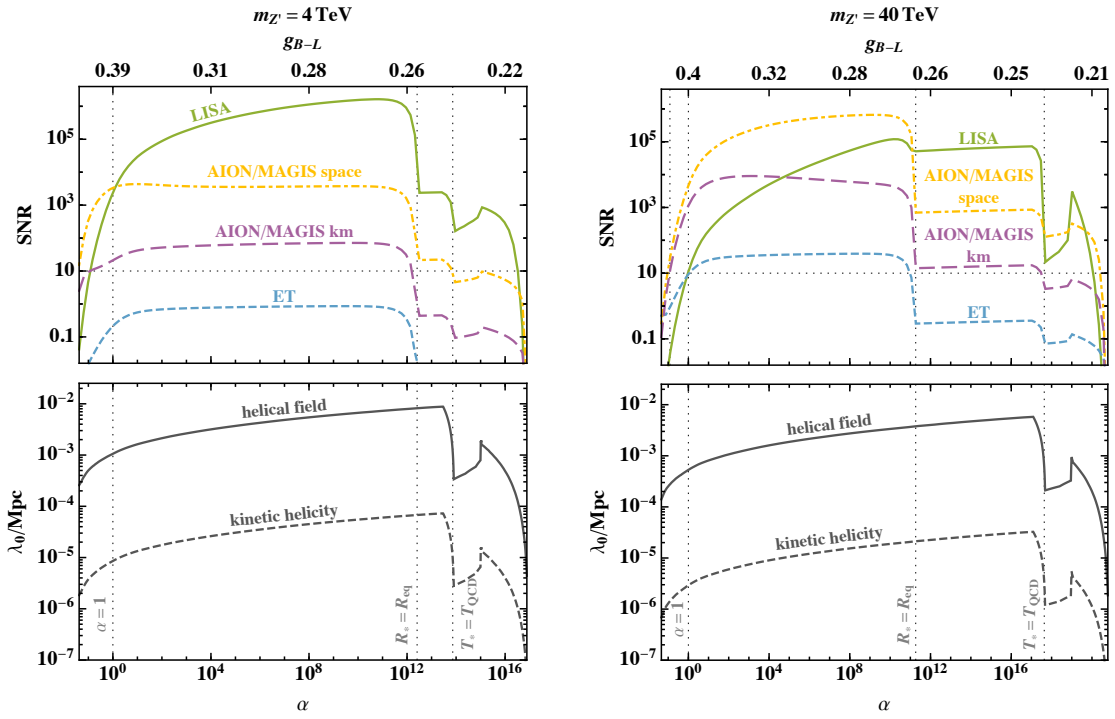

Fig. 9.9 *The lower panels show the coherence scale of the magnetic field produced in the phase transition for the two different evolutions shown in Fig. 9.6. The show the SNR of the GW signal from the phase transition for different future observatories.*

In Fig. 9.9 we demonstrate the promising opportunity for complimentary searches for evidence of a $U(1)_{B-L}$ phase transition by utilising upcoming GW experiments together with searches for evidence of an IGMF generated by such an event. In the upper panels we plot the projected SNR of GW signals as a function of the transition strength, α, for different upcoming GW experiments, whilst in the lower panels we plot coherence scale, λ_0, of the magnetic field against α. As seen as in the SM+H^6 model, the coherence scale of the peak of the magnetic field is below 0.01 Mpc in all the cases studied.

Chapter 10

Conclusion

In this thesis we have studied scenarios in quantum field theory that involve the decay of the false vacuum via bubble nucleation, putting particular emphasis on the application of this theory to situations in the early universe where the universe could have undergone a violent first order phase transition. Such an event could have left imprints on the sky that we could search for today using current and future experimental detection programmes and much of this thesis has been geared towards an analysis of the observational prospects of such a goal.

In Chapter 4 we employed a novel approach in terms of 'tunnelling potentials' [16, 17] to find false vacuum decay solutions in potential landscapes with multiple minima. We found that our algorithm can successfully find tunnelling solutions to non-adjacent minima in both single and two field scenarios but that the detailed shape of the potential and relationship of the energy density between successive vacua can have a bearing on whether a solution can be found. This work could form the basis of a more detailed investigation into whether the scenarios in which a solution is not found are due to numerical issues or whether tunnelling directly to non-adjacent minima is simply not possible for these potentials. In the latter situation the false vacuum would then have to decay via successive tunnelling events between neighbouring minima.

In Chapters 6 & 7 we studied phase transitions in hidden sectors that are cold relative to the visible sector and the possible resulting gravitational wave signals. Using a simple example model we have shown that phase transitions in extremely cold hidden sectors can proceed through nucleation of bubbles by tunnelling, as opposed to via thermal fluctuations as occurs if a hidden sector is at roughly the same temperature as the visible sector.

The gravitational wave signals of a tunnelling transition in a cold hidden sectors can be observably different to those produced by a typical thermal transition in a warm hidden sector, owing to the differing dynamics of the bubble walls in the two cases. In particular, in a sufficiently cold hidden sector there is no significant bath of hidden sector states, which if present transfer a proportion of the energy released by the phase transition to bulk

motions of the hidden sector plasma. [1] In this regard, a key difference between our results and earlier work (e.g. [101]) that considered the possibility of gravitational wave signals dominated by bubble collisions, is that we include the recently discovered γ_w dependent friction [54]. This prevents runaway walls in typical thermal transitions, even in those with significant supercooling (which is sufficient to render the γ_w independent friction negligible).

We have also seen that due to BBN constraints cold hidden sectors can lead to gravitational wave signals in a frequency range that would otherwise not be possible. These two effects mean that if a gravitational wave spectrum were to be discovered, it might be possible to show that it comes from a sector that is cold relative to the visible sector. Given that such a sector would be far out of reach of direct exploration by experiments, this would be an extremely interesting discovery. More pessimistically, gravitational wave signals from cold hidden sectors are strongly suppressed in thermally nucleated transitions if the hidden sector is extremely cold, and likewise in tunnelling transitions if the energy released is much smaller than the energy in the visible sector. Observable signals therefore only arise in relatively small regions of hidden sector parameter space.

In Chapter 8 we analysed the prospects for detection of circular polarisation of the stochastic GW background produced by a first-order phase transition at a temperature $T_* \geq 100$ GeV. We focused on an analytical model for the sourcing of GWs by MHD turbulence produced in the plasma during the transition. Crucially, the model allows us to describe not only a direct energy cascade in the plasma but also an inverse cascade that develops if there is some initial helicity fraction in the fluid motion, usually sourced from helicity left over in the magnetic field after the transition. The direct cascade describes energy transferred into smaller scales, and the resulting signal peak corresponds to the characteristic scale of the transition, which is related to the average bubble size R_*. The signal produced during the second stage of inverse cascade turbulence will be circularly polarised and, provided the initial helicity fraction is large enough, it results in an overall stochastic background with a significant degree of polarisation.

We have revisited the capability of future GW detectors to measure the polarisation of a SGWB background, focusing on LISA. We find that in the model we use to describe the signal arising from MHD turbulence following a phase transition, detection with $\mathrm{SNR}_{\mathrm{pol}} > 10$ could be possible. However, this would require a sufficiently strong phase transition with $\alpha \gtrapprox 1$ as well as either a large helicity fraction close to unity or large bubbles of sizes approaching the horizon size. The smaller the helicity fraction, the more supercooled the transition would have to be to produce an observable polarisation in

[1] At present, it is unknown if thermal transitions in unusual models could also lead to overwhelmingly bubble collision sourced spectra, and this is an important area for future work. However, even if such thermal transitions turn out to be possible, the theories that give rise to them will have to have unusual properties, so observation of a bubble collision dominated signal will remain exciting, even if it does not conclusively point to a cold hidden sector.

the stochastic GW background signal. We conclude that LISA may have a significant opportunity to measure polarisation of the SGWB, whilst also emphasising that the model we have used to calculate the amount of polarisation certainly requires improvement and should be tensioned against other models as they emerge.

Finally in Chapter 9 we revisited the possibility of generating magnetic fields during a first-order phase transition in the early universe. Since the electroweak phase transition is second-order in the SM, we have considered two well motivated beyond the Standard Model extensions. First we considered a dimension-6 extension of the Higgs potential that leads directly to a first-order phase transition. We showed that, in such a model, the strong coupling between the Higgs and the rest of the SM would result in friction that would slow the motion of bubble walls, suppressing the subsequent generation of magnetic fields. We also showed, however, that turbulence created by vorticity in gauge fields in the plasma could create magnetic fields with interesting magnitudes. We also calculated the corresponding gravitational wave signal associated with such phase transitions.

The second model we considered was a minimal extension of the SM with an additional scalar φ associated with a $B-L$ gauge symmetry. In this situation, the field φ can undergo a strong first-order phase transition where most of the energy goes into the bubble wall rather than the plasma. A part of this energy is later transmitted to the SM fields via a portal coupling, potentially leading to large magnetic fields. Again we have calculated the gravitational wave signal for this model. The strength of the magnetic field goes down as the mass of the Z' boson increases, and the existing limits on $m_{Z'}$ and g_{B-L} from the LHC leave open a region where it is possible to explain the observed magnetic fields. However, this window could be further constrained by baryon overproduction.

In case of the $U(1)_{B-L}$ model, whenever we are able to produce magnetic fields with sufficient magnitude to explain the *Fermi* data, we produce enough GWs to be detected by one of the future experiments. This is not the case in the $SM + H^6$ model, where GW experiments will be able to probe all of the relevant parameter space only if the magnetic field is seeded by kinetic helicity, whereas a fully helical magnetic field could be produced without a corresponding GW signal being within reach. In this model, however, the HL-LHC will be able to probe all of the relevant parameter space. These conclusions suggest that, generically, the production of strong intergalactic magnetic fields through a phase transition in the early universe may lead to other observable signals either in future GW experiments or at a future collider.

The renewed interest in strong first-order phase transitions due to recent developments in GW detection shows no sign of diminishing. When considering such phase transitions and their effects upon the SM gauge fields, it is natural to wonder if the magnetic fields seen in cosmic voids may have such a dramatic origin. This work shows that this is indeed possible under appropriate conditions.

References

[1] S. R. Coleman, *The Fate of the False Vacuum. 1. Semiclassical Theory*, *Phys. Rev.* **D15** (1977) 2929–2936.

[2] A. D. Linde, *Fate of the False Vacuum at Finite Temperature: Theory and Applications*, *Phys. Lett.* **100B** (1981) 37–40.

[3] LIGO SCIENTIFIC, VIRGO collaboration, B. P. Abbott et al., *Observation of Gravitational Waves from a Binary Black Hole Merger*, *Phys. Rev. Lett.* **116** (2016) 061102, [1602.03837].

[4] NANOGRAV collaboration, Z. Arzoumanian et al., *The NANOGrav 12.5 yr Data Set: Search for an Isotropic Stochastic Gravitational-wave Background*, *Astrophys. J. Lett.* **905** (2020) L34, [2009.04496].

[5] A. Addazi, Y.-F. Cai, Q. Gan, A. Marciano and K. Zeng, *NANOGrav results and Dark First Order Phase Transitions*, 2009.10327.

[6] Y. Nakai, M. Suzuki, F. Takahashi and M. Yamada, *Gravitational Waves and Dark Radiation from Dark Phase Transition: Connecting NANOGrav Pulsar Timing Data and Hubble Tension*, 2009.09754.

[7] W. Ratzinger and P. Schwaller, *Whispers from the dark side: Confronting light new physics with NANOGrav data*, *SciPost Phys.* **10** (2021) 047, [2009.11875].

[8] S. Blasi, V. Brdar and K. Schmitz, *Has NANOGrav found first evidence for cosmic strings?*, *Phys. Rev. Lett.* **126** (2021) 041305, [2009.06607].

[9] W. Buchmuller, V. Domcke and K. Schmitz, *From NANOGrav to LIGO with metastable cosmic strings*, *Phys. Lett. B* **811** (2020) 135914, [2009.10649].

[10] V. De Luca, G. Franciolini and A. Riotto, *NANOGrav Data Hints at Primordial Black Holes as Dark Matter*, *Phys. Rev. Lett.* **126** (2021) 041303, [2009.08268].

[11] J. Ellis and M. Lewicki, *Cosmic String Interpretation of NANOGrav Pulsar Timing Data*, *Phys. Rev. Lett.* **126** (2021) 041304, [2009.06555].

[12] V. Vaskonen and H. Veermäe, *Did NANOGrav see a signal from primordial black hole formation?*, *Phys. Rev. Lett.* **126** (2021) 051303, [2009.07832].

[13] M. Fairbairn, E. Hardy and A. Wickens, *Hearing without seeing: gravitational waves from hot and cold hidden sectors*, *JHEP* **07** (2019) 044, [1901.11038].

[14] J. Ellis, M. Fairbairn, M. Lewicki, V. Vaskonen and A. Wickens, *Detecting circular polarisation in the stochastic gravitational-wave background from a first-order cosmological phase transition*, *JCAP* **10** (2020) 032, [2005.05278].

[15] J. Ellis, M. Fairbairn, M. Lewicki, V. Vaskonen and A. Wickens, *Intergalactic Magnetic Fields from First-Order Phase Transitions*, *JCAP* **09** (2019) 019, [1907.04315].

[16] J. R. Espinosa, *A Fresh Look at the Calculation of Tunneling Actions*, *JCAP* **07** (2018) 036, [1805.03680].

[17] J. R. Espinosa and T. Konstandin, *A Fresh Look at the Calculation of Tunneling Actions in Multi-Field Potentials*, *JCAP* **01** (2019) 051, [1811.09185].

[18] L. I. Schiff, *Quantum Mechanics*. McGraw-Hill, third ed., 1968.

[19] T. Banks, C. M. Bender and T. T. Wu, *Coupled anharmonic oscillators. 1. Equal mass case*, *Phys. Rev.* **D8** (1973) 3346–3378.

[20] J.-L. Gervais and B. Sakita, *WKB Wave Function for Systems with Many Degrees of Freedom: A Unified View of Solitons and Instantons*, *Phys. Rev.* **D16** (1977) 3507.

[21] A. I. Vainshtein, V. I. Zakharov, V. A. Novikov and M. A. Shifman, *ABC's of Instantons*, *Sov. Phys. Usp.* **25** (1982) 195.

[22] R. P. R. P. Feynman, *Quantum Mechanics and Path Integrals*. New York:McGraw-Hill, 1965.

[23] E. Brezin, G. Parisi and J. Zinn-Justin, *Perturbation Theory at Large Orders for Potential with Degenerate Minima*, *Phys. Rev.* **D16** (1977) 408–412.

[24] T. Lancaster and S. J. Blundell, *Quantum Field Theory for the Gifted Amateur*. Oxford University Press, 2014.

[25] M. Mariño, *Instantons and Large N*. Cambridge University Press, 2015.

[26] E. J. Weinberg, *Classical solutions in quantum field theory*. Cambridge Monographs on Mathematical Physics. Cambridge University Press, 2015.

[27] S. R. Coleman, *"The uses of instantons" in Aspects of Symmetry: Selected Erice Lectures*. Cambridge University Press, 1985.

[28] E. C. G. Sudarshan, C. B. Chiu and V. Gorini, *Decaying States as Complex Energy Eigenvectors in Generalized Quantum Mechanics*, *Phys. Rev.* **D18** (1978) 2914.

[29] S. R. Coleman, *Quantum Tunneling and Negative Eigenvalues*, *Nucl. Phys.* **B298** (1988) 178–186.

[30] G. Munster and S. Rotsch, *Analytical calculation of the nucleation rate for first order phase transitions beyond the thin wall approximation*, *Eur. Phys. J.* **C12** (2000) 161–171.

[31] S. R. Coleman, V. Glaser and A. Martin, *Action Minima Among Solutions to a Class of Euclidean Scalar Field Equations*, *Commun. Math. Phys.* **58** (1978) 211.

[32] A. Megevand, *Development of the electroweak phase transition and baryogenesis*, *Int. J. Mod. Phys.* **D9** (2000) 733–756.

[33] K.-M. Lee and E. J. Weinberg, *TUNNELING WITHOUT BARRIERS*, *Nucl. Phys.* **B267** (1986) 181–202.

[34] A. Masoumi, K. D. Olum and B. Shlaer, *Efficient numerical solution to vacuum decay with many fields*, *JCAP* **01** (2017) 051, [1610.06594].

[35] C. L. Wainwright, *CosmoTransitions: Computing Cosmological Phase Transition Temperatures and Bubble Profiles with Multiple Fields*, *Comput. Phys. Commun.* **183** (2012) 2006–2013, [1109.4189].

[36] A. Masoumi, *Topics in vacuum decay*. PhD thesis, Columbia U., 2013. 1505.06397.

[37] K. Friston, J. Mattout, N. Trujillo-Barreto, J. Ashburner and W. Penny, *Variational free energy and the laplace approximation*, *Neuroimage* **34** (2007) 220–234.

[38] M. R. Douglas, *The Statistics of string / M theory vacua*, *JHEP* **05** (2003) 046, [hep-th/0303194].

[39] L. Susskind, *The cosmic landscape: String theory and the illusion of intelligent design*. 2005.

[40] S. Kachru, R. Kallosh, A. D. Linde and S. P. Trivedi, *De Sitter vacua in string theory*, *Phys. Rev. D* **68** (2003) 046005, [hep-th/0301240].

[41] R. Bousso and J. Polchinski, *Quantization of four form fluxes and dynamical neutralization of the cosmological constant*, *JHEP* **06** (2000) 006, [hep-th/0004134].

[42] A. Linde, *A brief history of the multiverse*, *Rept. Prog. Phys.* **80** (2017) 022001, [1512.01203].

[43] S. H. Henry Tye, *A New view of the cosmic landscape*, hep-th/0611148.

[44] K. Freese, J. T. Liu and D. Spolyar, *Chain inflation via rapid tunneling in the landscape*, hep-th/0612056.

[45] D. Chialva and U. H. Danielsson, *Chain inflation revisited*, *JCAP* **10** (2008) 012, [0804.2846].

[46] Q.-G. Huang and S. H. H. Tye, *The Cosmological Constant Problem and Inflation in the String Landscape*, *Int. J. Mod. Phys. A* **24** (2009) 1925–1962, [0803.0663].

[47] P. Athron, C. Balázs, M. Bardsley, A. Fowlie, D. Harries and G. White, *BubbleProfiler: finding the field profile and action for cosmological phase transitions*, *Comput. Phys. Commun.* **244** (2019) 448–468, [1901.03714].

[48] D. D. Morrison, J. D. Riley and J. F. Zancanaro, *Multiple shooting method for two-point boundary value problems*, *Commun. ACM* **5** (Dec., 1962) 613–614.

[49] G. H. Derrick, *Comments on nonlinear wave equations as models for elementary particles*, *J. Math. Phys.* **5** (1964) 1252–1254.

[50] K. Freese, J. T. Liu and D. Spolyar, *Inflating with the QCD axion*, *Phys. Rev. D* **72** (2005) 123521, [hep-ph/0502177].

[51] A. D. Linde, *Decay of the False Vacuum at Finite Temperature*, *Nucl. Phys.* **B216** (1983) 421.

[52] T. Prokopec, "Lecture notes for cosmology: The standard cosmological model." https://webspace.science.uu.nl/~proko101/2scm.pdf, 2008.

[53] D. Bodeker and G. D. Moore, *Can electroweak bubble walls run away?*, *JCAP* **0905** (2009) 009, [0903.4099].

[54] D. Bodeker and G. D. Moore, *Electroweak Bubble Wall Speed Limit*, *JCAP* **1705** (2017) 025, [1703.08215].

[55] J. R. Espinosa, T. Konstandin, J. M. No and G. Servant, *Energy Budget of Cosmological First-order Phase Transitions*, *JCAP* **1006** (2010) 028, [1004.4187].

[56] K. Kajantie, M. Laine, K. Rummukainen and M. E. Shaposhnikov, *Is there a hot electroweak phase transition at m(H) larger or equal to m(W)?*, *Phys. Rev. Lett.* **77** (1996) 2887–2890, [hep-ph/9605288].

[57] M. D'Onofrio, K. Rummukainen and A. Tranberg, *Sphaleron Rate in the Minimal Standard Model*, *Phys. Rev. Lett.* **113** (2014) 141602, [1404.3565].

[58] G. C. Dorsch, S. J. Huber, T. Konstandin and J. M. No, *A Second Higgs Doublet in the Early Universe: Baryogenesis and Gravitational Waves*, *JCAP* **1705** (2017) 052, [1611.05874].

[59] J. Ellis, M. Lewicki and J. M. No, *On the Maximal Strength of a First-Order Electroweak Phase Transition and its Gravitational Wave Signal*, *Submitted to: JCAP* (2018) , [1809.08242].

[60] B. S. Acharya, S. A. R. Ellis, G. L. Kane, B. D. Nelson and M. Perry, *Categorisation and Detection of Dark Matter Candidates from String/M-theory Hidden Sectors*, *JHEP* **09** (2018) 130, [1707.04530].

[61] P. Schwaller, *Gravitational Waves from a Dark Phase Transition*, *Phys. Rev. Lett.* **115** (2015) 181101, [1504.07263].

[62] M. Fairbairn, K. Kainulainen, T. Markkanen and S. Nurmi, *Despicable Dark Relics: generated by gravity with unconstrained masses*, 1808.08236.

[63] C. Marzo, L. Marzola and V. Vaskonen, *Phase transition and vacuum stability in the classically conformal B–L model*, *Eur. Phys. J. C* **79** (2019) 601, [1811.11169].

[64] J. Ellis, M. Lewicki, J. M. No and V. Vaskonen, *Gravitational wave energy budget in strongly supercooled phase transitions*, *JCAP* **1906** (2019) 024, [1903.09642].

[65] K. Kamada, Y. Tsai and T. Vachaspati, *Magnetic Field Transfer From A Hidden Sector*, *Phys. Rev.* **D98** (2018) 043501, [1803.08051].

[66] S. Iso, P. D. Serpico and K. Shimada, *QCD-Electroweak First-Order Phase Transition in a Supercooled Universe*, *Phys. Rev. Lett.* **119** (2017) 141301, [1704.04955].

[67] A. Katz and A. Riotto, *Baryogenesis and Gravitational Waves from Runaway Bubble Collisions*, *JCAP* **1611** (2016) 011, [1608.00583].

[68] T. Hambye, *Hidden vector dark matter*, *JHEP* **01** (2009) 028, [0811.0172].

[69] T. Hambye and A. Strumia, *Dynamical generation of the weak and Dark Matter scale*, *Phys. Rev.* **D88** (2013) 055022, [1306.2329].

[70] V. V. Khoze, C. McCabe and G. Ro, *Higgs vacuum stability from the dark matter portal*, *JHEP* **08** (2014) 026, [1403.4953].

[71] A. Karam and K. Tamvakis, *Dark matter and neutrino masses from a scale-invariant multi-Higgs portal*, *Phys. Rev.* **D92** (2015) 075010, [1508.03031].

[72] I. Baldes and C. Garcia-Cely, *Strong gravitational radiation from a simple dark matter model*, *JHEP* **05** (2019) 190, [1809.01198].

[73] T. Hambye, A. Strumia and D. Teresi, *Super-cool Dark Matter*, *JHEP* **08** (2018) 188, [1805.01473].

[74] J. Jaeckel, V. V. Khoze and M. Spannowsky, *Hearing the signal of dark sectors with gravitational wave detectors*, *Phys. Rev.* **D94** (2016) 103519, [1602.03901].

[75] S. R. Coleman and E. J. Weinberg, *Radiative Corrections as the Origin of Spontaneous Symmetry Breaking*, *Phys. Rev.* **D7** (1973) 1888–1910.

[76] J. I. Kapusta and C. Gale, *Finite-temperature field theory: Principles and applications*. Cambridge Monographs on Mathematical Physics. Cambridge University Press, 2011, 10.1017/CBO9780511535130.

[77] D. Curtin, P. Meade and H. Ramani, *Thermal Resummation and Phase Transitions*, 1612.00466.

[78] M. E. Carrington, *The Effective potential at finite temperature in the Standard Model*, *Phys. Rev.* **D45** (1992) 2933–2944.

[79] P. Fendley, *The Effective Potential and the Coupling Constant at High Temperature*, *Phys. Lett.* **B196** (1987) 175–180.

[80] J. R. Espinosa and M. Quiros, *Improved metastability bounds on the standard model Higgs mass*, *Phys. Lett.* **B353** (1995) 257–266, [hep-ph/9504241].

[81] P. Adshead, Y. Cui and J. Shelton, *Chilly Dark Sectors and Asymmetric Reheating*, *JHEP* **06** (2016) 016, [1604.02458].

[82] E. Hardy and J. Unwin, *Symmetric and Asymmetric Reheating*, *JHEP* **09** (2017) 113, [1703.07642].

[83] T. Flacke, C. Frugiuele, E. Fuchs, R. S. Gupta and G. Perez, *Phenomenology of relaxion-Higgs mixing*, *JHEP* **06** (2017) 050, [1610.02025].

[84] I. Affleck, *Quantum Statistical Metastability*, *Phys. Rev. Lett.* **46** (1981) 388.

[85] M. S. Turner, E. J. Weinberg and L. M. Widrow, *Bubble nucleation in first order inflation and other cosmological phase transitions*, *Phys. Rev.* **D46** (1992) 2384–2403.

[86] G. W. Anderson and L. J. Hall, *The Electroweak phase transition and baryogenesis*, *Phys. Rev.* **D45** (1992) 2685–2698.

[87] D. Huang and B.-Q. Lu, *Comment on "Hearing the signal of dark sectors with gravitational wave detectors"*, *Phys. Rev.* **D97** (2018) 068303, [1803.03180].

[88] A. Strumia, N. Tetradis and C. Wetterich, *The Region of validity of homogeneous nucleation theory*, *Phys. Lett.* **B467** (1999) 279–288, [hep-ph/9808263].

[89] A. Strumia and N. Tetradis, *Bubble nucleation rates for cosmological phase transitions*, *JHEP* **11** (1999) 023, [hep-ph/9904357].

[90] A. Strumia and N. Tetradis, *A Consistent calculation of bubble nucleation rates*, *Nucl. Phys.* **B542** (1999) 719–741, [hep-ph/9806453].

[91] A. Strumia and N. Tetradis, *Bubble nucleation rates for radiatively induced first order phase transitions*, *Nucl. Phys.* **B554** (1999) 697–718, [hep-ph/9811438].

[92] G. D. Moore and K. Rummukainen, *Electroweak bubble nucleation, nonperturbatively*, *Phys. Rev.* **D63** (2001) 045002, [hep-ph/0009132].

[93] B. W. Mintz, A. Bessa and E. S. Fraga, *On the nucleation of hadronic domains in the quark-hadron transition*, *Nucl. Phys.* **A820** (2009) 291C–294C, [0810.2798].

[94] A. Bessa, E. S. Fraga and B. W. Mintz, *Phase conversion in a weakly first-order quark-hadron transition*, *Phys. Rev.* **D79** (2009) 034012, [0811.4385].

[95] A. Megevand and S. Ramirez, *Bubble nucleation and growth in very strong cosmological phase transitions*, *Nucl. Phys.* **B919** (2017) 74–109, [1611.05853].

[96] J. R. Espinosa, T. Konstandin, J. M. No and M. Quiros, *Some Cosmological Implications of Hidden Sectors*, *Phys. Rev.* **D78** (2008) 123528, [0809.3215].

[97] A. H. Guth and E. J. Weinberg, *Could the Universe Have Recovered from a Slow First Order Phase Transition?*, *Nucl. Phys.* **B212** (1983) 321–364.

[98] T. Konstandin, G. Nardini and M. Quiros, *Gravitational Backreaction Effects on the Holographic Phase Transition*, *Phys. Rev.* **D82** (2010) 083513, [1007.1468].

[99] T. Konstandin and G. Servant, *Cosmological Consequences of Nearly Conformal Dynamics at the TeV scale*, *JCAP* **1112** (2011) 009, [1104.4791].

[100] V. Brdar, A. J. Helmboldt and J. Kubo, *Gravitational Waves from First-Order Phase Transitions: LIGO as a Window to Unexplored Seesaw Scales*, 1810.12306.

[101] C. Caprini et al., *Science with the space-based interferometer eLISA. II: Gravitational waves from cosmological phase transitions*, *JCAP* **1604** (2016) 001, [1512.06239].

[102] C. J. Hogan, *Nucleation of cosmological phase transitions*, *Phys. Lett.* **133B** (1983) 172–176.

[103] P. Binetruy, A. Bohe, C. Caprini and J.-F. Dufaux, *Cosmological Backgrounds of Gravitational Waves and eLISA/NGO: Phase Transitions, Cosmic Strings and Other Sources*, *JCAP* **1206** (2012) 027, [1201.0983].

[104] D. J. Weir, *Gravitational waves from a first order electroweak phase transition: a brief review*, *Phil. Trans. Roy. Soc. Lond.* **A376** (2018) 20170126, [1705.01783].

[105] C. Caprini, R. Durrer, T. Konstandin and G. Servant, *General Properties of the Gravitational Wave Spectrum from Phase Transitions*, *Phys. Rev.* **D79** (2009) 083519, [0901.1661].

[106] C. Caprini and D. G. Figueroa, *Cosmological Backgrounds of Gravitational Waves*, *Class. Quant. Grav.* **35** (2018) 163001, [1801.04268].

[107] D. Croon and G. White, *Exotic Gravitational Wave Signatures from Simultaneous Phase Transitions*, *JHEP* **05** (2018) 210, [1803.05438].

[108] E. Witten, *Cosmic Separation of Phases*, *Phys. Rev.* **D30** (1984) 272–285.

[109] C. J. Hogan, *Gravitational radiation from cosmological phase transitions*, *MRNAS* **218** (Feb., 1986) 629–636.

[110] A. Kosowsky, M. S. Turner and R. Watkins, *Gravitational radiation from colliding vacuum bubbles*, *Phys. Rev.* **D45** (1992) 4514–4535.

[111] A. Kosowsky, M. S. Turner and R. Watkins, *Gravitational waves from first order cosmological phase transitions*, *Phys. Rev. Lett.* **69** (1992) 2026–2029.

[112] A. Kosowsky and M. S. Turner, *Gravitational radiation from colliding vacuum bubbles: envelope approximation to many bubble collisions*, *Phys. Rev.* **D47** (1993) 4372–4391, [astro-ph/9211004].

[113] M. Kamionkowski, A. Kosowsky and M. S. Turner, *Gravitational radiation from first order phase transitions*, *Phys. Rev.* **D49** (1994) 2837–2851, [astro-ph/9310044].

[114] R. Jinno and M. Takimoto, *Gravitational waves from bubble collisions: An analytic derivation*, *Phys. Rev.* **D95** (2017) 024009, [1605.01403].

[115] R. Jinno, S. Lee, H. Seong and M. Takimoto, *Gravitational waves from first-order phase transitions: Towards model separation by bubble nucleation rate*, *JCAP* **1711** (2017) 050, [1708.01253].

[116] S. J. Huber and T. Konstandin, *Gravitational Wave Production by Collisions: More Bubbles*, *JCAP* **0809** (2008) 022, [0806.1828].

[117] D. J. Weir, *Revisiting the envelope approximation: gravitational waves from bubble collisions*, *Phys. Rev.* **D93** (2016) 124037, [1604.08429].

[118] D. Cutting, M. Hindmarsh and D. J. Weir, *Gravitational waves from vacuum first-order phase transitions: from the envelope to the lattice*, *Phys. Rev.* **D97** (2018) 123513, [1802.05712].

[119] M. Breitbach, J. Kopp, E. Madge, T. Opferkuch and P. Schwaller, *Dark, Cold, and Noisy: Constraining Secluded Hidden Sectors with Gravitational Waves*, 1811.11175.

[120] M. Hindmarsh, S. J. Huber, K. Rummukainen and D. J. Weir, *Gravitational waves from the sound of a first order phase transition*, *Phys. Rev. Lett.* **112** (2014) 041301, [1304.2433].

[121] M. Hindmarsh, S. J. Huber, K. Rummukainen and D. J. Weir, *Numerical simulations of acoustically generated gravitational waves at a first order phase transition*, *Phys. Rev.* **D92** (2015) 123009, [1504.03291].

[122] M. Hindmarsh, S. J. Huber, K. Rummukainen and D. J. Weir, *Shape of the acoustic gravitational wave power spectrum from a first order phase transition*, *Phys. Rev.* **D96** (2017) 103520, [1704.05871].

[123] M. Hindmarsh, *Sound shell model for acoustic gravitational wave production at a first-order phase transition in the early Universe*, *Phys. Rev. Lett.* **120** (2018) 071301, [1608.04735].

[124] R. Jinno and M. Takimoto, *Gravitational waves from bubble dynamics: Beyond the Envelope*, 1707.03111.

[125] LIGO SCIENTIFIC, VIRGO collaboration, B. P. Abbott et al., *Upper Limits on the Stochastic Gravitational-Wave Background from Advanced LIGO's First Observing Run*, *Phys. Rev. Lett.* **118** (2017) 121101, [1612.02029].

[126] LIGO SCIENTIFIC collaboration, J. Aasi et al., *Advanced LIGO*, *Class. Quant. Grav.* **32** (2015) 074001, [1411.4547].

[127] B. Sathyaprakash et al., *Scientific Objectives of Einstein Telescope*, *Class. Quant. Grav.* **29** (2012) 124013, [1206.0331].

[128] C. L. Carilli and S. Rawlings, *Science with the Square Kilometer Array: Motivation, key science projects, standards and assumptions*, *New Astron. Rev.* **48** (2004) 979, [astro-ph/0409274].

[129] G. Hobbs, A. Archibald, Z. Arzoumanian, D. Backer, M. Bailes, N. D. R. Bhat et al., *The International Pulsar Timing Array project: using pulsars as a gravitational wave detector*, *Classical and Quantum Gravity* **27** (Apr, 2010) 084013, [0911.5206].

[130] E. Thrane and J. D. Romano, *Sensitivity curves for searches for gravitational-wave backgrounds*, *Phys. Rev.* **D88** (2013) 124032, [1310.5300].

[131] G. Sigl, A. V. Olinto and K. Jedamzik, *Primordial magnetic fields from cosmological first order phase transitions*, *Phys. Rev.* **D55** (1997) 4582–4590, [astro-ph/9610201].

[132] T. Kahniashvili, A. G. Tevzadze and B. Ratra, *Phase Transition Generated Cosmological Magnetic Field at Large Scales*, *Astrophys. J.* **726** (2011) 78, [0907.0197].

[133] T. Kahniashvili, A. G. Tevzadze, A. Brandenburg and A. Neronov, *Evolution of Primordial Magnetic Fields from Phase Transitions*, *Phys. Rev.* **D87** (2013) 083007, [1212.0596].

[134] T. Kahniashvili, A. Brandenburg, L. Campanelli, B. Ratra and A. G. Tevzadze, *Evolution of inflation-generated magnetic field through phase transitions*, *Phys. Rev. D* **86** (2012) 103005, [1206.2428].

[135] T. Kahniashvili, A. Brandenburg and A. G. Tevzadze, *The evolution of primordial magnetic field since its generation*, *Phys. Scripta* **91** (2016) 104008, [1507.00510].

[136] A. Nicolis, *Relic gravitational waves from colliding bubbles and cosmic turbulence*, *Class. Quant. Grav.* **21** (2004) L27, [gr-qc/0303084].

[137] C. Caprini and R. Durrer, *Gravitational waves from stochastic relativistic sources: Primordial turbulence and magnetic fields*, *Phys. Rev.* **D74** (2006) 063521, [astro-ph/0603476].

[138] T. Kahniashvili, L. Kisslinger and T. Stevens, *Gravitational Radiation Generated by Magnetic Fields in Cosmological Phase Transitions*, *Phys. Rev.* **D81** (2010) 023004, [0905.0643].

[139] C. Caprini, R. Durrer and G. Servant, *The stochastic gravitational wave background from turbulence and magnetic fields generated by a first-order phase transition*, *JCAP* **0912** (2009) 024, [0909.0622].

[140] L. Kisslinger and T. Kahniashvili, *Polarized Gravitational Waves from Cosmological Phase Transitions*, *Phys. Rev.* **D92** (2015) 043006, [1505.03680].

[141] P. Niksa, M. Schlederer and G. Sigl, *Gravitational Waves produced by Compressible MHD Turbulence from Cosmological Phase Transitions*, *Class. Quant. Grav.* **35** (2018) 144001, [1803.02271].

[142] A. Roper Pol, S. Mandal, A. Brandenburg, T. Kahniashvili and A. Kosowsky, *Numerical simulations of gravitational waves from early-universe turbulence*, *Phys. Rev. D* **102** (2020) 083512, [1903.08585].

[143] J. Ellis, M. Lewicki and J. M. No, *Gravitational waves from first-order cosmological phase transitions: lifetime of the sound wave source*, *JCAP* **07** (2020) 050, [2003.07360].

[144] J. M. Cornwall, *Speculations on primordial magnetic helicity*, *Phys. Rev.* **D56** (1997) 6146–6154, [hep-th/9704022].

[145] T. Stevens, M. B. Johnson, L. S. Kisslinger, E. M. Henley, W.-Y. P. Hwang and M. Burkardt, *Role of Charged Gauge Fields in Generating Magnetic Seed Fields in Bubble Collisions during the Cosmological Electroweak Phase Transition*, *Phys. Rev. D* **77** (2008) 023501, [0707.1346].

[146] T. Stevens and M. B. Johnson, *Magnetic Seed Field Generation from Electroweak Bubble Collisions, with Bubble Walls of Finite Thickness*, *Phys. Rev. D* **80** (2009) 083011, [0903.2227].

[147] M. M. Forbes and A. R. Zhitnitsky, *Primordial galactic magnetic fields from domain walls at the QCD phase transition*, *Phys. Rev. Lett.* **85** (2000) 5268–5271, [hep-ph/0004051].

[148] L. S. Kisslinger, *Magnetic wall from chiral phase transition and CMBR correlations*, *Phys. Rev. D* **68** (2003) 043516, [hep-ph/0212206].

[149] C. J. Copi, F. Ferrer, T. Vachaspati and A. Achucarro, *Helical Magnetic Fields from Sphaleron Decay and Baryogenesis*, *Phys. Rev. Lett.* **101** (2008) 171302, [0801.3653].

[150] L. Campanelli, *Helical Magnetic Fields from Inflation*, *Int. J. Mod. Phys. D* **18** (2009) 1395–1411, [0805.0575].

[151] G. Gogoberidze, T. Kahniashvili and A. Kosowsky, *The Spectrum of Gravitational Radiation from Primordial Turbulence*, *Phys. Rev.* **D76** (2007) 083002, [0705.1733].

[152] T. Kahniashvili, L. Campanelli, G. Gogoberidze, Y. Maravin and B. Ratra, *Gravitational Radiation from Primordial Helical Inverse Cascade MHD Turbulence*, *Phys. Rev.* **D78** (2008) 123006, [0809.1899].

[153] I. Proudman, *The generation of noise by isotropic turbulence*, *Proc. R. Soc. London A* **214** (1952) 119–132.

[154] PLANCK collaboration, N. Aghanim et al., *Planck 2018 results. VI. Cosmological parameters*, 1807.06209.

[155] M. Hindmarsh and M. Hijazi, *Gravitational waves from first order cosmological phase transitions in the Sound Shell Model*, *JCAP* **12** (2019) 062, [1909.10040].

[156] C. Caprini et al., *Detecting gravitational waves from cosmological phase transitions with LISA: an update*, *JCAP* **03** (2020) 024, [1910.13125].

[157] R. Banerjee and K. Jedamzik, *Are cluster magnetic fields primordial?*, *Phys. Rev. Lett.* **91** (2003) 251301, [astro-ph/0306211].

[158] L. Campanelli, *Evolution of Magnetic Fields in Freely Decaying Magnetohydrodynamic Turbulence*, *Phys. Rev. Lett.* **98** (2007) 251302, [0705.2308].

[159] T. Kahniashvili, G. Gogoberidze and B. Ratra, *Gravitational Radiation from Primordial Helical MHD Turbulence*, *Phys. Rev. Lett.* **100** (2008) 231301, [0802.3524].

[160] D. Biskamp and W.-C. Müller, *Decay laws for three-dimensional magnetohydrodynamic turbulence*, *Phys. Rev. Lett.* **83** (1999) 2195–2198.

[161] M. Christensson, M. Hindmarsh and A. Brandenburg, *Inverse cascade in decaying three-dimensional magnetohydrodynamic turbulence*, *Phys. Rev. E* **64** (2001) 056405.

[162] R.-G. Cai, S. Pi and M. Sasaki, *Universal infrared scaling of gravitational wave background spectra*, 1909.13728.

[163] AEDGE collaboration, Y. A. El-Neaj et al., *AEDGE: Atomic Experiment for Dark Matter and Gravity Exploration in Space*, *EPJ Quant. Technol.* **7** (2020) 6, [1908.00802].

[164] B. Allen, *The Stochastic gravity wave background: Sources and detection*, in *Relativistic gravitation and gravitational radiation. Proceedings, School of Physics, Les Houches, France, September 26-October 6, 1995*, pp. 373–417, 1996. gr-qc/9604033.

[165] N. Bartolo et al., *Science with the space-based interferometer LISA. IV: Probing inflation with gravitational waves*, *JCAP* **12** (2016) 026, [1610.06481].

[166] T. Regimbau, *The astrophysical gravitational wave stochastic background*, *Res. Astron. Astrophys.* **11** (2011) 369–390, [1101.2762].

[167] M. S. Turner and L. M. Widrow, *Inflation Produced, Large Scale Magnetic Fields*, *Phys. Rev.* **D37** (1988) 2743.

[168] C. R. Contaldi, J. Magueijo and L. Smolin, *Anomalous CMB polarization and gravitational chirality*, *Phys. Rev. Lett.* **101** (2008) 141101, [0806.3082].

[169] N. Bartolo and G. Orlando, *Parity breaking signatures from a Chern-Simons coupling during inflation: the case of non-Gaussian gravitational waves*, *JCAP* **07** (2017) 034, [1706.04627].

[170] S. Alexander and N. Yunes, *Chern-Simons Modified General Relativity*, *Phys. Rept.* **480** (2009) 1–55, [0907.2562].

[171] N. Barnaby, E. Pajer and M. Peloso, *Gauge Field Production in Axion Inflation: Consequences for Monodromy, non-Gaussianity in the CMB, and Gravitational Waves at Interferometers*, *Phys. Rev. D* **85** (2012) 023525, [1110.3327].

[172] P. Adshead, E. Martinec and M. Wyman, *Perturbations in Chromo-Natural Inflation*, *JHEP* **09** (2013) 087, [1305.2930].

[173] E. Dimastrogiovanni, M. Fasiello and T. Fujita, *Primordial Gravitational Waves from Axion-Gauge Fields Dynamics*, *JCAP* **01** (2017) 019, [1608.04216].

[174] T. Kahniashvili, G. Gogoberidze and B. Ratra, *Polarized cosmological gravitational waves from primordial helical turbulence*, *Phys. Rev. Lett.* **95** (2005) 151301, [astro-ph/0505628].

[175] M. Kawasaki and M. Kusakabe, *Updated constraint on a primordial magnetic field during big bang nucleosynthesis and a formulation of field effects*, *Phys. Rev.* **D86** (2012) 063003, [1204.6164].

[176] D. Grasso and H. R. Rubinstein, *Magnetic fields in the early universe*, *Phys. Rept.* **348** (2001) 163–266, [astro-ph/0009061].

[177] T. R. Seshadri and K. Subramanian, *CMB bispectrum from primordial magnetic fields on large angular scales*, *Phys. Rev. Lett.* **103** (2009) 081303, [0902.4066].

[178] PLANCK collaboration, P. A. R. Ade et al., *Planck 2015 results. XIX. Constraints on primordial magnetic fields*, *Astron. Astrophys.* **594** (2016) A19, [1502.01594].

[179] K. Jedamzik, V. Katalinic and A. V. Olinto, *Damping of cosmic magnetic fields*, *Phys. Rev.* **D57** (1998) 3264–3284, [astro-ph/9606080].

[180] K. Jedamzik, V. Katalinic and A. V. Olinto, *A Limit on primordial small scale magnetic fields from CMB distortions*, *Phys. Rev. Lett.* **85** (2000) 700–703, [astro-ph/9911100].

[181] J. D. Barrow, P. G. Ferreira and J. Silk, *Constraints on a primordial magnetic field*, *Phys. Rev. Lett.* **78** (1997) 3610–3613, [astro-ph/9701063].

[182] R. Durrer, P. G. Ferreira and T. Kahniashvili, *Tensor microwave anisotropies from a stochastic magnetic field*, *Phys. Rev.* **D61** (2000) 043001, [astro-ph/9911040].

[183] D. G. Yamazaki, T. Kajino, G. J. Mathew and K. Ichiki, *The Search for a Primordial Magnetic Field*, *Phys. Rept.* **517** (2012) 141–167, [1204.3669].

[184] P. Trivedi, K. Subramanian and T. R. Seshadri, *Primordial Magnetic Field Limits from Cosmic Microwave Background Bispectrum of Magnetic Passive Scalar Modes*, *Phys. Rev.* **D82** (2010) 123006, [1009.2724].

[185] F. Tavecchio, G. Ghisellini, L. Foschini, G. Bonnoli, G. Ghirlanda and P. Coppi, *The intergalactic magnetic field constrained by Fermi/LAT observations of the TeV blazar 1ES 0229+200*, *Mon. Not. Roy. Astron. Soc.* **406** (2010) L70–L74, [1004.1329].

[186] S. Ando and A. Kusenko, *Evidence for Gamma-Ray Halos Around Active Galactic Nuclei and the First Measurement of Intergalactic Magnetic Fields*, *Astrophys. J.* **722** (2010) L39, [1005.1924].

[187] A. Neronov and I. Vovk, *Evidence for strong extragalactic magnetic fields from Fermi observations of TeV blazars*, *Science* **328** (2010) 73–75, [1006.3504].

[188] W. Essey, S. Ando and A. Kusenko, *Determination of intergalactic magnetic fields from gamma ray data*, *Astropart. Phys.* **35** (2011) 135–139, [1012.5313].

[189] W. Chen, J. H. Buckley and F. Ferrer, *Search for GeV -Ray Pair Halos Around Low Redshift Blazars*, *Phys. Rev. Lett.* **115** (2015) 211103, [1410.7717].

[190] FERMI-LAT collaboration, M. Ackermann et al., *The Search for Spatial Extension in High-latitude Sources Detected by the Fermi Large Area Telescope*, *Astrophys. J. Suppl.* **237** (2018) 32, [1804.08035].

[191] A. Schlüter and L. Biermann, *Interstellare Magnetfelder*, *Zeitschrift Naturforschung Teil A* **5** (1950) 237–251.

[192] R. M. Kulsrud, R. Cen, J. P. Ostriker and D. Ryu, *The Protogalactic origin for cosmic magnetic fields*, *Astrophys. J.* **480** (1997) 481, [astro-ph/9607141].

[193] N. Y. Gnedin, A. Ferrara and E. G. Zweibel, *Generation of the primordial magnetic fields during cosmological reionization*, *Astrophys. J.* **539** (2000) 505–516, [astro-ph/0001066].

[194] Y. B. Zel'dovich, A. A. Ruzmaikin, S. A. Molchanov and D. D. Sokolov, *Kinematic dynamo problem in a linear velocity field*, *Journal of Fluid Mechanics* **144** (1984) 1–11.

[195] A. Shukurov, D. Sokoloff, K. Subramanian and A. Brandenburg, *Galactic dynamo and helicity losses through fountain flow*, *Astron. Astrophys.* **448** (2006) L33–L36, [astro-ph/0512592].

[196] R. M. Kulsrud and E. G. Zweibel, *The Origin of Astrophysical Magnetic Fields*, *Rept. Prog. Phys.* **71** (2008) 0046091, [0707.2783].

[197] B. Ratra, *Cosmological 'seed' magnetic field from inflation*, *Astrophys. J.* **391** (1992) L1–L4.

[198] J. Martin and J. Yokoyama, *Generation of Large-Scale Magnetic Fields in Single-Field Inflation*, *JCAP* **0801** (2008) 025, [0711.4307].

[199] T. Kobayashi, *Primordial Magnetic Fields from the Post-Inflationary Universe*, *JCAP* **1405** (2014) 040, [1403.5168].

[200] A. G. Tevzadze, L. Kisslinger, A. Brandenburg and T. Kahniashvili, *Magnetic Fields from QCD Phase Transitions*, *Astrophys. J.* **759** (2012) 54, [1207.0751].

[201] T. Vachaspati, *Magnetic fields from cosmological phase transitions*, *Phys. Lett.* **B265** (1991) 258–261.

[202] J. R. Espinosa, T. Konstandin and F. Riva, *Strong Electroweak Phase Transitions in the Standard Model with a Singlet*, *Nucl. Phys.* **B854** (2012) 592–630, [1107.5441].

[203] M. Giovannini and M. E. Shaposhnikov, *Primordial magnetic fields, anomalous isocurvature fluctuations and big bang nucleosynthesis*, *Phys. Rev. Lett.* **80** (1998) 22–25, [hep-ph/9708303].

[204] N. Seehafer, *Nature of the α effect in magnetohydrodynamics*, *Phys. Rev. E* **53** (1996) 1283–1286.

[205] H. Ji, *Turbulent dynamos and magnetic helicity*, *Phys. Rev. Lett.* **83** (1999) 3198–3201, [astro-ph/0102321].

[206] A. Pouquet, M. Meneguzzi and U. Frisch, *Growth of correlations in magnetohydrodynamic turbulence*, *Phys. Rev.* **A33** (1986) 4266–4276.

[207] Y. Zhang, T. Vachaspati and F. Ferrer, *Magnetic field production at a first-order electroweak phase transition*, 1902.02751.

[208] R. Durrer and A. Neronov, *Cosmological Magnetic Fields: Their Generation, Evolution and Observation*, *Astron. Astrophys. Rev.* **21** (2013) 62, [1303.7121].

[209] A. Brandenburg, T. Kahniashvili, S. Mandal, A. R. Pol, A. G. Tevzadze and T. Vachaspati, *Evolution of hydromagnetic turbulence from the electroweak phase transition*, *Phys. Rev.* **D96** (2017) 123528, [1711.03804].

[210] R. Durrer and C. Caprini, *Primordial magnetic fields and causality*, *JCAP* **0311** (2003) 010, [astro-ph/0305059].

[211] A. N. Kolmogorov, *The local structure of turbulence in incompressible viscous fluid for very large reynolds numbers*, *Proceedings: Mathematical and Physical Sciences* **434** (1991) 9–13.

[212] L. D. Landau and E. M. Lifschitz, *Fluid Mechanics*. 1987.

[213] D. Biskamp and W.-C. Müller, *Decay laws for three-dimensional magnetohydrodynamic turbulence*, *Phys. Rev. Lett.* **83** (Sep, 1999) 2195–2198.

[214] D. Biskamp, *Magnetohydrodynamic Turbulence*. Cambridge University Press, 2003, 10.1017/CBO9780511535222.

[215] T. Vachaspati, *Estimate of the primordial magnetic field helicity*, *Phys. Rev. Lett.* **87** (2001) 251302, [astro-ph/0101261].

[216] A. Brandenburg, T. Kahniashvili, S. Mandal, A. R. Pol, A. G. Tevzadze and T. Vachaspati, *The dynamo effect in decaying helical turbulence*, *Phys. Rev. Fluids.* **4** (2019) 024608, [1710.01628].

[217] K. Dolag, M. Kachelriess, S. Ostapchenko and R. Tomas, *Lower limit on the strength and filling factor of extragalactic magnetic fields*, *Astrophys. J.* **727** (2011) L4, [1009.1782].

[218] A. M. Taylor, I. Vovk and A. Neronov, *Extragalactic magnetic fields constraints from simultaneous GeV-TeV observations of blazars*, *Astron. Astrophys.* **529** (2011) A144, [1101.0932].

[219] C. D. Dermer, M. Cavadini, S. Razzaque, J. D. Finke, J. Chiang and B. Lott, *Time Delay of Cascade Radiation for TeV Blazars and the Measurement of the Intergalactic Magnetic Field*, *Astrophys. J.* **733** (2011) L21, [1011.6660].

[220] F. P. Huang, P.-H. Gu, P.-F. Yin, Z.-H. Yu and X. Zhang, *Testing the electroweak phase transition and electroweak baryogenesis at the LHC and a circular electron-positron collider*, *Phys. Rev.* **D93** (2016) 103515, [1511.03969].

[221] M. Artymowski, M. Lewicki and J. D. Wells, *Gravitational wave and collider implications of electroweak baryogenesis aided by non-standard cosmology*, *JHEP* **03** (2017) 066, [1609.07143].

[222] M. Chala, C. Krause and G. Nardini, *Signals of the electroweak phase transition at colliders and gravitational wave observatories*, *JHEP* **07** (2018) 062, [1802.02168].

[223] P. W. Graham, J. M. Hogan, M. A. Kasevich and S. Rajendran, *Resonant mode for gravitational wave detectors based on atom interferometry*, *Phys. Rev.* **D94** (2016) 104022, [1606.01860].

[224] MAGIS collaboration, P. W. Graham, J. M. Hogan, M. A. Kasevich, S. Rajendran and R. W. Romani, *Mid-band gravitational wave detection with precision atomic sensors*, 1711.02225.

[225] O. Buchmuller, "The Atom Interferometer Observatory Network." https://indico.cern.ch/event/760005/contributions/3152426/attachments/1735965/2807829/AION-Oxford-17102018.pptx.pdf, 2018.

[226] D. Bodeker, L. Fromme, S. J. Huber and M. Seniuch, *The Baryon asymmetry in the standard model with a low cut-off*, *JHEP* **02** (2005) 026, [hep-ph/0412366].

[227] C. Delaunay, C. Grojean and J. D. Wells, *Dynamics of Non-renormalizable Electroweak Symmetry Breaking*, *JHEP* **04** (2008) 029, [0711.2511].

[228] D. Curtin, P. Meade and C.-T. Yu, *Testing Electroweak Baryogenesis with Future Colliders*, *JHEP* **11** (2014) 127, [1409.0005].

[229] A. Ashoorioon and T. Konstandin, *Strong electroweak phase transitions without collider traces*, *JHEP* **07** (2009) 086, [0904.0353].

[230] A. Beniwal, M. Lewicki, J. D. Wells, M. White and A. G. Williams, *Gravitational wave, collider and dark matter signals from a scalar singlet electroweak baryogenesis*, *JHEP* **08** (2017) 108, [1702.06124].

[231] ATLAS collaboration, *Search for high-mass dilepton resonances using* $139\,\text{fb}^{-1}$ *of pp collision data collected at* $\sqrt{s} = 13\,\text{TeV}$ *with the ATLAS detector*, *ATLAS-CONF-2019-001* (2019) .

[232] K. Kamada and A. J. Long, *Evolution of the Baryon Asymmetry through the Electroweak Crossover in the Presence of a Helical Magnetic Field*, *Phys. Rev.* **D94** (2016) 123509, [1610.03074].

[233] M. D'Onofrio and K. Rummukainen, *Standard model cross-over on the lattice*, *Phys. Rev.* **D93** (2016) 025003, [1508.07161].

[234] M. C. Bento, O. Bertolami and R. Rosenfeld, *Cosmological constraints on an invisibly decaying Higgs boson*, *Phys. Lett.* **B518** (2001) 276–281, [hep-ph/0103340].

[235] C. Pitrou, A. Coc, J.-P. Uzan and E. Vangioni, *Precision big bang nucleosynthesis with improved Helium-4 predictions*, *Phys. Rept.* **754** (2018) 1–66, [1801.08023].

[236] J. L. Feng, H. Tu and H.-B. Yu, *Thermal Relics in Hidden Sectors*, *JCAP* **0810** (2008) 043, [0808.2318].

[237] A. Fradette and M. Pospelov, *BBN for the LHC: constraints on lifetimes of the Higgs portal scalars*, *Phys. Rev.* **D96** (2017) 075033, [1706.01920].

[238] G. F. Giudice, E. W. Kolb and A. Riotto, *Largest temperature of the radiation era and its cosmological implications*, *Phys. Rev.* **D64** (2001) 023508, [hep-ph/0005123].

[239] H. L. Child and J. Giblin, John T., *Gravitational radiation from first-order phase transitions*, *Journal of Cosmology and Astro-Particle Physics* **2012** (Oct., 2012) 001, [1207.6408].

[240] A. Kosowsky, A. Mack and T. Kahniashvili, *Gravitational radiation from cosmological turbulence*, *Phys. Rev.* **D66** (2002) 024030, [astro-ph/0111483].

[241] T. Kahniashvili, A. Kosowsky, G. Gogoberidze and Y. Maravin, *Detectability of Gravitational Waves from Phase Transitions*, *Phys. Rev.* **D78** (2008) 043003, [0806.0293].

[242] T. Kalaydzhyan and E. Shuryak, *Gravity waves generated by sounds from big bang phase transitions*, *Phys. Rev.* **D91** (2015) 083502, [1412.5147].

[243] V. Domcke, J. Garcia-Bellido, M. Peloso, M. Pieroni, A. Ricciardone, L. Sorbo et al., *Measuring the net circular polarization of the stochastic gravitational wave background with interferometers*, *JCAP* **05** (2020) 028, [1910.08052].

[244] LISA collaboration, P. Amaro-Seoane et al., *Laser Interferometer Space Antenna*, 1702.00786.

[245] M. R. Adams and N. J. Cornish, *Discriminating between a Stochastic Gravitational Wave Background and Instrument Noise*, *Phys. Rev.* **D82** (2010) 022002, [1002.1291].

[246] N. J. Cornish, *Detecting a stochastic gravitational wave background with the Laser Interferometer Space Antenna*, *Phys. Rev. D* **65** (2002) 022004, [gr-qc/0106058].

[247] T. Robson, N. J. Cornish and C. Liu, *The construction and use of LISA sensitivity curves*, *Class. Quant. Grav.* **36** (2019) 105011, [1803.01944].

[248] LISA collaboration, "LISA Data Challenge Manual." https://lisa-ldc.lal.in2p3.fr/static/data/pdf/LDC-manual-001.pdf, 2018.

[249] N. Bartolo, V. Domcke, D. G. Figueroa, J. Garcìa-Bellido, M. Peloso, M. Pieroni et al., *Probing non-Gaussian Stochastic Gravitational Wave Backgrounds with LISA*, *JCAP* **11** (2018) 034, [1806.02819].

[250] J. Crowder and N. J. Cornish, *Beyond LISA: Exploring future gravitational wave missions*, *Phys. Rev. D* **72** (2005) 083005, [gr-qc/0506015].

[251] S. Kawamura et al., *Space gravitational-wave antennas DECIGO and B-DECIGO*, *Int. J. Mod. Phys. D* **28** (2019) 1845001.

[252] W.-T. Ni, G. Wang and A.-M. Wu, *Astrodynamical middle-frequency interferometric gravitational wave observatory AMIGO: Mission concept and orbit design*, 1909.04995.

Appendix A

Numerical scheme action derivatives

A.1 Computation of discretised S_t derivatives

In this appendix we provide analytical derivatives of the discretised action in Eq. (4.20) that we use in our code to ensure precision and speed of our numerical results. The discretised action from $i = 0$ to n takes the form

$$S_t = \frac{27\pi^2}{2}\sum_{i=0}^{n-1}[V(\underset{\sim}{\phi}_i) + V(\underset{\sim}{\phi}_{i+1}) - V_{t,i} - V_{t,i+1}]^2 \frac{[(\underset{\sim}{\phi}_{i+1} - \underset{\sim}{\phi}_i).(\underset{\sim}{\phi}_{i+1} - \underset{\sim}{\phi}_i)]^2}{(V_{t,i+1} - V_{t,i})^3}, \tag{A.1}$$

or

$$S_t = \frac{27\pi^2}{2}\sum_{i=0}^{n-1}[V(\underset{\sim}{\phi}_i) + V(\underset{\sim}{\phi}_{i+1}) - V_{t,i} - V_{t,i+1}]^2 \frac{[(\Delta\underset{\sim}{\phi}_i).(\Delta\underset{\sim}{\phi}_i)]^2}{(V_{t,i+1} - V_{t,i})^3}, \tag{A.2}$$

where

$$\Delta\underset{\sim}{\phi}_i = (\underset{\sim}{\phi}_{i+1} - \underset{\sim}{\phi}_i) = (\phi^x_{i+1} - \phi^x_i, \phi^y_{i+1} - \phi^y_i) = (\Delta\phi^x_i, \Delta\phi^y_i) \tag{A.3}$$

and

$$\Delta\underset{\sim}{\phi}_i.\Delta\underset{\sim}{\phi}_i = (\Delta\phi^x_i)^2 + (\Delta\phi^y_i)^2 \tag{A.4}$$

$$[\Delta\underset{\sim}{\phi}_i.\Delta\underset{\sim}{\phi}_i]^2 = [(\Delta\phi^x_i)^2 + (\Delta\phi^y_i)^2]^2 \tag{A.5}$$

so that in terms of the field coordinates ϕ^x and ϕ^y in field space we then have

$$S_t = \frac{27\pi^2}{2}\sum_{i=0}^{n-1}[V(\phi^x_i, \phi^y_i) + V(\phi^x_{i+1}, \phi^y_{i+1}) - V_{t,i} - V_{t,i+1}]^2 \frac{[(\Delta\phi^x_i)^2 + (\Delta\phi^y_i)^2]^2}{(V_{t,i+1} - V_{t,i})^3} \tag{A.6}$$

Let

$$G_i = [(\Delta\underset{\sim}{\phi}_i).(\Delta\underset{\sim}{\phi}_i)]^2 = [(\Delta\phi^x_i)^2 + (\Delta\phi^y_i)^2]^2 = [(\phi^x_{i+1} - \phi^x_i)^2 + (\phi^y_{i+1} - \phi^y_i)^2]^2 \tag{A.7}$$

$$F_{i,i\neq 0} = \frac{[V(\phi^x_i, \phi^y_i) + V(\phi^x_{i+1}, \phi^y_{i+1}) - V_{t,i} - V_{t,i+1}]^2}{(V_{t,i+1} - V_{t,i})^3} \tag{A.8}$$

and as the boundary condition requires that $V_{t,0} = V(\phi_0^x, \phi_0^y)$ we also have for the boundary node $i = 0$ that

$$F_{i=0} = \frac{[V(\phi_0^x, \phi_0^y) + V(\phi_1^x, \phi_1^y) - V_{t,0} - V_{t,1}]^2}{(V_{t,1} - V_{t,0})^3} = \frac{[V(\phi_1^x, \phi_1^y) - V_{t,1}]^2}{(V_{t,1} - V(\phi_0^x, \phi_0^y))^3} \tag{A.9}$$

so that

$$\begin{aligned} S_t &= \frac{27\pi^2}{2} \sum_{i=0}^{n-1} [(\Delta\underset{\sim}{\phi}_i).(\Delta\underset{\sim}{\phi}_i)]^2 F_i = \frac{27\pi^2}{2} \sum_{i=0}^{n-1} G_i F_i = \frac{27\pi^2}{2} \left(G_0 F_0 + \sum_{i=1}^{n-2} G_i F_i + G_{n-1} F_{n-1} \right) \\ &= \frac{27\pi^2}{2} \left(G_0 \frac{[V(\phi_1^x, \phi_1^y) - V_{t,1}]^2}{(V_{t,1} - V(\phi_0^x, \phi_0^y))^3} + \sum_{i=1}^{n-2} G_i F_i + G_{n-1} \frac{[V(\phi_{n-1}^x, \phi_{n-1}^y) - V_{t,1}]^2}{(V(\phi_n^x, \phi_n^y) - V_{t,n-1})^3} \right) \end{aligned} \tag{A.10}$$

where in (A.9) we have applied the boundary conditions $V_{t,0} = V(\phi_0^x, \phi_0^y)$.

See Appendix A.2 for a discussion of why we can still differentiate (A.9) to get local $F_{i=0}$ derivatives. To minimise the action (A.6) using a Newton iteration we need to evaluate the local gradients of S_t and Hessian of S_t at each path point "i" along the path in field space and use these gradients to shift the path to one with a lower action S_t. From (A.4) we have

$$\frac{\partial}{\partial \phi_i^x} [(\Delta\underset{\sim}{\phi}_{i-1}).(\Delta\underset{\sim}{\phi}_{i-1})] = +2(\Delta\phi_{i-1}^x) \tag{A.11}$$

$$\frac{\partial}{\partial \phi_i^x} [\Delta\underset{\sim}{\phi}_i.\Delta\underset{\sim}{\phi}_i] = -2(\Delta\phi_i^x) \tag{A.12}$$

$$\frac{\partial}{\partial \phi_i^y} [(\Delta\underset{\sim}{\phi}_{i-1}).(\Delta\underset{\sim}{\phi}_{i-1})] = +2(\Delta\phi_{i-1}^y) \tag{A.13}$$

$$\frac{\partial}{\partial \phi_i^y} [\Delta\underset{\sim}{\phi}_i.\Delta\underset{\sim}{\phi}_i] = -2(\Delta\phi_i^y) \tag{A.14}$$

$$\frac{\partial}{\partial \phi_{i-1}^x} [(\Delta\underset{\sim}{\phi}_{i-1}).(\Delta\underset{\sim}{\phi}_{i-1})] = -2(\Delta\phi_{i-1}^x) \tag{A.15}$$

$$\frac{\partial}{\partial \phi_{i+1}^x} [\Delta\underset{\sim}{\phi}_i.\Delta\underset{\sim}{\phi}_i] = +2(\Delta\phi_i^x) \tag{A.16}$$

$$\frac{\partial}{\partial \phi_{i-1}^y} [(\Delta\underset{\sim}{\phi}_{i-1}).(\Delta\underset{\sim}{\phi}_{i-1})] = -2(\Delta\phi_{i-1}^y) \tag{A.17}$$

$$\frac{\partial}{\partial \phi_{i+1}^y} [\Delta\underset{\sim}{\phi}_i.\Delta\underset{\sim}{\phi}_i] = +2(\Delta\phi_i^y) \tag{A.18}$$

Then from (A.7) and (A.11), (A.12), (A.13), (A.14) we have

$$\frac{\partial G_{i-1}}{\partial \phi_i^x} = \frac{\partial [(\Delta \underset{\sim}{\phi}_{i-1}).((\Delta \underset{\sim}{\phi}_{i-1})]^2}{\partial \phi_i^x} = +4[(\Delta \underset{\sim}{\phi}_{i-1}).(\Delta \underset{\sim}{\phi}_{i-1})]\Delta\phi_{i-1}^x \tag{A.19}$$

$$\frac{\partial G_i}{\partial \phi_i^x} = \frac{\partial [(\Delta \underset{\sim}{\phi}_i).(\Delta \underset{\sim}{\phi}_i)]^2}{\partial \phi_i^x} = -4[(\Delta \underset{\sim}{\phi}_i).(\Delta \underset{\sim}{\phi}_i)]\Delta\phi_i^x \tag{A.20}$$

$$\frac{\partial G_{i-1}}{\partial \phi_i^y} = \frac{\partial [(\Delta \underset{\sim}{\phi}_{i-1}).((\Delta \underset{\sim}{\phi}_{i-1})]^2}{\partial \phi_i^y} = +4[(\Delta \underset{\sim}{\phi}_{i-1}).(\Delta \underset{\sim}{\phi}_{i-1})]\Delta\phi_{i-1}^y \tag{A.21}$$

$$\frac{\partial G_i}{\partial \phi_i^y} = \frac{\partial [(\Delta \underset{\sim}{\phi}_i).(\Delta \underset{\sim}{\phi}_i)]^2}{\partial \phi_i^y} = -4[(\Delta \underset{\sim}{\phi}_i).(\Delta \underset{\sim}{\phi}_i)]\Delta\phi_i^y \tag{A.22}$$

and from (A.7) and (A.15), (A.16), (A.17), (A.18) we have

$$\frac{\partial G_{i-1}}{\partial \phi_{i-1}^x} = \frac{\partial [(\Delta \underset{\sim}{\phi}_{i-1}).((\Delta \underset{\sim}{\phi}_{i-1})]^2}{\partial \phi_{i-1}^x} = -4[(\Delta \underset{\sim}{\phi}_{i-1}).(\Delta \underset{\sim}{\phi}_{i-1})]\Delta\phi_{i-1}^x \tag{A.23}$$

$$\frac{\partial G_i}{\partial \phi_{i+1}^x} = \frac{\partial [(\Delta \underset{\sim}{\phi}_i).(\Delta \underset{\sim}{\phi}_i)]^2}{\partial \phi_{i+1}^x} = +4[(\Delta \underset{\sim}{\phi}_i).(\Delta \underset{\sim}{\phi}_i)]\Delta\phi_i^x \tag{A.24}$$

$$\frac{\partial G_{i-1}}{\partial \phi_{i-1}^y} = \frac{\partial [(\Delta \underset{\sim}{\phi}_{i-1}).((\Delta \underset{\sim}{\phi}_{i-1})]^2}{\partial \phi_{i-1}^y} = -4[(\Delta \underset{\sim}{\phi}_{i-1}).(\Delta \underset{\sim}{\phi}_{i-1})]\Delta\phi_{i-1}^y \tag{A.25}$$

$$\frac{\partial G_i}{\partial \phi_{i+1}^y} = \frac{\partial [(\Delta \underset{\sim}{\phi}_i).(\Delta \underset{\sim}{\phi}_i)]^2}{\partial \phi_{i+1}^y} = +4[(\Delta \underset{\sim}{\phi}_i).(\Delta \underset{\sim}{\phi}_i)]\Delta\phi_i^y \tag{A.26}$$

So, for example,

$$F_1 = \frac{[V(\phi_1^x, \phi_1^y) + V(\phi_2^x, \phi_2^y) - V_{t,1} - V_{t,2}]^2}{(V_{t,2} - V_{t,1})^3} \tag{A.27}$$

$$F_2 = \frac{[V(\phi_2^x, \phi_2^y) + V(\phi_3^x, \phi_3^y) - V_{t,2} - V_{t,3}]^2}{(V_{t,3} - V_{t,2})^3} \tag{A.28}$$

$$F_3 = \frac{[V(\phi_3^x, \phi_3^y) + V(\phi_4^x, \phi_4^y) - V_{t,3} - V_{t,3}]^2}{(V_{t,4} - V_{t,3})^3} \tag{A.29}$$

$$G_1 = [(\Delta \underset{\sim}{\phi}_1).(\Delta \underset{\sim}{\phi}_1)]^2 = [(\phi_2^x - \phi_1^x)^2 + (\phi_2^y - \phi_1^y)^2]^2 \tag{A.30}$$

$$G_2 = [(\Delta \underset{\sim}{\phi}_2).(\Delta \underset{\sim}{\phi}_2)]^2 = [(\phi_3^x - \phi_2^x)^2 + (\phi_3^y - \phi_2^y)^2]^2 \tag{A.31}$$

$$G_3 = [(\Delta \underset{\sim}{\phi}_3).(\Delta \underset{\sim}{\phi}_3)]^2 = [(\phi_4^x - \phi_3^x)^2 + (\phi_4^y - \phi_3^y)^2]^2 \tag{A.32}$$

The only components of S_t containing ϕ_j^x or ϕ_j^y in $\sum_{i=0}^n F_i G_i$ are F_{j-1}, F_j, G_{j-1} and G_j. Where

$$F_{j-1}G_{j-1} = [(\Delta \underset{\sim}{\phi}_{j-1}).(\Delta \underset{\sim}{\phi}_{j-1})]^2 F_{j-1} \tag{A.33}$$

and

$$F_j G_j = [(\Delta\underset{\sim}{\phi}_j).(\Delta\underset{\sim}{\phi}_j)]^2 F_j. \tag{A.34}$$

For example, for $j = 2$, the only components of S_t containing ϕ_2^x are F_1, F_2, G_1, G_2. So, in general, for all points apart from the boundary point at ϕ_0

$$\begin{aligned}\frac{\partial S_t}{\partial \phi^x_{j,j\neq 0}} &= \frac{\partial}{\partial \phi^x_j}\frac{27\pi^2}{2}\sum_{i=0}^{n} F_i G_i \\ &= \frac{27\pi^2}{2}\frac{\partial}{\partial \phi^x_j}[F_{j-1}G_{j-1} + F_j G_j] \\ &= \frac{27\pi^2}{2}[\frac{\partial F_{j-1}}{\partial \phi^x_j}G_{j-1} + F_{j-1}\frac{\partial G_{j-1}}{\partial \phi^x_j} + \frac{\partial F_j}{\partial \phi^x_j}G_j + F_j\frac{\partial G_j}{\partial \phi^x_j}].\end{aligned} \tag{A.35}$$

and

$$\frac{\partial S_t}{\partial \phi^y_{j,j\neq 0}} = \frac{27\pi^2}{2}[\frac{\partial F_{j-1}}{\partial \phi^y_j}G_{j-1} + F_{j-1}\frac{\partial G_{j-1}}{\partial \phi^y_j} + \frac{\partial F_j}{\partial \phi^y_j}G_j + F_j\frac{\partial G_j}{\partial \phi^y_j}]. \tag{A.36}$$

Whilst at the ϕ_0 boundary

$$\frac{\partial S_t}{\partial \phi^x_0} = \frac{27\pi^2}{2}[\frac{\partial F_0}{\partial \phi^x_0}G_0 + F_0\frac{\partial G_0}{\partial \phi^x_0}]. \tag{A.37}$$

$$\frac{\partial S_t}{\partial \phi^y_0} = \frac{27\pi^2}{2}[\frac{\partial F_0}{\partial \phi^y_0}G_0 + F_0\frac{\partial G_0}{\partial \phi^y_0}]. \tag{A.38}$$

The F derivatives required by (A.35) and (A.36) are $\frac{\partial F_{j-1}}{\partial \phi^x_j}$, $\frac{\partial F_j}{\partial \phi^x_j}$, $\frac{\partial F_{j-1}}{\partial \phi^y_j}$ and $\frac{\partial F_j}{\partial \phi^y_j}$ and excluding the boundary node $j = 0$ are obtained from (A.8) as

$$\frac{\partial F_{j-1}}{\partial \phi^x_j} = \frac{2[V(\phi^x_{j-1},\phi^y_{j-1}) + V(\phi^x_j,\phi^y_j) - V_{t,j-1} - V_{t,j}]}{(V_{t,j} - V_{t,j-1})^3}\frac{\partial V(\phi^x_j,\phi^y_j)}{\partial \phi^x_j} \tag{A.39}$$

$$\frac{\partial F_j}{\partial \phi^x_j} = \frac{2[V(\phi^x_j,\phi^y_j) + V(\phi^x_{j+1},\phi^y_{j+1}) - V_{t,j} - V_{t,j+1}]}{(V_{t,j+1} - V_{t,j})^3}\frac{\partial V(\phi^x_j,\phi^y_j)}{\partial \phi^x_j}. \tag{A.40}$$

$$\frac{\partial F_{j-1}}{\partial \phi^y_j} = \frac{2[V(\phi^x_{j-1},\phi^y_{j-1}) + V(\phi^x_j,\phi^y_j) - V_{t,j-1} - V_{t,j}]}{(V_{t,j} - V_{t,j-1})^3}\frac{\partial V(\phi^x_j,\phi^y_j)}{\partial \phi^y_j} \tag{A.41}$$

$$\frac{\partial F_j}{\partial \phi^y_j} = \frac{2[V(\phi^x_j,\phi^y_j) + V(\phi^x_{j+1},\phi^y_{j+1}) - V_{t,j} - V_{t,j+1}]}{(V_{t,j+1} - V_{t,j})^3}\frac{\partial V(\phi^x_j,\phi^y_j)}{\partial \phi^y_j}. \tag{A.42}$$

and for adjacent points,

$$\frac{\partial F_{j-1}}{\partial \phi^x_{j-1}} = \frac{2[V(\phi^x_{j-1},\phi^y_{j-1}) + V(\phi^x_j,\phi^y_j) - V_{t,j-1} - V_{t,j}]}{(V_{t,j} - V_{t,j-1})^3} \frac{\partial V(\phi^x_{j-1},\phi^y_{j-1})}{\partial \phi^x_{j-1}} \tag{A.43}$$

$$\frac{\partial F_j}{\partial \phi^x_{j+1}} = \frac{2[V(\phi^x_j,\phi^y_j) + V(\phi^x_{j+1},\phi^y_{j+1}) - V_{t,j} - V_{t,j+1}]}{(V_{t,j+1} - V_{t,j})^3} \frac{\partial V(\phi^x_{j+1},\phi^y_{j+1})}{\partial \phi^x_{j+1}}. \tag{A.44}$$

$$\frac{\partial F_{j-1}}{\partial \phi^y_{j-1}} = \frac{2[V(\phi^x_{j-1},\phi^y_{j-1}) + V(\phi^x_j,\phi^y_j) - V_{t,j-1} - V_{t,j}]}{(V_{t,j} - V_{t,j-1})^3} \frac{\partial V(\phi^x_{j-1},\phi^y_{j-1})}{\partial \phi^y_{j-1}} \tag{A.45}$$

$$\frac{\partial F_j}{\partial \phi^y_{j+1}} = \frac{2[V(\phi^x_j,\phi^y_j) + V(\phi^x_{j+1},\phi^y_{j+1}) - V_{t,j} - V_{t,j+1}]}{(V_{t,j+1} - V_{t,j})^3} \frac{\partial V(\phi^x_{j+1},\phi^y_{j+1})}{\partial \phi^y_{j+1}}. \tag{A.46}$$

while for the boundary node at $j = 0$ we have using (A.9)

$$\frac{\partial F_{j=0}}{\partial \phi^x_{j=0}} = \frac{\partial}{\partial \phi^x_{j=0}} \frac{[V(\phi^x_1,\phi^y_1) - V_{t,1}]^2}{(V_{t,1} - V(\phi^x_0,\phi^y_0))^3} = +3\frac{[V(\phi^x_1,\phi^y_1) - V_{t,1}]^2}{(V_{t,1} - V(\phi^x_0,\phi^y_0))^4} \frac{\partial V(\phi^x_0,\phi^y_0)}{\partial \phi^x_0} \tag{A.47}$$

$$\frac{\partial F_{j=0}}{\partial \phi^y_{j=0}} = +3\frac{[V(\phi^x_1,\phi^y_1) - V_{t,1}]^2}{(V_{t,1} - V(\phi^x_0,\phi^y_0))^4} \frac{\partial V(\phi^x_0,\phi^y_0)}{\partial \phi^y_0} \tag{A.48}$$

and for the point adjacent to the boundary,

$$\frac{\partial F_{j=0}}{\partial \phi^x_{j=1}} = \frac{\partial}{\partial \phi^x_1} \frac{[V(\phi^x_1,\phi^y_1) - V_{t,1}]^2}{(V_{t,1} - V(\phi^x_0,\phi^y_0))^3} = +2\frac{[V(\phi^x_1,\phi^y_1) - V_{t,1}]}{(V_{t,1} - V(\phi^x_0,\phi^y_0))^3} \frac{\partial V(\phi^x_1,\phi^y_1)}{\partial \phi^x_1} \tag{A.49}$$

$$\frac{\partial F_{j=0}}{\partial \phi^y_{j=1}} = +2\frac{[V(\phi^x_1,\phi^y_1) - V_{t,1}]}{(V_{t,1} - V(\phi^x_0,\phi^y_0))^3} \frac{\partial V(\phi^x_1,\phi^y_1)}{\partial \phi^y_1} \tag{A.50}$$

For the second derivatives with respect to ϕ^x_j and ϕ^y_j again only the S_t components F_{j-1}, F_j, G_{j-1} and G_j contain ϕ^x_j or ϕ^y_j. We therefore have using (A.35) and (A.36)

$$\frac{\partial^2 S_t}{\partial \phi^x_{j,j\neq 0} \partial \phi^x_{j,j\neq 0}} = \frac{27\pi^2}{2} \frac{\partial}{\partial \phi^x_j} [\frac{\partial F_{j-1}}{\partial \phi^x_j} G_{j-1} + F_{j-1} \frac{\partial G_{j-1}}{\partial \phi^x_j} + \frac{\partial F_j}{\partial \phi^x_j} G_j + F_j \frac{\partial G_j}{\partial \phi^x_j}] \tag{A.51}$$

$$\frac{\partial^2 S_t}{\partial \phi^y_{j,j\neq 0}\partial \phi^y_{j,j\neq 0}} = \frac{27\pi^2}{2}\frac{\partial}{\partial \phi^y_j}[\frac{\partial F_{j-1}}{\partial \phi^y_j}G_{j-1} + F_{j-1}\frac{\partial G_{j-1}}{\partial \phi^y_j} + \frac{\partial F_j}{\partial \phi^y_j}G_j + F_j\frac{\partial G_j}{\partial \phi^y_j}] \quad \text{(A.52)}$$

$$\frac{\partial^2 S_t}{\partial \phi^x_{j,j\neq 0}\partial \phi^y_{j,j\neq 0}} = \frac{27\pi^2}{2}\frac{\partial}{\partial \phi^y_j}[\frac{\partial F_{j-1}}{\partial \phi^x_j}G_{j-1} + F_{j-1}\frac{\partial G_{j-1}}{\partial \phi^x_j} + \frac{\partial F_j}{\partial \phi^x_j}G_j + F_j\frac{\partial G_j}{\partial \phi^x_j}] \quad \text{(A.53)}$$

giving

$$\frac{\partial^2 S_t}{\partial \phi^x_{j,j\neq 0}\partial \phi^x_{j,j\neq 0}} = \frac{27\pi^2}{2}[\frac{\partial^2 F_{j-1}}{\partial \phi^x_j\partial \phi^x_j}G_{j-1} + F_{j-1}\frac{\partial^2 G_{j-1}}{\partial \phi^x_j\partial \phi^x_j} + \frac{\partial^2 F_j}{\partial \phi^x_j\partial \phi^x_j}G_j + F_j\frac{\partial^2 G_j}{\partial \phi^x_j\partial \phi^x_j} + \frac{\partial F_{j-1}}{\partial \phi^x_j}\frac{\partial G_{j-1}}{\partial \phi^x_j} + \frac{\partial F_{j-1}}{\partial \phi^x_j}\frac{\partial G_{j-1}}{\partial \phi^x_j} + \frac{\partial F_j}{\partial \phi^x_j}\frac{dG_j}{\partial \phi^x_j} + \frac{\partial F_j}{d\phi^x_j}\frac{dG_j}{\partial \phi^x_j}]$$

$$\frac{\partial^2 S_t}{\partial \phi^y_{j,j\neq 0}\partial \phi^y_{j,j\neq 0}} = \frac{27\pi^2}{2}[\frac{\partial^2 F_{j-1}}{\partial \phi^y_j\partial \phi^y_j}G_{j-1} + F_{j-1}\frac{\partial^2 G_{j-1}}{\partial \phi^y_j\partial \phi^y_j} + \frac{\partial^2 F_j}{\partial \phi^y_j\partial \phi^y_j}G_j + F_j\frac{\partial^2 G_j}{\partial \phi^y_j\partial \phi^y_j} + \frac{\partial F_{j-1}}{\partial \phi^y_j}\frac{\partial G_{j-1}}{\partial \phi^y_j} + \frac{\partial F_{j-1}}{\partial \phi^y_j}\frac{\partial G_{j-1}}{\partial \phi^y_j} + \frac{\partial F_j}{\partial \phi^y_j}\frac{dG_j}{\partial \phi^y_j} + \frac{\partial F_j}{d\phi^y_j}\frac{dG_j}{\partial \phi^y_j}]$$

$$\frac{\partial^2 S_t}{\partial \phi^x_{j,j\neq 0}\partial \phi^y_{j,j\neq 0}} = \frac{27\pi^2}{2}[\frac{\partial^2 F_{j-1}}{\partial \phi^x_j\partial \phi^y_j}G_{j-1} + F_{j-1}\frac{\partial^2 G_{j-1}}{\partial \phi^x_j\partial \phi^y_j} + \frac{\partial^2 F_j}{\partial \phi^x_j\partial \phi^y_j}G_j + F_j\frac{\partial^2 G_j}{\partial \phi^x_j\partial \phi^y_j} + \frac{\partial F_{j-1}}{\partial \phi^x_j}\frac{\partial G_{j-1}}{\partial \phi^y_j} + \frac{\partial F_{j-1}}{\partial \phi^y_j}\frac{\partial G_{j-1}}{\partial \phi^x_j} + \frac{\partial F_j}{\partial \phi^x_j}\frac{dG_j}{\partial \phi^y_j} + \frac{\partial F_j}{d\phi^y_j}\frac{dG_j}{\partial \phi^x_j}]$$

so

$$\frac{\partial^2 S_t}{\partial \phi^x_{j,j\neq 0}\partial \phi^x_{j,j\neq 0}} = \frac{27\pi^2}{2}[\frac{\partial^2 F_{j-1}}{\partial \phi^x_j\partial \phi^x_j}G_{j-1} + F_{j-1}\frac{\partial^2 G_{j-1}}{\partial \phi^x_j\partial \phi^x_j} + \frac{\partial^2 F_j}{\partial \phi^x_j\partial \phi^x_j}G_j + F_j\frac{\partial^2 G_j}{\partial \phi^x_j\partial \phi^x_j} + 2\frac{\partial F_{j-1}}{\partial \phi^x_j}\frac{\partial G_{j-1}}{\partial \phi^x_j} + 2\frac{\partial F_j}{\partial \phi^x_j}\frac{\partial G_j}{\partial \phi^x_j}] \quad \text{(A.54)}$$

$$\frac{\partial^2 S_t}{\partial \phi^y_{j,j\neq 0}\partial \phi^y_{j,j\neq 0}} = \frac{27\pi^2}{2}[\frac{\partial^2 F_{j-1}}{\partial \phi^y_j\partial \phi^y_j}G_{j-1} + F_{j-1}\frac{\partial^2 G_{j-1}}{\partial \phi^y_j\partial \phi^y_j} + \frac{\partial^2 F_j}{\partial \phi^y_j\partial \phi^y_j}G_j + F_j\frac{\partial^2 G_j}{\partial \phi^y_j\partial \phi^y_j} + 2\frac{\partial F_{j-1}}{\partial \phi^y_j}\frac{\partial G_{j-1}}{\partial \phi^y_j} + 2\frac{\partial F_j}{\partial \phi^y_j}\frac{\partial G_j}{\partial \phi^y_j}] \quad \text{(A.55)}$$

$$\frac{\partial^2 S_t}{\partial \phi^x_{j,j\neq 0}\partial \phi^y_{j,j\neq 0}} = \frac{27\pi^2}{2}[\frac{\partial^2 F_{j-1}}{\partial \phi^x_j \partial \phi^y_j}G_{j-1} + F_{j-1}\frac{\partial^2 G_{j-1}}{\partial \phi^x_j \partial \phi^y_j} + \frac{\partial^2 F_j}{\partial \phi^x_j \partial \phi^y_j}G_j + F_j\frac{\partial^2 G_j}{\partial \phi^x_j \partial \phi^y_j} + \frac{\partial F_{j-1}}{\partial \phi^x_j}\frac{\partial G_{j-1}}{\partial \phi^y_j} + \frac{\partial F_{j-1}}{\partial \phi^y_j}\frac{\partial G_{j-1}}{\partial \phi^x_j} + \frac{\partial F_j}{\partial \phi^x_j}\frac{dG_j}{\partial \phi^y_j} + \frac{\partial F_j}{d\phi^y_j}\frac{dG_j}{\partial \phi^x_j}] \tag{A.56}$$

Where the terms $\frac{\partial F_{j-1}}{\partial \phi^x_j}$, $\frac{\partial F_j}{\partial \phi^x_j}$, $\frac{\partial F_{j-1}}{\partial \phi^y_j}$ and $\frac{\partial F_j}{\partial \phi^y_j}$ are given in (A.39) to (A.42) for $j > 0$ and the terms $\frac{\partial F_{j=0}}{\partial \phi^x_{j=0}}$ and $\frac{\partial F_{j=0}}{\partial \phi^x_{j=0}}$ are given in (A.47), (A.48) for $j = 0$.

The derivatives that include adjacent points are,

$$\frac{\partial^2 S_t}{\partial \phi^y_{j-1,j\neq 0}\partial \phi^x_{j,j\neq 0}} = \frac{27\pi^2}{2}\frac{\partial}{\partial \phi^y_{j-1}}[\frac{\partial F_{j-1}}{\partial \phi^x_j}G_{j-1} + F_{j-1}\frac{\partial G_{j-1}}{\partial \phi^x_j} + \frac{\partial F_j}{\partial \phi^x_j}G_j + F_j\frac{\partial G_j}{\partial \phi^x_j}] \tag{A.57}$$

$$\frac{\partial^2 S_t}{\partial \phi^y_{j+1,j\neq 0}\partial \phi^x_{j,j\neq 0}} = \frac{27\pi^2}{2}\frac{\partial}{\partial \phi^y_{j+1}}[\frac{\partial F_{j-1}}{\partial \phi^x_j}G_{j-1} + F_{j-1}\frac{\partial G_{j-1}}{\partial \phi^x_j} + \frac{\partial F_j}{\partial \phi^x_j}G_j + F_j\frac{\partial G_j}{\partial \phi^x_j}] \tag{A.58}$$

giving,

$$\frac{\partial^2 S_t}{\partial \phi^y_{j-1,j\neq 0}\partial \phi^x_{j,j\neq 0}} = \frac{27\pi^2}{2}[\frac{\partial^2 F_{j-1}}{\partial \phi^y_{j-1}\partial \phi^x_j}G_{j-1} + F_{j-1}\frac{\partial^2 G_{j-1}}{\partial \phi^y_{j-1}\partial \phi^x_j} + \frac{\partial^2 F_j}{\partial \phi^y_{j-1}\partial \phi^x_j}G_j + F_j\frac{\partial^2 G_j}{\partial \phi^y_{j-1}\partial \phi^x_j} + \frac{\partial F_{j-1}}{\partial \phi^x_j}\frac{\partial G_{j-1}}{\partial \phi^y_{j-1}} + \frac{\partial F_{j-1}}{\partial \phi^y_{j-1}}\frac{\partial G_{j-1}}{\partial \phi^x_j} + \frac{\partial F_j}{\partial \phi^x_j}\frac{dG_j}{\partial \phi^y_{j-1}} + \frac{\partial F_j}{d\phi^y_{j-1}}\frac{dG_j}{\partial \phi^x_j}]$$

$$\frac{\partial^2 S_t}{\partial \phi^y_{j+1,j\neq 0}\partial \phi^x_{j,j\neq 0}} = \frac{27\pi^2}{2}[\frac{\partial^2 F_{j-1}}{\partial \phi^y_{j+1}\partial \phi^x_j}G_{j-1} + F_{j-1}\frac{\partial^2 G_{j-1}}{\partial \phi^y_{j+1}\partial \phi^x_j} + \frac{\partial^2 F_j}{\partial \phi^y_{j+1}\partial \phi^x_j}G_j + F_j\frac{\partial^2 G_j}{\partial \phi^y_{j+1}\partial \phi^x_j} + \frac{\partial F_{j-1}}{\partial \phi^x_j}\frac{\partial G_{j-1}}{\partial \phi^y_{j+1}} + \frac{\partial F_{j-1}}{\partial \phi^y_{j+1}}\frac{\partial G_{j-1}}{\partial \phi^x_j} + \frac{\partial F_j}{\partial \phi^x_j}\frac{dG_j}{\partial \phi^y_{j+1}} + \frac{\partial F_j}{d\phi^y_{j+1}}\frac{dG_j}{\partial \phi^x_j}]$$

so

$$\frac{\partial^2 S_t}{\partial \phi^y_{j-1,j\neq 0}\partial \phi^x_{j,j\neq 0}} = \frac{27\pi^2}{2}[\frac{\partial^2 F_{j-1}}{\partial \phi^y_{j-1}\partial \phi^x_j}G_{j-1} + F_{j-1}\frac{\partial^2 G_{j-1}}{\partial \phi^y_{j-1}\partial \phi^x_j} + 0 + 0 + \tag{A.59}$$

$$\frac{\partial F_{j-1}}{\partial \phi^x_j}\frac{\partial G_{j-1}}{\partial \phi^y_{j-1}} + \frac{\partial F_{j-1}}{\partial \phi^y_{j-1}}\frac{\partial G_{j-1}}{\partial \phi^x_j} + 0 + 0\ ] \tag{A.60}$$

$$\frac{\partial^2 S_t}{\partial \phi^y_{j+1,j\neq 0}\partial \phi^x_{j,j\neq 0}} = \frac{27\pi^2}{2}[\quad 0 \quad + \quad 0 \quad + \frac{\partial^2 F_j}{\partial \phi^y_{j+1}\partial \phi^x_j} G_j + F_j \frac{\partial^2 G_j}{\partial \phi^y_{j+1}\partial \phi^x_j} + \tag{A.61}$$

$$0 \quad + \quad 0 \quad + \frac{\partial F_j}{\partial \phi^x_j}\frac{dG_j}{\partial \phi^y_{j+1}} \quad + \frac{\partial F_j}{d\phi^y_{j+1}}\frac{dG_j}{\partial \phi^x_j}] \tag{A.62}$$

Differentiating (A.39) to (A.42) then gives the remaining $F_{j>0}$ terms: $\frac{\partial^2 F_{j-1}}{\partial \phi^x_j \partial \phi^x_j}$ and $\frac{\partial^2 F_j}{\partial \phi^x_j \partial \phi^x_j}$ for (A.54), $\frac{\partial^2 F_{j-1}}{\partial \phi^y_j \partial \phi^y_j}$ and $\frac{\partial^2 F_j}{\partial \phi^y_j \partial \phi^y_j}$ for (A.55), $\frac{\partial^2 F_{j-1}}{\partial \phi^x_j \partial \phi^y_j}$ and $\frac{\partial^2 F_j}{\partial \phi^x_j \partial \phi^y_j}$ for (A.56) as

$$\frac{\partial^2 F_{j-1}}{\partial \phi^x_j \partial \phi^x_j} = \frac{2[V(\phi^x_{j-1},\phi^y_{j-1}) + V(\phi^x_j,\phi^y_j) - V_{t,j-1} - V_{t,j}]}{(V_{t,j} - V_{t,j-1})^3}\frac{\partial^2 V(\phi^x_j,\phi^y_j)}{\partial \phi^x_j \partial \phi^x_j} + \frac{2}{(V_{t,j} - V_{t,j-1})^3}(\frac{\partial V(\phi^x_j,\phi^y_j)}{\partial \phi^x_j})^2 \tag{A.63}$$

$$\frac{\partial^2 F_j}{\partial \phi^x_j \partial \phi^x_j} = \frac{2[V(\phi^x_j,\phi^y_j) + V(\phi^x_{j+1},\phi^y_{j+1}) - V_{t,j} - V_{t,j+1}]}{(V_{t,j+1} - V_{t,j})^3}\frac{\partial^2 V(\phi^x_j,\phi^y_j)}{\partial \phi^x_j \partial \phi^x_j} + \frac{2}{(V_{t,j+1} - V_{t,j})^3}(\frac{\partial V(\phi^x_j,\phi^y_j)}{\partial \phi^x_j})^2 \tag{A.64}$$

for (A.54),

$$\frac{\partial^2 F_{j-1}}{\partial \phi^y_j \partial \phi^y_j} = \frac{2[V(\phi^x_{j-1},\phi^y_{j-1}) + V(\phi^x_j,\phi^y_j) - V_{t,j-1} - V_{t,j}]}{(V_{t,j} - V_{t,j-1})^3}\frac{\partial^2 V(\phi^x_j,\phi^y_j)}{\partial \phi^y_j \partial \phi^y_j} + \frac{2}{(V_{t,j} - V_{t,j-1})^3}(\frac{\partial V(\phi^x_j,\phi^y_j)}{\partial \phi^y_j})^2 \tag{A.65}$$

$$\frac{\partial^2 F_j}{\partial \phi^y_j \partial \phi^y_j} = \frac{2[V(\phi^x_j,\phi^y_j) + V(\phi^x_{j+1},\phi^y_{j+1}) - V_{t,j} - V_{t,j+1}]}{(V_{t,j+1} - V_{t,j})^3}\frac{\partial^2 V(\phi^x_j,\phi^y_j)}{\partial \phi^y_j \partial \phi^y_j} \tag{A.66}$$

$$+ \frac{2}{(V_{t,j+1} - V_{t,j})^3}(\frac{\partial V(\phi^x_j,\phi^y_j)}{\partial \phi^y_j})^2 \tag{A.67}$$

for (A.55),

$$\frac{\partial^2 F_{j-1}}{\partial \phi^x_j \partial \phi^y_j} = \frac{2[V(\phi^x_{j-1},\phi^y_{j-1}) + V(\phi^x_j,\phi^y_j) - V_{t,j-1} - V_{t,j}]}{(V_{t,j} - V_{t,j-1})^3}\frac{\partial^2 V(\phi^x_j,\phi^y_j)}{\partial \phi^x_j \partial \phi^y_j} \tag{A.68}$$

$$+ \frac{2}{(V_{t,j} - V_{t,j-1})^3}(\frac{\partial V(\phi^x_j,\phi^y_j)}{\partial \phi^x_j})(\frac{\partial V(\phi^x_j,\phi^y_j)}{\partial \phi^y_j}) \tag{A.69}$$

$$\frac{\partial^2 F_j}{\partial \phi_j^x \partial \phi_j^y} = \frac{2[V(\phi_j^x,\phi_j^y)+V(\phi_{j+1}^x,\phi_{j+1}^y)-V_{t,j}-V_{t,j+1}]}{(V_{t,j+1}-V_{t,j})^3}\frac{\partial^2 V(\phi_j^x,\phi_j^y)}{\partial \phi_j^x \partial \phi_j^y} \tag{A.70}$$

$$+\frac{2}{(V_{t,j}-V_{t,j-1})^3}\left(\frac{\partial V(\phi_j^x,\phi_j^y)}{\partial \phi_j^x}\right)\left(\frac{\partial V(\phi_j^x,\phi_j^y)}{\partial \phi_j^y}\right) \tag{A.71}$$

for (A.56).

For the derivatives with adjacent points,

$$\frac{\partial^2 F_{j-1}}{\partial \phi_{j-1}^y \partial \phi_j^x} = \frac{2[V(\phi_{j-1}^x,\phi_{j-1}^y)+V(\phi_j^x,\phi_j^y)-V_{t,j-1}-V_{t,j}]}{(V_{t,j}-V_{t,j-1})^3}\frac{\partial^2 V(\phi_j^x,\phi_j^y)}{\partial \phi_{j-1}^y \partial \phi_j^x} \tag{A.72}$$

$$+\frac{2}{(V_{t,j}-V_{t,j-1})^3}\left(\frac{\partial V(\phi_j^x,\phi_j^y)}{\partial \phi_j^x}\right)\left(\frac{\partial V(\phi_{j-1}^x,\phi_{j-1}^y)}{\partial \phi_{j-1}^y}\right) \tag{A.73}$$

$$\frac{\partial^2 F_j}{\partial \phi_{j+1}^y \partial \phi_j^x} = \frac{2[V(\phi_j^x,\phi_j^y)+V(\phi_{j+1}^x,\phi_{j+1}^y)-V_{t,j}-V_{t,j+1}]}{(V_{t,j+1}-V_{t,j})^3}\frac{\partial^2 V(\phi_j^x,\phi_j^y)}{\partial \phi_{j+1}^y \partial \phi_j^x} \tag{A.74}$$

$$+\frac{2}{(V_{t,j+1}-V_{t,j})^3}\left(\frac{\partial V(\phi_j^x,\phi_j^y)}{\partial \phi_j^x}\right)\left(\frac{\partial V(\phi_{j+1}^x,\phi_{j+1}^y)}{\partial \phi_{j+1}^y}\right) \tag{A.75}$$

as the second derivative of the potential with respect to different points vanishes, we get

$$\frac{\partial^2 F_{j-1}}{\partial \phi_j^x \partial \phi_{j-1}^y} = 0 \tag{A.77}$$

$$+\frac{2}{(V_{t,j}-V_{t,j-1})^3}\left(\frac{\partial V(\phi_j^x,\phi_j^y)}{\partial \phi_j^x}\right)\left(\frac{\partial V(\phi_{j-1}^x,\phi_{j-1}^y)}{\partial \phi_{j-1}^y}\right) \tag{A.78}$$

$$\frac{\partial^2 F_j}{\partial \phi_j^x \partial \phi_{j+1}^y} = 0 \tag{A.80}$$

$$+\frac{2}{(V_{t,j+1}-V_{t,j})^3}\left(\frac{\partial V(\phi_j^x,\phi_j^y)}{\partial \phi_j^x}\right)\left(\frac{\partial V(\phi_{j+1}^x,\phi_{j+1}^y)}{\partial \phi_{j+1}^y}\right) \tag{A.81}$$

At the boundary ϕ_0 we have

$$\frac{\partial^2 S_t}{\partial \phi_0^x \partial \phi_0^x} = \frac{27\pi^2}{2}\left[\frac{\partial^2 F_0}{\partial \phi_0^x \partial \phi_0^x}G_0 + F_j\frac{\partial^2 G_0}{\partial \phi_0^x \partial \phi_0^x} + 2\frac{\partial F_0}{\partial \phi_0^x}\frac{\partial G_0}{\partial \phi_0^x}\right] \tag{A.82}$$

$$\frac{\partial^2 S_t}{\partial\phi_0^y\partial\phi_0^y} = \frac{27\pi^2}{2}[\frac{\partial^2 F_0}{\partial\phi_0^y\partial\phi_0^y}G_0 \quad + F_0\frac{\partial^2 G_0}{\partial\phi_0^y\partial\phi_0^y} + \\ + 2\frac{\partial F_0}{\partial\phi_0^y}\frac{\partial G_0}{\partial\phi_0^y}] \tag{A.83}$$

$$\frac{\partial^2 S_t}{\partial\phi_0^x\partial\phi_0^y} = \frac{27\pi^2}{2}[\frac{\partial^2 F_0}{\partial\phi_0^x\partial\phi_0^y}G_0 + F_0\frac{\partial^2 G_0}{\partial\phi_0^x\partial\phi_0^y} + \\ + \frac{\partial F_0}{\partial\phi_0^x}\frac{dG_0}{\partial\phi_0^y} + \frac{\partial F_0}{d\phi_0^y}\frac{dG_0}{\partial\phi_0^x}] \tag{A.84}$$

whilst for the derivative that includes the point adjacent to the boundary,

$$H_{01}^{\mathrm{xy}} = \frac{\partial^2 S_t}{\partial\phi_0^x\partial\phi_1^y} = \frac{27\pi^2}{2}\frac{\partial}{\partial\phi_1^y}[\frac{\partial F_0}{\partial\phi_0^x}G_0 + F_0\frac{\partial G_0}{\partial\phi_0^x}] = \frac{27\pi^2}{2}[\frac{\partial^2 F_0}{\partial\phi_1^y\partial\phi_0^x}G_0 + F_0\frac{\partial^2 G_0}{\partial\phi_1^y\partial\phi_0^x} + \\ + \frac{\partial F_0}{\partial\phi_0^x}\frac{\partial G_0}{\partial\phi_1^y} + \frac{\partial F_0}{d\phi_1^y}\frac{dG_0}{\partial\phi_0^x}] \tag{A.85}$$

$$H_{10}^{\mathrm{xy}} = \frac{\partial^2 S_t}{\partial\phi_1^x\partial\phi_0^y} = \frac{27\pi^2}{2}\frac{\partial}{\partial\phi_1^x}[\frac{\partial F_0}{\partial\phi_0^y}G_0 + F_0\frac{\partial G_0}{\partial\phi_0^y}] = \frac{27\pi^2}{2}[\frac{\partial^2 F_0}{\partial\phi_1^x\partial\phi_0^y}G_0 + F_0\frac{\partial^2 G_0}{\partial\phi_1^x\partial\phi_0^y} + \\ + \frac{\partial F_0}{\partial\phi_0^y}\frac{\partial G_0}{\partial\phi_1^x} + \frac{\partial F_0}{\partial\phi_1^x}\frac{dG_0}{\partial\phi_0^y}] \tag{A.86}$$

For the boundary terms with $F_{j=0}$ we differentiate (A.47) and (A.48) to give

$$\frac{\partial}{\partial\phi_{j=0}^x}\frac{\partial F_{j=0}}{\partial\phi_{j=0}^x} = +3\frac{\partial}{\partial\phi_{j=0}^x}(\frac{[V(\phi_1^x,\phi_1^y)-V_{t,1}]^2}{(V_{t,1}-V(\phi_0^x,\phi_0^y))^4}\frac{\partial V(\phi_0^x,\phi_0^y)}{\partial\phi_0^x})$$

$$\frac{\partial}{\partial\phi_{j=0}^y}\frac{\partial F_{j=0}}{\partial\phi_{j=0}^y} = +3\frac{\partial}{\partial\phi_{j=0}^y}(\frac{[V(\phi_1^x,\phi_1^y)-V_{t,1}]^2}{(V_{t,1}-V(\phi_0^x,\phi_0^y))^4}\frac{\partial V(\phi_0^x,\phi_0^y)}{\partial\phi_0^y})$$

$$\frac{\partial}{\partial\phi_{j=0}^y}\frac{\partial F_{j=0}}{\partial\phi_{j=0}^x} = +3\frac{\partial}{\partial\phi_{j=0}^y}(\frac{[V(\phi_1^x,\phi_1^y)-V_{t,1}]^2}{(V_{t,1}-V(\phi_0^x,\phi_0^y))^4}\frac{\partial V(\phi_0^x,\phi_0^y)}{\partial\phi_0^x})$$

$$\frac{\partial}{\partial\phi_1^y}\frac{\partial F_0}{\partial\phi_0^x} = +3\frac{\partial}{\partial\phi_1^y}(\frac{[V(\phi_1^x,\phi_1^y)-V_{t,1}]^2}{(V_{t,1}-V(\phi_0^x,\phi_0^y))^4}\frac{\partial V(\phi_0^x,\phi_0^y)}{\partial\phi_0^x})$$

$$\frac{\partial}{\partial\phi_0^y}\frac{\partial F_0}{\partial\phi_1^x} = +2\frac{\partial}{\partial\phi_0^y}(\frac{[V(\phi_1^x,\phi_1^y)-V_{t,1}]}{(V_{t,1}-V(\phi_0^x,\phi_0^y))^3}\frac{\partial V(\phi_1^x,\phi_1^x)}{\partial\phi_1^x})$$

so that

$$\frac{\partial^2 F_{j=0}}{\partial \phi^x_{j=0} \partial \phi^x_{j=0}} = +3\frac{[V(\phi^x_1,\phi^y_1)-V_{t,1}]^2}{(V_{t,1}-V(\phi^x_0,\phi^y_0))^4}\frac{\partial^2 V(\phi^x_0,\phi^y_0)}{\partial \phi^x_0 \partial \phi^x_0} \tag{A.87}$$

$$+12\frac{[V(\phi^x_1,\phi^y_1)-V_{t,1}]^2}{(V_{t,1}-V(\phi^x_0,\phi^y_0))^5}(\frac{\partial V(\phi^x_0,\phi^y_0)}{\partial \phi^x_0})^2 \tag{A.88}$$

$$\frac{\partial^2 F_{j=0}}{\partial \phi^y_{j=0} \partial \phi^y_{j=0}} = +3\frac{[V(\phi^x_1,\phi^y_1)-V_{t,1}]^2}{(V_{t,1}-V(\phi^x_0,\phi^y_0))^4}\frac{\partial^2 V(\phi^x_0,\phi^y_0)}{\partial \phi^y_0 \partial \phi^y_0} \tag{A.89}$$

$$+12\frac{[V(\phi^x_1,\phi^y_1)-V_{t,1}]^2}{(V_{t,1}-V(\phi^x_0,\phi^y_0))^5}(\frac{\partial V(\phi^x_0,\phi^y_0)}{\partial \phi^y_0})^2 \tag{A.90}$$

and

$$\frac{\partial^2 F_{j=0}}{\partial \phi^x_{j=0} \partial \phi^y_{j=0}} = +3\frac{[V(\phi^x_1,\phi^y_1)-V_{t,1}]^2}{(V_{t,1}-V(\phi^x_0,\phi^y_0))^4}\frac{\partial^2 V(\phi^x_0,\phi^y_0)}{\partial \phi^x_0 \partial \phi^y_0} \tag{A.91}$$

$$+12\frac{[V(\phi^x_1,\phi^y_1)-V_{t,1}]^2}{(V_{t,1}-V(\phi^x_0,\phi^y_0))^5}(\frac{\partial V(\phi^x_0,\phi^y_0)}{\partial \phi^x_0})(\frac{\partial V(\phi^x_0,\phi^y_0)}{\partial \phi^y_0}) \tag{A.92}$$

whilst

$$\frac{\partial^2 F_0}{\partial \phi^x_0 \partial \phi^y_1} = \quad 0 \quad +6\frac{[V(\phi^x_1,\phi^y_1)-V_{t,1}]}{(V_{t,1}-V(\phi^x_0,\phi^y_0))^4}(\frac{\partial V(\phi^x_0,\phi^y_0)}{\partial \phi^x_0})(\frac{\partial V(\phi^x_1,\phi^y_1)}{\partial \phi^y_1}) \tag{A.93}$$

$$\frac{\partial^2 F_0}{\partial \phi^x_1 \partial \phi^y_0} = \quad 0 \quad +6\frac{[V(\phi^x_1,\phi^y_1)-V_{t,1}]}{(V_{t,1}-V(\phi^x_0,\phi^y_0))^4}(\frac{\partial V(\phi^x_1,\phi^y_1)}{\partial \phi^x_1})(\frac{\partial V(\phi^x_0,\phi^y_0)}{\partial \phi^y_0}) \tag{A.94}$$

Using (A.11) to (A.14) to help differentiate (A.19) to (A.22) then gives

$$\frac{\partial^2 G_{j-1}}{\partial \phi^x_j \partial \phi^x_j} = +4[(\Delta\underset{\sim}{\phi}_{j-1}).(\Delta\underset{\sim}{\phi}_{j-1})] + 8(\Delta\phi^x_{j-1})^2 \tag{A.95}$$

$$\frac{\partial^2 G_j}{\partial \phi^x_j \partial \phi^x_j} = +4[(\Delta\underset{\sim}{\phi}_j).(\Delta\underset{\sim}{\phi}_j)] + 8(\Delta\phi^x_j)^2 \tag{A.96}$$

$$\frac{\partial^2 G_{j-1}}{\partial \phi^y_j \partial \phi^y_j} = +4[(\Delta\underset{\sim}{\phi}_{j-1}).(\Delta\underset{\sim}{\phi}_{j-1})] + 8(\Delta\phi^y_{j-1})^2 \tag{A.97}$$

$$\frac{\partial^2 G_j}{\partial \phi^y_j \partial \phi^y_j} = +4[(\Delta\underset{\sim}{\phi}_j).(\Delta\underset{\sim}{\phi}_j)] + 8(\Delta\phi^y_j)^2 \tag{A.98}$$

$$\frac{\partial^2 G_{j-1}}{\partial \phi^x_j \partial \phi^y_j} = +4[(\Delta\underset{\sim}{\phi}_{j-1}).(\Delta\underset{\sim}{\phi}_{j-1})] + 8(\Delta\phi^x_{j-1})(\Delta\phi^y_{j-1}) \tag{A.99}$$

$$\frac{\partial^2 G_j}{\partial \phi_j^x \partial \phi_j^y} = +4[(\Delta \underset{\sim}{\phi}_j).(\Delta \underset{\sim}{\phi}_j)] + 8(\Delta \phi_j^x)(\Delta \phi_j^y) \tag{A.100}$$

and for the second order derivatives that include adjacent points we have

$$\frac{\partial^2 G_{j-1}}{\partial \phi_{j-1}^y \partial \phi_j^x} = -4[(\Delta \underset{\sim}{\phi}_{j-1}).(\Delta \underset{\sim}{\phi}_{j-1})] - 8(\Delta \phi_{j-1}^y)(\Delta \phi_{j-1}^x) \tag{A.101}$$

$$\frac{\partial^2 G_j}{\partial \phi_{j+1}^y \partial \phi_j^x} = -4[(\Delta \underset{\sim}{\phi}_j).(\Delta \underset{\sim}{\phi}_j)] - 8(\Delta \phi_j^y)(\Delta \phi_j^x) \tag{A.102}$$

To evaluate a Hessian block,

$$H_{xy} = \frac{\partial^2 S_t}{\partial \phi^x \partial \phi^y} = \begin{pmatrix} \frac{\partial^2 S_t}{\partial \phi_1^x \partial \phi_1^y} & \frac{\partial^2 S_t}{\partial \phi_1^x \partial \phi_2^y} & 0 & & & 0 & 0 & 0 \\ \frac{\partial^2 S_t}{\partial \phi_2^x \partial \phi_1^y} & \frac{\partial^2 S_t}{\partial \phi_2^x \partial \phi_2^y} & \frac{\partial^2 S_t}{\partial \phi_2^x \partial \phi_3^y} & \cdots & & 0 & 0 & 0 \\ 0 & \frac{\partial^2 S_t}{\partial \phi_3^x \partial \phi_2^y} & \frac{\partial^2 S_t}{\partial \phi_3^x \partial \phi_3^y} & & & 0 & 0 & 0 \\ 0 & 0 & \frac{\partial^2 S_t}{\partial \phi_4^x \partial \phi_3^y} & & & 0 & 0 & 0 \\ & \vdots & & \ddots & & \vdots & & \\ 0 & 0 & 0 & & \frac{\partial^2 S_t}{\partial \phi_{n-2}^x \partial \phi_{n-3}^y} & \frac{\partial^2 S_t}{\partial \phi_{n-2}^x \partial \phi_{n-2}^y} & \frac{\partial^2 S}{\partial \phi_{n-2}^x \partial \phi_{n-1}^y} \\ 0 & 0 & 0 & \cdots & 0 & \frac{\partial^2 S_t}{\partial \phi_{n-1}^x \partial \phi_{n-2}^y} & \frac{\partial^2 S_t}{\partial \phi_{n-1}^x \partial \phi_{n-1}^y} \end{pmatrix} \tag{A.103}$$

we therefore use $\frac{\partial^2 S_t}{\partial \phi_{j-1,j\neq 0}^y \partial \phi_{j,j\neq 0}^x}$ from (A.59), $\frac{\partial^2 S_t}{\partial \phi_{j+1,j\neq 0}^y \partial \phi_{j,j\neq 0}^x}$ from (A.61) and $\frac{\partial^2 S_t}{\partial \phi_{j,j\neq 0}^x \partial \phi_{j,j\neq 0}^y}$ from (A.56).

To evaluate the gradient, ∇S_t, where

$$\underset{\sim}{\nabla} S_t = \begin{bmatrix} \nabla_x S_t \\ \nabla_y S_t \end{bmatrix} = \begin{bmatrix} \frac{\partial S_t}{\partial \phi_1^x} \\ \vdots \\ \frac{\partial S_t}{\partial \phi_{n-1}^x} \\ \frac{\partial S_t}{\partial \phi_1^y} \\ \vdots \\ \frac{\partial S_t}{\partial \phi_{n-1}^y} \end{bmatrix}. \tag{A.104}$$

we use $\frac{\partial S_t}{\partial \phi_j^x}$ from (A.35) and $\frac{\partial S_t}{\partial \phi_j^y}$ from (A.36).

A.2 Boundary Conditions

Consider variations of the action, S_t, under variations of the path $\underset{\sim}{\phi}$. Here we keep $V_t(\underset{\sim}{\phi})$ fixed with $V_t(\underset{\sim}{\phi}) = V_t(\underset{\sim}{\phi} + \delta\underset{\sim}{\phi})$. This cannot be done if $\underset{\sim}{\phi}_0$ is also varied in the modified path and $V(\underset{\sim}{\phi}) \neq V(\underset{\sim}{\phi} + \delta\underset{\sim}{\phi})$ ($\underset{\sim}{\phi}_+$ is always fixed at the false vacuum). In that case we can always extend the original (or deformed) path from $\underset{\sim}{\phi}_0$ to $\underset{\sim}{\phi}_0 + \delta\underset{\sim}{\phi}_0$ by keeping $V_t = V$ and $V_t^{'} \neq 0$ in that interval. This extended path has the same action as the un-extended path as it corresponds to the original path to $\underset{\sim}{\phi}_0$ plus an extended path component from $\underset{\sim}{\phi}_0$ to $\underset{\sim}{\phi}_0 + \delta\underset{\sim}{\phi}_0$ that is entirely in the V surface. From (4.20) we have

$$S_t = 54\pi^2 \int_{\varphi_+}^{\varphi_0} d\varphi \frac{(V - V_t)^2}{(-V_t)^3}$$

where we can rewrite the action by introducing an aditional variable α that parameterises the path so that

$$S_t = 54\pi^2 \int_{\alpha_0}^{\alpha_+} d\alpha \frac{(V - V_t)^2}{(\frac{dV_t}{d\alpha})^3} \left(\frac{d\underset{\sim}{\phi}}{d\alpha} . \frac{d\underset{\sim}{\phi}}{d\alpha} \right)^2$$

This action is evidently invariant under a reparameterisation of the path $\alpha \to \bar{\alpha}(\alpha)$ as α was chosen arbitrarily in the first place as any parameter that parameterises the path.

A generic change of path $\underset{\sim}{\phi}$ and tunneling potential $V_t(\varphi)$ to reduce the action S_t towards a lower value can be decomposed into a change of $V_t(\varphi)$ that keeps the path $\underset{\sim}{\phi}$ fixed and a change of path $\underset{\sim}{\phi}$ that keeps $V_t(\varphi)$ fixed. This is because, in the latter case, if the length of the path is modified we can still keep $V_t(\varphi)$ fixed by using the α reparameterisation invariance. From (4.20) using V_t as the path variable

$$S_t = 54\pi^2 \int_{\alpha_0}^{\alpha_+} d\alpha \frac{(V - V_t)^2}{(\frac{dV_t}{d\alpha})^3} \left(\frac{d\underset{\sim}{\phi}}{d\alpha} . \frac{d\underset{\sim}{\phi}}{d\alpha} \right)^2 = 54\pi^2 \int_{V_t(\varphi_0)=V(\underset{\sim}{\phi}_0)}^{V_t(\varphi_+)=V(\underset{\sim}{\phi}_+)} dV_t (V - V_t)^2 \left(\frac{d\underset{\sim}{\phi}}{dV_t} . \frac{d\underset{\sim}{\phi}}{dV_t} \right)^2$$

so that

$$\frac{\partial S_t(\phi_0^x, \phi_0^y)}{\partial \phi_0^x} = 54\pi^2 \frac{\partial S_t(\phi_0^x, \phi_0^y)}{\partial \phi_0^x} \int_{\varphi_+}^{\varphi_0} d\varphi \frac{(V - V_t)^2}{(-V_t)^3} \tag{A.105}$$

and $V_t = V$ with $V_t^{'} \neq 0$ means that the integrand remains at zero at $\underset{\sim}{\phi}_0 + \delta\underset{\sim}{\phi}_0$. The changed portion of the Action integral (A.6) from $\underset{\sim}{\phi}_0$ to $\underset{\sim}{\phi}_0 + \delta\underset{\sim}{\phi}_0$ is then

$$\delta S_{t,0} = \frac{27\pi^2}{2} [V(\phi_0^x + \delta\phi_0^x, \phi_0^y + \delta\phi_0^y) + V(\phi_1^x, \phi_1^y) - V_{t,0} - V_{t,1}]^2 \frac{[(\Delta\phi_0^x)^2 + (\Delta\phi_0^y)^2]^2}{(V_{t,1} - V_{t,0})^3} \tag{A.106}$$

or

$$\delta S_{t,0} = \frac{27\pi^2}{2} [V(\phi_1^x, \phi_1^y) - V_{t,1}]^2 \frac{[(\Delta\phi_0^x)^2 + (\Delta\phi_0^y)^2]^2}{(V_{t,1} - V(\phi_0^x + \delta\phi_0^x, \phi_0^y + \delta\phi_0^y))^3} \tag{A.107}$$

which only depends on the original (ϕ_0^x, ϕ_0^y) values through $V(\phi_0^x, \phi_0^y)$ and $V(\phi_1^x, \phi_1^y) - V_{t,1}$. From (A.107) we then have

$$\delta S_{t,0} = \frac{27\pi^2}{2}[V(\phi_1^x, \phi_1^y) - V_{t,1}]^2 \frac{[(\Delta\phi_0^x)^2 + (\Delta\phi_0^y)^2]^2}{(V_{t,1} - V(\phi_0^x, \phi_0^y))^3} \tag{A.108}$$

To minimise the action with respect to the release point $\underset{\sim}{\phi}_0$ we need to find a change in $\underset{\sim}{\phi}_0$ that reduces the action S_t by evaluating $\frac{\partial S_t}{\partial \phi_0^x}$ and $\frac{\partial S_t}{\partial \phi_0^y}$.

Appendix B

Cosmological Constraints on non-thermalised sectors

B.1 Maintaining a Temperature Hierarchy

A necessary condition to maintain a temperature difference between the hidden and visible sector is that they stay out of thermal equilibrium with each other. This is the case if the (temperature dependent) interaction rate between them, Γ_I, satisfies

$$\Gamma_I < H \ , \tag{B.1}$$

at all times between reheating and the hidden sector phase transition. The form of Γ_I depends on which of the hidden and visible sectors is hotter. We assume that the visible sector is hotter, in which case Eq. (B.1) becomes

$$\langle \sigma v \rangle \, n_{\rm v} < H(T_{\rm v}) \ , \tag{B.2}$$

where $\langle \sigma v \rangle$ is the thermally averaged cross section between the visible and hidden sectors and $n_{\rm v}$ is the number density of the relevant states in the visible sector.[1]

For relatively small temperature differences the condition in Eq. (B.1) is approximately sufficient to maintain a hierarchy. However, for large temperature ratios a stronger condition is required. The hidden sector temperature must not be increased by energy transfer from the visible sector, even if this energy is not enough for the two sectors to reach the same temperature. The resulting constraint can be estimated by demanding that the energy density transferred per Hubble time to the hidden sector is smaller than that already present

[1] A hidden sector that is hotter than the visible sector is less interesting. The universe must be dominated by the visible sector before BBN, so in this case the energy density in the hidden sector must be transferred to the visible sector before this time. There are regions of parameter space in which this is possible. However the gravitational wave signal that would arise is similar in shape and amplitude to if the two sectors were in thermal equilibrium throughout.

in the hidden sector, all times prior to the phase transition. This corresponds to

$$\frac{n_{\mathrm{v}}^2 \langle \sigma v \rangle T_{\mathrm{v}}}{H^4} \lesssim \frac{T_{\mathrm{h}}^4}{H^3} \,, \tag{B.3}$$

where we have dropped factors of order 1. If a hidden sector is initially colder than this, but the portal coupling is not large enough for full thermalisation, it would be partially heated up until Eq. (B.3) is satisfied.

The hidden sector that we consider can couple to the visible sector in multiple different ways, and we focus on a simple Higgs portal operator as an example. This interaction takes the form

$$\mathscr{L} \supset -\frac{1}{2}\lambda_p |\Phi|^2 |H|^2 \,, \tag{B.4}$$

where H is the SM Higgs doublet. Although $\lambda_p = 0$ is technically natural, it is not unreasonable to suppose a non-zero value might be present, for example due to heavy states that couple to both sectors.

If the hidden sector phase transition happens when the visible sector temperature is above the scale of the electroweak (EW) phase transition, the cross section between the two sectors at the relevant times is

$$\langle \sigma v \rangle \sim \frac{\lambda_p^2}{32\pi T_{\mathrm{v}}^2} \,, \tag{B.5}$$

and Eq. (B.3) becomes

$$\lambda_p \lesssim 10^{-8} \varepsilon^{3/2} \left(\frac{w}{\mathrm{GeV}}\right)^{1/2} \,. \tag{B.6}$$

When $\varepsilon = 1$ this matches the previously known condition for the two sectors to not thermalise at temperatures above the EW scale $\lambda \lesssim 10^{-7}$ [234]. As expected, smaller values of the portal couplings are required to maintain a large temperature hierarchy between the two sectors, and tiny portal couplings are needed if $\varepsilon \ll 1$.

The condition on λ_p is different if the hidden sector phase transition happens when the visible sector temperature is below the EW scale. In this case the dominant energy transfer from the visible sector happens immediately after the EW phase transition, since at this point the decay channel $h \to \phi\phi$ is open and there is still a thermal population of the SM Higgs (which will later be exponentially suppressed).[2] The resulting energy transfer can be approximated from the Higgs branching fraction to the hidden sector [234], which leads to the constraint to maintain a temperature hierarchy

$$\lambda_p \lesssim 10^{-10} \varepsilon^2 \,. \tag{B.7}$$

[2] Since we assume that the hidden sector is colder than the visible sector this is automatically kinematically allowed.

This again matches the condition for thermalisation when $\varepsilon = 1$, and it is much stronger for small ε. Such tiny portal couplings are far beyond the reach of any direct experimental searches.[3]

B.2 Constraints from dark matter

In this section we will use well known observational upper bounds on the relic density of dark matter to put constrains on either the temperature ratio, ε, or the strength of the transition, α, for a variety of cosmological scenarios involving a cold hidden sector. To do this we will first consider bounds on the hidden ϕ particle in the case that where it is stable, where it can decay to lighter hidden sector states and where it can decay to SM particles (such as the SM Higgs or visible sector fermions) respectively. Finally we will also asses how the relic abundance of hidden gauge bosons can affect bounds on ε and α.

First we estimate the relic abundance of ϕ if it is stable. Assuming that its number changing interactions become inefficient immediately after the hidden sector phase transition, the relic yield of ϕ is

$$Y_\phi = \frac{n_\phi}{s_\mathrm{v}} \,, \tag{B.8}$$

where s_v is the visible sector entropy density at this time (which is assumed to dominate the universe). If the energy released by the phase transition is small compared to the energy in the hidden sector at this time, i.e. $\alpha_\mathrm{h} \lesssim 1$, the relic yield is

$$Y_\phi \sim \frac{80}{g_\mathrm{v} g^2} \varepsilon^3 \tag{B.9}$$

where g_v and ε are evaluated at the time of the phase transition. For the relic population of ϕ not to exceed the observed DM abundance

$$Y_\phi < \frac{4.4 \times 10^{-10}\ \mathrm{GeV}}{m_\phi} \,, \tag{B.10}$$

which constrains

$$\varepsilon \lesssim 2 \times 10^{-3} \left(\frac{\mathrm{GeV}}{w}\right)^{1/3} \left(\frac{g_\mathrm{v}}{106.75}\right)^{1/3} \,, \tag{B.11}$$

[3] A temperature difference could be maintained with larger values of the portal coupling if the reheating temperature of the universe was below the EW scale. In this case energy is only transferred to the hidden sector through scattering of light SM fermions via an off-shell Higgs, and the rate that this occurs at is strongly suppressed. Portal couplings that are large enough to have observational consequences might be possible in this case, although we do not investigate it further.

at the time of the phase transition.[4]

If the energy released by the phase transition is large compared to that previously in the hidden sector thermal bath, the relic abundance of ϕ constrains α rather than ε. Since the hidden sector is reheated to a temperature $T_{\rm h} \lesssim w$, the number of ϕ states produced is approximately $\rho_{\rm vac}/m_\phi$ and the yield of ϕ can be estimated as

$$Y_\phi \sim \frac{1}{g_{\rm v}^{1/4}} \alpha^{3/4} \,. \tag{B.12}$$

For this to not over close the universe requires[5]

$$\alpha \lesssim 10^{-11} \left(\frac{g_{\rm v}}{106.75}\right)^{1/3} \left(\frac{\rm GeV}{g^2 w}\right)^{2/3} \,. \tag{B.13}$$

Although they are only very approximate, Eq. (B.11) and (B.13) are sufficient to show that if ϕ is stable then values of $\varepsilon \sim 1$ are not viable regardless of how little energy is released by the hidden sector phase transition. If $\varepsilon \ll 10^{-3}$ and $\alpha \ll 10^{-11}$ there is no danger of a relic population of ϕ over closing the universe. However, we will see that the gravitational wave signals from a sector satisfying these conditions are unobservably small, so we now consider models in which ϕ is unstable.

If the Higgs portal operator Eq. (6.6) is present ϕ can decay to the visible sector once it has a VEV. Its decay rate to a pair of visible sector fermions with mass m_f (after the EW phase transition) is

$$\Gamma_\phi = \frac{\lambda_p^2}{4\pi} \frac{w^2 m_f^2 m_\phi}{m_h^4} \left(1 - \frac{4m_f^2}{m_\phi^2}\right)^{3/2} \,, \tag{B.14}$$

which, considering visible sector fermions with $m_f \ll m_\phi$, corresponds to a lifetime

$$\Gamma_\phi^{-1} \simeq \left(\frac{10^{-7}}{\lambda_p}\right)^2 \left(\frac{\rm GeV^2}{m_f w}\right)^2 {\rm s} \,. \tag{B.15}$$

If ϕ is sufficiently heavy it can also decay directly to the SM Higgs. This is possible while the SM is in the unbroken EW phase (due to the Higgs thermal mass this still requires $m_\phi > 2m_h$), but for our purposes it is enough to note that its decay rate once EW symmetry

[4] We assume that the hidden sector is in internal thermal equilibrium immediately before it undergoes its phase transition. This will be the case unless there is an extreme hierarchy between the hidden and visible sectors' temperatures, which would result in a negligibly small relic abundance from energy in the hidden sector prior to the transition.

[5] If the energy in the hidden sector thermal bath immediately before the transition is similar to that released, so $\alpha_{\rm h} \sim 1$, the constraints Eq. (B.11) and Eq. (B.13) coincide, as expected.

is broken, assuming $m_\phi \gg m_h$, is

$$\Gamma_\phi \simeq \frac{\lambda_p^2 w^2}{32\pi m_\phi} \,, \tag{B.16}$$

which leads to a lifetime

$$\Gamma_\phi^{-1} \simeq \left(\frac{10^{-12}}{\lambda_p}\right)^2 \left(\frac{100 \text{ GeV}}{w}\right) \text{s} \,. \tag{B.17}$$

In some parts of parameter space Eqs. (B.15) and (B.17) allow ϕ to decay before BBN for values of λ_p that do not destroy the temperature hierarchy between the hidden and visible sectors. However, this is not possible if ϕ is relatively light. In such cases, the simplest option to obtain a viable model is to introduce light hidden sector fermions, with mass m_ψ, that ϕ can decay to. We assume that the coupling of ϕ to these states is sufficiently large that it decays fairly fast, but that these states only interact with each other weakly and after the phase transition their comoving number density is constant. If $\alpha_\text{h} \gtrsim 1$ their yield can be estimated similarly to Eq. (B.12) and to avoid overclosure of the universe requires

$$m_\psi \lesssim \frac{\text{eV}}{\alpha^{3/4}} \,, \tag{B.18}$$

while if $\alpha_\text{h} \lesssim 1$ we need

$$m_\psi \lesssim \frac{\text{eV}}{\varepsilon^3} \,, \tag{B.19}$$

similarly to how Eq. (B.9) was derived. If $\alpha \sim 1$ the relic population of ψ forms a warm dark matter component, which must be subdominant to the main cold dark matter.

There can also be a significant relic abundance of the hidden sector gauge bosons. Given our assumption about the hierarchy of masses in the hidden sector these have an annihilation channel to ϕ (with a cross section that is proportional to g^2/w^2), so their relic abundance is set by freeze-out.

If the hidden sector is at approximately the same temperature as the visible sector, the gauge boson relic abundance is the same as has been studied in the literature. In this case there are large regions of parameter space that have either an under-abundance of gauge boson dark matter, or the full required abundance (provided that $w \lesssim 10^5$ GeV due to the usual unitarity bound) [68]. If the hidden sector is cold relative to the visible sector, this will affect the gauge boson relic abundance. The Hubble parameter will be larger when the hidden sector temperature drops below m_A, owing to the energy density in the visible sector, so freeze-out will happen at a slightly higher hidden sector temperature than would otherwise be the case. On the other hand, the final dark matter yield will be dramatically decreased since the entropy of the universe is higher, which typically more than compensates the previous effect.

An upper bound on the gauge boson yield can be obtained similarly to that of ϕ in Eq. (B.9) and (B.12). This corresponds to assuming that gauge boson annihilations become inefficiently immediately after the phase transition. Since we consider parts of parameter space in which the gauge bosons masses are similar to the mass of ϕ, the resulting bounds on α and ε are similar to Eqs. (B.11) and (B.13).

We therefore conclude that if α and ε are such that a population of stable ϕ particles is cosmologically safe, the hidden sector gauge bosons will also not overclose the universe. Models in which ϕ can decay to the visible sector via a Higgs portal operator are only possible with not too different hidden and visible sector temperatures (otherwise the temperature hierarchy would be erased), so there are large regions of parameter space such that the gauge boson relic abundance is viable. Finally in models that require light hidden sector fermions for ϕ to decay to, these states can break the hidden sector custodial symmetry, and therefore allow the gauge bosons to also decay.

B.3 Bounds from BBN and CMB

In this section we consider observational constraints on the additional number of relativistic degrees of freedom from BBN and the CMB to put constraints on the phase transition strength, α and tempaerture ratio at the time of the transition ε. To do this we first use observational constraints to put bounds on ε at BBN/CMB times before utilising arguments regarding conservation of entropy discussed in Sec. 6.1.1 to put bounds on ε at reheating and the time of the phase transition.

The current observational constraint on the effective number of additional relativistic degrees of freedom $g_{\rm new}$ at the time of BBN is (at 95% confidence level) [235]

$$g_{\rm new} < 0.263 \,, \tag{B.20}$$

which, following [236], can be interpreted as a constraint on cold hidden sectors. A hidden sector that contains $g_{\rm h,BBN}$ relativistic degrees of freedom with a temperature $T_{\rm h,BBN}$ at the time of BBN gives a contribution to $g_{\rm new}$ of

$$\begin{aligned} \Delta g_{\rm new} &= g_{\rm h,BBN} \left(\frac{T_{\rm h,BBN}}{T_{\rm v,BBN}} \right)^4 \\ &= g_{\rm h,BBN} \, \varepsilon_{\rm BBN}^4 \end{aligned} \tag{B.21}$$

where BBN denotes quantities evaluated at the time of BBN.[6]

[6] It is straightforward to extend these expressions to include hidden sector states that are on the threshold of becoming non-relativistic.

If the hidden sector phase transition happens after BBN (so the hidden sector Higgs and gauge fields are relativistic at this time), Eq. (B.21) constrains

$$\varepsilon_{\rm BBN} < 0.40 \,, \tag{B.22}$$

assuming there are no additional hidden sector degrees of freedom. If an additional hidden sector Dirac fermion is introduced so that ϕ can decay the constraint is slightly stronger

$$\varepsilon_{\rm BBN} < 0.37 \,. \tag{B.23}$$

Assuming that entropy is conserved between reheating and the hidden sector phase transition, these can be converted into bounds on ε at the time of reheating via Eq. (6.4)

$$\begin{aligned} \varepsilon_{\rm BBN} &\simeq 0.47 \varepsilon_{\rm RH} \left(\frac{106.75}{g_{\rm v,RH}}\right)^{1/3} \\ \implies \varepsilon_{\rm RH} &< 0.76 \left(\frac{106.75}{g_{\rm v,RH}}\right)^{1/3} \,, \end{aligned} \tag{B.24}$$

where we assume the presence of light hidden sector fermions in the last line.

If the phase transition happens before BBN and ϕ is stable, the relic density constraints, Eqs. (B.11) and (B.13), are much stronger than BBN bounds so the latter are automatically satisfied in viable models. If ϕ decays to the visible sector prior to BBN there are also no constraints from this source.[7]

If the phase transition happens prior to BBN and there are light hidden sector fermions, the constraints from BBN can be significant. Shortly after the phase transition all of the hidden sector's energy density is transferred to a population of ψ, and the relic density bound requires that the mass of these is such that they remain relativistic until the time of BBN (assuming a relatively large α for an observable signal). As a result we require

$$\alpha < 0.024 \,, \tag{B.25}$$

if $\alpha_{\rm h} \gtrsim 1$, and $\varepsilon < 0.23$ at the time of the phase transition otherwise.

CMB bounds on the additional number of relativistic degrees of freedom might also be relevant. Analogously to Eq. (B.21), these can be converted to a constraint on a cold hidden sector

$$g_{\rm h,CMB}\, \varepsilon_{\rm CMB}^4 \leq 0.0518 \;\; (95\% \;\; {\rm CL}) \,, \tag{B.26}$$

at the time of photon decoupling [154].

[7] Models in which there are decays of hidden sector states to the visible sector around the time of BBN, or subsequently, are strongly constrained [237], however we focus on parts of parameter space safely away from this issue.

We assume that the hidden sector phase transition happens long before the formation of the CMB. In this case CMB limits are only important if the hidden sector contains light fermions. We assume α is not too small (as is required for observable gravitational wave signals), so the relic ψ states are still relativistic at CMB time from Eq .(B.18). Then Eq. (B.26) is satisfied if

$$\alpha < 0.015 \,, \tag{B.27}$$

and

$$\varepsilon < 0.2 \,, \tag{B.28}$$

at the time of the phase transition. These limits are slightly, but not dramatically, stronger than the constraints from BBN.

The strong dependence of Eq. (B.21) on ε means that only a mild temperature hierarchy between the hidden and visible sectors is needed to accommodate BBN and CMB observations. Despite this, the temperature difference resulting from the large change in the visible sector number of relativistic degrees of freedom at the QCD phase transition and electron/positron annihilation is not quite sufficient for the constraints to be satisfied if the hidden and visible sectors are initially at the same temperature, and an initial temperature difference is required.[8]

B.4 Transitions after low scale reheating in the hidden sector

In this section we analyse the impact of relaxing our previous assumption that the hidden sector is reheated above the temperature at which its high temperature phase is favoured. In doing so we show that a tunelling transition still only occurs if the hidden sector is cold relative to the visible sector.

The hidden sector might be reheated to a temperature that is below the scale at which its symmetry is restored, or it may not be reheated at all. If the hidden sector is in the symmetry preserving phase at the end of inflation, this can result in a phase transition happening through tunnelling rather than thermal fluctuations. Such initial conditions arise most naturally if the Hubble parameter during inflation is above the symmetry restoration scale. We will see that this scenario is easily possible in models with a significant temperature difference between the hidden and visible sectors, but it cannot occur for hidden sectors at the same temperature as the visible sector if the scale of the phase transition is $\lesssim$ TeV.[9]

[8] We assume the SM high temperature value of $g_{\rm v}$ at reheating.

[9] It may be possible to arrange for these initial conditions despite a lower Hubble scale during inflation, evading our argument, by introducing a more complex prior cosmological history. However this simply postpones the question of the initial conditions to earlier times.

We suppose that the Hubble scale during inflation $H_I > w$, and for the moment we also assume that the hidden and visible sectors are at the same temperature. The visible sector reheat temperature must be $\gtrsim 5$ MeV to preserve the successful predictions of BBN. This constrains the inflaton decay rate $\Gamma_{\rm inf}$ to

$$\text{MeV} \lesssim \left(\Gamma_{\rm inf} M_{\rm Pl}\right)^{1/2} , \tag{B.29}$$

which means that the maximum temperature after inflation $T_{\rm max}$ (which is larger than the reheating temperature) will be [238]

$$\begin{aligned} T_{\rm max} &\simeq \left(H_I M_{\rm Pl}^2 \Gamma_{\rm inf}\right)^{1/4} \\ &\gtrsim 3000\,\text{GeV} \left(\frac{H_I}{100\ \text{GeV}}\right)^{1/4} . \end{aligned} \tag{B.30}$$

Therefore for hidden sectors at a scale $w \lesssim$ TeV the universe automatically reaches a temperature at which the hidden sector symmetry is restored if $H_I \gtrsim w$. Subsequently, as the temperature drops a thermal transition will happen in preference to a tunnelling transition, as in the previously considered case.[10]

For hidden sectors at higher scales it is possible that its symmetry is restored during inflation and the sector subsequently undergoes a tunnelling transition, despite being at the same temperature as the visible sector. This requires $T_{\rm max} < w$, and that the tunnelling transition happens before H drops below $\sim w^2/M_{\rm Pl}$, when the universe would reenter an inflationary phase. The conflicting pressures of reheating above the scale of BBN and having $T_{\rm max} < w$ mean that tunnelling transitions only happen in a small region of parameter space. Additionally, the entropy injection by the inflaton decays after the phase transition dilute the present day gravitational wave signal in this case.

These issues are avoided if the hidden sector is cold relative to the visible sector. The Hubble scale during inflation can be sufficiently high that the hidden sector symmetry is restored, $H > w$. However, if the inflaton decays dominantly to the visible sector the hidden sector temperature might never get close to w, despite the visible sector being reheated above the scale of BBN. In this case a thermal transition will not take place, but provided S_4 is sufficiently large a tunnelling transition can happen before the hidden sector vacuum energy density dominates the universe.

The condition that a tunnelling transition completes is $\Gamma_4 \gtrsim \sqrt{\rho_{\rm vac}}/\left(3M_{\rm Pl}\right)$, as before. The parts of parameter space that satisfy this condition are those in Fig. 6.4 right that

[10] A minor caveat to this argument is that the relation between the Hubble parameter and temperature is altered during reheating, because the universe is matter dominated. This makes it slightly less likely that a transition completes through thermal fluctuations. In practice the difference between the two actions, e.g. from Eqs. (6.11) and (6.12), is sufficiently large that this does not lead to a tunnelling transition in any of the parameter space of our model.

undergo a transition (including parts shown as going through a thermal transition in the previous context of that plot). The visible sector temperature at the time of the transition is again given by Eq. (6.17) (assuming, for simplicity, that the transition happens after reheating completes i.e. when the Hubble parameter is $\lesssim H\left(T_{\mathrm{RH}}\right)$).

Appendix C

Gravitational waves signals

Here we summarise results from the literature that support the parameterised fits of the gravitational waves signals that we use in Chapter 7, and our neglect of emission from turbulence and field oscillations. In particular, we argue that despite uncertainty on the details of the signals, the prediction of a significantly steeper fall off in the spectrum from sound waves compared to that from bubble collisions is robust.

Theoretical uncertainty arises because results from numerical simulations require extrapolation to the large scale separations in the physical phase transitions. In particular, there is a large difference between the scale of the microscopic physics fixing the critical bubble radius and bubble wall thickness, and that of the Hubble distance setting the typical bubble radius at collision. Meanwhile theoretical predictions require simplifying approximations. Consequently, a combination of these approaches is required to maximise the reliability of predictions.

C.1 Bubble collisions

The envelope approximation has been used to make theoretical predictions of frequency dependence of the gravitational wave spectrum emitted by bubble collisions. The low frequency part of the gravitational wave spectrum is fixed by causality to have a power law $h^2\Omega_{\mathrm{GW}}(f) \propto f^3$ (where f is the frequency), since its source is uncorrelated on time scales bigger than $1/\beta$. As early as 1992, Kosowsky et al. proposed that the high frequency tail follows a power law $f^{-1.5}$. This work has since been complemented with an independent analytical estimate in [114] that predicts a f^{-1} dependence. The subsequent inclusion of a slight time dependence of the bubble nucleation rate, as might be the case in a thermal transition, only altered this prediction by $\mathcal{O}(10\%)$ and seems to leave the peak magnitude of the signal unchanged [115].

Numerical simulations using the envelope approximation were performed in [116] and support the idea of a gradual high frequency fall-off, finding a result that is closer to f^{-1}.

Subsequent work in [117], also using the envelope approximation, obtained compatible results, and argues that this is independent of the bubble nucleation rate.

More recently, facilitated by advances in computational power and techniques, [118] carried out large simulations of the gravitational wave emission in vacuum phase transition, by directly evolving a scalar field with a suitable potential. This allowed the validity of the envelope approximation itself to be tested precisely. They found a signal with an $f^{-1.5}$ high frequency decay and an overall magnitude that is the same as is obtained using the envelope approximation to within a factor of a few.[1] We will for the moment put this potentially important result to one side, and work with the established results from the envelope approximation, in the knowledge that the precise magnitude and spectrum of our expected signal might change slightly.

C.2 Sound waves

The gravitational wave power spectrum from acoustic waves has been studied in increasingly large simulations, in a range of hydrodynamic regimes and with different bubble wall velocities, in [120–122]. Even with the limited scale separations accessible in simulations, the sound waves are found to be an important source of gravitational waves if a significant fluid component exists, and that emission continues for at least a Hubble time after the bubbles collide. Following this numerical progress, [123] and [124] proposed analytical models for the emission of gravitational waves from sound waves.

[121] also discusses the extrapolation to the physical regime in the scenario that the bubble walls reach a terminal velocity and emission by sound waves overwhelmingly dominates that from bubble collisions. The model in [123] was also tested on the lattice in [122] and the two descriptions were found to be in broad agreement.

C.3 Turbulence in the plasma

The collision of acoustic sound shells stirs the plasma, and potentially produces turbulent flows. These start at the scale of the average bubble radius R_*, and cascade to smaller scales, until damped by viscosity [240, 241, 152, 242]. Gravitational waves are emitted during this process, potentially over a period of several Hubble times. If the hidden sector plasma is ionised with respect to a light gauge field, the evolution of the system is more complex. In this case hidden sector magnetic fields, sourced by the phase transition, are

[1] The earlier direct simulation of a scalar field [239] finds a gravitational wave signal with an amplitude dramatically smaller than the theoretical prediction, however this was not confirmed by [118], and the origin of this result remains unclear.

amplified dramatically and feed in to the dynamics, leading to a magneto-hydrodynamical (MHD) system [137, 139, 138].

Studying turbulence with numerical simulations is challenging, owing to the characteristic wide range of scales in the problem. The largest available simulations of gravitational wave production from phase transition, [121, 122], find no evidence for a significant turbulent contribution to the gravitational wave spectrum in a thermal transition, in the case that MHD effects are not included. However, these simulations are of relatively weak transitions. Numerical results analysing systems with larger fluid velocities, for which turbulence is expected to be more important, would be very welcome in determining the impact of this contribution (although existing simulations are already a numerical tour de force, and involve substantial computational resources).

When considering phase transitions in the visible sector, for which the plasma is ionised and MHD is the correct description of the system, the spectrum of gravitational waves emitted by turbulence is often assumed to take the standard Kolmogorov form, with an analytically calculated amplitude [139]. This can be parameterised as [101]

$$h^2\Omega_{\rm turb}(f) = 3.35\times10^{-4}\left(\frac{H_*}{\beta}\right)\left(\frac{\kappa_{\rm turb}\alpha}{1+\alpha}\right)^2\left(\frac{100}{g_*}\right)^{\frac{1}{3}} v_{\rm w}\, S_{\rm sw}(f) \tag{C.1}$$

where $\kappa_{\rm turb}$ is the fraction of latent heat released in the phase transition that is converted into turbulent flows. The spectral shape is

$$S_{\rm turb}(f) = \left(\frac{f}{f_{\rm turb}}\right)^3\left(\frac{1}{[1+(f/f_{\rm turb})]^{11/3}(1+8\pi f/h_*)}\right)^{7/2}, \tag{C.2}$$

where

$$h_* = 1.65\times10^{-3}\ \mu{\rm Hz}\left(\frac{T_{\rm v*}}{100\ {\rm GeV}}\right)\left(\frac{g_{\rm v*}}{100}\right)^{1/6}, \tag{C.3}$$

and the approximate peak frequency is

$$f_{\rm turb} = 2.7\times10^{-2}\,\mu{\rm Hz}\,\frac{1}{v_{\rm w}}\left(\frac{\beta}{H_*}\right)\left(\frac{T_{v*}}{100\,{\rm GeV}}\right)\left(\frac{g_{\rm v*}}{100}\right)^{\frac{1}{6}} \tag{C.4}$$

The fraction of the total energy density available for turbulent flows is parameterised as $\kappa_{\rm turb} = \varepsilon_{\rm turb}\kappa_{\rm sw}$, where $\varepsilon_{\rm turb}$ accounts for the efficiency with which bulk motion is converted to vorticity. It is generally thought that $\varepsilon_{\rm turb} \simeq 0.05 - 0.1$, although this is not conclusive.

For our present purposes, we assume that the contribution to the gravitational wave spectrum from turbulence is subleading to that from sound waves, which is accurate if the fits in Eq. (7.8) and (C.1) are accurate. If this is the case, the gravitational wave emission by turbulence will not affect any of the observational features that we subsequently identify, and can be safely neglected. Such an assumption is however not fully justified for the

model that we consider. As discussed, emission from the plasma will only be significant if the bubble walls reach a terminal speed, but the value of γ_w in such cases is still typically large. Despite this, we use the existing fits as a reasonable first approximation, which could be improved in future work.

C.4 Long lived oscillations after collisions

When bubbles collide they produce large amplitude non-linear oscillations in the scalar field, which act as a relatively long lasting source of gravitational waves. These were observed in [239], and studied carefully in [118] using large numerical simulations. This component of the spectrum is clearly identifiable in simulations of vacuum transitions, however it appears to be subsumed in (or simply subdominant to) the sound wave emission in simulations of thermal transitions.

The gravitational wave spectrum produced in long lived oscillations (in simulations of vacuum transitions) has a peak frequency that appears to be $\sim 1/l_0$, where l_0 is the thickness of the bubble walls, which has the parametric form [118]

$$l_0 \simeq \frac{1}{\sqrt{d^2V/d\phi^2}} \,. \tag{C.5}$$

The limited scale separations achievable in simulations means that the low frequency tail contribution from this source is mixed into the spectrum of gravitational waves from bubble collisions. At the physically relevant scale separation between H_*^{-1} and l_0, this emission would presumably lead to an extremely high frequency peak in the gravitational wave spectrum, well separated from the signal from bubble collisions.

In the largest simulations carried out so far, the gravitational wave spectrum from this source is found to still be growing when the simulations are ended [118], and at this time their contribution to the energy in gravitational waves is starting to exceed that from bubble collisions. However, as argued in [118], this appears to be an artifact of the limited scale separations in simulations. By analysing the rate at which the spectrum grows in simulations, and using the physical expectation that oscillations only persist for a time H_*^{-1}, they predict that the relative energy in the gravtiational waves produced by such oscillations $\Omega_{\rm osc}$ compared to that from bubble collisions scales as

$$\frac{\Omega_{\rm osc}}{\Omega_{\rm coll}} \simeq 10^2 \frac{l_0^2}{H_*^2} \,. \tag{C.6}$$

In the physically relevant regime, Eq. (C.6) predicts, very approximately, $\Omega_{\rm osc}/\Omega_{\rm coll} \lesssim w^2/M_{\rm Pl}^2$ (dropping numerical factors, gauge couplings, and factors of β/H_*). Therefore, in transitions happening in an effective vacuum, Eq. (C.6) means that a completely negligible

fraction of the total energy density in gravitational waves comes from long lived field oscillations sourced this way[2] The suppression in transitions with finite bubble walls speeds will be even stronger, since the vast majority of the energy released by the transition goes directly into the plasma. As a result, we do not need to consider this source when we subsequently study the gravitational wave spectra from hidden sectors.

[2]If further investigation reveals that the amplitude of the signal from this source is larger than predicted by Eq. (C.6), it would be interesting to investigate if it could lead to observable high frequency signals in some models.

Appendix D

Measurements of the SGWB and its polarisation

The signal-to-noise ratio (SNR) for combining two GW detector channels O and O' is

$$\mathrm{SNR}_{OO'} = \sqrt{\int_0^{t_{\rm obs}} \mathrm{d}t \int \mathrm{d}f \frac{S^*_{OO'}(f) S_{OO'}(f)}{P_{n,O}(f) P_{n,O'}(f)}}\,, \tag{D.1}$$

where $t_{\rm obs}$ is the total duration of the measurement and $P_{n,O}(f)$ and $P_{n,O'}(f)$ are the noise spectral functions in the channels O and O'. Following Ref. [243], the signal function $S_{OO'}(f)$ for a stochastic GW background, defined via the Fourier transform of the correlator of the GW signals passing through the O and O' channels, can be expanded as a function of the peculiar velocity of the solar system $v = 1.23 \times 10^{-3}$ as

$$S_{OO'}(f) = \frac{3H_0^2}{8\pi^2 f^3} \sum_\lambda \left\{ \mathscr{M}^\lambda_{OO'}(f)\, \Omega^\lambda_{\rm GW}(f) - 4iv\, \mathscr{D}^\lambda_{OO'}(f) \left[\Omega^\lambda_{\rm GW}(f) - \frac{f}{4} \frac{\mathrm{d}\Omega^\lambda_{\rm GW}(f)}{\mathrm{d}f} \right] + \mathscr{O}(v^2) \right\}, \tag{D.2}$$

where $\lambda = \pm 1$ is the GW helicity and

$$\begin{aligned} \mathscr{M}^\lambda_{OO'}(k) &= 4 \int \frac{\mathrm{d}\Omega_k}{4\pi} e_{ab,\lambda}(\hat{k}) e_{cd,\lambda}(-\hat{k}) \mathscr{Q}^{ab}_O(\vec{k}) \mathscr{Q}^{cd}_{O'}(-\vec{k})\,, \\ \mathscr{D}^\lambda_{OO'}(k,\hat{v}) &= 4i \int \frac{\mathrm{d}\Omega_k}{4\pi} e_{ab,\lambda}(\hat{k}) e_{cd,\lambda}(-\hat{k}) \mathscr{Q}^{ab}_O(\vec{k}) \mathscr{Q}^{cd}_{O'}(-\vec{k})\, \hat{k}\cdot\hat{v}\,, \end{aligned} \tag{D.3}$$

are the monopole and dipole response functions and $k \equiv |\vec{k}| = 2\pi f$. The matrices $\mathscr{Q}^{ab}_{O,O'}(\vec{k})$ contain the geometries of the detector channels, and the product of the polarisation operators appearing in the above expressions is given by

$$e_{ab,\lambda}(\hat{k}) e_{cd,\lambda}(-\hat{k}) = \frac{1}{4} \left(\delta_{ac} - \hat{k}_a \hat{k}_c - i\lambda \varepsilon_{ace} \hat{k}^e \right) \left(\delta_{bd} - \hat{k}_b \hat{k}_d - i\lambda \varepsilon_{bde} \hat{k}^e \right). \tag{D.4}$$

LISA consists of three spacecraft arranged in an equilateral triangle whose sides provide three baselines, and the combinations of pairs of these baselines form three laser interferometers. We denote the positions of the vertices of the triangle by $\vec{x}_i$ and we fix the side length to $L = 2.5 \times 10^6\,\mathrm{km}$ [244]. Linear combinations of the three interferometers can be used to construct three detector channels: A, E and T [245]. In the following we focus on the A and E channels, which are antisymmetric combinations of the three interferometers. The T channel, known as the null channel, is symmetric between the three interferometers and is relatively insensitive to the GW signal. The noise function, assumed to be equal for the A and E channels so that $P_{n,A} = P_{n,E} \equiv P_n$, is given by [246, 247] [1]

$$P_n(f) = \frac{1}{3}\left[2+\cos\left(f/f_0\right)\right]P_{\mathrm{IMS}}(f) + \frac{4}{3}\left[1+\cos\left(f/f_0\right)+\cos^2\left(f/f_0\right)\right]P_{\mathrm{Acc}}(f)\,, \quad \text{(D.5)}$$

where $f_0 = 1/(2\pi L) = 0.019\,\mathrm{Hz}$ and the interferometer measurement system noise is

$$P_{\mathrm{IMS}}(f) = 3.6\times 10^{-41}\,\mathrm{Hz}^{-1}\left[1+\left(\frac{2\mathrm{mHz}}{f}\right)^4\right], \quad \text{(D.6)}$$

and the acceleration noise is

$$P_{\mathrm{Acc}}(f) = 9.2\times 10^{-52}\,\mathrm{Hz}^{-1}\left(\frac{f}{\mathrm{Hz}}\right)^{-4}\left[1+\left(\frac{0.4\mathrm{mHz}}{f}\right)^2\right]\left[1+\left(\frac{f}{8\mathrm{mHz}}\right)^4\right]. \quad \text{(D.7)}$$

The $\mathscr{Q}_O^{ab}(\vec{k})$ matrices for the $O = A, E, T$ channels are linear combinations of those in the Michelson basis ($i = 1,2,3$): $\mathscr{Q}_O^{ab}(\vec{k}) = \sum_{i=1,2,3} c_O^i \mathscr{Q}_i^{ab}(\vec{k})$ [249], where

$$c = \begin{pmatrix} \frac{2}{3} & -\frac{1}{3} & -\frac{1}{3} \\ 0 & -\frac{1}{\sqrt{3}} & \frac{1}{\sqrt{3}} \\ \frac{1}{3} & \frac{1}{3} & \frac{1}{3} \end{pmatrix} \quad \text{(D.8)}$$

and

$$\mathscr{Q}_i^{ab}(\vec{k}) = \frac{1}{4}e^{-i\vec{k}\cdot\vec{x}_i}\left[\mathscr{T}(kL,\hat{k}\cdot\hat{l}_i)\hat{l}_i^a\hat{l}_i^b - \mathscr{T}(kL,-\hat{k}\cdot\hat{l}_{i+2})\hat{l}_{i+2}^a\hat{l}_{i+2}^b\right]. \quad \text{(D.9)}$$

Here $\hat{l}_i = (\vec{x}_{i+1}-\vec{x}_i)/L$ is the unit vector pointing from spacecraft i to spacecraft $i+1$, all indices $i, i+1, \ldots$ are modulo 3, and the detector transfer function is given by

$$\mathscr{T}(kL,\hat{k}\cdot\hat{l}) = e^{-ikL(1+\hat{k}\cdot\hat{l})/2}\,\mathrm{sinc}\left[\frac{kL}{2}(1-\hat{k}\cdot\hat{l})\right] + e^{i\pi kL(1-\hat{k}\cdot\hat{l})/2}\,\mathrm{sinc}\left[\frac{kL}{2}(1+\hat{k}\cdot\hat{l})\right]. \quad \text{(D.10)}$$

Using these we can calculate the monopole and dipole functions for LISA.

[1] See also the LISA Data Challenge Manual [248].

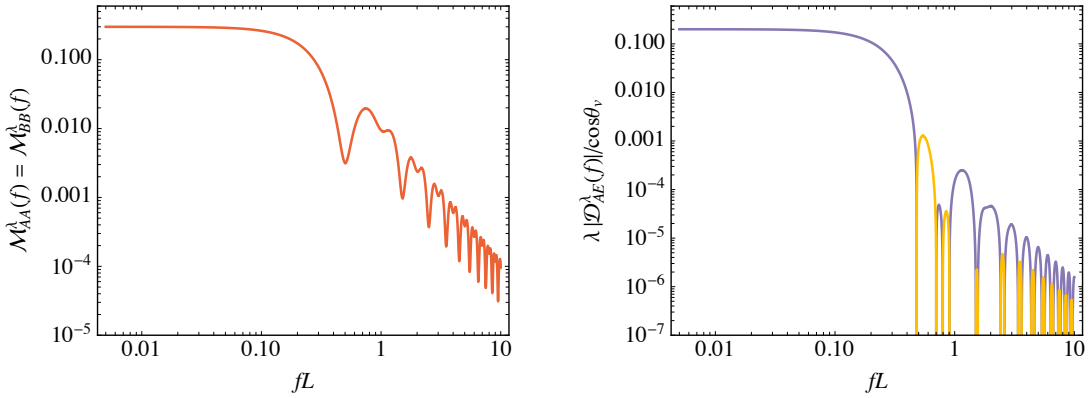

Fig. D.1 *non-zero monopole response function (left panel) and the dipole response function (right panel) for LISA. In the right panel the purple and yellow colours indicate positive and negative values for* $\lambda\,\mathscr{D}^{\lambda}_{AE}$.

The monopole functions $\mathscr{M}^{\lambda}_{AA}$ and $\mathscr{M}^{\lambda}_{EE}$ are equal, non-zero and independent of the helicity λ, whereas the corresponding dipole functions vanish: $\mathscr{D}^{\lambda}_{AA} = \mathscr{D}^{\lambda}_{EE} = 0$. Moreover, $\mathscr{M}^{\lambda}_{AE} = 0$, so the signal-to-noise ratio for LISA observing a GW monopole signal is therefore

$$\mathrm{SNR}_{\mathrm{tot}} = \sqrt{\mathrm{SNR}^2_{AA} + \mathrm{SNR}^2_{EE}} = \sqrt{2}\,\mathrm{SNR}_{AA}\,. \tag{D.11}$$

The dipole response function for the AE channel combination is instead non-zero. It depends on the angle θ_v between the normal of the LISA's detector plane and the direction of motion of the solar system, and the helicity of the signal, $\mathscr{D}^{\lambda}_{AE} \propto \lambda\cos\theta_v$. The AE channel therefore probes the circular polarisation of the GW signal and the signal-to-noise ratio for observing a circularly-polarised signal with LISA is given by

$$\mathrm{SNR}_{\mathrm{pol}} = \sqrt{\mathrm{SNR}^2_{AE} + \mathrm{SNR}^2_{EA}} = \sqrt{2}\,\mathrm{SNR}_{AE}\,. \tag{D.12}$$

The non-zero response functions $\mathscr{M}^{\lambda}_{AA} = \mathscr{M}^{\lambda}_{EE}$ and $\mathscr{D}^{\lambda}_{AE}$ are displayed in Fig. D.1.

In the left panel of Fig. D.2 we show the LISA sensitivities for the total GW signal and its polarisation defined as

$$P_{\mathrm{tot}}(f) = \frac{P_n(f)}{\mathscr{M}^{\lambda}_{AA}(f)}\,, \qquad P_{\mathrm{pol}}(f) = \frac{P_n(f)}{4v\mathscr{D}^{\lambda}_{AE}(f)\,\mathscr{P}_{\mathrm{GW}}}\,, \tag{D.13}$$

where $\mathscr{P}_{\mathrm{GW}}$ denotes the fractional polarisation of the GW signal (see Eq. (8.35)). In the right panel of Fig. D.2 we show the power-law integrated sensitivity curves for LISA assuming $t_{\mathrm{obs}} = 4\,\mathrm{y}$ and the threshold $\mathrm{SNR} = 10$, for different values of the polarisation fraction $\mathscr{P}_{\mathrm{GW}}$. We find that LISA can observe the polarisation of a fully-polarised GW signal down to $h_0^2\Omega_{\mathrm{GW}} = 4\times10^{-11}$, in agreement with Ref. [243]. The sensitivity scales as a function of the polarisation fraction of the signal as $1/\mathscr{P}_{\mathrm{GW}}$.

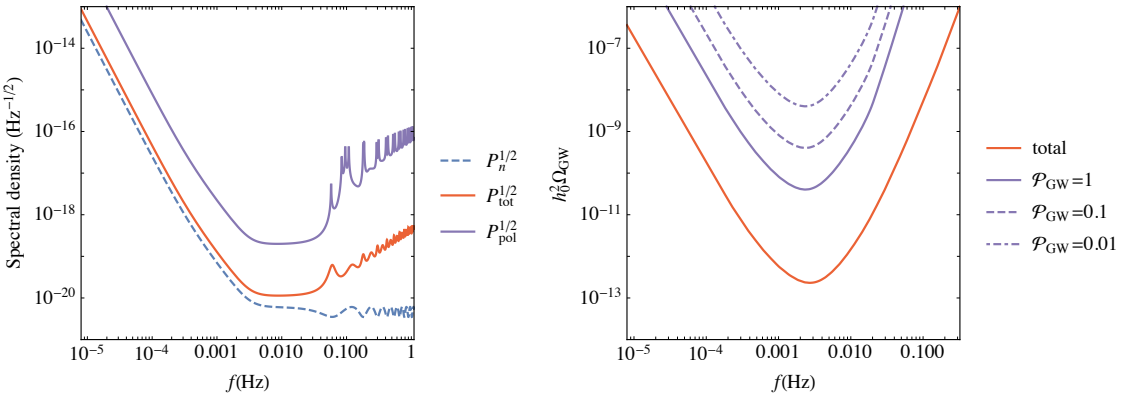

Fig. D.2 *Left panel: The dashed line shows the noise spectral density $P_n^{1/2}$ for LISA, the solid red line the corresponding sensitivity for the total GW signal and the solid purple line the corresponding sensitivity for a fully polarised GW signal, $\mathscr{P}_{\rm GW} = 1$. Right panel: The power-law integrated LISA sensitivity curves for the total GW signal and polarisation of the GW signal for a 4-year integration time with different values of the polarisation fraction $\mathscr{P}_{\rm GW}$ (see Eq.* (8.35)*).*

It is clear from the above discussion that detectors with just a single interferometer channel, such as a single LIGO detector, cannot detect circular polarisation of the SGWB. Nor, indeed, can AEDGE or a pair of such detectors. On the other hand, missions with one or more triangular sets of interferometers such as ALIA, BBO [250], DECIGO [251] and AMIGO [252] would be sensitive to polarisation of the SGWB at higher frequencies than LISA.